Deep Water Formation and Spreading Dynamics in the subpolar North Atlantic from Observations and high-resolution Ocean Models

Dissertation

zur Erlangung des Doktorgrades

der Mathematisch-Naturwissenschaftlichen Fakultät

der Christian-Albrechts-Universität zu Kiel

vorgelegt von:

Patricia Vera Klara Handmann

Kiel, 2019

Referent	Prof. Dr. Martin Visbeck
Koreferent	Prof. Dr. Claus Böning
Tag der mündlichen Prüfung:	08.10.2019
Zum Druck genehmigt:	08.10.2019

Gez. Prof. Dr. Frank Kempken, Dekan

Erklärung

Hiermit erkläre ich an Eides Statt, dass ich die vorliegende Dissertation, abgesehen von der Beratung durch meinen Betreuer Prof. Dr. Martin Visbeck, selbstständig und ohne fremde Hilfe angefertigt, keine anderen als die angegebenen Quellen und Hilfsmittel benutzt und die den benutzten Quellen wörtlich oder inhaltlich entnommenen Stellen als solche kenntlich gemacht habe. Diese Arbeit hat in gleicher oder ähnlicher Form noch keiner Prüfungsbehörde vorgelegen. Sie ist unter Einhaltung der Regeln guter wissenschaftlicher Praxis der Deutschen Forschungsgemeinschaft entstanden. Mir, Patricia Vera Klara Handmann, wurde bis zum jetzigen Zeitpunkt noch kein akademischer Grad entzogen.

Kiel,18.07.2019

_____

(Patricia Vera Klara Handmann)

Abstract

The subpolar North Atlantic (SPNA) circulation is comprised of a complex interplay between the wind-driven gyre circulation and the buoyancy driven meridional overturning circulation (MOC). As the Atlantic MOC (AMOC) plays an essential role in our climate system due to the associated meridional transport of heat, mass and freshwater it is of fundamental importance to understand its forcing mechanisms, variability and impacts on various different time scales. Due to its role in the formation of North Atlantic Deep Water (NADW), the SPNA is of crucial importance to the understanding of the AMOC. This thesis presents selected aspects of the SPNA circulation dynamics, based on various observational data sets in combination with two high-resolution ocean general circulation models (OGCMs; VIKING20, VIKING20X).

In order to understand observations in correspondence with OGCM output, the model fidelity in comparison to observed quantities has to be secured. These quantities should be available for sufficiently long time scales and should be determined similarly in the OGCM and the observations. Using observational data in the vicinity of 53°N in the Labrador Sea and the ocean model VIKING20, the following comparable robust integral quantities were defined: the magnitude and spatial and temporal variability of integral circulation elements on the regional scale (NADW transport at 53°N; 33 Sv model, 31 Sv observations), the horizontal and vertical extend of the March Mixed Layer Depth in the Labrador Sea and the gyre scale baroclinicity. The models' boundary current system is more barotropic and indicates stronger monthly to interannual transport variability compared to the observations. Furthermore, during periods of enhanced deep convection an increased correlation between different components of NADW is found in the model, which is found to be the result of a complex modulation of wind stress and buoyancy forcing on regional and basin wide scale. Apart from the challenging to measure AMOC strength, these above mentioned regional and basin scale quantities were found to be suitable for model verification.

The export routes of deep water from the Labrador Sea with a specific focus on the connection to the Irminger Sea are further investigated using different Lagrangian particle tracking experiments based on both the Argo observations as well as the VIKING20X model output. The connection between the Labrador- and Irminger Sea on the Labrador Sea water (LSW) depth is evaluated with pure advective trajectory integration as well with a simple additional diffusion parametrization. Advective experiments with the temporarily varying model output and seeding in the central Labrador Sea and the advective-diffusive experiments with the Argo based Eulerian velocity fields resulted in $\sim 20\%$ of the total particles connecting the two regions

within 1.5 - 2.5 years, with shorter transit times in the model ($\sim$ 1.5 years). The DWBC export of LSW towards the south was found to be strongly decreased with the applied diffusion parameterization. A relatively simple method reproduced a similar connection of the two regions as derived from various observations.

The relation between the SPNA AMOC and the horizontal circulation of the subpolar gyre was then subject to a model only study with VIKING20. Current transports and the AMOC strength are evaluated along the "Overturning in the Subpolar North Atlantic Program" (OSNAP) array and a section spanning the Greenland-Scotland Ridge (GSR), where for both recently observational estimates became available. The AMOC strengths (GSR 6.6 ± 0.9 Sv, OSNAP eastern leg 17.2 ± 3.0 Sv) are comparable with observational values. However, due to the limited time series of observations, the variability of the AMOC can only be determined with the model on longer than interannual time scales. In VIKING20 all SPNA currents, the AMOC and the subpolar gyre index exhibit strong interannual to decadal variability. Using a simple box model, water mass transformation in the SPNA showed similar formation rates in the Labrador Sea (7.7 ± 3.0 Sv) compared to the Irminger Sea (1.6 ± 2.8 Sv) and Iceland basin (5.1 ± 1.2 Sv) combined. During periods of deep convection (1990's) the transport of the boundary currents and the North Atlantic current import through the Iceland basin is particularly enhanced suggesting a similar forcing mechanism.

Zusammenfassung

Das subpolare nordatlantische Strömungssystem besteht aus der windgetriebenen horizontalen Zirkulation des subpolaren Wirbels und der auftriebsgetriebenen vertikalen Umwälzzirkulation (MOC). Es wird von komplexen Mechanismen auf verschiedenen Raum- und Zeitskalen angetrieben. Da die atlantische MOC (AMOC) durch ihren meridionalen Transport von Wärme, Masse und Frischwasser eine wichtige Rolle in unserem Klimasystem spielt, ist es fundamental wichtig ihre Antriebsmechanismen, Variabilität und ihren Einfluss auf verschiedenen Zeitskalen zu verstehen. Aufgrund seiner Rolle in der Bildung von Nordatlantischem Tiefenwasser (NADW) ist der subpolare Nordatlantik wichtig für das Verständnis der AMOC. Mit Hilfe von Messdaten und zwei hochaufgelösten Ozeanmodellen (VIKING20, VIKING20X) behandelt diese Arbeit verschiedene Aspekte der Zirkulationsdynamik im subpolaren Nordatlantik.

Um Messungen im Zusammenhang mit Ozeanmodellen zu verstehen muss zunächst die Realitätsnähe des Models mit gemessenen Größen sicher gestellt werden. Diese Messgrößen sollten für genügend lange Zeiträume verfügbar und im Modell gleich definiert sein. Messdaten aus dem Umfeld von $53°$N in der Labrador See und das Ozeanmodel VIKING20 wurden hier benutzt. Die folgenden robust vergleichbaren Größen wurden definiert: Die Stärke sowie örtliche und zeitliche Variabilität der Strömungen auf der regionalen Ebene (NADW Transport bei $53°$N; 33 SV Model, 31 Sv Messungen), die horizontale und vertikale Ausdehnung der Vermischungsschicht im März sowie die groß-skalige Baroklinizität. Im Modell ist das Randstromsystem barotroper und zeigt stärkere monatliche bis interannuale Schwankungen als in den Messungen. Während Perioden mit stärkerer Tiefenkonvektion wurde eine verstärkte Korrelation zwischen den verschiedenen NADW Komponenten im Modell festgestellt. Diese wurden als Ergebnis der komplexen Interaktion zwischen Wind- und Auftriebsantrieb auf regionaler und beckenskaliger Ebene interpretiert. Abgesehen von der Stärke der Umwälzzirkulation, deren Messung eine Herausforderung darstellt, sind diese regionalen und groß-skaligen Größen verwendbar für die Evaluierung von Ozeanmodellen.

Anschließend wurde das Ozeanmodell VIKING20X in Verbindung mit Argo-basierten Geschwindigkeitsfeldern für eine Lagrangesche Konnektivitätsstudie benutzt. Mittels advektiver und advektiv-diffusiver Trajektorienbestimmung wurde die Verbindung zwischen der Labrador- und der Irmingersee auf der Tiefe von Labradorsee Wasser (LSW) untersucht. Die rein advektiven Experimente mit dem zeitlich variablen Ozeanmodell, bei denen die Partikel in der Labradorsee eingesetzt wurden, sowie die Argo-basierten advektiv-diffusiven Experimente resultierten in einer Menge von $\sim 20\%$ der eingesetzten Partikel, die die Labrador-

mit der Irmingersee in 1.5 - 2.5 Jahren verbinden. Kürzere Transitzeiten sind hier in den Modellexperimenten zu finden ($\sim$ 1.5 Jahre). Zusätzlich wurde eine Verminderung des südwärtigen Exportes entlang des tiefen westlichen Randstromes im Zusammenhang mit der angewendeten Diffusion festgestellt. Mit einer relativ einfachen Methode konnten so aufwändig gemessene Konnektivitäten der beiden Regionen reproduziert werden.

Abschließend wurde die Interaktion zwischen der dichtegetriebenen atlantischen Umwälzzirkulation und der windgetriebenen Zirkulation des subpolaren Wirbels in VIKING20 untersucht. Die Strömungen und die Stärke der Umwälzzirkulation wurden an zwei Messabschnitten, dem „Overturning in the Subpolar North Atlantic Program“ (OSNAP) Verankerungsarray und entlang des Grönland-Schottland-Rücken, bestimmt. Die Stärke der ermittelten simulierten Umwälzzirkulation (GSR 6.6 ± 0.9 Sv, OSNAP östlicher Abschnitt 17.2 ± 3.0 Sv) ist vergleichbar mit gemessenen Werten . Aufgrund der relativ kurzen Messzeitserien kann nur im Modell die Variabilität auf längeren Zeitskalen untersucht werden. Starke interannuale (1 Jahr) und dekadische (15-20 Jahre) Variabilität ist in allen Strömungszeitserien, sowie in der Stäke der Umwälzzirkulation und der Beckenzirkluation zu finden. Mit einem einfachen Boxmodell wurde die Wassermassentransformation der drei subpolaren Becken bestimmt. Die Labradorsee (7.7 ± 3.0 Sv) bildet soviel Labradorsee Wasser wie die Irmingersee (1.6 ± 2.8 Sv) und das Islandbecken (5.1 ± 1.2 Sv) zusammen. Während der Periode vermehrter Tiefenwasserbildung in den 1990er Jahren ist der Transport der Randströme, entlang von Grönland und Neufundland, und des Nordatlantikstromes durch das Islandbecken erhöht, was einen gemeinsamen Antriebsmechanismus nahe legt.

Contents

1. Introduction

1.1 Role of the Ocean in the Climate System

Due to its proximity and importance for the European seafarer nations the North Atlantic has been systematically studied since the early 19^{th} century. Understanding the large scale circulation of the ocean has long been one of the major challenges. For example, 1512 the Gulf Stream was first mentioned [*Fernández-Armesto*, 2007] but it took over 400 years until Henry Stommel theoretically explained the Gulf Stream as the western intensification caused by the latitudinal variation of the Coriolis force. Based upon relatively simple theory a more sophisticated view of the ocean emerged. The oceans thermal structure and stratification, the global abyssal circulation, convection events as well as its high temporal variability and its turbulent nature attracted scientific attention [*Wunsch*, 1997], which finally started to reveal the role of the ocean circulation in our climate system [*Rahmstorf* , 1994; *Stocker and Wright*, 1991].

An oceanic key component of the global climate system is the meridional overturning circulation (MOC) [*Buckley and Marshall*, 2015; *Jackson et al.*, 2016]. Together with the atmosphere it moves heat from equatorial regions to the high latitudes balancing the latitudinal differences in the solar energy input. As indicated in the name the MOC is mainly comprised of an overturning movement. However, the overturning interacts with the persistent wind-driven circulation, the subtropical and the subpolar gyre, leading to a complex three dimensional circulation pattern encircling the entire globe. Hence, it is driven by a combination of forcing parameters including winds (easterlies, westerlies and trade winds), buoyancy forcing (evaporation, precipitation, heating, and cooling) and mixing due to winds and tides. However, the respective influence of each of these drivers is still under debate (e.g. *Biastoch et al.* [2008]; *Buckley and Marshall* [2015]; *Richardson* [1983]; *Visbeck* [2007]; *Yang et al.* [2015]).

The MOC is distributing heat, mass, fresh water and tracers around the globe (Figure 1.1) [*Lozier*, 2012; *Talley et al.*, 2011]. The Atlantic MOC (AMOC) mainly determines the oceanic component of the northward heat transport from low to high latitudes. Furthermore, it connects the northern and southern hemisphere and is the principal reason for inter-hemispheric climate and energy asymmetries, namely the warmer northern hemisphere through northward cross-equatorial ocean heat transport [*Buckley and Marshall*, 2015; *Kang et al.*, 2015; *Ruzmaikin et al.*, 2015; *Trenberth et al.*, 2014]. The heat which is lost during its way north through the Gulf Stream and the NAC, keeps the Northern Hemisphere and particularly western Europe warmer than the zonal mean.

Mathematically, the AMOC is characterized by the maximum of the overturning stream function in density or depth space. It is defined as the zonal and vertical integral of the northward volume transport V ([Sv], where 1 Sv $= 1 \times 10^6\ m^3 s^{-1}$). Its strength, is defined at time t at each latitude (ϕ) to be the maximum of the overturning stream function Ψ:

$$\begin{aligned} AMOC(\phi, t) &= max(\Psi(\phi, d, t)) \\ &= max\left[\int_{d_{bottom}}^{d_{top}} \int_{\theta_w}^{\theta_e} V(\theta, \phi, d, t) \mathrm{d}\theta \mathrm{d}d\right] \\ &= max\left[\sum_{d_{bottom}}^{d_{top}} \sum_{\theta_w}^{\theta_e} V(\theta, \phi, d, t)\right] \end{aligned} \tag{1.1}$$

where the integral can be built over density σ or depth d and θ is the longitude where the subscript e/w stand for east/west. The integral becomes discrete for the application on gridded data (observations, ocean models).

In the Atlantic the MOC (AMOC) is comprised of 2 vertical circulation cells: The "upper cell" emanating in the northern North Atlantic, which ventilates the upper ∼2 km of the ocean and the "lower cell", which originates around Antarctica and supplies the abyssal ocean with very dense water [*Buckley and Marshall*, 2015]. In this thesis I focus on the "upper cell" of the AMOC in the subpolar North Atlantic (SPNA). It is associated with the transformation of warm and saline northward flowing surface waters to cold and fresh deep waters. The deep waters then move southward being enlightened and returned to the surface in different parts of the world ocean and then return as the warm northward return flow. This relatively warm and salty "upper" AMOC limb in the SPNA consists of the Gulf Stream and its northern extension, the North Atlantic Current (NAC), which supply these warm and salty waters to the northeast Atlantic (Figure 1.1a,b). The NAC splits into a branch toward the Nordic seas, via the Iceland-Scotland Ridge and a branch reaching the Irminger Sea via the Reykjanes Ridge [*Church*, 2007; *Nansen*, 1912; *Siedler et al.*, 2001]. This warm and salty "upper" AMOC water is transformed to the cold and fresh "lower" AMOC limb in the SPNA. This water mass transformation, termed deep convection, depends not only on the prevailing heat/buoyancy loss, but also on the preconditioning formed by initial stratification and the regional circulation patterns. Deep convection occurs at multiple locations in the worlds oceans. In the subpolar North Atlantic it occurs in the Nordic Seas, the Irminger and the Labrador Sea [*Lazier*, 1973; *Lazier et al.*, 2001; *Marshall and Schott*, 1999; *Pickart et al.*, 2005]. Hence, the SPNA is a region of importance for the meridional exchange of heat, freshwater and tracers in the Atlantic basin (e.g. reviewed by *Buckley and Marshall* [2015]; *Daniault et al.* [2016]). AMOC variations on decadal to multidecadal timescales are often related to shifts in the earths climate [*Broecker*, 1991, 1997; *Rahmstorf*, 1994; *Stocker and Wright*, 1991]. Hence, fluctuations in the strength of the overturning might have a significant influence on climate variations in Northern Europe and the Northern Hemisphere [*Delworth and Mann*, 2000].

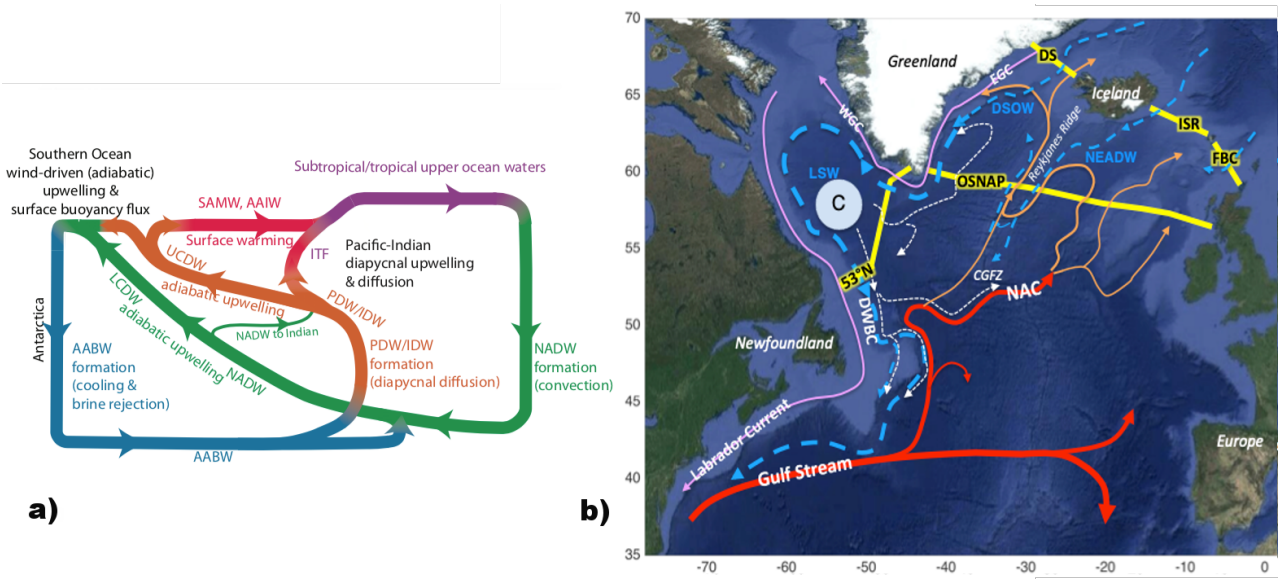

Figure 1.1: *a) 2-d schematic of the Atlantic MOC cells. Showing the interconnection between the different water masses of the global ocean (Surface waters: purple, intermediate waters: red, NADW: green, Indian Ocean Deep Water IDW: orange, Pacific Deep Water PDW: orange and Antarctic Bottom Water AABW: blue)[Talley et al., 2011]. b) Schematic map of the current system in the subpolar North Atlantic related to the AMOC Warm and salty surface current pathways (Gulf Stream/NAC) are marked in red. The deep components are depicted via a blue dashed line (DWBC). Names of currents (white, West Greenland Current (WGC), East Greenland Current (EGC)), water masses (thick blue, LSW, DSOW,NEADW), the convection region(C) and hydrographic sections(yellow) are marked above the related subject. Possible export pathways of LSW from the central Labrador Sea into the subpolar North Atlantic are marked via dashed white lines (adapted from Handmann et al. [2018]).*

Since the industrialization the amount of greenhouse gases in the atmosphere has risen to levels unprecedented during the last 800,000 years [*Keeling et al.*, 2005; *Lüthi et al.*, 2008]. Rising atmospheric and ocean surface temperatures, shifted wind patterns and the melting of glaciers and ice sheets are related to these changes in the atmosphere and affect the solubility of carbon dioxide in sea water, sea water density and the feedback processes between the ocean surface and the atmosphere above [*Stocker et al.*, 2013]. The highly complex system of interaction between the ocean and the atmosphere complicates the task to understand and predict the consequences of the global warming and pollution.

From the current understanding the AMOC strength on decadal to centennial timescales, is related to the sea surface temperatures (SST) within the North Atlantic [*Ba et al.*, 2014; *Delworth et al.*, 1993; *Delworth and Mann*, 2000; *Gastineau and Frankignoul*, 2012; *Knight et al.*, 2005; *Latif et al.*, 2004]. Although, the exact forcing mechanisms and related forcing parameters influencing SST are still under debate (aerosol concentration and the respective influence on the shortwave radiation or the AMOC strength) the AMOC

strength has been shown to play a major role [*Booth et al.*, 2012; *Delworth and Mann*, 2000; *Drews and Greatbatch*, 2016; *Latif et al.*, 2004]. An increase in AMOC strength leads to a general warming of the North Atlantic. It is further associated with less sea ice and a warmer climate in the Arctic as well as a northward displacement of the ITCZ (e.g. *Zhang and Delworth* [2005]). A slow-down of the AMOC would consequently lead to a cooling of the SSTs, which was hypothesized to enhance the extent of Arctic sea ice and invoke an equatorward shift of the Intertropical Convergence Zone (ITCZ), which is then related to a weaker rainfall [*Zhang and Delworth*, 2006]. In general changes in SSTs influence the atmosphere and can affect the rainfall over the Sahel zone [*Folland et al.*, 1986], India [*Zhang and Delworth*, 2006] and Brazil [*Kayano and Capistrano*, 2014], the hurricane activity over the Atlantic [*Goldenberg et al.*, 2001], the summer climate in Europe and North America [*Enfield et al.*, 2001; *Sutton and Hodson*, 2005], the amount of Arctic sea ice [*Chylek et al.*, 2009] and the melting of the Greenland Ice Sheet [*Hurrell and Deser*, 2010]. Hence, observing and understanding the AMOC, its variability and the related impacts is of great societal interest.

Furthermore, changes in the AMOC could be related to the observed warming of the oceans [*Budéus et al.*, 1998; *Johnson et al.*, 2008; *Levitus et al.*, 2012; *Patara and Boning*, 2014; *Purkey and Johnson*, 2010]. Other aspects of increasing sea water temperatures are that they lower the solubility of oxygen in sea water and can lead to deoxygenation [*Schmidtko et al.*, 2017]. Additionally, the warming can be related to a global shift of fresh and saline waters [*Chanut et al.*, 2008; *Curry et al.*, 2003], which combined with the warming trend, can impact the formation of deep waters via deep convection [*Behrens et al.*, 2013; *Böning et al.*, 2016]. This is particularly interesting in light of the fact that north of 50°N, the Atlantic accounts for 20% of the annual mean carbon uptake [*Khatiwala et al.*, 2013; *Takahashi et al.*, 2009]. In summary, to understand and predict the changes the earths climate system will experience under a warming climate the links between AMOC changes and changes in the formation and spreading of deep-water are crucial.

1.1.1 Deep Water Formation in the subpolar North Atlantic

Deep water formation in the subpolar North Atlantic occurs due to strong ocean-atmosphere interaction, mostly during winter, when sufficiently strong heat loss prevails which leads to comparably high densities and finally to static instability. This eventually introduces deep mixing and convection both in the open ocean [*Haine et al.*, 2008; *Lazier*, 1973; *Lazier et al.*, 2001; *Marshall and Schott*, 1999] and near the shelf breaks of the basins [*Spall and Pickart*, 2003]. The vertical sinking entrains lighter water from the surroundings and the final mixing depth depends on the details of the mixing processes and of course on the surrounding densities. The prevailing cyclonic circulation patterns at various locations in the Nordic Seas, the Irminger and Labrador Sea further preconditions deep convection due to a doming of isopycnals exposing density surfaces with a comparably high density to strong surface fluxes [*Marshall and Schott*, 1999]. The freshly formed deep waters are named regarding their formation region North Atlantic Deep Water (NADW) and

are further classified depending on their respective formation region Labrador Sea Water (LSW), Northeast Atlantic Deep Water (NEADW) and Denmark strait Overflow Water (DSOW) (Figure 1.1 b). NADW formation through deep convection is associated with fluxes of salt and other substances such as oxygen, anthropogenic carbon and other nutrients towards depth and hence ventilates the deep oceans. This deep and cold newly formed NADW then leaves the formation region and while travelling southward contributes to the "lower" limb of the AMOC [*Olbers et al.*, 2012].

As mentioned above, NADW is a combination of three water masses with different origins. The upper component, the LSW, is formed through deep convection processes in the central Labrador and the Irminger Sea [*Marshall and Schott*, 1999]. The mid-component, the NEADW, is overflow water from the Iceland-Scotland Ridge (ISR,Figure 1.1 b) experiencing property changes along its pathway along the topography of the Iceland basin, the Reykjanes Ridge and the Irminger basin on its way south. The densest component is the DSOW entering the Irminger Sea from the Nordic Seas through the Denmark Strait (DS, Figure 1.1 b). NEADW and DSOW form the Lower North Atlantic Deep Water (LNADW) and represent the densest water masses of the lower AMOC limb. Both components of the LNADW are formed in the region north of the Greenland-Scotland-Ridge in the Nordic Seas and mainly trespass towards the south via the Denmark Strait, the Faroe Bank Channel (FBC, Figure 1.1 b), and the Iceland-Faroe Ridge [*Dickson and Brown*, 1994]. The Denmark Strait is thought to give passage to the largest overflow plume [*Jochumsen et al.*, 2012]. The processes imprinting variability on the LNADW components remains a subject of discussion [*Zantopp et al.*, 2017], though *Olsen et al.* [2008] showed compensation of the barotropic and baroclinic responses to the wind forcing at the Greenland-Scotland Ridge giving rise to a very stable overflow into the subpolar North Atlantic. From the overflows these waters spread into the subpolar North Atlantic through interior [*Holliday et al.*, 2009] and boundary current pathways and eventually get exported to the south. The connection between the formation of overflow waters in the Nordic Seas and the overall AMOC variability is still a matter of active research due to the possibility of interior pathways [*Holliday et al.*, 2009; *Lozier*, 2010].

The LSW as the upper component of the North Atlantic Deep Water(e.g. *Lazier* [1973]) has a cold and low salinity signature combined with an anomalously low potential vorticity and a high concentration of dissolved oxygen and anthropogenic tracers (CFC, anthropogenic CO_2 etc. [*Rhein et al.*, 2002, 2017; *Smethie Jr. and Fine*, 2001; *Talley and McCartney*, 1982; *Yashayaev and Loder*, 2016]. The formation of LSW was shown to be strongly affected by the phase of the North Atlantic Oscillation (NAO, [*Dickson and Brown*, 1994]. The NAO is a dominant feature of atmospheric variability related to the strength of the cyclonic circulation over the region [*Hurrell*, 1995]. It controls the strength and direction of westerly winds and location of storm tracks across the North Atlantic through the strength of a bipolar atmospheric pressure pattern between Iceland and the Azores [*Hurrell*, 1995]. During a positive phase of the NAO, when

the Icelandic low is anomalously deep and the Azores high is anomalously high, there is greater cyclonic activity bringing stronger, cold and dry westerlies from the Canadian Arctic to the SPNA enhancing heat loss from the ocean surface to the atmosphere in the Labrador Sea [*Group*, 1998].

Over the past decades LSW was only thought to be formed in the central Labrador Sea (hence the name) and only recently the southwestern Irminger Sea was found to possess the distinctive properties to act as a possible formation region of LSW [*Bacon et al.*, 2003; *de Jong et al.*, 2016, 2018; *Falina et al.*, 2007; *Pickart et al.*, 2003a; *Piron et al.*, 2016; *Våge et al.*, 2008]. The LSW then spreads into the subpolar North Atlantic and towards the south through interior pathways and follows the pathway of the deep western boundary currents (DWBC). As the spreading of LSW is subject to chapter 3 it will be more thoroughly introduced there.

As mentioned above the AMOC strength in the SPNA is related to the transformation of upper AMOC limb water to NADW through deep convection. Measuring deep water formation rates (temporally and spatially) is very challenging and is only recently becoming more feasible since the advent of the Argo era, but is still drawing a fragmentary picture. Over the past decades, the formation rate of LSW and the DWBC transport were thought to be closely related [*Eden and Willebrand*, 2001; *Schweckendiek and Willebrand*, 2005]. However, *Schott et al.* [2004] showed that DWBC transports at Grand Banks at $43°$N appeared very similar during periods of enhanced deep convection 1993-1995 and periods of extremely weak LSW formation 1999-2001 [*Lazier et al.*, 2002]. This was further established by demonstrating that there is no clear link between the export at $53°$N and LSW production [*Zantopp et al.*, 2017]. Parallel to the efforts based on observational methods, multiple modeling studies assessed the basin-wide and DWBC response to deep water formation and concluded strong correlations between them [*Böning et al.*, 2006; *Brandt et al.*, 2007]. Furthermore, it was shown that the measurements at $53°$N can serve as an indicator for thermohaline induced MOC variability [*Böning et al.*, 2006; *Eden and Willebrand*, 2001; *Jayne and Marotzke*, 2001; *Lozier*, 2012]. *Straneo* [2006] proposed a simple two layer, two element model to tackle the interaction between the interior and boundary currents in the Labrador Sea. Here, LSW fills the depths of the interior Labrador Sea capped with an upper layer and a two layer boundary current encircles this interior. After deep convection the interior is colder and fresher than the surroundings and through an eddy driven heat exchange the boundary current gets denser. *Palter et al.* [2008] support this interaction scheme, showing the influence of strong eddy heat fluxes between the boundary current and the interior on the variability of the LSW export through the DWBC. Furthermore, *Pickart and Spall* [2007] showed minimal impact of strong wintertime convection to the strength of the overturning cell. Thus the variability found in the boundary current transport is expected to be dependent on the property gradients between the interior and the boundary currents and the strength of the overall eddy field [*Straneo*, 2006] rather than

being directly connected to the overall variability of the AMOC in the SPNA [*Lozier et al.*, 2019]. The actual link between the LSW formation and the AMOC is hence still widely discussed [*Lozier*, 2010; *Zou and Lozier*, 2016].

1.2 Observations in the subpolar North Atlantic

Repeated measurements with high spatial resolution are required to monitor the oceans variability. Long time series of high precision are crucial to detect circulation changes and the inherent variability on different time scales.

While hydrographic measurements were already available at a certain precision in the early 1900, only electronic and mechanical development lead to the first short term (max. 30 days) direct current measurements in 1960/70. Until the 1990's mainly local survey programs were conducted. 1990 marks the transition to more international collaborations under the premise of gaining long-term time series with high quality and sustained measurements: the World Ocean Circulation Experiment (WOCE). Until WOCE estimates of the AMOC were computed solely by computing the respective transport from geostrophic velocities derived from hydrographic data. For the deep flow these estimates revealed a transport of 7 Sv towards the south from the North Atlantic [*Sverdrup et al.*, 1942; *Worthington*, 1976]. Estimates from coast-to-coast hydrographic sections in the 1980's then increased the expected overturning volume to 18 Sv [e.g *Hall and Bryden* [1982]; *Roemmich and Wunsch* [1985]] which is still considered a valid estimate. These studies provided the first estimates of the magnitude and structure of the subtropical AMOC. They relied on ship transects which could, due to their snapshot like nature, only grant a limited view on the AMOC state, which could be biased towards a season or a certain mesoscale dominated state. The sustained observing programs of WOCE were using a combination of repeated ship sections, satellite altimetry, hydrography, and other quasi-global datasets to compute the first MOC estimates serving as ground truth for satellite observations and to tune ocean model parameterizations and damping parameters or simply to compare the model performance to observations [*Gould et al.*, 2013; *Wunsch and Heimbach*, 2013a]. The challenges of interpreting sparsely sampled in-situ data especially when trying to characterize long-term changes in the oceans became more apparent [*Wunsch*, 2001].

The observation of the AMOC at only one latitude is already very cost intensive and requires measurements spanning the entire ocean basin. Since the 2000's multiple efforts emerged to estimate the AMOC at the basin scale at different latitudes. These multi-nation programs use a combination of shipboard, satellite, Argo floats, gliders and moored measurements at key east-west sections across the Atlantic basin. These programs include the SAMOC/SAMBA array in the subtropical South Atlantic since 2009 [*Meinen et al.*, 2018], the first basin wide array RAPID-MOCHA-WBTS since 2004 [*Smeed et al.*, 2016] in the subtropical North Atlantic at $26.5°N$, the regular coverage of the Ovide shipboard section since 1993 [*Mercier et al.*,

2015] and the OSNAP section since 2016 [*Lozier et al.*, 2017] in the subpolar North Atlantic. The data gained from these transbasin efforts led to multiple estimates of the AMOC strength and its short term variability and opened the discussion for the role of multi-annual to decadal variability and its relation to surface variables like the SST or possible long term trends [*Rahmstorf et al.*, 2017; *Smeed et al.*, 2014].

These efforts are measuring the AMOC related transports at different latitudes. *Bingham et al.* [2007] and *Baehr et al.* [2009] showed in modelling studies that the AMOC transports are coherent within the gyres (subtropical/subpolar) themself over the course of years but that there is no coherence across the gyre-gyre boundary ($\sim 40°$N). Consequently, the AMOC variability measured at one latitude in one gyre e.g at RAPID/MOCHA array in the subtropical gyre is not necessarily representing the variability at a different latitude in a different gyre e.g at OSNAP in the subpolar gyre. However, the transbasin AMOC estimates at the various latitudes open the possibility to further investigate the inter-hemispheric and hemispheric meridional coherence of the AMOC between the subpolar regions and subtropics on multi-annual to decadal timescales if long enough in place.

For the decadal to centennial timescales of AMOC related variability of dynamic and hydrographic properties, its complexity and spatial extent, observations are sparse and commonly of short temporal length [*Böning et al.*, 2016; *Le Bras et al.*, 2018; *Longworth and Bryden*, 2007; *Mielke et al.*, 2015; *Srokosz et al.*, 2012; *van Sebille et al.*, 2011]. Generally, direct velocity measurements are even more sparse than hydrographic measurements. While the efforts of the past and present are temporarily and spatially unevenly distributed, the launched initiatives already tackle the interannual to decadal timescales. Additionally, other projects that have been continuously measuring parts of the AMOC concentrate on the western boundary regions for longer time spans [e.g. *Hummels et al.* [2015]; *Toole et al.* [2017]; *Zantopp et al.* [2017]] and open the opportunity to study multi-annual to decadal variability of the western boundary AMOC components [*Mercier et al.*, 2015].

An area with an especially high number of observations is the central Labrador Sea. Hydrographic data is available from many different sources: the Ocean Weather Ship BRAVO (OWS; 1928 until 1974), CTD sections (regular occupation of Atlantic Repeat Hydrography Line 7 West (AR7W) since 1990), and profiling Argo floats [*Holte and Straneo*, 2017; *Lazier*, 1973; *Lazier et al.*, 2002; *Pickart et al.*, 2002; *Yashayaev and Loder*, 2016; *Yashayaev et al.*, 2015]. Because of the challenging weather and sea conditions the shipboard data is strongly seasonally biased towards the summer months [*Higginson et al.*, 2011]. Velocity data is sparse and only available through shipboard (lowered) Acoustic Doppler Current Profilers ((L)ADCP) measurements, moorings equipped with current meters or ADCP's or surface drifters and Argo floats [*Gould et al.*, 2004]. The velocities of the surface drifters and the Argo floats are computed from their displacement. Geostrophic velocities can be computed from hydrographic sections or as well at the surface from satellite data.

At $53°N/52°W$ on the Newfoundland shelf break, GEOMAR installed a mooring array in 1997 in order to survey the dynamics of the three water mass components LSW, NEADW and DSOW composing the DWBC [*Fischer et al.*, 2004; *Zantopp et al.*, 2017]. Since then, every maintenance cruise (about every 2 years) collected hydrographic and velocity data using a shipboard CTD with a mounted LADCP system and an additional shipboard ADCP. Since 2016 the $53°N$ mooring array is embedded in an international effort to estimate the AMOC transport in the subpolar North Atlantic across the entire basin, the "Overturning in the subpolar North Atlantic Program" (OSNAP) [*Lozier et al.*, 2017]. This program spans the Labrador Sea, the Irminger and Iceland Sea and the Rockall Plateau and Trough (Figure 1.1 b). It relies on mooring arrays in the boundary current systems in the Labrador Sea and at the east Greenland shelf break as well as moorings at the Reykjanes Ridge and the Rockall Trough. It further uses Argo profiles and glider missions as well as satellite data to accomplish its aim to estimate the transports over the entire section [*Holliday N. et al.*, 2018; *Lozier et al.*, 2019].

1.3 Ocean General Circulation Models of the subpolar North Atlantic

Parallel to the efforts in ocean observations the attempts to numerically simulate the ocean increased starting from the 1960s [*Bryan*, 1969; *Bryan and Cox*, 1972]. There are two types of ocean models: First, mechanistic or process oriented ocean models, which are based on simplified geometry and are intended to study the basic physical mechanisms. Second, ocean general circulation models that are used for a comparison with actual oceanographic observations and for future projections under changing forcing fields. This second type should reproduce/predict features like the hydrography and dynamics. It requires accurate topography and boundary conditions on e.g. momentum, heat, moisture and buoyancy fluxes at the ocean surface [*Pond and Bryan*, 1976].

Additionally to the large-scale circulation, the ocean features an abundance of smaller scale circulation features. These inherent turbulent motions are ubiquitous on several spatial and temporal scales. They can be introduced due to instabilities at steep topography, due to barotropic instabilities arising from large horizontal velocity gradients, or due to baroclinic instability emerging from horizontal density gradients. So-called mesoscale eddies live on time scales of days to months and spatial scales of radii of about 10 to 200 km. Mesoscale eddies, fronts and jets are essential to reproduce the global ocean circulation [*Chassignet and Marshall*, 2008; *Chelton et al.*, 2011; *Stammer and Wunsch*, 1999]. The positions of major currents, like the Gulf Stream, have been shown to be overall dependent on grid resolution as well as in the choices made for subgrid scale parameterizations of e.g. energy dissipation [*Bryan et al.*, 2007; *Chassignet and Marshall*, 2008].

To simulate the oceanic mesoscale, the spatial resolution of the model needs to be smaller than the first baroclinic Rossby radius of deformation, which is strongly dependent on the latitude, stratification and ocean depth [*Hallberg*, 2013]. Depending on the relation of the spatial model resolution to the local first baroclinic Rossby radius [*Chelton et al.*, 2011] ocean models are eddy parameterizing (resolution $\geq 1^\circ$), permitting (resolution $< 1^\circ$) or resolving ocean eddies [*Chassignet and Marshall*, 2008; *Dickey*, 2003]. In the subtropics and tropics, where the first baroclinic Rossby Radius of deformation varies between 30 - 230 km [*Chelton et al.*, 1998], a resolution of 25 km $\sim 1/4^\circ$ is sufficient to resolve the oceanic mesoscale. However, in the subpolar regions of the North Atlantic the first baroclinic Rossby Radius of deformation is significantly smaller $\leq$ 10 km, which introduces the need for high spatial model resolutions ($\sim$8 km $\sim 1/12^\circ$ or smaller) to capture the hydrodynamical instability processes [*Eden and Böning*, 2002; *Gerdes et al.*, 1991].

Apart from the need of high model resolutions the subpolar North Atlantic is very challenging to simulate. Buoyancy contrasts and overflows from the neighboring seas, as well as the winds, force the currents at a similar magnitude. The low stratification leads to topographic steering of the currents. Even though water masses are well defined in observations, the salinity differences are small enough that ocean models have great difficulty to maintain them [*Tréguier et al.*, 2005]. Thermohaline factors like heat and freshwater fluxes at the ocean surface, the overflow at the Denmark strait and the Iceland-Scotland strait as well as small scale mixing play a crucial role in the subpolar North Atlantic dynamics but are difficult to implement with sub-grid scale parameterizations in coarse resolution ocean models [*Redler and Böning*, 1997].

Even though ocean models are confronted with multiple challenges in the subpolar North Atlantic, they represent a valuable tool to investigate the AMOC and the physical mechanisms related to it. The realism and the model fidelity complicate the comparability to observations and lead to systematic errors due to e.g. the representation of the hydrography or the spatial structure and position of major currents e.g the Gulf Stream or the North Atlantic Current (NAC) [*Tréguier et al.*, 2005; *Yeager and Danabasoglu*, 2012]. Previous work suggests that the variability and magnitude of the AMOC depend on the details of the single model setup, the parameterized physics and on model resolution (e.g *Bryan et al.* [2007]). The various simulated dominant AMOC time-scales cover a wide range 20 - 100 years [*Yeager and Danabasoglu*, 2012]. The simulation with higher-resolution, eddy-resolving models can overcome some of these biases, like e.g the position, spatial extent end strength of the western boundary currents (Gulf Stream), resulting in a more realistic subpolar North Atlantic [*Marzocchi et al.*, 2015].

In this thesis the data of two high resolution ocean models of the subpolar North Atlantic, VIKING20 and VIKING20x, are used. Both are high-resolution ocean models with $1/20^\circ$($\sim$ 3 km around Greenland) resolution in the SPNA. The models are presented in detail in the respective sections 2.2.2, 3.3.2 and 4.3.1.

1.4 Scientific Questions of this Thesis

Both, model and observational data, contain several challenges when analyzing them for comparable properties. Observational shipboard data are temporal snap shots and are especially in the subpolar North Atlantic, due to the weather and sea conditions, strongly seasonally biased towards the summer months, which can mask low frequency variability. The coverage with satellites, Argo floats or surface drifters is not constant over time and space and mooring arrays can have periods of lower spatial coverage or temporal gaps in their data time series due to instrument loss or funding reasons. While shipboard data, satellite, Argo float and surface drifter data are available in (near) real time, the mooring data is only retrieved at maintenance cruises [*Gould et al.*, 2004]. Eulerian mooring time series measurements are generally available in a delayed mode, but may provide high temporal resolution data. High-resolution ocean general circulation models do not face the challenges of temporal resolution, but their results have been shown to strongly depend on their horizontal and vertical resolution as well as on their choices of numerical factors such as advection/diffusion schemes to parameterize the subgrid scale and secure model stability [*Chassignet and Marshall*, 2008; *Eden and Böning*, 2002; *Gerdes et al.*, 1991; *Tréguier et al.*, 2005]. The representation of the observed hydrography is usually biased towards more saline and warmer waters [*Tréguier et al.*, 2012]. Moreover the circulation patterns and convection sites can differ strongly in their location and strength from the observed patterns [*Swingedouw et al.*, 2013; *Tréguier et al.*, 2005; *Willebrand et al.*, 2001; *Zelenko and Resnyansky*, 2007; *Zhu et al.*, 2014].

One major element describing the state and variability of the ocean circulation is the determination of the oceanic mass transport. The magnitude of the AMOC is defined as the maximum of the zonally integrated and vertically accumulated meridional transport as a function of depth. Compared with satellite and ship board values of the sea surface temperature (SST) and sea surface salinity (SSS) it is the most important state estimate for ocean models to reproduce [*Stammer et al.*, 2003; *Wunsch and Heimbach*, 2013b]. As the AMOC itself is very difficult to observe over longer time periods [*Lozier et al.*, 2019; *McCarthy et al.*, 2015], other integral and robust quantities which could be equally well determined from both observations and model studies are compared in order to evaluate the performance of the high resolution ocean model (**chapter 2**). Only if the comparison of variables in models and observations is based on careful data treatment taking the different data aspects into account, detailed insight into the underlying ocean dynamics can be gained. To evaluate this task the output of the high-resolution ocean model VIKING20 was used in conjunction with observational data from multiple sources (shipboard, 53°N mooring array, Argo, satellite) from the Labrador Sea and the SPNA. The convection depth and location as well as the gyre scale baroclinicity were analyzed on the basin scale. The spatial and temporal variability of integral circulation elements was analyzed on the regional scale at 53°N.

A major element of the SPNA is the circulation pattern in the western basin, that connects LS with the Irminger Basin. As explained above the formation of deep water is expected to be altered under a warming climate. The magnitude of deep water formation and the exact regions of deep convection remain subjects of ongoing studies and discussion. However, understanding the connection between the central Labrador and the Irminger Sea on mid-ocean depth is fundamental to understand the mechanisms that control the subpolar LSW circulation, deep water formation and export and possible links to the AMOC strength. This led to the more recent debate of how, and at which time scales the LSW spreads from one basin to the other [*de Jong et al.*, 2018; *Pickart et al.*, 2003b; *Rhein et al.*, 2002; *Straneo et al.*, 2003; *Zou and Lozier*, 2016]. Hence, **chapter 3** focusses on the connection of the central Labrador and the Irminger Sea on the LSW level within a time frame of four years. A simple Markov model of order zero was used to evaluate the spreading timescales and pathways between these two regions. Two kinds of spreading experiments were performed: 1) advection only, and 2) advection/diffusion driven particle displacements. These experiments are performed for both observational based Eulerian velocity fields and high-resolution ocean model VIKING20x output.

In analogy to the subtropical investigations of the AMOC by the RAPID consortium [*McCarthy et al.*, 2015; *Smeed et al.*, 2016], a basin scale AMOC observatory (OSNAP) has been installed in the subpolar North Atlantic in 2016 [*Lozier et al.*, 2017]. Bringing this basin scale effort, which measures the transport constituents of the currents of the SPNA, in relation to the exchange of the SPNA with the Nordic Seas via the Greenland-Scotland Ridge (GSR) is subject of **chapter 4**. In a study based on the output of the high-resolution VIKING20 model, the current transports and the AMOC-strength time series at OSNAP and the GSR are brought into context with water mass formation rates in the three enclosed basins: the Labrador and the Irminger Sea and the Iceland basin. Transport time series, water mass formation rates and common modes of variability are evaluated on the basin scale in the model and are brought into context with literature.

This thesis represents an evaluation of subpolar circulation pattern related to the AMOC. Scientifically, the focus is on regional to basin scale and from intra-seasonal to decadal variations of the AMOC system. Technically, a combination of model output and observations is used in this thesis.

2. The Deep Western Boundary Current in the Labrador Sea From Observations and a High-Resolution Model

The major aim of this chapter is define robust integral features of the subpolar North Atlantic and specifically the Labrador Sea, which are equally well defined in observations and a high resolution model run. Comparison of OGCMs and observations is particularly challenging since both data types contain different weaknesses and strengths. Comparison of the same variable in an OGCM and in observations does not necessarily mean to look at the same process. For example the quantity AMOC strength is due to the nature of observational data very differently derived than in ocean models. Nonetheless, this quantity is widely used to verify OGCMs. This chapter aims at defining integral features which are valid for a comparison between the high resolution ocean model VIKING20 and observations based on the same methods applied to the different data sets, but bearing their weaknesses and strengths in mind.

The content of this chapter was published in the Journal of Geophysical Research: Oceans.

Citation: **Patricia Handmann , Jürgen Fischer , Martin Visbeck, Johannes Karstensen , Arne Biastoch , Claus Böning, and Lavinia Patara (2018):The Deep Western Boundary Current in the Labrador Sea From Observations and a High-Resolution Model, Journal of Geophysical Research: Oceans, 123, 2829-2850. https://doi.org/10.1002/2017JC013702**

Author Contributions

The following lists the contributions to the manuscript Patricia Handmann , Jürgen Fischer , Martin Visbeck, Johannes Karstensen , Arne Biastoch , Claus Böning, and Lavinia Patara (2018):The Deep Western Boundary Current in the Labrador Sea From Observations and a High-Resolution Model, Journal of Geophysical Research: Oceans, 123, 2829-2850. https://doi.org/10.1002/2017JC013702.

- All authors contributed to the design of the study and commented on the manuscript.
- Patricia Handmann performed the analysis, produced all figures and wrote the manuscript.

- Jürgen Fischer, Martin Visbeck and Johannes Karstensen contributed to the observational data acquisition, and performed previous studies in the region. They helped evolve the concepts and ideas concerning the observational aspects of this paper.
- Arne Biastoch, Claus W. Böning and Lavinia Patara contributed to the development of the model aspects in the paper and provided the analyzed model run.

Journal of Geophysical Research: Oceans

RESEARCH ARTICLE
10.1002/2017JC013702

The Deep Western Boundary Current in the Labrador Sea From Observations and a High-Resolution Model

Patricia Handmann[1,2], Jürgen Fischer[1], Martin Visbeck[1,2], Johannes Karstensen[1], Arne Biastoch[1], Claus Böning[1,2], and Lavinia Patara[1]

[1]GEOMAR, Helmholz Centre for Ocean Research, Kiel, Germany, [2]Kiel University, Kiel, Germany

Key Points:
- Model more barotropic than found in the observations
- Model overall reproduces the mean and amplitude of the seasonal to interannual transport variability of the DWBC in the Labrador Sea
- Increased correlation between LSW and LNADW model southeastward transport at 53°N during 20 year intervals containing deep convection

Correspondence to:
P. Handmann,
phandmann@geomar.de

Citation:
Handmann, P., Fischer, J., Visbeck, M., Karstensen, J., Biastoch, A., Böning, C., & Patara, L. (2018). The deep western boundary current in the Labrador Sea from observations and a high-resolution model. *Journal of Geophysical Research: Oceans*, *123*. https://doi.org/10.1002/2017JC013702

Received 12 DEC 2017
Accepted 27 MAR 2018
Accepted article online 6 APR 2018

Abstract Long-term observations from a 17 year long mooring array at the exit of the Labrador Sea at 53°N are compared to the output of a high-resolution model (VIKING20). Both are analyzed to define robust integral properties on basin and regional scale, which can be determined and evaluated equally well. While both, the observations and the model, show a narrow DWBC cyclonically engulfing the Labrador Sea, the model's boundary current system is more barotropic than in the observations and spectral analysis indicates stronger monthly to interannual transport variability. Compared to the model, the observations show a stronger density gradient, hence a stronger baroclinicity, from center to boundary. Despite this, the observed temporal evolution of the temperature in the central Labrador Sea is reproduced. The model results yield a mean export of North Atlantic Deep Water (NADW) (33.0 ± 5.7 Sv), which is comparable to the observed transport (31.2 ± 5.5 Sv) at 53°N. The results also include a comparable spatial pattern and March mixed layer depth in the central Labrador Sea (maximum depth ~2,000 m). During periods containing enhanced deep convection (1990s) our analyses show increased correlation between LSW and LNADW model transport at 53°N. Our results indicate that the transport variability in LSW and LNADW at 53°N is a result of a complex modulation of wind stress and buoyancy forcing on regional and basin wide scale.

1. Introduction

The Atlantic Meridional Overturning Circulation (AMOC) plays an essential role in our climate system by facilitating the meridional exchange of heat, mass, fresh water, and tracer within the Atlantic basin (Lozier, 2012). The Gulf Stream and its northern extension, the North Atlantic Current, constitute the upper limb of the northern AMOC. Both transport warm and salty waters to the northeast Atlantic (Figure 1). From there the surface current bifurcates into a flow toward the Nordic seas, via the Iceland-Scotland Ridge, and a flow toward the Irminger Sea across the Reykjanes Ridge (Church, 2007; Siedler et al., 2001). Heat loss from the ocean to the atmosphere mostly during the winter season combined with the regional circulation pattern facilitate deep mixing and convection at various locations in the Nordic Seas, the Irminger Sea, and the Labrador Sea (Lazier, 1973; Lazier et al., 2001; Marshall & Schott, 1999). The newly formed North Atlantic Deep Water (NADW) interacts in a complex way with the boundary current systems and it eventually merges and flows southward as part of the Deep Western Boundary Current (DWBC) (Dickson & Brown, 1994; Molinari et al., 1998) and some interior pathways within the basin (Bower et al., 2009). The DWBC connects high-latitude regions, where deep water is formed, with the global ocean (Buckley & Marshall, 2015). These deep flows are the other key component of the AMOC and form its lower limb (Lozier, 2010).

The southward flow of the North Atlantic Deep Water (NADW) in the subpolar North Atlantic occurs largely in the DWBC along Greenland and the American continent. It is observed in a depth range between 400 and 4,000 m and has a volume transport estimated to range from about 10 to 40 Sv (Buckley & Marshall, 2015; Dengler et al., 2004; Mertens et al., 2014; Schott et al., 2004, 2006; Send et al., 2011; Toole et al., 2011, 2017b). At 53°N, the NADW exits the Labrador Sea (Figure 2) (Dengler et al., 2006; Dickson & Brown, 1994; Fischer et al., 2004; Pickart et al., 2002; Zantopp et al., 2017).

Along the Labrador shelf the oceanic currents reveal the following structure (Figures 1 and 2): a shallow Labrador Current transports cold fresh water of Polar and Hudson Bay origin, while the DWBC advects all three NADW components southward and contributes to the transport of ocean properties such as heat,

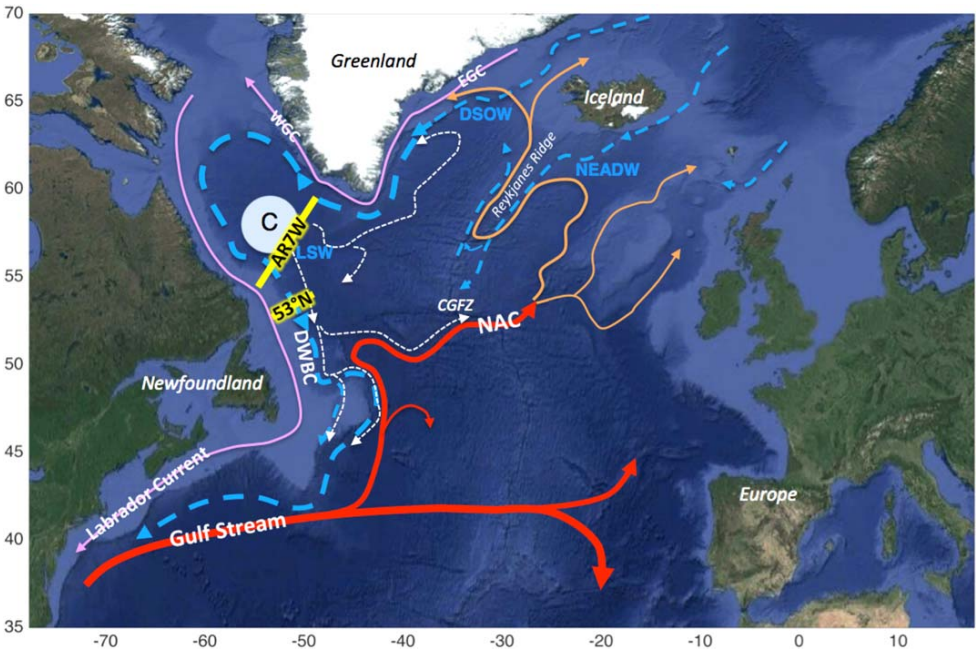

Figure 1. Schematic map of the subpolar North Atlantic with the pathways of the Gulf Stream, North Atlantic Current (NAC) (red), and components of the Deep Western Boundary Current (DWBC) (blue dashed). The current names are superimposed in white to their schematic pathway (West Greenland Current (WGC), East Greenland Current (EGC)). The names of the deep-water masses are inserted in thick blue (Labrador Sea Water (LSW), Denmark Strait Overflow Water (DSOW), and Northeast Atlantic Deep Water (NEADW)). The yellow lines mark the 53°N mooring array and the AR7W hydrographic section. The white circle marked with the C shows the schematic position of the convection area in Labrador Sea. The white dashed lines show possible export pathways of LSW from the convection area into the subpolar North Atlantic.

freshwater, oxygen, and carbon dioxide (Haine et al., 2008; Pickart et al., 1997; Sabine et al., 2004; Yashayaev et al., 2007). The shallowest component of the NADW, commonly called Labrador Sea Water (LSW), is mainly modified at the deep convection site in the center of the Labrador Sea but is also modified in other regions like the Irminger Sea (reviewed by, e.g., Marshall and Schott (1999), Pickart et al. (2003), and Kieke et al.

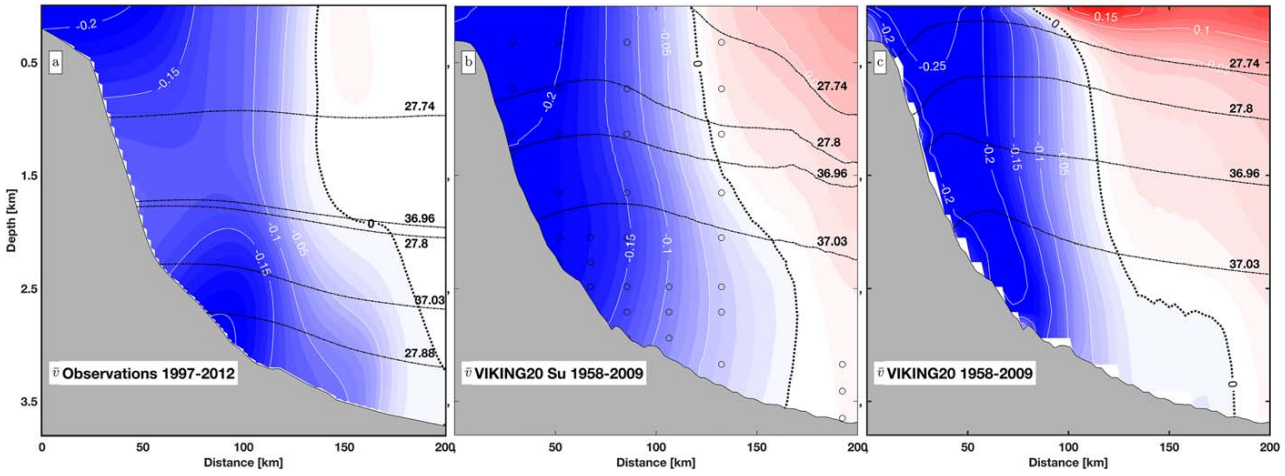

Figure 2. Mean velocity field along the 53°N section, computed from (a) LADCP and mooring data (1997–2014); (b) the horizontally and vertically subsampled model output (1958–2009), and (c) from the full resolution model output from VIKING20 (1958–2009). The mean velocity fields are superimposed by isotachs in m s^{-1} (white) and σ_2 and σ_0 mean isopycnals. Additionally the 0 isotach is marked in dotted black. Blue velocities are directed to the southeast and red velocities are directed to the northwest.

(2006)). The lower NADW (LNADW) is composed of two water masses that enter the subpolar basin by crossing the shallow sills of the Greenland-Scotland Ridge. The upper component of the LNADW, the Northeast Atlantic Deep Water (NEADW), enters the Irminger Sea via troughs in the Reykjanes Ridge and the Charlie Gibbs Fracture Zone (CGFZ) (Dengler et al., 2006; Hansen & Østerhus, 2000; Jochumsen et al., 2015; Østerhus et al., 2001), whereas the deeper component of the NADW, the Denmark Strait Overflow (DSOW) enters the northwest Atlantic (Irminger Sea) via the Denmark Strait (Macrander et al., 2005; Swift et al., 1980; von Appen et al., 2014).

Actively investigated and subject to debate is the understanding of the detailed mechanisms that control the variations in the strength of the water mass transformation and the DWBC transport and its connections to the AMOC (Böning et al., 2006; Lozier, 2010; Mielke et al., 2015). The AMOC transport variability appears to imprint on sea surface temperatures, which in turn strongly influence the climate as a whole (Eden & Greatbatch, 2003; Marshall et al., 2001). Coupled climate models suggest that the strength of the AMOC will change in future decades under a warming climate (Cubasch et al., 2001; Gregory et al., 2005; Stocker et al., 2014). In observation and modeling studies, AMOC transport time series, derived in the subtropical and subpolar gyres, do not appear to be meridionally coherent on interannual time scales. In contrast, on decadal time scales model and observational AMOC transport estimates generally exhibit meridional coherent modes of variability (Bingham et al., 2007; Buckley & Marshall, 2015; Mielke et al., 2015; Wunsch & Heimbach, 2013).

However, observations documenting the AMOC dynamics and its hydrographic properties are, due to its spatial extent and complexity, sparse and often of short duration (Böning et al., 2016; Le Bras et al., 2017; Longworth & Bryden, 2007; Mielke et al., 2015; Srokosz et al., 2012; van Sebille et al., 2011). In the past two decades, multiple efforts were undertaken to measure the AMOC continually and directly with a combination of shipboard, satellite, Argo, and moored measurements at key sections across the Atlantic basin, e.g., Ovide (Mercier et al., 2015), RAPID-MOCHA-WBTS (Smeed et al., 2016), OSNAP (Lozier et al., 2017), and SAMOC/SAMBA (Perez et al., 2011). All of these multination projects survey the Atlantic basin on a particular east-west section. For model evaluation, usually one or more of these existing AMOC transport time series is used as a benchmark.

While the observational time series are long enough for the analysis of the high-frequency spectrum, they contain significantly less information about the decadal variability of the MOC in the northern North Atlantic (Mercier et al., 2015). Therefore, smaller scale projects measuring the transports of the DWBC, which exist for longer time spans, can be very useful to understand the multiannual to decadal variability of the AMOC (Hummels et al., 2015; Toole et al., 2017a; Zantopp et al., 2017). Still, finding correlations and enhanced coherence on multiannual to decadal time scales between AMOC transport and the transports of the DWBC remains a challenge.

One of the DWBC transport records available is from the 53°N mooring array in the Labrador Sea. The array captures all three NADW constituents that exit the Labrador Sea at 53°N via the DWBC. First installed in 1997, it spans almost two decades until 2016, and is arguably one of the longest arrays in the open ocean (Fischer et al., 2004, 2010; Zantopp et al., 2017). In the following, transport time series, hydrography, and current structure from the 53°N observatory and the output of the high-resolution eddy-resolving NEMO-based ocean general circulation model VIKING20 (Behrens, 2013; Böning et al., 2016) are compared with focus on the intermediate and deep circulation. The model successfully reproduces key features of the North Atlantic circulation and provides 60 years (1948–2009) of monthly mean data (Behrens, 2013; Behrens et al., 2017; Böning et al., 2016; Breckenfelder et al., 2017; Mertens et al., 2014). The model output facilitates the study of the longer-term variability of the DWBC transport magnitude in the Labrador Sea (e.g., at 53°N off the Labrador shelf break), and helps to interpret observational features in conjunction with the AMOC.

One of the major goals of the present study is to identify and derive integral quantities that can be equally well determined from model data and observations. On the basin scale these include convection depth and location in the Labrador Sea and gyre scale baroclinicity. On regional scales, we examine integral circulation elements and their spatial and temporal variability. In section 2, the observational and model data sets used for the study are described and the methods to derive the different integral quantities are explained. Section 3 presents the comparison of dynamic and hydrographic properties as simulated and observed. In section 4, the results are discussed.

2. Data and Methods

2.1. Observational Data

Long-term hydrographic observations are available for the central Labrador Sea from a variety of sources. They include data from Ocean Weather Ship BRAVO (OWS; 1928 until 1974), CTD sections (regular occupation of Atlantic Repeat Hydrography Line 7 West (AR7W) since 1990), and profiling Argo floats (Holte & Straneo, 2017; Lazier, 1973; Lazier et al., 2002; Pickart et al., 2002; Yashayaev et al., 2015; Yashayaev & Loder, 2016). Due to ice along the shelf and harsh winter weather conditions in the Labrador Sea, the hydrographic and shipboard velocity data are seasonally biased toward the summer months whereas data from the moorings, Argo and the OWS are seasonally unbiased (Higginson et al., 2011). The seasonal bias, could be aliasing the low frequency variability observed in the region. Data on circulation properties are rare and long-term observations of the DWBC are just available for the past two decades. By using all available data from the hydrographic section AR7W, the OWS and Argo floats in the central Labrador Sea (Holte et al., 2017; Yashayaev & Loder, 2016), the temporal and spatial coverage permits a good view of the evolution of hydrographic properties in the central Labrador Sea (Figure 3a).

The setup of the mooring array at 53°N/51°W (the 53°N observatory) is thoroughly discussed and described in earlier publications; we refer to Zantopp et al. (2017) and include only a brief description herein. The moorings are located at strategically chosen positions to simultaneously sample all three North Atlantic Deep Water (NADW) constituents of the DWBC exiting the Labrador Sea at 53°N. The array reveals a complex velocity structure (Figure 2) (Dengler et al., 2004; Fischer et al., 2004, 2010). The high-resolution temporal sampling (12 h subsampled) and the dense spatial coverage of the moored stations facilitate the computation of transport time series (Figure 4) and their inherent variability at different time scales. It has been pointed out that the 53°N transport signals contain a superposition of multiple time scales from days to decades. Potential decadal changes of the transport could arise from variations in the subarctic deep-water formation or from large-scale decadal wind forcing. Regional wind forcing on the other hand may possibly cause high-frequency fluctuations (e.g., interannual to multiannual). The two forcing mechanisms, wind stress curl on the large scale and wind stress on the regional scale, are difficult to detangle (Baehr et al., 2008; Fischer et al., 2014).

Additionally 13 hydrographic surveys have been conducted during the bi-annual maintenance cruises for the mooring array. Almost two decades of data from the 53°N array, from 1997 to 2014 are used in this paper (Figure 4).

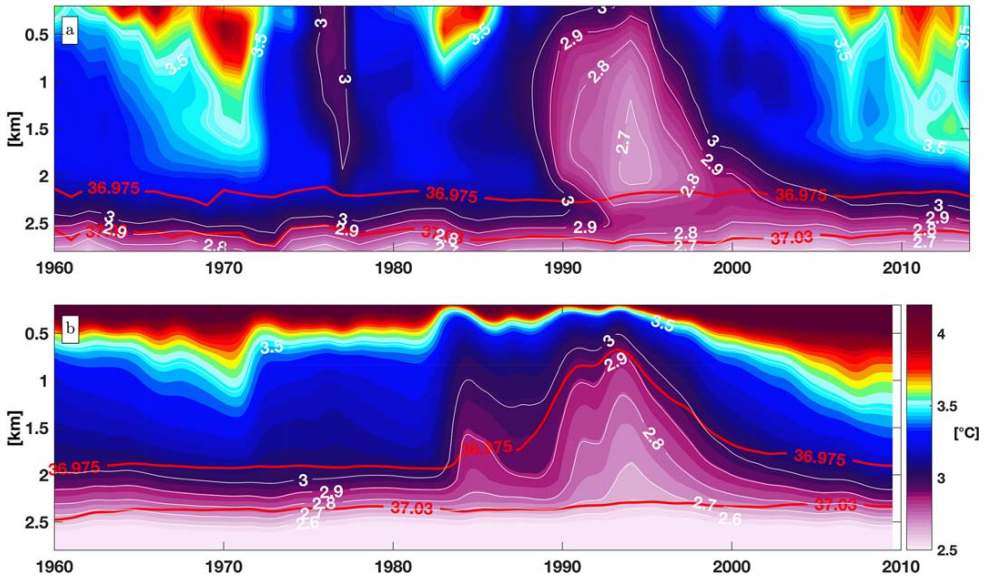

Figure 3. Time-depth evolution of annual potential temperature (colors, white contours) superimposed with potential density lines referenced to 2,000 m (σ_2, red). (a) Observational data from the central Labrador Sea as published in Yashayaev and Loder (2016) and (b) output from the model VIKING20 in the central Labrador Sea. A constant offset of 0.5°C was subtracted from the model data (Behrens, 2013).

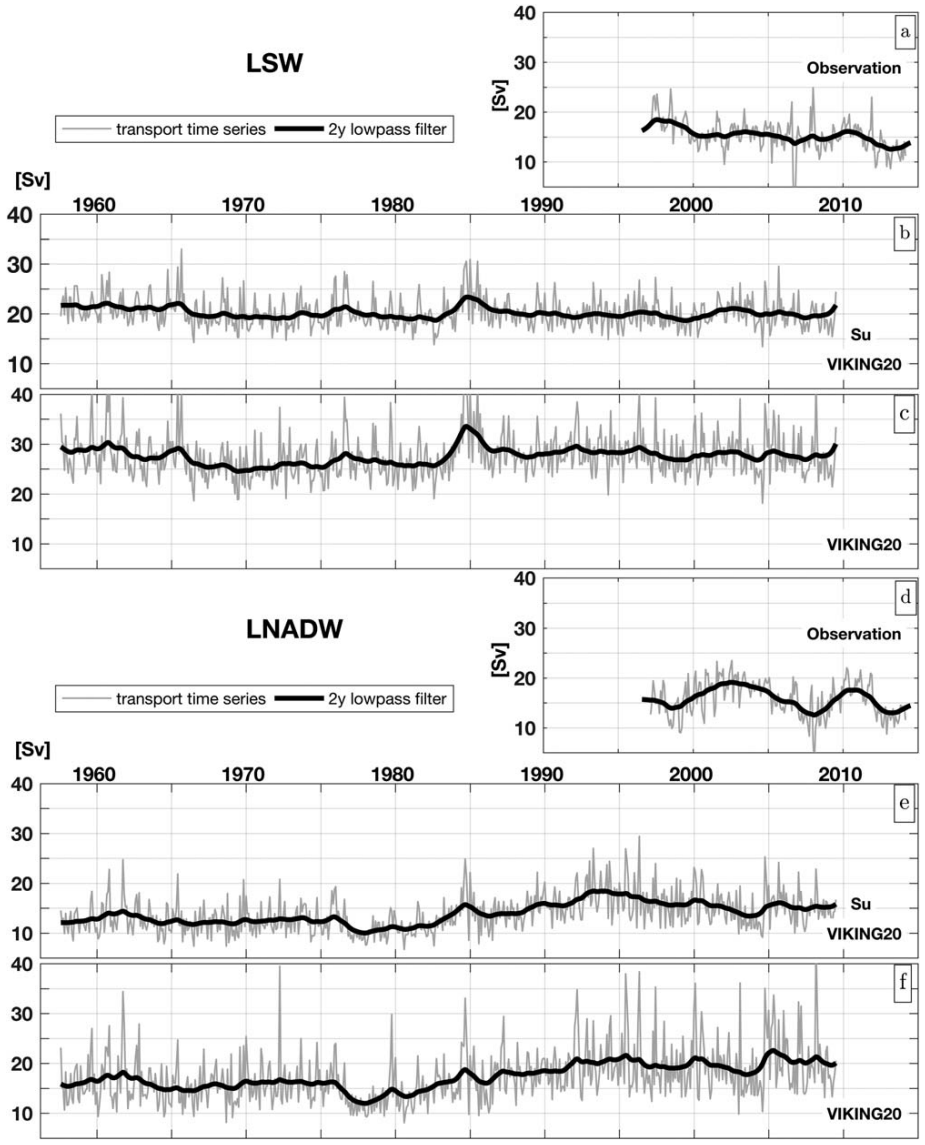

Figure 4. Southeastward transport time series for the section at 53°N at monthly resolution (grey) and 2 year low-pass filtered (black). (a) LSW and (d) LNADW transport computed from observations at 53°N array (Zantopp et al., 2017). (b) LSW and (e) LNADW transports computed from horizontally and vertically subsampled VIKING20 at 53°N section (Su VIKING20). (c) LSW and (f) LNADW transport computed from full resolution VIKING20 output at 53°N observatory.

2.2. Ocean Circulation Model

The ocean circulation model VIKING20 (Behrens, 2013; Böning et al., 2016) is based on the ocean-sea ice model NEMO-LIM2 (Fichefet & Maqueda, 1997; Madec, 2008). It includes an Adaptive Grid Refinement in Fortran nest (AGRIF two-way nesting) (Debreu et al., 2008; Sheng et al., 2005) to enhance the horizontal resolution between 32°N and 85°N in the subpolar North Atlantic. Specifically, a 1/20° eddy-resolving nest (∼3 km resolution near Greenland) was embedded within a 1/4° global eddy-permitting configuration of NEMO (ORCA025), which is developed within DRAKKAR (Barnier et al., 2015).

VIKING20 contains 46 vertical levels ranging in thickness between 6 m at the surface and 250 m below 1,000 m. The refined model nest in the subpolar North Atlantic benefits from very high resolved bathymetry from ETOPO2 (ETOPO, 2001) and GEBCO (Ioc, 2008) and the implementation of partially filled bottom cells. This is especially reflected in realistic depiction of the steep slopes of the shelf breaks and boundary current

regimes. The six-decades long hind-cast simulations from 1948 to 2009 were forced with the Co-ordinated Ocean-ice Reference Experiments forcing data set (CORE.v2) (Griffies et al., 2009; Large & Yeager, 2009). Due to a persistent drift in the hydrography in the first 10 years after the spin-up period (1948–1958), the model output from 1958 to 2009 is used here.

Common weaknesses of ocean models in dynamically complicated regions with low stratification and topographic steering are: (i) the proper representation of scales and position of important circulation elements (e.g., Gulf Stream, NAC) (Breckenfelder et al., 2017), (ii) inadequate representation of the underlying topography, (iii) a strong drift in water mass properties, and (iv) the representation of the overflow components (Tréguier et al., 2005). These reasons make it difficult to directly compare model results from eddy-permitting or coarser resolution models to observations.

Now with the availability of the high-resolution model VIKING20 (1958–2009) as well as longer observational data of surface drifters (1979-ongoing) (Flatau et al., 2003; Reverdin et al., 2003) and Argo data (2000-ongoing) (Bower et al., 2002; Lavender et al., 2000), as well as almost two decades of Eulerian current measurements at 53°N section (1997-ongoing) a quantitative comparison with the hind-cast model output and data is possible.

VIKING20 is capable of representing the properties of the circulation in the subpolar North Atlantic in magnitude and scale (Figure 5). Relative to previous attempts to simulate the subpolar North Atlantic, VIKING20

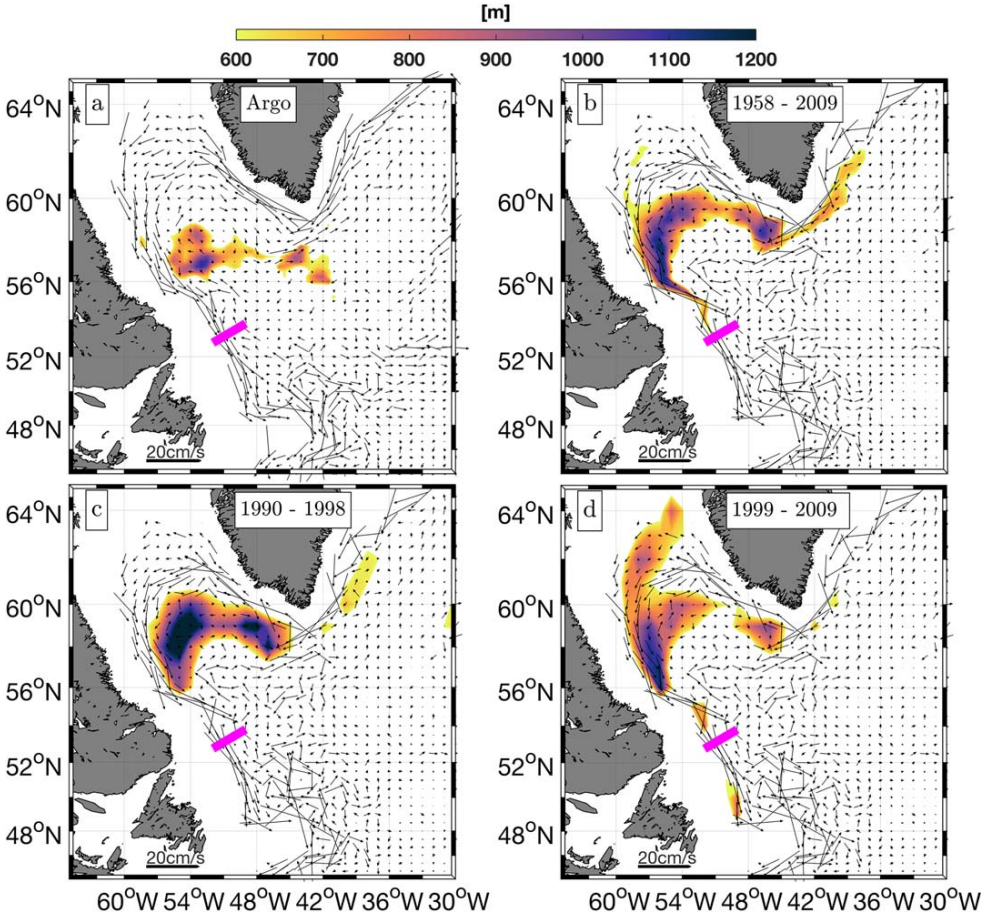

Figure 5. Mean March mixed layer depth (MLD) super imposed to the mean velocity field at 1,500 m derived from (a) Argo velocity data from 1999 to 2017 (Lebedev et al., 2007) and Argo climatology (Holte et al., 2017) and from VIKING20 model output for the time intervals of (b) 1958–2009, (c) 1990–1998, and (d) 1999–2009. Colors represent the depth and the arrows represent the velocities in all figures.

improves the representation of the scales and location of the DWBC, the eddy field in the North Atlantic and the location of the convection region (Böning et al., 2016, further discussion in section 2.3). In both, the model and the observations, the Labrador Sea circulation is characterized by a 100–150 km wide cyclonic boundary current and anticyclonic recirculation (return flow) (Böning et al., 2016; Lavender et al., 2000) in the interior of the Labrador Sea (Figures 3 and 5). Large-scale model features of the North Atlantic circulation are comparable to observations (e.g., altimetry data, observed transport, etc.), and even local conditions and circulation details are well represented by VIKING20. As one important example, the model simulates the local circulation elements in the Denmark Strait and north of Iceland. This is mainly achieved by the fine model mesh, which allows explicit resolution of mesoscale features in the complex current system (Behrens et al., 2017).

However, details such as the location of the Northwest Corner and the zonal NAC pathway may differ with observations (Breckenfelder et al., 2017). Moreover, VIKING20 is too warm and salty in the subpolar North Atlantic in comparison with observed hydrography. This complicates the comparison of water mass transports and requires adaptation of the water mass boundary definitions used in the model (Xu et al., 2012) (further discussion in section 2.3).

2.2.1. Model Atmospheric Forcing

In the northern hemisphere, the North Atlantic Oscillation is the most important mode of atmospheric variability which is closely related to the strength of the westerly winds blowing across the North Atlantic Ocean between 40°N and 60°N (Greatbatch, 2000; Hurrell, 1995; Hurrell & Deser, 2010). During high North Atlantic Oscillation (NAO), stronger than normal westerly winds bring cold and dry air over the Labrador Sea that can enhance convection depths to 2,000 m (Marshall & Schott, 1999). Understanding the interaction between wind stress forcing and the ocean surface on the large scale and on the regional scale is still a matter of current research and plays a major role in elucidating ocean dynamics.

VIKING20 is an ocean-only model simulation (no active atmosphere) using an atmospheric forcing based on the interannually varying CORE.v2 (Griffies et al., 2009; Large & Yeager, 2009) atmospheric forcing, which is a reanalysis product for atmospheric quantities, such as radiation and precipitation. The precipitation north of 62°N was reduced by 10% to account for uncertainties in the freshwater fluxes in CORE.v2 reanalysis and counter act a long-term drift in water masses (Behrens et al., 2013). The atmosphere-ocean fluxes are defined by bulk formula described in Large and Yeager (2009). In the following discussion, the VIKING20 output was used to compute the wind stress curl from the model wind stress and the sea level pressure from the applied atmospheric forcing CORE.v2 was used to compute the NAO index. We verified that the observed NAO was well reproduced in the model output in order to work on the relationships between the modeled transport time series of the DWBC and the atmospheric model parameters (e.g., NAO, wind stress curl).

The tri-polar model output from VIKING20 was projected onto a Mercator grid to avoid errors due to grid-rotation. Wind stress curl and NAO were calculated for the area defined in Hurrell (1995): 90°W–40°E, 20°N–80°N. The first principal component (PC1) of the North Atlantic winter sea level pressure (NAO winter index (djfm)) was calculated via EOF analysis from the detrended model output and is highly correlated to the commonly used NAO index in observations (PC1 based) (Hurrell, 1995). Furthermore, the winter wind stress curl (djfm) PC1 computed from VIKING20 is highly correlated to the NAO djfm index (0.77 ± 0.1). The VIKING20 output reproduces the spatial pattern of the first EOF mode of the observed wind stress curl published in Häkkinen and Rhines (2004).

2.3. Model Hydrography and Water Mass Boundaries

Transport comparisons between model and observations for different water masses require consistent water mass boundary definitions. Even though the salinities in the model are very different and the potential temperature in the central Labrador Sea is about 0.5°C warmer in VIKING20 than in the observations, the changes in model temperatures over the past two decades (1995–2009) reproduce the observed temperature increase of ~0.5°C/decade (not shown) (Behrens, 2013; Böning et al., 2016; Zantopp et al., 2017). As a consequence of the different model hydrography, isopycnals are located shallower in the model than in the observations (Figures 2 and 3). Thus, the definition of the model water mass boundary between LSW and LNADW needs to be adjusted. This need for water mass boundary adjustment is known from other models

as well (Xu et al., 2013). We first validated the spatial and temporal structures of the mixed layer depth and then computed the model water mass boundary as described below.

On the basin scale, we investigate the open ocean convection in both model and observations. The mean March mixed layer depth (MLD, diagnosed from a density difference criterion: $\Delta\sigma_0 = 0.01$ kg/m^3) was used to determine the structure and depth of convection (Yashayaev & Loder, 2009). In observed hydrographic data, the deep convection in the Labrador Sea is confined within a small region in the southwest part of the basin reaching a mean depth of 1,200 m (Figure 5) and a maximum depth of about 2,000 m (Figure 3) (Holte et al., 2017; Lavender et al., 2000; Pickart et al., 2002; Yashayaev & Loder, 2016; Zhu et al., 2014). Previous studies of ocean circulation models (OGCMs) demonstrated a limitation in their ability to represent deep convection in the Labrador Sea (Swingedouw et al., 2013; Tréguier et al., 2005; Willebrand et al., 2001; Zelenko & Resnyansky, 2007; Zhu et al., 2014), thus we will only give a brief description of the possible challenges. OGCMs (coarse-resolution as well as some high-resolution) often show excessive, almost bottom reaching convection and if they are noneddy resolving they tend to misrepresent the convection pattern. Factors limiting the ability of the OGCMs are very diverse and include uncertainties from the subgridscale parameterizations (mesoscale processes), surface forcing, and unresolved physical processes. VIKING20 resolves mesoscale processes due to its horizontal resolution (∼3 km). Its mean March MLD (Figure 5b) is located near the boundary current regime and the general pattern is very regular, even though it is shifted to the west relative to observations. The mean March MLD pattern of VIKING20 captures the observed depth and location more realistically in contrast to coarser resolved models, such as the standalone base model ORCA025 (Figure 5a) (for further discussion of the convection in VIKING20 see Behrens, 2013) (Böning et al., 2016; Marshall et al., 1998; Pickart et al., 2002; Yashayaev & Loder, 2016). Depending on the convection activity, the MLD pattern is stretched or compressed. During the period of deep convection (e.g., 1990–1998; Figure 3), the convection pattern in the model is shifted to the southeast and is more similar to the observed MLD pattern. During the 1990s, the model MLD features the dynamic "isolation" from the boundary current regime found in the observations. This "isolation" is caused by the recirculation in Labrador Sea and its respective weak advection and its low eddy activity (Figure 5c). In contrast to this, during years of shallow convection (e.g., 1999–2009), the model convection pattern is shifted northwestward and extends into the boundary current (Figure 5d).

When winter convection reaches a certain isopycnal a seasonal cycle becomes frequently apparent in the depth variation of that density surface. Deeper isopycnals are less frequently reached and thus exhibit low seasonal amplitude with a displacement magnitude of just a few meters (Figure 6c). Thus, isopycnals that remain unventilated most of the years show low variability in their vertical position. After subtracting a linear trend and the mean seasonal signal from each isopycnal-depth time series, the standard deviation of each isopycnal mean depth was computed (Figure 6b). The uppermost isopycnal with the lowest statistical depth variation reflects the deepest ventilation of LSW and thus defines the water mass boundary between LSW and LNADW. Below this minimum, the standard deviation of deeper water masses can increase due to their own formation variability, which also includes seasonal to interannual variability (Behrens et al., 2017). In contrast to the model data, the observed ship based hydrography is seasonally biased (mostly spring/summer). Yet, the same method without subtracting the seasonal cycle can be used with the observational hydrographic data from the central Labrador Sea (Yashayaev & Loder, 2016) (Figures 3 and 6a).

Using this method, the water mass boundary in the observations is found to be at $\sigma_2 = 36.975$ kg m^{-3} (Figure 6a) and in the model $\sigma_2 = 37.03$ kg m^{-3} (Figure 6b and Table 1). The observed isopycnal is found at 2,200 m in the central Labrador Sea and at a depth of 1,980 m at 53°N observatory whereas the 37.03 kg m^{-3} isopycnal in the model is found at 2,360 m in the central Labrador Sea and at 2,200 m depth at 53°N array (Figure 6). The water mass boundary found for the observations is in the range of values used in literature ($\sigma_2 = 36.95$ kg m^{-3} (Zantopp et al., 2017), 36.97 kg m^{-3} (van Sebille et al., 2011)). The spatially averaged model isopycnals for the central Labrador Sea reproduce the observed interannual depth variability (Yashayaev & Loder, 2016). They feature an increase in deep convection between the late 1980s and early 1990s found in observational data (Figure 3). However, the model produces deep convection in the 1980s, which is not apparent in observations.

2.4. Transport Calculations

Transports for the observed data were taken from Zantopp et al. (2017) and the respective calculations are explained briefly here. The moored current meter data were rotated to the mean topographic orientation

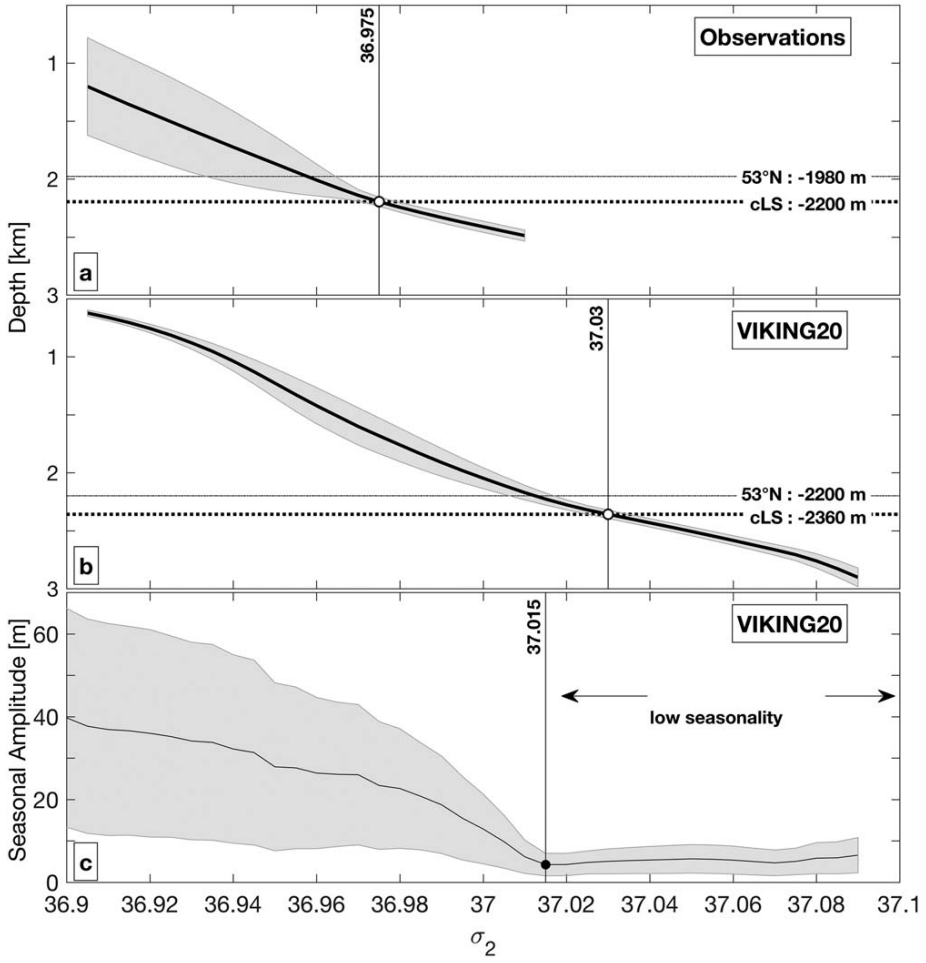

Figure 6. Mean isopycnal depth with standard deviation (grey) of the detrended data in the central Labrador Sea (cLS). The thick dashed line marks the mean depth of the isopycnal with the lowest standard deviation in the cLS. The depth of this same isopycnal at 53°N observatory is marked as a dotted line. The σ_2-value corresponding to the lowest standard deviation is marked with a circle. (a) Observations (Yashayaev & Loder, 2016). (b) VIKING20 with removed seasonality. (c) Seasonal amplitude in model and its standard deviation (grey) in the cLS with its minimum of seasonal amplitude at $\sigma_2 = 37.015$.

and interpolated to a regular grid via two-dimensional (vertical and cross-shore distance) Gaussian interpolation. The used weights and associated spatial scales were deduced from spatially much better resolved flow fields from lowered ADCP (LADCP) profiles gathered routinely during the mooring maintenance cruises on each CTD station. Transports were then determined by multiplying the grid dimensions with the interpolated current. The horizontal integration bounds were 49°W–52°W along the 53°N section (Figures 1 and 3). Vertically, we subdivided the transport layers by either depth levels or density (σ_0 and σ_2) definitions from observations (Table 1). In Zantopp et al. (2017), it was found that the position of the water mass boundary (from hydrographic ship sections) at $\sigma_2 = 36.95$ kg m^{-3} was very constant and therefore the transports were calculated with the mean depth level and hence mirror the variability in the velocity field.

Since moored arrays usually lack the measurements close to the surface an upper boundary of the DWBC at 400 m was used. This depth is resolved by the 53°N array and for consistency we took the same limit for the model evaluation. For the same temporal resolution in observations and model, monthly means were calculated from the observational transport time series.

Transports from the model output were calculated by multiplying the monthly mean velocity sections with the corresponding grid cell area below or above the water mass boundary (with respect to partial cells) and

Table 1
Transport Calculations for Different Water Mass Definitions in VIKING20 in Comparison With the Transports Calculated From Observations (Last Two Lines "Obs."), Published in Zantopp et al. (2017)

		Water mass definitions													
		Literature												Adjusted	
		Depth (m)					σ_2 (kg m^{-3})		σ_0 (kg m^{-3})					σ_2 (kg m^{-3})	
		NADW	LSW	LNADW	NEADW	DSOW	LSW	LNADW	NADW	LSW	LNADW	NEADW	DSOW	LSW	LNADW
		>400	400–1,850	>1,850	1,850–2,800	>2,800	400–36.96	>36.96	>27.68	27.6–27.8	>27.8	27.80-27.88	>27.88	400 m–37.03	>37.03
Mean water mass boundary definition 1958–2009															
Model 1958–2009	Mean	27.2	16.5	10.7	10.2	0.5	8.4	18.8	29.9	5.1	24.8	20.8	4.0	16.7	10.5
	σ	17.2	8.3	9.2	5.4	3.9	4.4	13.0	20.6	5.9	16.0	10.2	6.1	8.3	9.2
Monthly water mass boundary definition															
Model Su 1958–2009	Mean	21.3	13.7	7.6	7.1	0.5	6.5	15.1	26.3	5.8	20.5	18.1	2.4	13.2	8.2
	σ	9.5	5.3	4.8	2.6	2.7	3.8	8.3	11.5	5.2	10.7	8.3	3.7	5.1	5.1
Model 1958–2009	Mean	-See mean field values-					7.9	19.3	29.7	5.1	24.7	21.5	3.3	17.1	10.0
	σ						5.3	14.7	20.9	5.4	18.0	12.6	5.98	8.6	9.1
Northwest return flow															
Model Su 1958–2009	Mean	11.6	7.3	4.3	2.5	1.8	4.2	7.6	15.2	4.2	11.1	8.6	2.5	7.1	4.5
	σ	6.8	3.9	3.3	1.7	1.8	2.8	5.5	8.4	3.8	7.6	6.0	2.3	3.8	3.4
Model 1958–2009	Mean	17.7	10.1	7.6	5.0	2.6	5.2	13.0	24.8	6.7	18.1	14.3	3.8	10.4	7.3
	σ	12.5	6.4	6.3	3.8	2.5	4.1	10.8	15.9	5.5	14.1	11.1	3.5	6.6	6.1
Southeast outflow															
Model Su 1958–2009	Mean	33.0	21.1	11.9	9.6	2.3	10.7	22.7	41.5	9.9	31.6	26.7	4.9	20.3	12.6
	σ	5.7	3.1	3.0	1.8	1.5	4.0	7.9	6.5	7.1	10.2	9.1	2.4	3.1	3.4
Model 1958–2009	Mean	44.9	26.6	18.3	15.2	3.13	13.1	32.3	54.6	11.7	42.9	35.8	7.1	27.5	17.4
	σ	8.8	4.1	5.1	3.0	2.3	5.7	11.3	10.4	6.4	12.7	10.5	3.9	4.3	5.4
Obs. 1997–2014	**Mean**	**31.2**	**15.3**	**16**	**5.1**	**10.9**	**14.5**	**15.8**				**11.1**	**4.6**		
	σ	**5.5**	**3.3**	**3.4**	**1.3**	**2.3**	**3.8**	**3.8**				**2.7**	**1.3**		

Note. Transports are calculated for the mean field (1958–2009) and the monthly derived fields of density (σ_0, σ_2) and depth. The net transport presented in Lines 1–3 is the sum of the northwestward and southeastward flows at 53°N observatory (calculation described in section 2.4) Lines 4–7. Model Su presents the output for the subsampled and interpolated model output (2,000 m horizontal and 20 m vertical). The boxes are included to facilitate orientation during the discussion in the text.

subsequently integrating grid cells of the desired water mass. The upper boundary to compute the complete NADW transport was held at 400 m. For the "Mean water mass boundary definition" (Table 1), the mean position of the isopycnal $\sigma_2 = 37.03$ kg m^{-3} was computed for the period from 1958 to 2009. The transports calculated with this reflect only the variability of the velocity field, because the area is held constant (similar to observations). For the "Monthly water mass boundary definition" (Table 1), the position of the water mass boundary is computed for every monthly mean. The resulting transport time series of the "Mean water mass boundary definition" and the "Monthly water mass boundary definition" are nearly identical (correlation greater than 0.99 $\pm$ 0.0013 with an average offset of less than 2% of the mean transport). Thus, the respective transports reflect the variability of the velocity field and the effect of the varying area due to the variability of the hydrographic field is very small. To calculate the northwestward/southeastward transport (Figure 4) along the topography, all positive/negative velocities of the 49–52°W section at 53°N were used. The net transport is the sum of the southeastward and northwestward transport components (Table 1, Lines 1–3).

The horizontal resolution of the observational data is coarse (mooring array ~20–50 km/shipboard lowered ADCP profile locations ~20 km apart) in relation to the horizontal model resolution of the section (~3 km). In contrast, the vertical resolution of the full-depth lowered ADCP velocity data is relatively high (~11–100 m) while the vertical mooring resolution is lower (~100–1,000 m) than in the original model output (~6–250 m/46 vertical levels). For comparison, the vertical model resolution near the water mass boundary of LSW versus LNADW in the model is ~200 m.

First, the transports are calculated as described above for the model output resolution. Second, we were interested in the representation of the transport magnitude and variability in a subsampled model section

in comparison to the full model resolution transports in order to verify the quality of the observed data. Hence, the model was subsampled to reflect the observational data density in the moored array (Figure 2b, horizontal and vertical subsamplings to a virtual mooring array) and then treated with a Gaussian interpolation algorithm, which is similar to the treatment of the mooring data in Zantopp et al. (2017). The spatial scales in the model were deduced from the mean structure of the velocity field (Figure 2c) and the virtual moorings were positioned to resolve the major features of the mean model flow field at 53°N section. The typical horizontal scales of the boundary current were found to be of 20–50 km (cf. first baroclinic Rossby radius ~10 km), and vertical scales of several hundred meters to more than 1,000 m in the LSW range. These scales are similar to the scales found in observations (Zantopp et al., 2017). Thus, the virtual array corresponds to the "full" observational array composition at 53°N (2012–2014) (Zantopp et al., 2017) and produces gapless monthly data. The new, interpolated grid has 2,000 m horizontal and 20 m vertical resolution. The

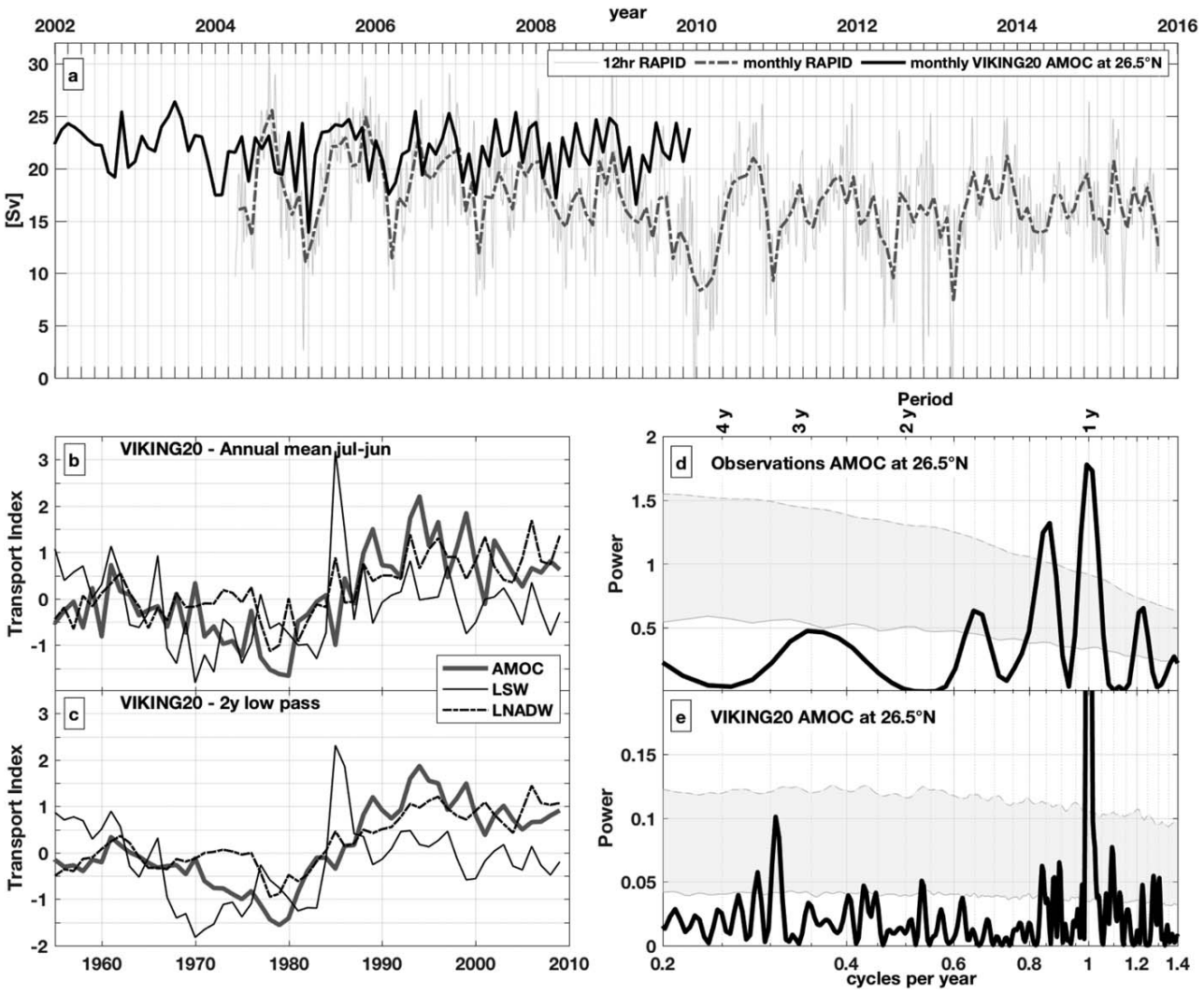

Figure 7. (a) AMOC at 26.5°N calculated as maximum of the stream function at 26.5°N in the model (black) and from RAPID-MOCHA-WBTS array observations (grey/blue) (Smeed et al., 2016). (b) July–June annual mean index of AMOC at 26.5°N and southeastward transports of LSW and LNADW at 53°N section computed from the full resolution model output. (c) July–June annual means with 2 year low-pass filter. (d) Spectrum computed from RAPID monthly mean observational data with Lomb-Scargle Fourier transformation. The confidence bounds are calculated by Monte Carlo approach with 1,000 realizations of pure red noise (AR1 process) containing same autocorrelation, mean, variance, and data distribution as data. The upper 0.95 confidence boundary is marked with a dashed line, whereas the 50% mean state is marked with the lower solid line. The confidence interval is shaded grey. Every value that exceeds the upper solid line is a significant value. (e) Spectrum computed from monthly mean model AMOC at 26.5°N with the same algorithm as in Figure 7d.

interpolation method works like a spatial low-pass filter. The subsampling therefore produces different transport values with lower variability than in the full resolution transport calculations (Figure 4 and Table 1). The Gaussian interpolation resolves the general structure properties of the currents observed and modeled along the 53°N array (Figure 2). The net, southeastward and northwestward transports for the full resolution model output (Table 1—Model), the subsampled and interpolated model output (Table 1—Model Su (subsampled)) and the observations are presented in Table 1 and are discussed in detail in section 3.2.

Additionally to the study of the DWBC at 53°N, the AMOC transport at 26.5°N was computed outside the high-resolution nest of VIKING20 model (global configuration ORCA025) as the stream function for the zonally integrated meridional volume transport in depth coordinates. The resulting AMOC transport time series was then compared and analyzed with respect to the observational data from the 26.5°N RAPID-MOCCA observational array (Smeed et al., 2016) (section 3.2.1).

2.5. Variability Analysis

For spectral analysis of the transport time series, Lomb-Scargle Fourier transformation was used (Lomb, 1976; Scargle, 1982). The confidence bounds were calculated using Monte Carlo approach with 1,000

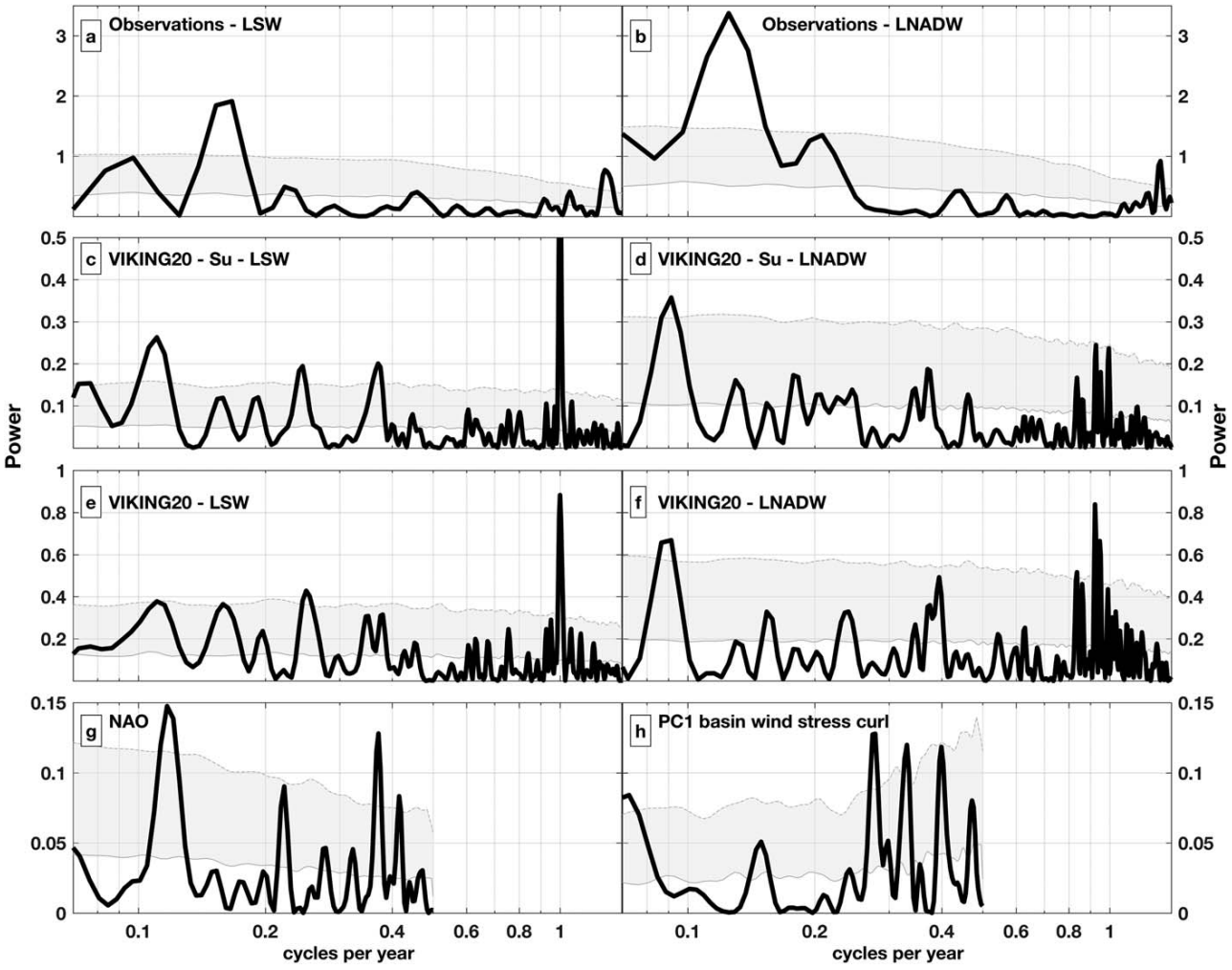

Figure 8. Lomb-Scargle periodogram of the southeastward transport time series of LSW and LNADW. The 95% confidence level is marked with the upper dashed line and the 50% mean state is marked with the lower solid line. The confidence interval is shaded grey. Every value that exceeds the upper solid line is a significant value. Periodogram for (a and b) observational data; (c and d) VIKING20 subsampled transport data; (e and f) the full model resolution transport time series; (g) the Lomb-Scargle periodogram of the Winter (December–March) NAO (COREv.2); and (h) the first principal component (PC1) of the winter wind stress curl in the subpolar North Atlantic basin computed from VIKING20 output. Confidence intervals are marked as in Figure 7.

realizations of pure red noise (AR1 process) containing the same autocorrelation, mean, variance, and data distribution as the data (Overland et al., 2006; Rudnick & Davis, 2003). This method was used since the length of the observed transport time series is too short for other confidence estimation. For consistency the same method was used for the observational and model data, even though the length of the model data would permit other techniques. In Figures 7d, 7e, and 8a–8e, the 95% confidence level is marked with the upper dashed line and the 50% mean state is marked with the lower solid line. The confidence interval is shaded grey in every spectral figure. Every value that exceeds the upper solid line is a significant value.

In this whole article, the significance threshold for all given Pearson correlation coefficients was set at $p \leq 0.05$. The correlation values are given with the mean of their respective confidence interval, which implies significance if small compared to the correlation value (e.g., 0.99 ± 0.001) and no significance if greater than the R-value (e.g., 0.4 ± 0.5). If the confidence interval contains the zero value, the R-value is not significant.

3. Results

3.1. The DWBC at the 53°N Array—Mean Flow in Observations and Model

In observations the boundary current system at 53°N contains a defined velocity maximum at the surface, the Labrador Current extending down to about 500 m, a weakly sheared current in the LSW density range and a deep velocity maximum of the DWBC at depth with very stable velocities, with maximum speeds reaching 40 cm s^{-1} and annual averages of typically 25 cm s^{-1} (Figure 2a). Hence, the velocity structure of the DWBC at the 53°N section is baroclinic. The seaward current structure is more barotropic and less distinguished in depth and the captured northwestward recirculation flow is not very strong with velocities of about 3 cm s^{-1} (Zantopp et al., 2017). This structure has been characterized as a robust feature over the last two decades (Dengler et al., 2006; Fischer et al., 2014; Zantopp et al., 2017).

The mean circulation deduced from full resolution VIKING20 at 1,500 m reproduces the structure of the horizontal circulation (Figure 5). VIKING20 captures the mean current strength, width and location of the upper and deep core of the western boundary current, as well as the bottom intensification at the 53°N section (Figures 2b and 2c). Comparing the observational mean velocity field with the model mean velocity field, in both, the upper velocity maximum stretches down to about 500 m. It has a magnitude of 25 cm s^{-1}, 10 cm s^{-1} stronger in the model than in the observations. Within the uncertainties, the maximum mean bottom velocity is similar in the model (23 cm s^{-1}) and in the observations (19 cm s^{-1}). Furthermore, the western boundary current band is less vertically sheared in the model than in the observations. The model contains a stronger southeastward and northwestward flow components and the 0 cm s^{-1} isotach is shifted toward the Labrador shelf break. Hence, the model DWBC is slightly narrower in the mean than in the observations.

3.1.1. Subsampling to Idealized Mooring Array

A well-known challenge in designing mooring arrays is the lateral extent and offshore termination of the array. In the case of the boundary current observatory at 53°N, the position of the core of the DWBC is relatively stable (Zantopp et al., 2017). Depending on the spatial scales of variability at the respective region, the terminating mooring should always be positioned such that it captures the transition to a possible recirculation via the 0 isotach, thereby terminating the dynamical offshore edge of the boundary current. In high-energy environments, this can be very challenging due to submooring resolution dynamics such as eddies. To clarify whether eddies are common or temporarily changing the velocity structure at the mooring array additional data analysis of satellite data (sea surface height), ARGO floats, surface drifters, or ship sections is needed in order to estimate the implied uncertainties due to eddies.

To evaluate the capabilities of the 53°N array to capture variability and transport of LSW and LNADW, an idealized mooring array was situated at locations in the model comparable to the positions in the observations (section 2.4). The subsampled array data are available at the temporal resolution of the model (monthly mean data). In contrast to the observations, where a mean ADCP profile is used as a terminating profile for the Gaussian interpolation, the model contains a terminating mooring at the end of the section for each time step. When using a mean profile to terminate the array in the model subsampling, the southeastward export from the Labrador Sea at 53°N was highly correlated with the full model resolution southeastward transport time series. However, the mean northwestward recirculation NADW transport was reduced by ~3 Sv to 8.81 ±3.66 Sv in comparison to the monthly termination (cf. Table 1, Line 4 NADW

transport: 11.6 ± 6.8 Sv) and its long-term variability was changed in comparison to the monthly termination. Furthermore, the mean profile termination introduces a monthly transport variability of ± 5 Sv in comparison to the transports calculated with the monthly profile termination.

Using a mean profile from a collection of shipboard measurements and other available data (e.g., Argo, surface drifters, AVISO SSH) to terminate a mooring array already provides enough information for the 53°N array to capture the southeastward transport variability of LSW and LNADW. Hence, these results support the assumption that the position of the termination of a mooring array to estimate transports is crucial to the captured (long-term) variability and net volume transport by the array.

3.2. Transport and Variability in Observations and Model

Robust integral quantities for comparison between model and observations include not only the mean flow structure and magnitude but also interannual to long-term variations in the computed transport estimates.

3.2.1. The AMOC at 26.5°N

The AMOC transport was calculated from the 0.25° global configuration (ORCA025) of the VIKING20 model (section 2.4, Figure 7). The mean model AMOC transport and its standard deviation for the overlapping 5 year periods, from April 2004 to December 2009, ranges within the observational data errors (model: 21.7 ± 2.4 Sv, observations: 17.9 ± 3.5 Sv (Smeed et al., 2016)). AMOC estimates from both, observations as well as the model, indicate variability of the same magnitude as the mean transport on interannual and seasonal time scales and smaller variability on multiannual to decadal time scales (see Buckley and Marshall (2015) for a recent AMOC review). At the same time, the observed and modeled monthly AMOC time series are not correlated strongly (0.44 ± 0.2). The model AMOC transport increases by 2.4 Sv from 1958 to 2009 and its mean is slightly smaller (21 ± 2.8 Sv) than in the overlapping period where no trend could be detected. Spectral analysis of both, model and observation (Figures 7d and 7e), show a significant peak for the annual time scale. Due to the limited length of observational data, a spectral comparison is not possible on longer time scales.

Comparing the model transport indices of the AMOC at 26.5°N and the southeastward transports of LSW and LNADW at the 53°N array, we find increasing significant correlation (up to 0.9 ± 0.02) on multiannual and longer time scales (Figures 7b and 7c). For the monthly transport time series at both locations, the correlations were low <0.5. A similar relation was found in previous studies, where enhanced meridional coherence on longer time scales indicates the potential of the DWBC to serve as a subpolar transport index of the AMOC, as DWBC transports show a similar long-term variability as the AMOC (Böning et al., 2006; Buckley & Marshall, 2015).

3.2.2. The DWBC at 53°N

The mean transports for the full resolution model section, the subsampled model section, and the observational data are presented with their respective standard deviations in Table 1. The net along-topography transports for the full model resolution (Table 1—Model) and the subsampled and interpolated model (Table 1—Model Su) show a transport difference in NADW (i.e., sum of southeastward and northwestward) of about 20% (Model 27.2 ± 17.2 Sv/Model Su 21.3 ± 9.5 Sv, Table 1, Lines 1 and 2). The southeastward NADW transport computed from the subsampled model section (33 ± 5.7 Sv) is very close to the southeastward NADW transport calculated from observations (31.2 ± 5.5 Sv) (Zantopp et al., 2017) and even the overall statistical variability is similar. The southeastward transport computed from the full model resolution exceeds this observed value by more than 10 Sv at 44.9 ± 8.8 Sv. The subsampled model reproduces about ∼70% of the original model southeastward transport (Figure 4 and Table 1, southeastward outflow).

However, the northwestward return flow is stronger in the model (17.7 ± 12.5 Sv, subsampled 11.6 ± 6.8 Sv) than in the observations (between 3 and 4 Sv) (Zantopp et al., 2017) (Figures 3 and 5, Table 1). The recirculation flow is not well captured by the observational mooring array and only recently a mooring was added at the deep-water tail of the array. This may in part explain the low representation of the northwestward circulation in the transport estimates from the observational data.

The partitioning of the NADW transport in the DWBC into LSW and LNADW components and their respective variances is strongly influenced by the displacement of the mean water mass boundary to 220 m deeper than in the observations (Figures 6a and 6b) and the model's more barotropic velocity structure at the 53°N array, where higher velocities than in the observations are found in the LSW layer (see σ_0/σ_2 definitions in Table 1). The estimation of the respective model transports with the previously described water

Table 2
Correlation Coefficient for Observed and Modeled Southeastward Transport Time Series of LSW and LNADW at 53°N Array

	Type	Correlation LSW-LNADW
Observation (1997–2014)	Monthly	0.34 ± 0.04
	Two year low-pass	0.18 ± 0.05
VIKING20 (1958–2009)	Monthly	0.65 ± 0.07
	Two year low-pass	0.19 ± 0.11
VIKING20 (1975–1990)	Monthly	0.65 ± 0.07
	Two year low-pass	0.45 ± 0.1

Note. The coefficients are calculated for monthly data and for the 2 year low-pass filtered signals.

mass boundary between LSW and LNADW results in magnitudes of southeastward transport in the subsampled model (LSW 20.3 ± 3.1 Sv/LNADW 12.6 ± 3.4 Sv), which are comparable (within their standard deviations) with the observed values (LSW 14.5 ± 3.8 Sv/LNADW 15.8 ± 3.8 Sv). The standard deviation of the northwestward transport is in the same range of magnitude as the mean northwestward transport itself (Lines 4 and 5 in Table 1). In comparison, the southeastward transports have smaller standard deviations than the mean, which are more comparable to the observed values (∼20% of the mean transport value). The major part of the variance of the net export at 53°N is caused by the northwestward transport (Line 3, Table 1).

The southeastward transport time series of LSW and LNADW computed in VIKING20 (full resolution and subsampled) covary strongly (Table 2) and contain higher variability on the interannual to multiannual time scale than found in the observations (Figure 4). Furthermore, the results of the spectral analysis of the southeastward model transport time series of LSW and LNADW resemble each other in the high-frequency range (<2 years; Figures 8c–8f). The spectra show significant peaks at 9, 4, and ∼2 years for LSW and 11 years for LNADW subsampled southeastward transport and at 4 and 1 years for LSW and 11 and 1.5 years for LNADW southeastward full model resolution transport. High-frequency variability dominates both of the full (Figures 8e and 8f) and subsampled (Figures 8c and 8d) model transport time series. The southeastward model LNADW component shows a significant peak at 11 years, this is similar to the observations, where the LNADW transport component contains a quasi-decadal spectral peak, which is not apparent in the LSW transport spectrum. Similar to the study of the 0.08° resolution HYCOM model by Xu et al. (2013), the temporal variability in VIKING20 is lower on interannual and longer time scales than on shorter time scales (<1 year).

In contrast to the model transport time series, the observed transport time series of LSW and LNADW at 53°N section (Figures 4a and 4d) appear less similar to each other and produce two distinct spectra in which different periods dominate (Zantopp et al., 2017) (Figures 8a and 8b). In the observational data time series, well-defined peaks at 9 months and 6 years for LSW and 9 months and 8 years for LNADW are present. The high-frequency peaks could be caused by topographic waves, whereas the longer periods could be related to basin scale forcing (Brandt et al., 2004; Lilly et al., 2003).

The visual impression of spectral similarity of the model time series is supported by a high correlation coefficient of the transport time series of the two NADW components. The model transport time series (1975–2009) of LSW and LNADW are significantly correlated with 0.65 ± 0.07 for the monthly values and 0.45 ± 0.1 for the 2 year low-pass filtered signal (Table 2). The observational data yields much lower correlation values with 0.3 ± 0.04 for the monthly mean values and 0.2 ± 0.05 for the 2 year low-pass filtered signal. In both, model and observations, the 2 year low-pass filtered time series of LSW and LNADW are less correlated with each other than the monthly time series. The difference between the correlations of the monthly time series and the low-pass filtered time series is very similar in the model and the observations (∼0.2) (Table 2). The stronger barotropic nature of the model can cause higher correlation than in the observations.

In observations, the linkage between periods of intense deep convection (related to the formation of LSW, e.g., mid-1990s, Figure 3) to an enhanced export of LSW from Labrador Sea is discussed in various papers using indirect methods (Bower et al., 2009; Lazier et al., 2001; Molinari et al., 1998). In this case, only the transport of LSW should be affected in the respective period. On the other hand, a response of LSW and LNADW could be a result of strong basin wide atmospheric forcing over the subpolar North Atlantic (strong NAO and associated wind stress curl). This would increase the correlation between LSW and LNADW for the respective period.

Since we are interested in the multiyear to quasi-decadal variability of the transport time series and the overall length of the observed time series is close to 20 years, the model time series of LNADW and LSW southeastward transport were partitioned with a sliding window into 32 segments each 20 years long. Correlations were estimated for each of these 20 year segments to separate intervals of higher and lower correlation between LSW and LNADW transport time series in the model (Figure 9a). The results show high

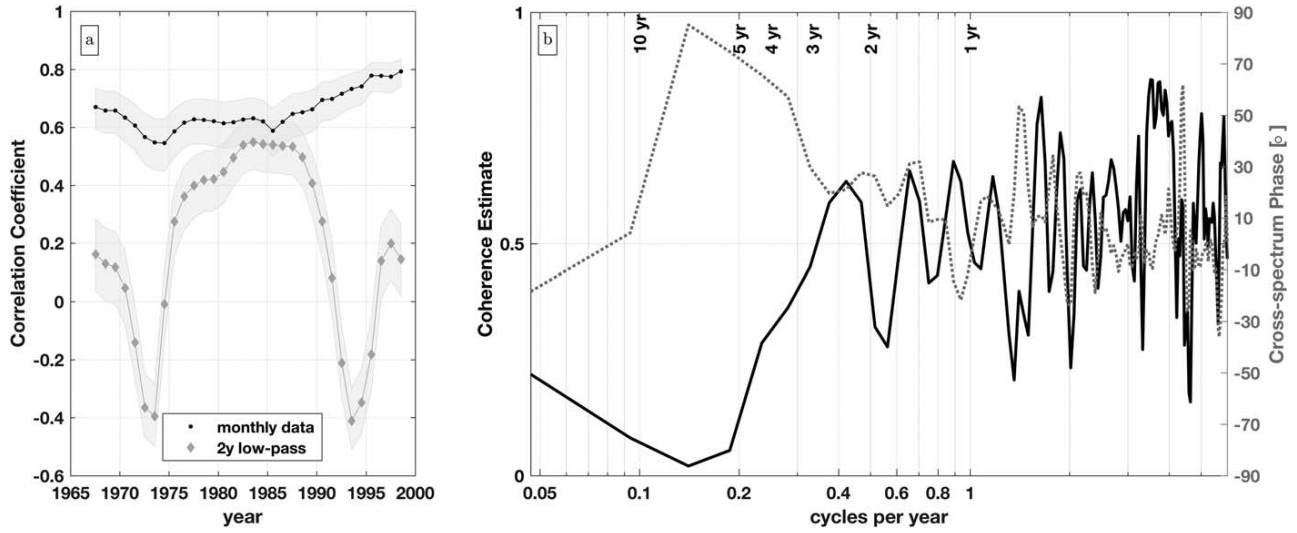

Figure 9. (a) Correlation coefficient of LSW and LNADW southeastward transport time series. The monthly data correlation (black dots) and the correlation of the 2 year low-pass filtered signal (grey diamond) are computed for 20 year windows in VIKING20. The data point is situated in the middle of the 20 year window and the confidence interval is shaded in grey around the data points as explained in section 2.5. (b) Cospectrum for the LSW and LNADW southeastward transport time series from VIKING20.

correlation for all 20 year segments of the monthly model transport time series (1958–2009) with values between 0.55 ± 0.08 and 0.79 ± 0.04 and values between −0.41 ± 0.1 and 0.55 ± 0.08 for the 2 year low-pass filtered signal. The filtered transport time series in the model are low or not correlated for the first 26 years (1958–1984). Then the correlation increases for the period from 1977 to 2005 and leads to a maximum correlation of 0.55 ± 0.08. The higher correlation period 1977 to 2005 coincides with enhanced deep convection in the 1990s (Figure 3). During the rest of the model run, the correlation of the 2 year low-pass filtered LSW and LNADW is lower and could thus be more related to large-scale wind stress curl than to regional influences in the Labrador Sea.

Additionally the cospectrum calculated for the model time series of LSW and LNADW (Figure 9b) shows high coherence (∼0.6) for the high-frequency part (frequencies up to 1 cycle/yr). The coherence then starts to decrease at frequencies of 0.5 cycles/yr (∼2 years) to nearly 0 at 0.1 cycles/yr (∼10 years). The cospectrum phase is low and between −30° and 90°. This implies that the low frequency part of the southeastward transport time series in LSW and LNADW is less coherent than their high-frequency content.

As transport variability may be driven on different time scales by buoyancy and wind forcing, the connection between model atmospheric forcing and the southeastward transports at the 53°N observatory were analyzed. To study this linkage between transport variability in the two defined water masses LSW and LNADW at the 53°N section in the model, with the applied atmospheric forcing (CORE.v2), the NAO winter index, the time series of the first basin wide winter wind stress curl principle component (PC1), and of the regional wind stress curl, a correlation calculation was done.

Table 3
Correlation Coefficient for Modeled Southeastward Winter (December–March) Transport Time Series of LSW and LNADW at 53°N Section With the PC1 of the Winter (December–March) Wind Stress Curl Over the North Atlantic and the Winter (December–March) NAO Index

VIKING20 (1958–2009)	North Atlantic wind stress curl PC1	NAO
LSW	−0.4 ± 0.2	0.2 ± 0.2
LNADW	−0.3 ± 0.2	0.3 ± 0.2

For the period 1958–2009, the winter LSW and LNADW transports (December–March) are correlated with ∼0.4 ± 0.2 to the PC1 of the basin wide North Atlantic winter wind stress curl and with ∼0.3 ± 0.2 to the NAO djfm index (Table 3). The correlation of LSW and LNADW to the regional wind stress curl found a maximum correlation near the Northwest Corner (∼0.4 ± 0.2) (not shown). Even though these correlations are not high (Table 3), the transport spectra contain some similar peaks with the NAO and the basin wide winter wind stress curl (Figures 8g and 8h). The observed southeastward flowing LNADW (Figure 8b) shows an 8 year peak similar to the NAO spectrum (Figure 8k).

4. Discussion and Conclusions

This study identified robust and comparable features in a high-resolution hind-cast model and almost two decades of velocity and hydrographic observations from the lower limb of the AMOC at the exit of the Labrador Sea at 53°N. Below the results are discussed in the following order: After addressing the spatial and temporal characteristics on the subpolar gyre scale, we discuss possible challenges connected to the model setup and the applied atmospheric forcing. Then the focus is shifted to the region of the 53°N mooring array followed by a more detailed discussion of the possible limitations of the mooring array and our conclusions.

First, gyre scale horizontal maps of the mean velocity field and the winter maximum mean mixed layer depths were analyzed from Argo data (Holte et al., 2017) as well as from the model output (Figure 5). The model reproduces the main observed structures of the horizontal circulation and the depth and structure of the maximum winter mixed layer depth in March in the subpolar North Atlantic. However, in comparison to observations (Figure 5a) (Yashayaev & Loder, 2016), in the model, the region with deep reaching mixed layers is stretched further southeastward into the region of the boundary current regime. Other model studies with eddy-resolving model configurations, e.g., Brandt et al. (2007) (1/12° FLAME) found a comparable horizontal shift of the mean March mixed layer pattern. This southward stretched region of maximum mixed layer depth could explain the main export pathway of LSW via the DWBC in the model (Brandt et al., 2007). It seems that the pattern of the deepest mixed layer depth in the VIKING20 model is different for periods with deep convection and "normal" years. Where in "normal" years (e.g., 1999–2009, Figures 3 and 5d), the shift to the south into the boundary current regime is apparent, in years of deep convection (e.g., 1990–1998, Figures 3 and 5c), the MLD pattern is centered in the central Labrador Sea. The mechanisms causing the shift of the deepest mixed layer position in the model are unknown presently. The dynamic "isolation" of the convection zone from the DWBC via the anticyclonic recirculation in Labrador Sea as found in observations is only reproduced in the model for the period of deep convection (Figure 5c). In "normal" years without enhanced mixed layer depths, the model convection reaches into the boundary current regime (Figures 5b and 5d).

Despite these discrepancies, the model is able to reproduce the observed hydrographic changes from 1960 to 2009 in the central Labrador Sea including similar winter mixed layer depths (Figures 3 and 5). Although the model hydrography is very different than the observed, it reproduces the cooling of the intermediate water masses (500–2,500 m) during the early 1990s and the warming since the 1990s.

In a previous study (Böning et al., 2016), the change in deep convection during the 1990s was found to have a direct impact on the AMOC. We investigated several periods with strong convection in the model and there was no significant response seen in the boundary circulation downstream from the convection sites. This is contradictory to previously published observed and modeled results, which found a response of the boundary current intensity to enhanced deep convection (Häkkinen & Rhines, 2004; Xu et al., 2013). Some past studies related the strength of the DWBC to the North-South position of the Gulf Stream, which could introduce buoyancy anomalies due to large North-South shifts in the buoyancy gradient position (Joyce & Zhang, 2010; Peña-Molino et al., 2011; Peña-Molino & Joyce, 2008; Toole et al., 2011). Other studies related the strength of the DWBC to changes in the strength of the subtropical and subpolar gyre driven by changes in the wind stress curl (related to NAO) (Häkkinen & Rhines, 2004; Hatun et al., 2005). This indicates, that the DWBC transports in previous studies as well as in the VIKING20 model are not simply linearly related to the buoyancy forcing but to a complex mixture of atmospheric and buoyancy responses.

As a proxy for the basin scale baroclinicity we constructed a gyre scale isopycnal-depth gradient by using the depth of the above defined water mass boundary between LSW and LNADW in the central Labrador Sea and at the boundary current at the 53°N section (Figure 6). The depth gradient in the model is less pronounced than in the observations, which has an impact on both, layer thickness as well as the gyre scale baroclinicity. This implies that the observations are more baroclinic than this model. Although more barotropic than the observations, the vertical structure of the horizontal velocity in VIKING20 at 53°N appears less barotropic than in the study of Xu et al. (2013) with the 0.08° HYCOM model.

Second, ocean models are generally set up to reproduce specific aspects of the ocean dynamics. This can lead to weaknesses of the model in ocean dynamics, which are not in the focus of the model setup. VIKING20 reproduces the magnitude and interannual to seasonal variability of the observed AMOC and

DWBC transport, but it shows different variability on longer time scales at 53°N, a too saline and warm hydrography and a northward shift of the Northwest Corner (Breckenfelder et al., 2017). The weakness of the VIKING20 model to reproduce realistic salinities (generally too high) is likely related to the precipitation reduction that was adopted north of 62°N, where the precipitation from atmospheric reanalysis forcing is reduced by 10% to account for uncertainties in the freshwater fluxes in CORE.v2 and counter act a long-term drift in water masses. The influence of the reduced precipitation on the AMOC in the global configuration (ORCA025) of the VIKING20 model north of 55°N was evaluated in sensitivity experiments in Behrens et al. (2013) and was found to have a massive impact on the AMOC strength and long-term trend. Since VIKING20 only contains reduced precipitation north of 62°N the influence should be less than in this previous study since the subpolar North Atlantic is only partially, not fully affected by the rain reduction. Furthermore, VIKING20 contains a very weak sea surface salinity (SSS) restoring toward climatology. There is no SSS restoring applied near rivers and in regions where sea ice is present as well as around Greenland (Behrens et al., 2017) and there is no salt restoring in the Gulf of Cadiz (Mediterranean outflow). This potentially generates too high salinity values in the intermediate water masses in VIKING20, which could have a far reaching impact on the gyre scale salinity (Tréguier et al., 2012a, 2012b).

Third, the model was subsampled with an idealized mooring array to evaluate the performance of boundary current arrays, with a particular emphasis on the interior termination of the boundary current. The array in the model was able to capture the variability and ∼70% of the entire southeastward transport. Until recently, the 53°N observatory only partially captured the recirculation (Zantopp et al., 2017). In May 2016, a dedicated mooring was added to act as a terminating mooring.

Structural analysis of the velocity field at 53°N and the respective transports can be conducted. But due to the interpolation of the measured velocities to a regular grid, the transport signals are spatially low-pass filtered in the observations.

The water mass definition to compute transports in the observations is computed from the CTD sections collected during the service cruises, which are seasonally biased. However, as Zantopp et al. (2017) showed, the water mass boundary in σ_2 is rather stable in depth over the period of service cruises; hence, a depth definition of the water mass transport calculations served very well at 53°N.

The 53°N array was designed to be located well downstream of main convection sites of the inner Labrador Sea and well upstream of the northward extension of the NAC and its Northwest Corner. At 53°N the shelf break is rather steep and consequently topographic waves in the boundary current regime are dominated by short time scales (around 10 days) and a rather narrow frequency band (Fischer et al., 2014). In comparison with the position of the 53°N array, at other possible DWBC locations in the subpolar regime (e.g., the Grand Banks (Clarke et al., 1980; Schott et al., 2006)) the topography is more complex leading to multiple frequencies and longer periods. Additionally when the Gulfstream/NAC is directly in contact with the DWBC, transport estimates are more difficult to obtain in terms of instrument coverage and subsequent analysis of the measured flow field (Spall, 1996). These results imply that for boundary current mooring arrays like 53°N, the terminating mooring is crucial to correctly capture the variability of the boundary current by resolving the transition zone between the (southeastward) flow and the (northwestward) recirculation.

Fourth, transport time series of the two water masses LSW and LNADW were computed from both, model and observational data, and were analyzed for the 53°N section. In the observations, the spectra of LSW and LNADW show different behaviors on longer time scales. The respective formation locations, history, and forcing mechanisms could cause this difference on longer periods in the spectra. In comparison to this, the model spectra are more similar in the high-frequency regime and the transport time series of LSW and LNADW are very coherent.

The model and the observations show comparable mean transports and variance for the southeastward transport exiting Labrador Sea. Furthermore, the variability in both is similar on interannual time scales. Nevertheless the spectral composition of LSW and LNADW transport at 53°N and the AMOC estimate at 26.5°N in the model and the observations differ on longer than annual time scales and the model contains frequency bands, which are not found in the observations (Figures 7d, 7e, and 8).

The model suggests high correlation on longer time scales between the AMOC transport at 26.5°N and the LSW and LNADW southeastward transports at 53°N array (Figure 7). Due to the limitation to two decades of

comparable observational transport time series at, e.g., at 53°N and Ovide, and even less than that for RAPID-MOCHA, the analysis of the correlation of these longer time scales is not yet possible. However, on short time scales, the model and observations both show low to no correlation of the AMOC with the DWBC transport at 53°N.

Previous studies found that the AMOC variability is sensitive to the model parameterization, which influences the water mass formation through convection and mixing and the formation of baroclinic Rossby waves through atmospheric forcing (Buckley & Marshall, 2015). Since VIKING20 reproduces the winter convection depth and location reasonably well (although shifted to the southwest into the boundary current region), and it reproduces the spatial pattern of the first EOF mode of the winter wind stress curl in the observations (Häkkinen & Rhines, 2004), the connection between model transports at 53°N section and the applied wind forcing was analyzed. Because, at these latitudes, the baroclinic Rossby wave phase speed is low and the respective first baroclinic Rossby radius is small (Chelton et al., 1998), a quick barotropic model response would be expected on high-frequency, large-scale forcing variations. The baroclinic response takes longer and therefore the ocean acts as a low-pass filter that integrates the high-frequency wind stress forcing (Fedorov, 2008). We found that the modeled transports at 53°N are correlated slightly stronger to the basin wide wind stress curl than with regional wind stress curl. In contrast to this model result, Zantopp et al. (2017) found that in observations the near decadal fluctuations of LNADW transport are in phase with the NAO modulated wind fluctuations.

A possible reason for this model-observation divergence in the correlations might be the nature of the applied atmospheric forcing. By assimilating observational data and constructing coarse reanalysis forcing products like the COREv.2 forcing, with a resolution of $2° \times 2°$, small-scale variability of the wind field is lost. These small-scale signals could play an important role interacting with the DWBC in the subpolar North Atlantic. The response of the model to small-scale wind forcing, e.g., on the continental shelves, in the region of interest can therefore not be evaluated. However, the exact interaction mechanisms of atmospheric forcing, hydrography, and velocity field in midlatitudes are still not understood and remain a topic for further research.

As shown and discussed above, the VIKING20 model is a valuable tool evaluating observational time series like the mooring time series obtained from the 53°N observatory. A number of integral properties can be equally well defined and evaluated in model and observations. Despite the shortcomings of the model in comparison to the observations, in particular the different hydrography and the southwestward stretching of the convection into the boundary current regime, it can be used for further studies of possible mechanisms imprinting variability on the large scale in the model setup. Hence, the results of this study confirm that the observational effort needs to continue for longer time periods, to open up the possibility to analyze longer time scale variability and its connections to the atmospheric forcing. Comparisons like these allow the evaluation and verification of hind-cast models and forecast models on time scales longer than decadal. Such an observational effort would further increase the value of the time series at 53°N in the context of understanding the AMOC system and its transport variability. The limited length of observational records allows the observation of baroclinic Rossby waves in subtropical latitudes on shorter time scales, but leaves a challenge for the latitudes of the subpolar gyre due to the slow phase speed. In particular, the exact mechanisms at play of the basin wide baroclinic response of the boundary currents and the AMOC transport to the wind forcing attract future research interest.

Acknowledgments
The research leading to these results has received funding from the German Ministry of Research and Education (RACE Program) and the European Union's Seventh Framework Program (FP7/2007-2013) under grant agreement 308299 (NACLIM). The 53°N array is part of the OceanSITES network (www.oceansites.org). We thank Erik Behrens (National Institute for Water and Atmospheric Research, Wellington, New Zealand) and Klaus Getzlaff (GEOMAR Helmholtz Centre for Ocean Research Kiel, Kiel, Germany). The used Argo mixed layer data are available online at http://mixedlayer.ucsd.edu. The Argo velocities were downloaded from the two Global Data Assembly Centers indicated at the international Argo website http://www.argo.ucsd.edu/Argo_data_and.html. We thank Igor Yashayaev (Fisheries and Oceans Canada, Bedford Institute of Oceanography, Dartmouth, Nova Scotia, Canada) for the hydrographic data from the central Labrador Sea (Yashayaev & Loder, 2016). We appreciate the constructive comments by numerous colleagues.

References

Baehr, J., Keller, K., & Marotzke, J. (2008). Detecting potential changes in the meridional overturning circulation at 26°N in the Atlantic. *Climatic Change*, *91*(1–2), 11–27.

Barnier, B., Blaker, A., Biastoch, A., Böning, C. W., Coward, A., Deshayes, J., et al. (2015). DRAKKAR: Developing high resolution ocean components for European Earth system models. *Clivar Exchanges*, *65*, 18–21.

Behrens, E. (2013). *The oceanic response to Greenland melting: The effect of increasing model resolution* (dissertation). Kiel, Germany: Christian-Albrechts-Universität.

Behrens, E., Biastoch, A., & Böning, C. W. (2013). Spurious AMOC trends in global ocean sea-ice models related to subarctic freshwater forcing. *Ocean Modelling*, *69*, 39–49.

Behrens, E., Våge, K., Harden, B., Biastoch, A., & Böning, C. W. (2017). Composition and variability of the Denmark Strait Overflow Water in a high-resolution numerical model hindcast simulation. *Journal of Geophysical Research: Oceans*, *122*, 2830–2846. https://doi.org/10.1002/2016JC012158

Bingham, R. J., Hughes, C. W., Roussenov, V., & Williams, R. G. (2007). Meridional coherence of the North Atlantic meridional overturning circulation. *Geophysical Research Letters*, *34*, L23606. https://doi.org/10.1029/2007GL031731

Böning, C. W., Behrens, E., Biastoch, A., Getzlaff, K., & Bamber, J. L. (2016). Emerging impact of Greenland meltwater on deepwater formation in the North Atlantic Ocean. *Nature Geoscience*, *9*, 523–527.
Böning, C. W., Scheinert, M., Dengg, J., Biastoch, A., & Funk, A. (2006). Decadal variability of subpolar gyre transport and its reverberation in the North Atlantic overturning. *Geophysical Research Letters*, *33*, L21S01. https://doi.org/10.1029/2006GL026906
Bower, A., Le Cann, B., Rossby, T., Zenk, W., Gould, J., Speer, K., et al. (2002). Directly measured mid-depth circulation in the northeastern North Atlantic Ocean. *Nature*, *419*(6907), 603–607.
Bower, A. S., Lozier, M. S., Gary, S. F., & Böning, C. W. (2009). Interior pathways of the North Atlantic meridional overturning circulation. *Nature*, *459*(7244), 243–247.
Brandt, P., Funk, A., Czeschel, L., Eden, C., & Böning, C. W. (2007). Ventilation and transformation of Labrador Sea Water and its rapid export in the deep Labrador Current. *Journal of Physical Oceanography*, *37*(4), 946–961.
Brandt, P., Schott, F. A., Funk, A., & Martins, C. S. (2004). Seasonal to interannual variability of the eddy field in the Labrador Sea from satellite altimetry. *Journal of Geophysical Research*, *109*, C02028. https://doi.org/10.1029/2002JC001551
Breckenfelder, T., Rhein, M., Roessler, A., Böning, C. W., Biastoch, A., Behrens, E., et al. (2017). Flow paths and variability of the North Atlantic Current: A comparison of observations and a high-resolution model. *Journal of Geophysical Research: Oceans*, *122*, 2686–2708. https://doi.org/10.1002/2016JC012444
Buckley, M. W., & Marshall, J. (2015). Observations, inferences and mechanisms of Atlantic MOC variability: A review. *Reviews of Geophysics*, *54*, 5–63. https://doi.org/10.1002/2015RG000493
Chelton, D. B. A. D., Roland, A., Schlax, M. G., El Naggar, K., & Siwertz, N. (1998). Geographical variability of the first baroclinic Rossby radius of deformation. *Journal of Physical Oceanography*, *28*(3), 433–460.
Church, J. A. (2007). A change in circulation? *Science*, *317*(5840), 908–909.
Clarke, R. A., Hill, H. W., Reiniger, R. F., & Warren, B. A. (1980). Current system south and east of the Grand Banks of Newfoundland. *Journal of Physical Oceanography*, *10*(1), 25–65.
Cubasch, U., Meehl, G., Boer, G., Stouffer, R., Dix, M., Noda, A., et al. (2001). Projections of future climate change. In Houghton, J. T., et al. (Eds.), *Climate change 2001: The scientific basis: Contribution of working group I to the third assessment report of the intergovernmental panel* (pp. 526–582). Cambridge, UK: Cambridge University Press.
Debreu, L., Vouland, C., & Blayo, E. (2008). AGRIF: Adaptive grid refinement in Fortran. *Computers & Geosciences*, *34*(1), 8–13.
Dengler, M., Fischer, J., Schott, F. A., & Zantopp, R. (2006). Deep Labrador Current and its variability in 1996–2005. *Geophysical Research Letters*, *33*, L21S06. https://doi.org/10.1029/2006GL026702
Dengler, M., Schott, F., Eden, C., Brandt, P., Fischer, J., & Zantopp, R. J. (2004). Break-up of the Atlantic deep western boundary current into eddies at 8 S. *Nature*, *432*(7020), 1018–1020.
Dickson, R. R., & Brown, J. (1994). The production of North Atlantic Deep Water: Sources, rates, and pathways. *Journal of Geophysical Research*, *99*(C6), 12319–12341.
Eden, C., & Greatbatch, R. J. (2003). A damped decadal oscillation in the North Atlantic climate system. *Journal of Climate*, *16*(24), 4043–4060.
ETOPO, U. (2001). *2-minute gridded global relief data*. Silver Spring, MD: Department of Commerce, National Oceanic and Atmospheric Administration, National Geophysical Data Center.
Fedorov, A. V. (2008). Ocean-atmosphere coupling. In Goudie, A. & Cuff, D. (Eds.), *Oxford companion to global change* (pp. 369–374). Oxford, UK. Oxford University Press.
Fichefet, T., & Maqueda, M. (1997). Sensitivity of a global sea ice model to the treatment of ice thermodynamics and dynamics. *Journal of Geophysical Research*, *102*(C6), 12609–12646.
Fischer, J., Karstensen, J., Zantopp, R., Visbeck, M., Biastoch, A., Behrens, E., et al. (2014). Intra-seasonal variability of the DWBC in the western subpolar North Atlantic. *Progress in Oceanography*, *132*, 233–249.
Fischer, J., Schott, F. A., & Dengler, M. (2004). Boundary circulation at the exit of the Labrador Sea. *Journal of Physical Oceanography*, *34*(7), 1548–1570.
Fischer, J., Visbeck, M., Zantopp, R., & Nunes, N. (2010). Interannual to decadal variability of outflow from the Labrador Sea. *Geophysical Research Letters*, *37*, L24610. https://doi.org/10.1029/2010GL045321
Flatau, M. K., Talley, L., & Niiler, P. P. (2003). The North Atlantic Oscillation, surface current velocities, and SST changes in the subpolar North Atlantic. *Journal of Climate*, *16*(14), 2355–2369.
Greatbatch, R. J. (2000). The north Atlantic oscillation. *Stochastic Environmental Research and Risk Assessment*, *14*(4), 213–242.
Gregory, J., Dixon, K., Stouffer, R., Weaver, A., Driesschaert, E., Eby, M., et al. (2005). A model intercomparison of changes in the Atlantic thermohaline circulation in response to increasing atmospheric CO_2 concentration. *Geophysical Research Letters*, *32*, L12703. https://doi.org/10.1029/2005GL023209
Griffies, S. M., Biastoch, A., Böning, C., Bryan, F., Danabasoglu, G., Chassignet, E. P., et al. (2009). Coordinated ocean-ice reference experiments (COREs). *Ocean Modelling*, *26*(1), 1–46.
Haine, T., Böning, C., Brandt, P., Fischer, J., Funk, A., Kieke, D., et al. (2008). North Atlantic deep water formation in the Labrador Sea, recirculation through the subpolar gyre, and discharge to the subtropics. In Dickson, R. R., Meincke, J., & Rhines, P. (Eds.), *Arctic-subarctic ocean fluxes* (pp. 653–701). Dordrecht, Netherlands: Springer.
Häkkinen, S., & Rhines, P. B. (2004). Decline of subpolar North Atlantic circulation during the 1990s. *Science*, *304*(5670), 555–559.
Hansen, B., & Østerhus, S. (2000). North Atlantic-Nordic Seas exchanges. *Progress in Oceanography*, *45*(2), 109–208.
Hatun, H., Britt, S. A., Drange, H., Hansen, B., & Valdimarsson, H. (2005). Influence of the Atlantic Subpolar Gyre on the thermohaline circulation. *Science*, *309*(5742), 1841–1844.
Higginson, S., Thompson, K., Huang, J., Véronneau, M., & Wright, D. (2011). The mean surface circulation of the North Atlantic subpolar gyre: A comparison of estimates derived from new gravity and oceanographic measurements. *Journal of Geophysical Research*, *116*, C08016. https://doi.org/10.1029/2010JC006877
Holte, J., & Straneo, F. (2017). Seasonal overturning of the Labrador Sea as observed by Argo Floats. *Journal of Physical Oceanography*, *47*(10), 2531–2543.
Holte, J., Talley, L. D., Gilson, J., & Roemmich, D. (2017). An Argo mixed layer climatology and database. *Geophysical Research Letters*, *44*, 5618–5626. https://doi.org/10.1002/2017GL073426
Hummels, R., Brandt, P., Dengler, M., Fischer, J., Araujo, M., Veleda, D., et al. (2015). Interannual to decadal changes in the Western boundary circulation in the Atlantic at 11°S. *Geophysical Research Letters*, *42*, 7615–7622. https://doi.org/10.1002/2015GL065254
Hurrell, J. W. (1995). Decadal trends in the North Atlantic oscillation. *Science*, *269*, 676–679.
Hurrell, J. W., & Deser, C. (2010). North Atlantic climate variability: The role of the North Atlantic Oscillation. *Journal of Marine Systems*, *79*(3), 231–244.

Ioc, I. (2008). *BODC, 2003. Centenary Edition of the GEBCO Digital Atlas, published on CD-ROM on behalf of the Intergovernmental Oceanographic Commission and the International Hydrographic Organization as part of the General Bathymetric Chart of the Oceans*. Liverpool, UK: British Oceanographic Data Centre.

Jochumsen, K., Köllner, M., Quadfasel, D., Dye, S., Rudels, B., & Valdimarsson, H. D. (2015). On the origin and propagation of Denmark Strait overflow water anomalies in the Irminger Basin. *Journal of Geophysical Research: Oceans*, *120*, 1841–1855. https://doi.org/10.1002/2014JC010397

Joyce, T. M., & Zhang, R. (2010). On the path of the Gulf Stream and the Atlantic meridional overturning circulation. *Journal of Climate*, *23*(11), 3146–3154.

Kieke, D., Rhein, M., Stramma, L., Smethie, W. M., LeBel, D. A., & Zenk, W. (2006). Changes in the CFC inventories and formation rates of Upper Labrador Sea Water, 1997–2001. *Journal of Physical Oceanography*, *36*(1), 64–86.

Large, W., & Yeager, S. (2009). The global climatology of an interannually varying air-sea flux data set. *Climate Dynamics*, *33*(2–3), 341–364.

Lavender, K. L., Davis, R. E., & Owens, W. B. (2000). Mid-depth recirculation observed in the interior Labrador and Irminger Seas by direct velocity measurements. *Nature*, *407*(6800), 66–69.

Lazier, J. (1973). The renewal of Labrador Sea water. *Deep-Sea Research and Oceanographic Abstracts*, *20*, 341–353.

Lazier, J., Hendry, R., Clarke, A., Yashayaev, I., & Rhines, P. (2002). Convection and restratification in the Labrador Sea, 1990–2000. *Deep-Sea Research Part I*, *49*(10), 1819–1835.

Lazier, J., Pickart, R., & Rhines, P. (2001). Deep convection. *International Geophysics Series*, *77*, 387–400.

Lebedev, K. V., Yoshinari, H., Maximenko, N. A., & Hacker, P. W. (2007). Velocity data assessed from trajectories of Argo floats at parking level and at the sea surface. *IPRC Technical Note*, *4*(2), 1–16.

Le Bras, I. A., Yashayaev, I., & Toole, J. (2017). Tracking Labrador Sea water property signals along the Deep Western Boundary Current. *Journal of Geophysical Research: Oceans*, *122*, 5348–5366. https://doi.org/10.1002/2017JC012921

Lilly, J. M., Rhines, P. B., Schott, F., Lavender, K., Lazier, J., Send, U., et al. (2003). Observations of the Labrador Sea eddy field. *Progress in Oceanography*, *59*(1), 75–176.

Lomb, N. R. (1976). Least-squares frequency analysis of unequally spaced data. *Astrophysics and Space Science*, *39*(2), 447–462.

Longworth, H. R., & Bryden, H. L. (2007). Discovery and quantification of the Atlantic meridional overturning circulation: The importance of 25°N. In Schmittner, A., Chiang, J. C., & Hemming, S. R. (Eds.), *Ocean circulation: Mechanisms and impacts—Past and future changes of meridional overturning* (pp. 5–18). Washington, DC: American Geophysical Union.

Lozier, M. S. (2010). Deconstructing the conveyor belt. *Science*, *328*(5985), 1507–1511.

Lozier, M. S. (2012). Overturning in the North Atlantic. *Annual Review of Marine Science*, *4*, 291–315.

Lozier, M. S., Bacon, S., Bower, A. S., Cunningham, S. A., Femke de Jong, M., De Steur, L., et al. (2017). Overturning in the Subpolar North Atlantic Program: A new international ocean observing system. *Bulletin of the American Meteorological Society*, *98*(4), 737–752.

Macrander, A., Send, U., Valdimarsson, H., Jónsson, S., & Käse, R. H. (2005). Interannual changes in the overflow from the Nordic Seas into the Atlantic Ocean through Denmark Strait. *Geophysical Research Letters*, *32*, L06606. https://doi.org/10.1029/2004GL021463

Madec, G. (2008). NEMO ocean engine (IPSL Tech. Note, 332).

Marshall, J., Dobson, F., Moore, K., Rhines, P., Visbeck, M., D'asaro, E., et al. (1998). The Labrador Sea deep convection experiment. *Bulletin of the American Meteorological Society*, *79*(10), 2033–2058.

Marshall, J., Johnson, H., & Goodman, J. (2001). A study of the interaction of the North Atlantic Oscillation with ocean circulation. *Journal of Climate*, *14*(7), 1399–1421.

Marshall, J., & Schott, F. (1999). Open-ocean convection: Observations, theory and models. *Reviews of Geophysics*, *37*(1), 1–64.

Mercier, H., Lherminier, P., Sarafanov, A., Gaillard, F., Daniault, N., Desbruyères, D., et al. (2015). Variability of the meridional overturning circulation at the Greenland-Portugal OVIDE section from 1993 to 2010. *Progress in Oceanography*, *132*, 250–261.

Mertens, C., Rhein, M., Walter, M., Böning, C. W., Behrens, E., Kieke, D., et al. (2014). Circulation and transports in the Newfoundland Basin, western subpolar North Atlantic. *Journal of Geophysical Research: Oceans*, *119*, 7772–7793. https://doi.org/10.1002/2014JC010019

Mielke, C. L., Baehr, J., & Gary, S. (2015). *The North Atlantic deep western boundary current: Seasonal cycle, decadal variability and relation to the Atlantic meridional overturning circulation*. Hamburg, Germany: Universität Hamburg.

Molinari, R. L., Fine, R. A., Wilson, W. D., Curry, R. G., Abell, J., & McCartney, M. S. (1998). The arrival of recently formed Labrador Sea Water in the deep western boundary current at 26.5°N. *Geophysical Research Letters*, *25*(13), 2249–2252.

Østerhus, S., Turrell, W. R., Hansen, B., Lundberg, P., & Buch, E. (2001). Observed transport estimates between the North Atlantic and the Arctic Mediterranean in the Iceland-Scotland region. *Polar Research*, *20*(2), 169–175.

Overland, J. E., Percival, D. B., & Mofjeld, H. O. (2006). Regime shifts and red noise in the North Pacific. *Deep-Sea Research Part I*, *53*(4), 582–588.

Peña-Molino, B., & Joyce, T. M. (2008). Variability in the slope water and its relation to the Gulf Stream path. *Geophysical Research Letters*, *35*, L03606. https://doi.org/10.1029/2007GL032183

Peña-Molino, B., Joyce, T. M., & Toole, J. M. (2011). Recent changes in the Labrador Sea Water within the deep western boundary current southeast of Cape Cod. *Deep-Sea Research Part I*, *58*(10), 1019–1030.

Perez, R. C., Garzoli, S. L., Meinen, C. S., & Matano, R. P. (2011). Geostrophic velocity measurement techniques for the meridional overturning circulation and meridional heat transport in the South Atlantic. *Journal of Atmospheric and Oceanic Technology*, *28*(11), 1504–1521.

Pickart, R., Spall, M., & Lazier, J. (1997). Mid-depth ventilation in the western boundary current system of the sub-polar gyre. *Deep-Sea Research Part I*, *44*(6), 1025–1054.

Pickart, R. S., Straneo, F., & Moore, G. (2003). Is Labrador sea water formed in the Irminger basin? *Deep-Sea Research Part I*, *50*(1), 23–52.

Pickart, R. S., Torres, D. J., & Clarke, R. A. (2002). Hydrography of the Labrador Sea during active convection. *Journal of Physical Oceanography*, *32*(2), 428–457.

Reverdin, G., Niiler, P., & Valdimarsson, H. (2003). North Atlantic Ocean surface currents. *Journal of Geophysical Research*, *108*(C1), 3002. https://doi.org/10.1029/2001JC001020

Rudnick, D. L., & Davis, R. E. (2003). Red noise and regime shifts. *Deep-Sea Research Part I*, *50*(6), 691–699.

Sabine, C. L., Feely, R. A., Gruber, N., Key, R. M., Lee, K., Bullister, J. L., et al (2004). The oceanic sink for anthropogenic CO_2. *Science*, *305*(5682), 367–371.

Scargle, J. D. (1982). Studies in astronomical time series analysis. II-Statistical aspects of spectral analysis of unevenly spaced data. *The Astrophysical Journal*, *263*, 835–853.

Schott, F. A., Fischer, J., Dengler, M., & Zantopp, R. (2006). Variability of the deep western boundary current east of the Grand Banks. *Geophysical Research Letters*, *33*, L21S07. https://doi.org/10.1029/2006GL026563

Schott, F. A., Zantopp, R., Stramma, L., Dengler, M., Fischer, J., & Wibaux, M. (2004). Circulation and deep-water export at the western exit of the subpolar North Atlantic. *Journal of Physical Oceanography*, *34*(4), 817–843.

Send, U., Lankhorst, M., & Kanzow, T. (2011). Observation of decadal change in the Atlantic meridional overturning circulation using 10 years of continuous transport data. *Geophysical Research Letters*, *38*, L24606. https://doi.org/10.1029/2011GL049801

Sheng, J., Greatbatch, R. J., Zhai, X., & Tang, L. (2005). A new two-way nesting technique for ocean modeling based on the smoothed semi-prognostic method. *Ocean Dynamics*, *55*(3–4), 162–177.

Siedler, G., Gould, J., & Church, J. A. (2001). *Ocean circulation and climate: Observing and modelling the global ocean*. Cambridge, MA: Academic Press.

Smeed, D., McCarthy, G., Rayner, D., Moat, B., Johns, W., Baringer, M., et al. (2016). *Atlantic meridional overturning circulation observed by the RAPID-MOCHA-WBTS (RAPID-Meridional Overturning Circulation and Heatflux Array-Western Boundary Time Series) array at 26°N from 2004 to 2015*. UK: British Oceanographic Data Centre.

Spall, M. A. (1996). Dynamics of the Gulf Stream/deep western boundary current crossover. Part I: Entrainment and recirculation. *Journal of Physical Oceanography*, *26*(10), 2152–2168.

Srokosz, M., Baringer, M., Bryden, H., Cunningham, S., Delworth, T., Lozier, S., et al. (2012). Past, present, and future changes in the Atlantic meridional overturning circulation. *Bulletin of the American Meteorological Society*, *93*(11), 1663–1676.

Stocker, T., Qin, D., Plattner, G.-K., Tignor, M., Allen, S. K., Boschung, J., et al. (2014). *Climate change 2013: The physical science basis*. Cambridge, UK: Cambridge University Press.

Swift, J. H., Aagaard, K., & Malmberg, S.-A. (1980). The contribution of the Denmark Strait overflow to the deep North Atlantic. *Deep-Sea Research Part A*, *27*(1), 29–42.

Swingedouw, D., Rodehacke, C. B., Behrens, E., Menary, M., Olsen, S. M., Gao, Y., et al. (2013). Decadal fingerprints of freshwater discharge around Greenland in a multi-model ensemble. *Climate Dynamics*, *41*(3–4), 695–720.

Toole, J., Curry, R., Joyce, T., McCartney, M., & Peña-Molino, B. (2011). Transport of the North Atlantic deep western boundary current about 39°N, 70°W: 2004–2008. *Deep-Sea Research Part II*, *58*(17), 1768–1780.

Toole, J. M., Andres, M., Le Bras, I. A., Joyce, T. M., & McCartney, M. S. (2017a). Moored observations of the Deep Western Boundary Current in the NW Atlantic: 2004–2014. *Journal of Geophysical Research: Oceans*, *122*, 7488–7505. https://doi.org/10.1002/2017JC012984

Toole, J. M., Andres, M., Le Bras, I. A., Joyce, T. M., & McCartney, M. S. (2017b). Moored observations of the Deep Western Boundary Current in the NW Atlantic: 2004–2014. *Journal of Geophysical Research: Oceans*, *122*, 7488–7505. https://doi.org/10.1002/2017JC012984

Tréguier, A.-M., Deshayes, J., Lique, C., Dussin, R., & Molines, J.-M. (2012b). Eddy contributions to the meridional transport of salt in the North Atlantic. *Journal of Geophysical Research*, *117*, C05010. https://doi.org/10.1029/2012JC007927

Tréguier, A.-M., Ferron, B., & Dussin, R. (2012a). Buoyancy-driven currents in eddying ocean models. In Chassignet, E., Cenedese, C., & Verron, J. (Eds.), *Buoyancy-driven flows* (pp. 281–311). Cambridge, UK: Cambridge University Press.

Tréguier, A.-M., Theetten, S., Chassignet, E. P., Penduff, T., Smith, R., Talley, L., et al. (2005). The North Atlantic subpolar gyre in four high-resolution models. *Journal of Physical Oceanography*, *35*(5), 757–774.

van Sebille, E., Baringer, M. O., Johns, W. E., Meinen, C. S., Beal, L. M., de Jong, M. F., et al. (2011). Propagation pathways of classical Labrador Sea water from its source region to 26°N. *Journal of Geophysical Research*, *116*, C12027. https://doi.org/10.1029/2011JC007171

von Appen, W.-J., Koszalka, I. M., Pickart, R. S., Haine, T. W., Mastropole, D., Magaldi, M. G., et al. (2014). The East Greenland Spill Jet as an important component of the Atlantic meridional overturning circulation. *Deep-Sea Research Part I*, *92*, 75–84.

Willebrand, J., Barnier, B., Böning, C., Dieterich, C., Killworth, P. D., Le Provost, C., et al. (2001). Circulation characteristics in three eddy-permitting models of the North Atlantic. *Progress in Oceanography*, *48*(2), 123–161.

Wunsch, C., & Heimbach, P. (2013). Two decades of the Atlantic meridional overturning circulation: Anatomy, variations, extremes, prediction, and overcoming its limitations. *Journal of Climate*, *26*(18), 7167–7186.

Xu, X., Hurlburt, H., Schmitz, W., Zantopp, R., Fischer, J., & Hogan, P. (2013). On the currents and transports connected with the Atlantic meridional overturning circulation in the subpolar North Atlantic. *Journal of Geophysical Research: Oceans*, *118*, 502–516. https://doi.org/10.1002/jgrc.20065

Xu, X., Schmitz, W. Jr., Hurlburt, H., & Hogan, P. (2012). *Mean Atlantic meridional overturning circulation across 26.5 degs N from eddy-resolving simulations compared to observations* (report, DTIC document). Fort Belvoir, VA: Defense Technical Information Center.

Yashayaev, I., & Loder, J. W. (2009). Enhanced production of Labrador Sea water in 2008. *Geophysical Research Letters*, *36*, L01606. https://doi.org/10.1029/2008GL036162

Yashayaev, I., & Loder, J. W. (2016). Recurrent replenishment of Labrador Sea Water and associated decadal scale variability. *Journal of Geophysical Research: Oceans*, *121*, 8095–8114. https://doi.org/10.1002/2016JC012046

Yashayaev, I., Seidov, D., & Demirov, E. (2015). A new collective view of oceanography of the Arctic and North Atlantic basins. *Progress in Oceanography*, *132*, 1–21.

Yashayaev, I., van Aken, H. M., Holliday, N. P., & Bersch, M. (2007). Transformation of the Labrador Sea water in the subpolar North Atlantic. *Geophysical Research Letters*, *34*, L22605. https://doi.org/10.1029/2007GL031812

Zantopp, R., Fischer, J., Visbeck, M., & Karstensen, J. (2017). From interannual to decadal—17 years of boundary current transports at the exit of the Labrador Sea. *Journal of Geophysical Research: Oceans*, *122*, 1724–1748. https://doi.org/10.1002/2016JC012271

Zelenko, A., & Resnyansky, Y. D. (2007). Deep convection in the ocean general circulation model: Variability on the diurnal, seasonal, and interannual time scales. *Oceanology*, *47*(2), 191–204.

Zhu, J., Demirov, E., Zhang, Y., & Polomska-Harlick, A. (2014). Model simulations of mesoscale eddies and deep convection in the Labrador Sea. *Advances in Atmospheric Sciences*, *31*(4), 743–754.

3. LSW spreading dynamics connecting the central Labrador and Irminger Sea

The aim of this chapter is to evaluate proposed pathways connecting the central Labrador with the Irminger Sea. Lagrangian particle experiments, using Argo based velocity fields [*Fischer et al.*, 2018] and high resolution ocean model output (VIKING20X) on the LSW depth, were conducted and the resulting connectivity between the two regions will be presented.

3.1 Abstract

Deep water formed in the subpolar North Atlantic, namely Labrador Sea Water (LSW) gets exported southward and connects the high latitudes with the rest of the oceans, as the lower Atlantic meridional overturning (AMOC) limb. Here, the possible export routes connecting the Labrador and Irminger Sea are explored in detail with simulated Lagrangian particle trajectories. For the particle track integration Eulerian velocity fields from a high-resolution ocean model and derived from Argo floats ("Argo based") are used with a purely advective integration as well as with additional diffusion parameterization. $\sim 20\%$ of the overall seeded particles connect the two regions in the Argo based advective-diffusive and the advective experiments using the temporarily varying model output. A 2.5 to 3.5 year travel time was estimated for the Argo based advective-diffusive particle trajectory integration between the Labrador and the Irminger Sea. The experiments with the temporarily varying high resolution model output reveal shorter spreading times of $\sim$ 1.5 - 2 years. With a relatively simple method similar spreading values derived from various observations can be reproduced. The connectivity between the two regions is weaker in the experiments based on the mean velocity output of the model than in those based on the Argo derived fields.

3.2 Introduction

The subpolar North Atlantic (SPNA) is playing a key role in our climate system [*Buckley and Marshall*, 2015; *Wunsch*, 1997]. It is a region which is connecting the "upper" and "lower" limb of the Atlantic meridional overturning circulation (AMOC) through deep convection and the respective conversion of relatively warm and salty waters to cold and fresh North Atlantic Deep Water (NADW) [*Lazier*, 1973; *Lazier et al.*, 2001; *Marshall and Schott*, 1999; *Pickart et al.*, 2005].

The Labrador Sea water (LSW) is the upper component of the North Atlantic Deep Water(e.g. *Lazier* [1973]). It has a cold and low salinity signature combined with an anomalously low potential vorticity and a high concentration of dissolved oxygen [*Yashayaev and Loder*, 2016] and anthropogenic tracers (e.g. CFC, anthropogenic CO_2) [*Rhein et al.*, 2002, 2017; *Smethie Jr. and Fine*, 2001; *Talley and McCartney*, 1982]. Over the past decades LSW was only thought to be built in the central Labrador Sea (hence the name) and three major export pathways were identified [*Fischer et al.*, 2018; *Rhein et al.*, 2002; *Sy et al.*, 1997; *Talley and McCartney*, 1982]:

1. Northeastward via the recirculation from the Labrador Sea to the Irminger Sea (Figure 3.1 **pathway 1**)

2. Southward via the DWBC towards the subtropical gyre (Figure 3.1 **pathway 2**)

3. Eastward into the Northeast Atlantic via the northern flank of the North Atlantic Current (NAC) (Figure 3.1 **pathway 3**)

More recent studies [*Bacon et al.*, 2003; *de Jong et al.*, 2016, 2018; *Falina et al.*, 2007; *Pickart et al.*, 2003a; *Piron et al.*, 2016; *Våge et al.*, 2008] support the previous view of *Nansen* [1912], that deep convection also occurs at the southeast of the southern tip of Greenland, though not as deep as in the central Labrador Sea but resulting in a similar density, low PV and tracer concentration. If the heat flux from the weakly stratified upper water column (upper 300 m) is strong enough through e.g. Greenland Tip Jet events [*Holdsworth and Myers*, 2015; *Pickart et al.*, 2003a, 2008], deep convection is possible in the southern Irminger Sea and along the export pathways following the recirculation in the Labrador Sea. The exact geographic positioning of the convective regions each winter is still a difficult task [*Böning et al.*, 2006; *Brandt et al.*, 2007; *Handmann et al.*, 2018; *Holte et al.*, 2017]. Overall, LSW formation rates vary within literature from 1-12.5 Sv (e.g.*Clarke and Gascard* [1983]; *Rhein et al.* [2002]; *Smethie et al.* [2000]; *Smethie Jr. and Fine* [2001]; *Worthington* [1976]). Multiple observational and modeling studies focused on the spreading of LSW in an Lagrangian framework. Neutrally buoyant floats launched in the entire SPNA [*Lavender et al.*, 2005] or floats seeded into the LSW water mass in the DWBC near $50°$N [*Bower et al.*, 2009; *Fischer and Schott*, 2002] were tracked and suggested that the majority of the floats do not get exported to the subtropics via the DWBC beyond $44°$N but instead they are exported towards the south via interior pathways [*Bower et al.*, 2011, 2009; *Lozier*, 2012; *Zou and Lozier*, 2016]. When the floats were seeded directly into the DWBC only 8% made it to the subtropical basin, 30% of them reached the subtropics within two years and the remaining 70% stayed in the SPNA and recirculated [*Bower et al.*, 2009]. For freshly formed LSW *Rhein et al.* [2002] quantified that 21% of the inventory would be directly exported by the DWBC and was found south of $53°$N on the southward pathway towards the subtropical gyre (pathway), 20% were entering the Irminger Sea, 31% were found in the Iceland basin and 28% stayed in the Labrador Sea. Further the

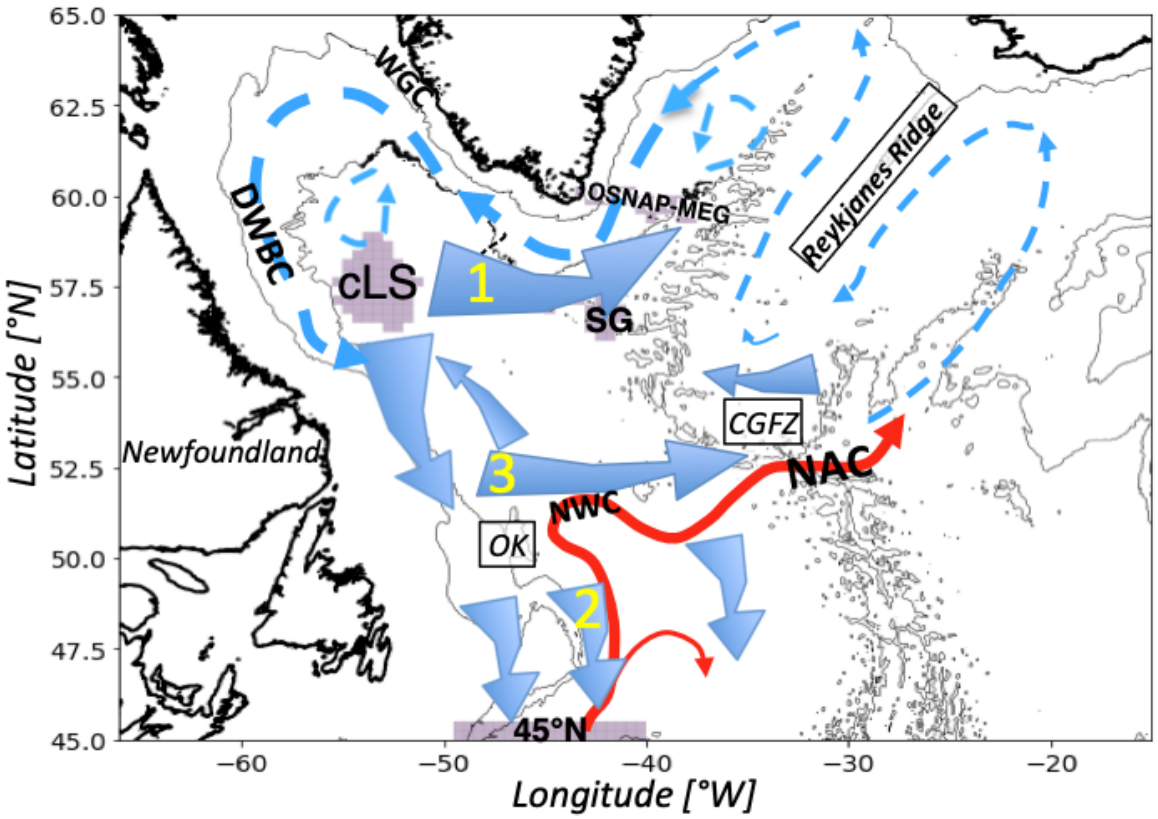

Figure 3.1: *Schematic map of LSW spreading routes (1,2,3) from the central Labrador Sea into the subpolar North Atlantic. The red arrow marks the North Atlantic Current (NAC), with its Northwest Corner (NWC). The convection region [Holte and Straneo, 2017] in the central Labrador Sea (cLS) and the southern Tip of Greenland (***SG***) as well as the sections of interest to this study are marked with a gray patches and the respective abbreviation. Further geographic regions (OK - Orphan Knoll region, CGFZ-Charlie-Gibbs-Fracture-Zone) as well as the DWBC-Deep Western Boundary Current are marked with their abbreviations.*

link between DWBC export and LSW formation is vividly discussed, where some studies find a correlation between the two (e.g. *Böning et al.* [2006]; *Brandt et al.* [2007]) and others result in the contrary (e.g. *Dengler et al.* [2006]; *Schott et al.* [2004]; *Willebrand et al.* [2001]).

Studies relying on salinities [*Cunningham and Haine*, 1995; *Read and Gould*, 1992] or transient tracers like chlorofluorocarbon (CFC) [*Rhein et al.*, 2002; *Smethie et al.*, 2000; *Weiss et al.*, 1985] or tritium-helium [*Top et al.*, 1987] deduced slow spreading rates: 1.5 cm/s in the western boundary and 0.5 cm/s in the interior. Before the Argo era, wintertime data from the Labrador Sea was not available to the observational studies, the travel time from Labrador Sea into Irminger Sea could have been largely underestimated because quick restratification after deep convection is able to mask local deep convection [*Lilly et al.*, 1999]. These slow spreading would result in travel times from observations of around 2 years from the LSW formation region into e.g central Irminger Sea [*Falina et al.*, 2007; *Yashayaev et al.*, 2007]. *Lavender et al.* [2000,

2005] found 1 - 1.5 years from direct velocity measurements from subsurface profiling floats, whereas *Yashayaev et al.* [2008] derived travel times of 1 - 4 years for the shallower component of the LSW from hydrography. Contradicting to these timescales *Sy et al.* [1997] estimates spreading rates of up to 4.5 cm/s from temperature, salinity and CFC data unraveling 0.5 year travel time from the western central Labrador Sea to the central Irminger Sea. Advective-diffusive numerical models with a simulated spreading of an ideal tracer estimate travel times of 2 years which is within the observed [*Straneo et al.*, 2003].

The interaction between the ocean basins and the boundary currents and the link between LSW formation and its eventual export are closely connected to mean circulation patterns and eddy activity. Ocean eddies represent deviations of the mean flow and redistribute oceanic quantities such as heat, salt, potential vorticity or biogeochemical tracers in geophysical flows from the sub-mesoscale O($\sim 1km$) to the large-scale O(~ 1000km) through turbulent processes and their respective rate of particle dispersal [*Delworth et al.*, 2012; *Rypina et al.*, 2016]. Mesoscale eddies ($\sim 10 - 100$ km) and jets disperse fluid particles quickly and increase the rate of mass, momentum and tracer spreading which in turn implies accelerated mixing [*LaCasce*, 2008]. The turbulent flow is widely described via Reynolds decomposition, where the total turbulent flow $\mathbf{u}$ is described in terms of a long-term or slowly varying mean velocity $\bar{\mathbf{u}}$ and the residual eddy component $\mathbf{u}'$:

$$\mathbf{u} = \bar{\mathbf{u}} + \mathbf{u}'. \tag{3.1}$$

Dependent on the choice of the mean, the residual eddy component can include additionally to the mesoscale also the seasonal to inter-annual variability [*Laurindo et al.*, 2017; *Rieck et al.*, 2015; *Uchida et al.*, 2017] or processes not resolved by the flow field [*Rypina et al.*, 2016].

In Ocean General Circulation Models (OGCM) the ocean is simulated by the Navier-Stokes equations (primitive equations) with approximations coming from scale considerations and a nonlinear equation of state, which couple the temperature and salinity as active tracers to the velocities [*Madec et al.*, 2017]. Because momentum is dissipated by friction on the molecular scale and the primitive equations are discretized (spatial and temporal), processes smaller than the model grid-scale are not completely resolved, neither for the velocity nor for the active tracer fields (temperature/salinity). These processes are hence parameterized following the turbulent closure hypothesis as turbulent fluxes, expressed as larger-scale features of a diffusive nature (viscosity-momentum,diffusivity-active tracer) [*Durbin*, 2018; *Madec*, 2008]. The spatial resolution of the model is of great importance, because the resolved dynamic processes transfer an amount of energy to smaller scales, which due to the spatial resolution is then trapped at the grid-scale. To suppress the accumulation of energy at the grid-scale, which can produce unstable waves that can lead to the instability of the model, the viscosity parameterization dissipates this energy at the grid-scale. Hence, viscosity is implemented to account for energy transfer and dissipation at small scales. It further ensures the numerical stability of the ocean model [*Rieck*, 2019].

In Lagrangian mechanics the concept of Lagrangian eddy diffusivity (κ) is similarly used to express the rate of dispersal caused by eddies. The parameter of the mesoscale eddy diffusion is accounting for the dominant energy containing unresolved features on the sub-grid-scale [*Abernathey and Wortham*, 2015; *Berloff et al.*, 2002; *Döös et al.*, 2011; *Griffa*, 1996]. Whenever the terms "diffusivity" or "mesoscale eddy diffusion" are mentioned in this chapter, the effect of mesoscale eddies on the particle motion on an isobar is meant.

Deriving the mid-depth circulation patterns from observations estimating their advective ($\bar{\mathbf{u}}$) and mesoscale eddy diffusive ($\mathbf{u}'$) component was attempted in previous studies [*Davis et al.*, 2001; *Davis*, 2005; *Klocker et al.*, 2012; *Koszalka et al.*, 2011; *Ollitrault and Rannou*, 2013; *Roach et al.*, 2016]. A recent study by *Fischer et al.* [2018] estimated the intermediate circulation at 1000 - 1500 m depth by mapping PV-conserving [*Davis*, 1998] displacement estimates from Argo floats [*Lebedev et al.*, 2007] in high resolution to the SPNA. These velocity maps open the possibility to do isobaric particle spreading experiments in a Lagrangian frame. The estimates for mesoscale eddy diffusion in the North Atlantic on intermediate depth (1000 - 2000 m) range in a wide interval between 0 and 700 m^2/s^2 [*Armi and Stommel*, 1983; *Cole et al.*, 2015; *Roach et al.*, 2018; *Spall et al.*, 1993; *Zika et al.*, 2010] and suggest high spatial variability, though the methods and resolution to derive it vary strongly with authors.

This study is evaluating the following questions:

- What are the timescales and pathways of transport from the Labrador Sea convection region to the central Irminger Sea with and without accounting for the effect of mesoscale eddies?
- Which regions in the central Labrador Sea are connected to the central Irminger Sea within a time frame of four years?

Using Lagrangian particle experiments based on the one hand on Argo based velocity fields and on the other on a high-resolution ocean model data will be conducted. Transport pathways and associated travel times between the central Labrador Sea convection region and the Irminger Sea will be estimated.

3.3 Data and Methods

3.3.1 Argo velocity fields

For the particle experiments the mean and residual velocity fields from *Fischer et al.* [2018] which are based on the available displacement data at the Argo parking depth between 1000 - 1500m until 03/2017 from *Lebedev et al.* [2007] (YoMaHa'07) were used. The displacement data was interpolated with potential vorticity (PV)-constraints following *Davis* [1998]. This lead to a mean advective velocity $\bar{\mathbf{u}}$ for each measurement position. Then the residual velocities ($\mathbf{u}'$) were derived for the original float positions using

the relation from equation 3.1. By subsequently interpolating these values with PV-constraints a regular grid with 0.5° longitude x 0.25° latitude resolution (~ 25 km horizontal resolution) was derived . Whenever this chapter mentions "Argo based" or "**Obs**", experiments using the Eulerian velocity field derived by *Fischer et al.* [2018] is meant.

3.3.2 Ocean Circulation Model velocity fields

Additionally to the Argo based velocity fields, the velocity output of the high resolution ocean circulation model VIKING20X is used for the Lagrangian particle experiments. The model is based on the Nucleus for European Modelling of the Ocean (NEMO) [*Barnier et al.*, 2015] code version 3.6 which is coupled with the Louvain-la-Neuve Ice Model version 2 sea-ice component (NEMO-LIM2) [*Fichefet and Maqueda*, 1997; *Madec et al.*, 2017]. Its global, orthogonal, curvilinear, tripolar Arakawa-C grid has a resolution of $1/4^\circ$. A $1/20^\circ$ Adaptive Grid Refinement in Fortran nest (AGRIF two-way nesting)[*Debreu and Blayo*, 2008; *Sheng et al.*, 2005] is used to enhance the horizontal resolution between 34°S and 70°N in the Atlantic. The z-level model contains 46 vertical levels (thickness 6 m - (below 1,000 m)250 m), with partial cells at the bottom [*Barnier et al.*, 2007] and high resolved bathymetry from ETOPO1 [*ETOPO*, 2001]. The model is forced with the 6-hourly CORE.v2 atmospheric forcing [*Griffies et al.*, 2009; *Large and Yeager*, 2009] from 1958 to 2009 and the associated bulk formulations.

The 30 year spin up is starting from rest using an initial temperature and salinity field from the PHC2.1 climatology [*Steele et al.*, 2001] and an initial sea-ice field reflecting a reasonable sea-ice representation at the start of the spin up (31.12.1992) period from a previous $1/4^\circ$ simulation. Then during the spin up period (1980 - 2009) the model is forced with interannually varying atmospheric forcing CORE.v2 [*Griffies et al.*, 2009]. The last spin-up time-step was then used to initiate the hindcast simulations from 1958 - 2009. A weak sea surface salinity restoring to climatology of 33.33 mm/day is applied. Due to the importance of the lateral boundary conditions to the formation of Irminger Rings in the West Greenland Current (WGC) a no-slip condition was implemented at ($43 - 51^\circ$W, $59 - 62^\circ$N) in the overall free-slip model domain to account for the topographic effect on the current crucial to introduce instabilities [*Rieck et al.*, 2018].

The ability of models to resolve the mesoscale at a given latitude is commonly measured by the ratio of the local grid cell size to the first baroclinic Rossby radius of deformation, which depends on latitude, stratification and the ocean's depth[*Chelton et al.*, 1998; *Hallberg*, 2013]. A model of e.g. $1/20^\circ$ ($\sim$ 3 km near Greenland) resolution is capable to resolve most mesoscale features in the subpolar North Atlantic, where the Rossby radius is small ($\sim$ 10 km) [*Deshayes et al.*, 2013; *Maltrud and McClean*, 2005; *Smith et al.*, 2000]. A viscosity parameterization is implemented to account for energy transfer and dissipation at small scales [*Madec*, 2008; *Rieck*, 2019].

VIKING20X reproduces the circulation features in the subpolar North Atlantic in magnitude and scale (Figure 3.2) [*Rieck*, 2019]. In the western subpolar North Atlantic both model and observational fields are characterized by the 100 – 150 km wide cyclonic boundary current and anticyclonic recirculation (return flow). In comparison with the earlier version VIKING20 the position of the Northwest Corner and the North Atlantic Current (NAC) is improved and reaches less far north. Similar to VIKING20 the model represents the spatial extend and location of the DWBC, the eddy field in the North Atlantic and the location of the convection region (Figure 3.3) [*Handmann et al.*, 2018; *Rieck et al.*, 2018].

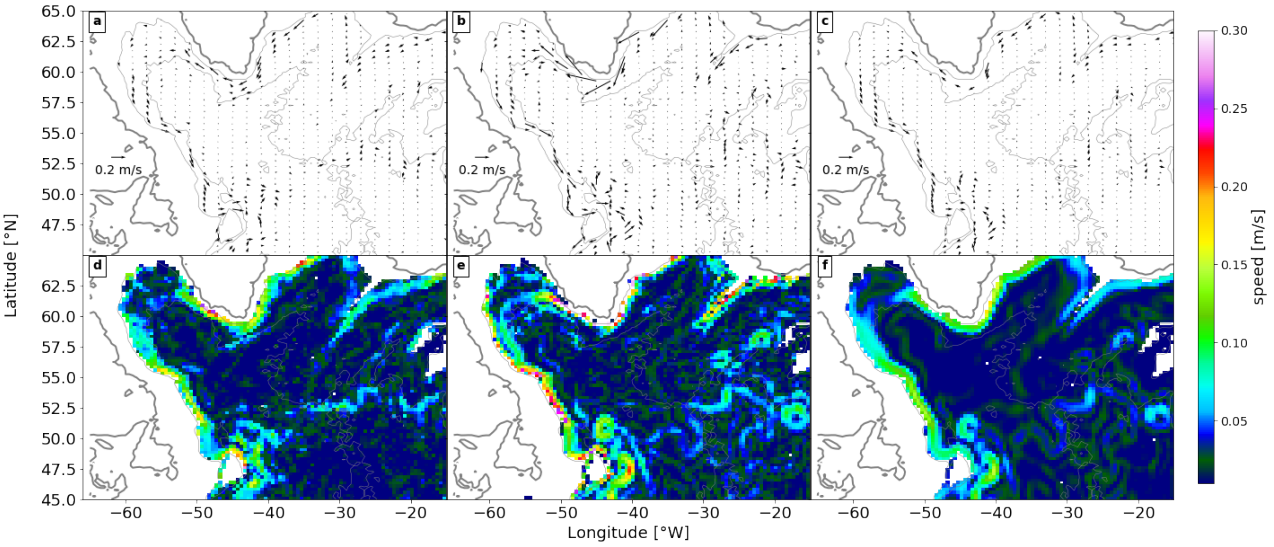

Figure 3.2: *a),d) Argo based velocity field (mean 1990 - 2017). b),e) VIKING20X velocities (2005) either linearly interpolated or c),f) interpolated with PV-constraints [Davis, 1998] to the Argo based velocity fields* $0.5°$ *x* $0.25°$*. The upper row represents the vector velocities and the lower line facilitates speed comparison.*

2005 is in terms of convection (Figure 3.3) and dynamically (Figure 3.4) an average year in the full VIKING20X run and was used for the experiments of this study. The structure of the velocity field on the chosen LSW depth (depth level 24 $\sim$ 989 m) is very similar between model and observations, showing velocity maxima in the boundary currents around Greenland, the Reykjanes Ridge and the Labrador shelf break (Figure 3.2). There is no strong drift or large jumps from January to December in the velocity output of this year (Figure 3.4).

The model velocity fields of 2005 was used in different spatial and temporal resolutions for comparability with the experiments conducted with the Argo based Eulerian velocity fields. The temporarily varying fields (daily/monthly means) and the annual mean output were used with the original spacial resolution of $1/20°$. For comparability with the Argo based experiments the model mean velocity fields were rotated to contain real North-South and East-West velocities. Then the fields were interpolated with two methods to the

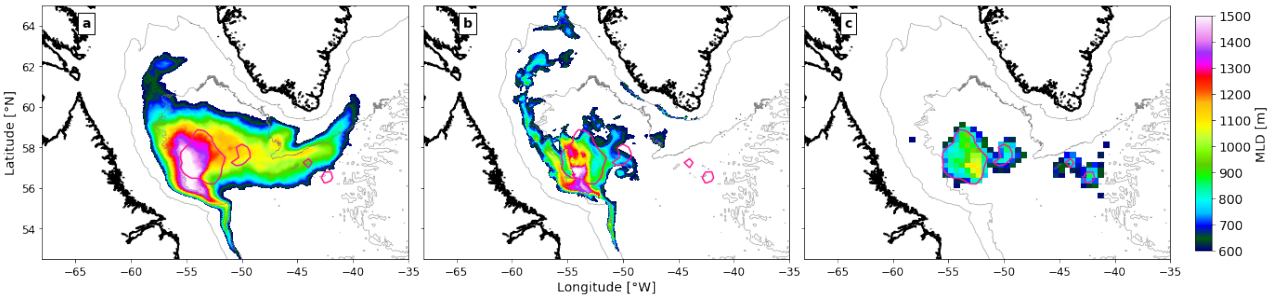

Figure 3.3: *a) March mean MLD VIKING20X (1958-2009), b) march MLD 2005 VIKING20X, c) Maximum march MLD from Holte and Straneo [2017] climatology. The 750m MLD line from Holte and Straneo [2017] is marked purple in all three maps.*

same resolution as the Argo based fields ($0.5°$ longitude x $0.25°$ latitude). Once the field was interpolated linearly to the desired resolution and once it was interpolated using the previously mentioned PV-constraints [*Davis*, 1998] (Figure 3.2).

The type of weighting used during gridding of the high resolution model data to this lower resolution is expected to play a crucial role in the connection or separation of advective pathways in the respective region. Using the linear interpolation can smear strong currents out and connect regions which in the $1/20°$ model mean are not connected (Figure 3.2).

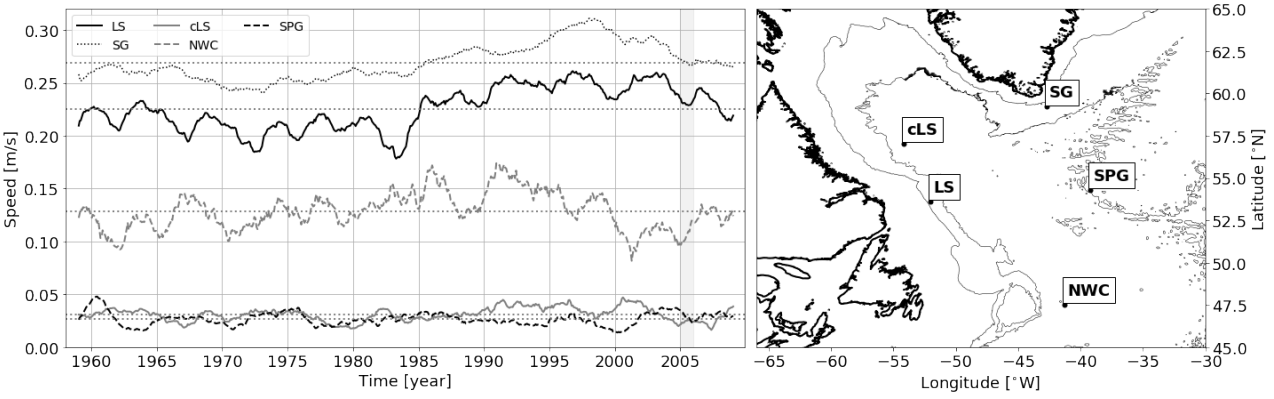

Figure 3.4: *(upper) Annual moving average of model speeds 1958 - 2009 at selected locations (see map) in the SPNA at z-level 24 (989m). (lower) Locations of the time series in the upper panel where the abbreviations stand for : LS - position in the DWBC at $53°N$ array, cLS - central Labrador Sea at K1, SPG - subpolar gyre at the western flank of the Reykjanes Ridge, NWC - Northwest Corner region and SG - Southern Tip of Greenland.*

3.3.3 Lagrangian Particle Experiments

One way of describing the ocean is by Lagrangian studies. The resulting trajectories from single Lagrangian particle experiments can be used to study the flow within the Eulerian velocity fields based on Argo or the high-resolution OGCM VIKING20X. The applied techniques will be introduced briefly, please find a detailed review on the techniques in *van Sebille et al.* [2017] and *Griffies et al.* [2009]. The resulting ensemble of the particle trajectories show, via statistical analysis, the major pathways in the velocity field and their associated time scales. They contain the whole history of the virtual particles, which opens the possibility to analyze the connectivity between two regions and its statistics [*Rühs et al.*, 2019; *van Sebille et al.*, 2017], here between the Labrador and the Irminger Sea. In the ocean a set of trajectories moving with an infinitesimal fluid parcel fully describe the fluid motion. The entire fluid motion is hence an accumulation of particle movement. For each particle the time derivative of its trajectory equals its velocity:

$$\frac{\mathrm{d}\mathbf{X}_n(t)}{\mathrm{d}t} = \mathbf{u}(\mathbf{X}_n(t), t) \tag{3.2}$$

where $\mathbf{X}(t)$ is the position and $\mathbf{u}(t) = (u, v, w)$ is the velocity of the n_{th} particle at time t. The velocity field $\mathbf{u}$ is assumed to be composed of the the mean velocity ($\bar{\mathbf{u}}$) and the residual velocity ($\mathbf{u}'$) at the mesoscale, where $\mathbf{u}'$ is associated with the magnitude of the eddy diffusivity(Equation 3.1)[*Davis et al.*, 2001; *Davis*, 2005; *Ollitrault and Rannou*, 2013]. Assuming a nearly incompressible fluid (Boussinesq fluid), the used velocity field is non-divergent ($\nabla \cdot \mathbf{u} = 0$ - Fokker-Planck equation). Due to changing spatial and temporal coverage and overall varying currents the derived velocity fields from *Fischer et al.* [2018] have a non-zero horizontal divergence. Additionally, in Lagrangian experiments the particles are associated with a certain defined mass or volume. This limits among others, the accuracy of the derived connectivity measures [*van Sebille et al.*, 2017]. Hence corresponding Lagrangian particle experiments will not map volume transport pathways. However, the preferred pathways and connectivity measures will provide diagnostic information [*van Sebille et al.*, 2017].

The Lagrangian experiments were performed with the version 1.0.2 (Argo based experiments) and version 2.0.0 (model based experiments) of Ocean Parcels, which is written in Python and generates fast running low-level C-Code [*Lange and van Sebille*, 2017]. This opens the opportunity to run big numbers of particle experiments. The particle trajectories are computed offline using a zeroth-order Markov model by adding stochastic noise to the particle positions:

$$\mathbf{X}(t + \Delta t) \;=\; \mathbf{X}(t) + \int_t^{t+\Delta t} \mathbf{u}(\mathbf{x}, \tau)\, \mathrm{d}\tau + \Delta \mathbf{X}_b(t) \tag{3.3}$$

with [*Hunter*, 1987; *Roach et al.*, 2018; *van Sebille et al.*, 2017]:

$$\Delta \mathbf{X}_b(t) = \chi * \sqrt{2 * \kappa * \Delta t} \tag{3.4}$$

where $\mathbf{X}(t)$ is the two-dimensional position of a particle, $\mathbf{u}(\mathbf{x}, t)$ is the two-dimensional advective velocity field at that location and $\Delta\mathbf{X}_b(t)$ is a change in position due to diffusivity. $\chi \epsilon N(0, 1)$ is a random number drawn from a normal distribution with zero mean and unit variance, and κ is a constant diffusivity. Without the diffusion term $\Delta\mathbf{X}_b(t)$ equation 3.4 describes an advective scheme, which shows spreading of particles with the resolved flow. Unrealistic accumulation of particles can be resulting from this scheme if the Eulerian velocity fields do not sufficiently capture mesoscale eddies[*Hunter et al.*, 1993].

The Eulerian velocity fields used here are defined on discretized grids. However, particle trajectories are defined on continuous velocity fields, hence the computation of the Lagrangian trajectories demands for interpolation to each particle position $\mathbf{X}(t + \Delta t)$. Linear interpolation in space and time was applied in this study [*Böning and Cox*, 1988; *Lange and van Sebille*, 2017; *van Sebille et al.*, 2017]. Especially if the temporal difference between the velocity fields is bigger than a few days this method can introduce large errors [*Da Costa and Blanke*, 2004; *Dormand and Prince*, 1980; *Li and Pareschi*, 2014]. Equation 3.3 was time-stepped by applying a 4th order Runge-Kutta scheme for $\int_t^{t+\Delta t} \mathbf{u}(\mathbf{x}, \tau)\, \mathrm{d}\tau$. With this method the velocity field is interpolated on four temporal increments between t_n and t_{n+1}. Especially for temporally varying input fields the choice of the Δt is crucial.

3.3.3.1 Seeding

For all following experiments trajectories were calculated starting from two defined seeding regions (Figure 3.1). One region represents a line connecting the moorings ('CF1', 'CF2', 'CF3', 'CF4', 'CF5', 'CF6','CF7', 'M1', 'M2', 'M3', 'GI04FLMA', 'GI04FLMB','GI04FLMA', 'GI04FLMB', 'M4' and 'M5') close to the Greenland shelf break, which belong to the "Overturning in the subpolar North Atlantic Program" (OSNAP) [*Lozier et al.*, 2017]. Particles were randomly seeded over the line connecting the moorings. In the following this line will be called "**OSNAP-MEG**" (OSNAP-Moorings East Greenland) and all experiments with seeding at this location are integrated backward in time.

The second seeding region is defined by the area which is expected to exceed a maximum march convection depth of 750 m in the Labrador Sea (West of $45°W$). The *Holte and Straneo* [2017] climatology derived from Argo floats was used to determine this convection patch, which is named "**cLS**" or "convection patch" in the following. All particle trajectories departing from the convection patch are integrated forward. The same region is used in the Argo based and model based experiments, since the region of deep convection are sufficiently comparable (Figure 3.3).

In all experiments apart from the ones conducted with the daily model output, 12000 particle trajectories where computed. In the experiments conducted with mean Eulerian velocity fields, the total number of particles was randomly seeded over the section or patch. For the experiments using the daily model output,

each day of the first year 34 particles were randomly distributed over the seeding region (12410 particles). Using the monthly model output, 1000 particles were randomly seeded each month at the respective seeding patch or section (12000 particles).

For later analysis the region south of Greenland and east of $45°W$, where maximum mixed layer depth in march from the *Holte and Straneo* [2017] climatology trespasses 750 m is here called "south Greenland convection patch" (**SG**). Additionally, a line crossing the DWBC from the Canada shelf from -50°W to -40°W was defined to estimate the southward connection and is called 45°N section. All described seeding areas and analysis regions are marked in gray in Figure 3.1.

3.3.3.2 Diffusion Kernel

The defined diffusion kernel (Equation 3.4) introduces a temporal perturbation of the mean velocity field, since χ is recalculated for each particle position and time step [*Berloff and McWilliams*, 2003]. The magnitude of the perturbation is further dependent of the choice of the diffusivity κ. It is defined to be directly related to the square root of the eddy kinetic energy ($\kappa \sim \sqrt{EKE}$) [*Roach et al.*, 2018; *Sallée et al.*, 2008], though its exact definition is an ongoing topic of research and discussion [*Klocker et al.*, 2012; *Roach et al.*, 2018; *Sallée et al.*, 2008]. Estimates of diffusivity values at 1000-1500 m depth in the SPNA vary widely in magnitude, time and space (κ = 100 - 700 m^2/s) [*Armi and Stommel*, 1983; *Cole et al.*, 2015; *Davis*, 1991; *Holloway*, 1986; *Roach et al.*, 2018; *Spall et al.*, 1993; *Zika et al.*, 2010]).

One could define a spatially constant diffusivity field $\kappa(\mathbf{X}, t) = const$ or a spatially varying diffusivity field $\kappa(\mathbf{X}, t) = \kappa(\mathbf{X})$ (Figure 3.5 a) with a set probability density function (pdf) (Figure 3.5 c).

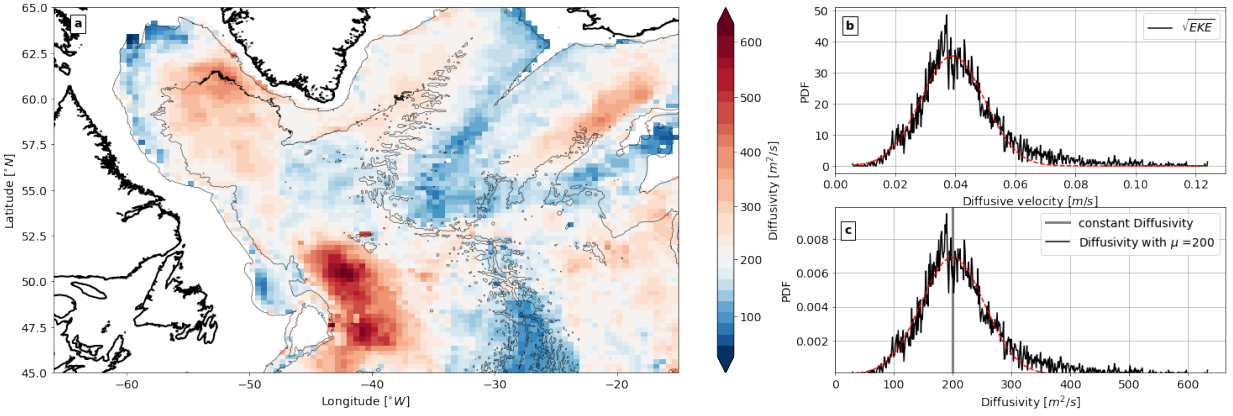

Figure 3.5: *a) Map of locally varying diffusivities κ with the c) respective pdf of diffusivities . b)PDF of the residual velocities* $\mathbf{u}'$ *computed from the EKE field from Fischer et al. [2018], which served as a base for the pdf c) and spatial distribution a) of κ.*

A first set of pre-experiments was launched to asses the effect of locally varying diffusivities in comparison to a constant diffusivity on the connectivity between the Labrador and Irminger Sea in our experimental set up. The mean velocity fields from *Fischer et al.* [2018] were used to calculated two year backward particle trajectories from the **OSNAP-MEG**. One experiment with a constant diffusivity and another with a spatially varying diffusivity were conducted. The spatially varying diffusivity was defined to vary with the EKE magnitude in the region (Figure 3.5 a). After two year particle trajectory integration, a very low difference in estimated travel times between the **OSNAP-MEG** and the **cLS** with the two spatial distributions of κ is found (Figure 3.6). The particle pathways taken are nearly identical (Figure 3.6, upper panel). Given, that errors in the trajectory integrations accumulate over time the main experiments for the Argo based fields were always conducted with both diffusivity definitions but did not reveal great differences in the total number of particles arriving nor in the travel times. Hence, the effect of the spatially varying diffusivity can be assumed negligible here.

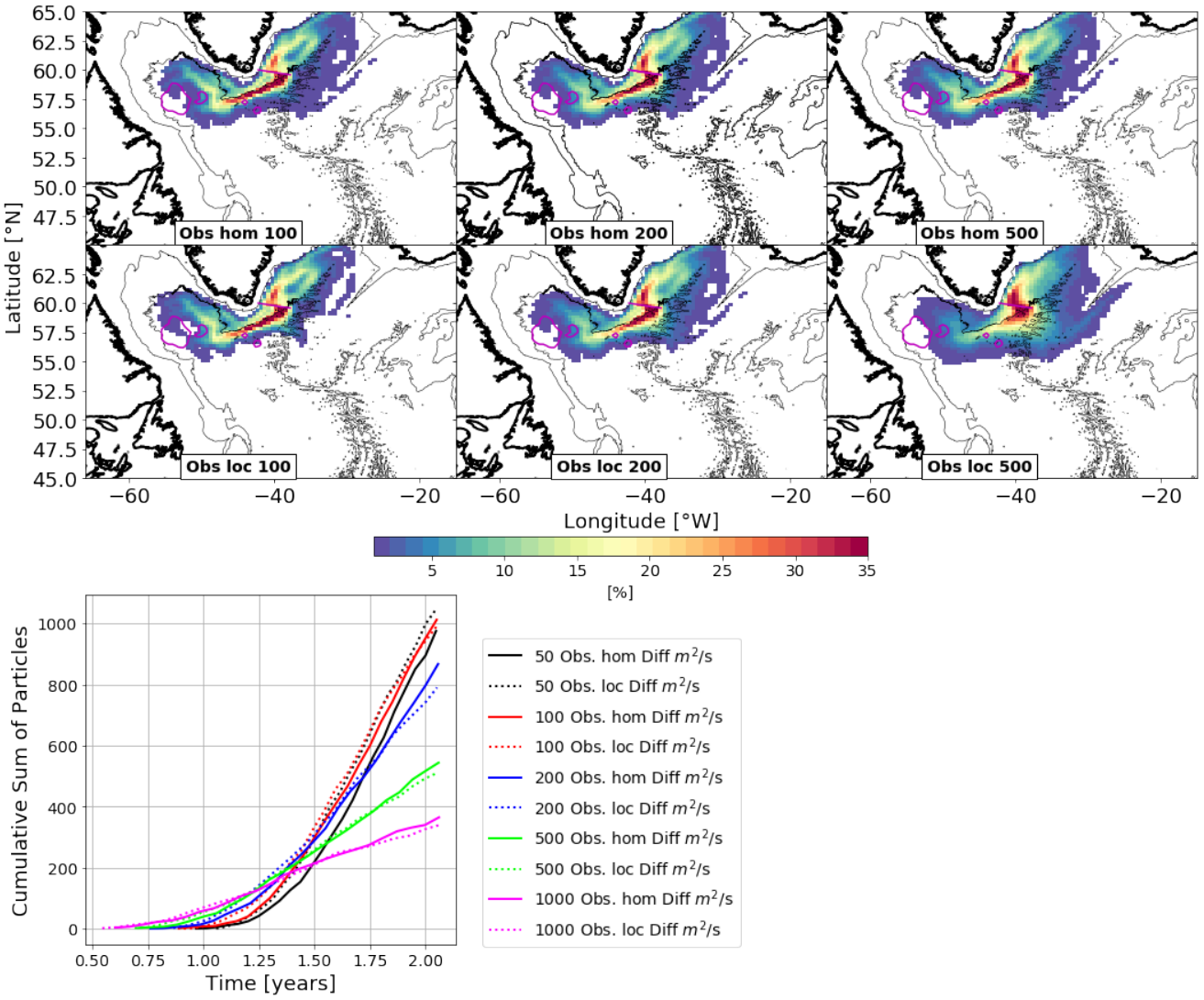

Figure 3.6: *(upper) Probability maps of particle experiments seeded at OSNAP-MEG with different constant (Obs hom) and locally (Obs loc) varying κ. The respective κ is given in m^2/s in each experiments text box. The probability of a particle passing through the respective bin at least once on its pathway. Probabilities range between 0% and 100% (section 3.4). (lower)Respective transit time distribution backward from OSNAP-MEG to cLS. Lines show experiments with constant diffusivities and dashed lines with spatially varying diffusivities.*

The regional variation of κ was hence treated as negligible for the main experiments and a second set of pre-experiments was then conducted to asses the influence of the magnitude of the diffusivities $\kappa = [5, 15, 25, 50, 100, 200, 500, 1000]\ m^2/s$ on the estimated arrival time of the particles from **OSNAP-MEG** backwards to the **cLS**. The experiments revealed that the total amount of particles arriving within a time frame of two years decreased drastically with increasing diffusivity, setting the time of arrival of the majority of the particles towards longer timescales (Figure 3.6). Hence, taking the interval of expected travel time between the two regions and the diffusivities in the SPNA proposed in literature into account, the value for the diffusivity in all following advective-diffusive experiments was chosen spatially constant with $\kappa = 200$ m^2/s.

During offline advection of virtual particles using the daily/monthly velocity output of the model, the sub-grid scale parameterizations acting on tracer and momentum of the fluid are only implicitly included. The viscosity parameterization acting on the simulated particles is hence expected to be smaller in offline than during online simulation (during model simulation run). Advective experiments with temporarily varying model output are hence not solely advective but contain to a certain extend the influence of the sub-grid scale parameterization. Introducing an additional parameterization of Lagrangian diffusion to account for the 'missing' sub-grid scale diffusivity during offline experiments via an stochastic component is proposed, but the way to appropriately define it and how and when to implement it is still under discussion. Furthermore, the underlying model physics might be harmed by the introduction of these stochastic terms [*Berloff and McWilliams*, 2002; *Döös et al.*, 2011; *Griffa*, 1996; *Rühs et al.*, 2018]. Since the model spatial resolution is eddy resolving, the experiments with the temporarily varying model output (monthly/daily) were purely advective experiments with $\kappa = 0\ m^2/s$ and with no consideration for the "missing" sub-grid scale are conducted.

3.3.3.3 Experimental Design

To assess the connectivity between the central Labrador and the Irminger Sea, first purely advective experiments with $\Delta\mathbf{X}_b(t) = 0$ were performed with all Eulerian velocity fields and second advective-diffusive experiments with κ =200 m^2/s were conducted only with the mean fields. Experiments were conducted starting from both seeding positions in both set ups.

In the experiments with the temporarily and spatially resolved model output (daily, monthly) the output of 2005 was looped for the duration of the experiments. As mentioned before, the net effect of the looping on the particle trajectories is expected to be negligible since the model does not express a big trend or large jumps between the end and the beginning of the year, which could introduce unphysical jumps in the computed Lagrangian particle trajectories (Figure 3.4) [*van Sebille et al.*, 2017].

Pre-experiments	Eulerian velocity field	Diffusivity
Type = **advective-diffusive**	Argo based	constant Diffusivity
Duration = 2 years		local varying Diffusivity
Seeding location : OSNAP-MEG		Diffusivities:
		5,10,15,25,50,100,200,500,1000m^2s^{-1}
Main experiments	**Eulerian velocity field**	**Abbreviation**
Type = **advective**	Argo based	**Obs**
Diffusivity = 0 m^2s^{-1}	Daily model output 2005	**Vik daily**
Duration = 4 years	Monthly model output 2005	**Vik monthly**
Seeding location = cLS,OSNAP-MEG	Annual mean model output 2005	**Vik mean**
	Annual mean Model output 2005 lin. interp.	**Vik mean Argo**
	Annual mean model output 2005 PV. interp.	**Vik mean Argo PV**
"advective - diffusive"	Argo based	200 **Obs** hom
Diffusivity = 200 m^2s^{-1}		local varying Diffusivity - 200 **Obs** loc
Duration = 4 years	Annual mean model output 2005	200 **Vik mean**
Seeding location = cLS,OSNAP-MEG	Annual mean Model output 2005 lin. interp.	200 **Vik mean Argo**
	Annual mean model output 2005 PV. interp.	200 **Vik mean Argo PV**

Table 3.1: *All conducted experiments with their respective length and abbreviation. cLS stands for the central Labrador Sea and "OSNAP-MEG" for the OSNAP moorings on the east Greenland shelf. "lin. interp." and "PV interp" describe the annual mean velocity output rotated to the real N-S velocities and interpolated to* $0.25 \times 0.5^\circ$ *for the former linearly and the latter using PV-constraints [Davis, 1998]*

Straneo et al. [2003] estimated the Lagrangian time scale T_L to be between 4 to 10 days and the dominating spatial scales related to convective eddies and Irminger rings in the Labrador Sea to be of the order of 10 -20 km. The daily model output resolves these temporal and spatial scales properly, while the monthly and the mean $(1/20^\circ)$ resolve the spatial but not the temporal variations. The temporal resolution of the model output is expected to have an non negligible influence on the particle trajectories [*Blanke et al.*, 2012; *Poje et al.*, 2010; *Qin et al.*, 2014]. To evaluate this influence comparison to the experiments with the mean model field experiments with the same spatial resolution is performed. The influence of the spatial resolution was evaluated by comparing results from the $1/20^\circ$ mean model field and the interpolated versions $(0.5^\circ x 0.25^\circ)$. The results of these evaluations are then brought in context with the experiments with the Argo based fields.

In the following all experiments were performed over periods of 4 years. This timeframe covers the life cycle of Argo and RAFOS floats for comparability of the experiments with literature ([*Bower et al.*, 2009; *Fischer and Schott*, 2002; *Jayne et al.*, 2017]). Table 3.1 represents the full set of experiments and their respective abbreviations which will be used in the following paragraphs.

The time steps for the trajectory integration Δt were chosen to be 12h in the mean-field experiments with the spatial resolution of 0.5° x 0.25°. This time-step is small enough for each particle to have at least 2-4 steps in critical grid boxes containing high velocities e.g. near the southern tip of Greenland (Figure 3.2). For **Vik daily** experiments Δt was chosen to be 5 minutes due to the high spatial and temporal resolution. This time step is large enough to provide 10+ trajectory positions per grid cell. This sufficiently small Lagrangian integration time step was also utilized for the monthly and long term mean (**Vik mean**, **Vik monthly**). The calculated trajectories are saved for all experiments with a temporal resolution of 24h for 4 years forward or backward.

3.4 Results

For the following trajectory and travel time analysis the trajectories were binned into 0.5° x 0.25° boxes aligned with the Argo based grid. The results are presented for each experiment (advective and advective-diffusive) for the respective seeding location (**OSNAP-MEG** or **cLS**). In that way the forward and backward connectivity can be compared easily and changes in the connectivity in the advective-diffusive experiments compared to the advective experiments are more evident.

Probability or spreading maps show the probability of a particle passing through the respective bin at least once on its pathway. The number of different particles in the bin is divided by the total number of particles seeded [*van Sebille et al.*, 2017]. The probability for each bin can hence range between 0 and 100% (total number of particles seeded), were only bins with larger than 1% probability are included in the maps. Additionally, average age maps represent the median propagation time of all seeded particles to the respective bin. The average age is defined as the median of the first arrival time of all particles passing through the bin, where the first arrival time per particle is the first time a particle enters a certain bin.

The transit time distribution (TTD) is interpreted as the age of the bulk of Lagrangian particles. Since the bulk of Lagrangian particles is described by multiple particle trajectories, that take distinct pathways between two regions during different time intervals, the age of a water parcel is not a unique value but a probability distribution [*Haine and Hall*, 2002; *Phelps et al.*, 2013]. The respective timescales can be expressed by the range (25, 50, 75%), maximum or the variance of the TTD, where the TTD is strongly dependent on the resolved spatial scales of the underlying binning [*Rühs et al.*, 2013; *van Sebille et al.*, 2017] (Figure 3.7). Each particle is only counted during its first arrival at the respective section to exclude the effect of recirculation and distinguish different possible particle pathways. If particles take multiple pathways or origin from different parts of the seeding area more than one peak will appear in the number of particle arrival over time and lead to a multi-plateau TTD.

In the following transit times will be given in tables as the times when 25%, 50% and 75% of the total arriving particles have reached the section. The text will only present the 50% times and the total number of particles arriving within 4 years to enhance readability.

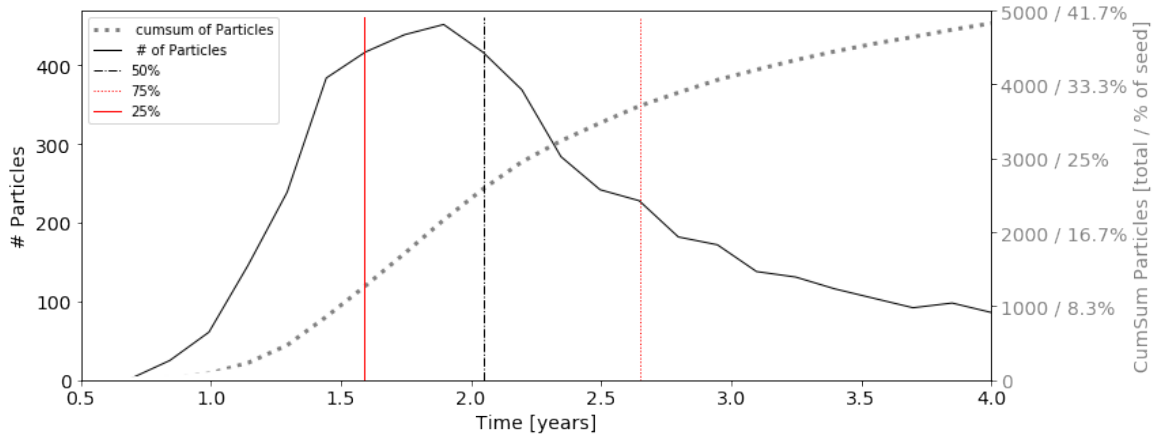

Figure 3.7: *Example transit time distribution (TTD) (grey) for an example of particle arrivals. (solid black line) histogram of the total number of particles arriving at time t. The 25% of particles arrive after 1.6 years, 50% after 2.1 years and the 75% after 2.7 years.*

3.4.1 Seeding at OSNAP-MEG

In order to determine the origin and further fate of water parcels populating the area at the **OSNAP-MEG** section, two experiments were carried out - advection only and advective-diffusive experiments.

3.4.1.1 advective Experiments

The probability maps for the backward advective (Table 3.1) experiments **Obs**, **Vik mean** and **Vik mean Argo** show the most populated pathway connecting the **OSNAP-MEG** and the **cLS** region via the anti-cyclonic recirculation in the Labrador Sea (Figure 3.8 a, b, c) (Figure 3.1, **pathway 1**). The respective average age maps (3.9 a,b,c) indicate median advective travel times of 2.5 - 4 years. Concurrent, the resulting TTDs (Figure 3.10 lower panel) imply that $\sim 2\%$ of the total seeded particles in the **Obs** arrive in a single particle arrival peak at ~ 2.4 years (Figure 3.10 upper panel), $\sim 3\%$ arrive in **Vik mean** at ~ 3.3 years and $\sim 20\%$ of the total seeded particles arrive in **Vik mean Argo** in two peaks at ~ 2.5 and ~ 3.7 years. The two peaks in **Vik mean Argo** can be related to two different pathways the particles take between **OSNAP-MEG** and **cLS** recirculation time in the Irminger Sea which was estimated to $\sim 1-2$ years (Figure 3.9c). All respective percentiles of the TTDs concerning the connectivity between **OSNAP-MEG** and **cLS** are collected in table 3.2.

No connection between the two regions is simulated in the **Vik daily** , **monthly** and **Vik mean Argo PV** experiments (Figure 3.8 d, e, f), where the **Vik mean Argo PV** and the **Vik monthly** show a pathway starting at **OSNAP-MEG** until the southern tip of Greenland which is turning back to the northeast,

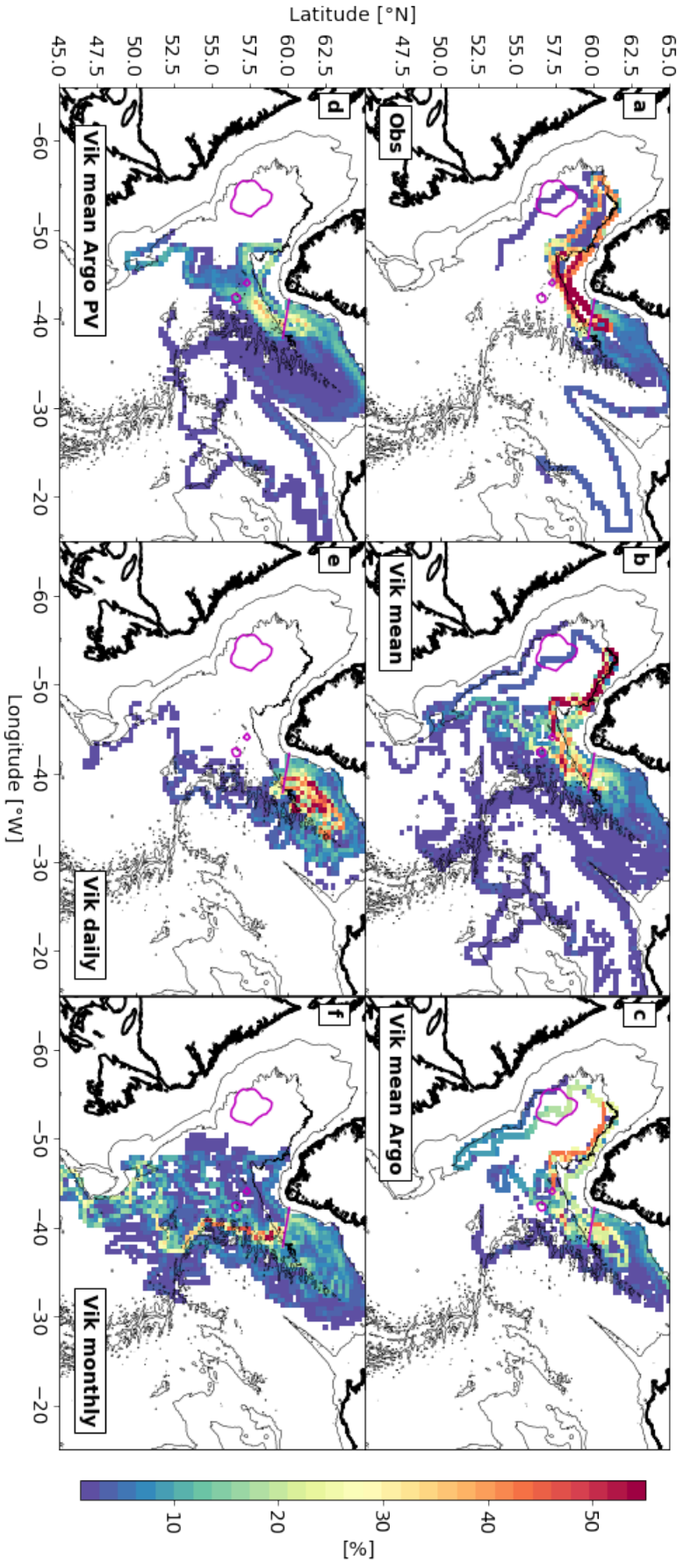

Figure 3.8: *Probability maps of advective Lagrangian experiments with particles seeded at OSNAP-MEG. Abbreviations used as indicated in table 3.1.*

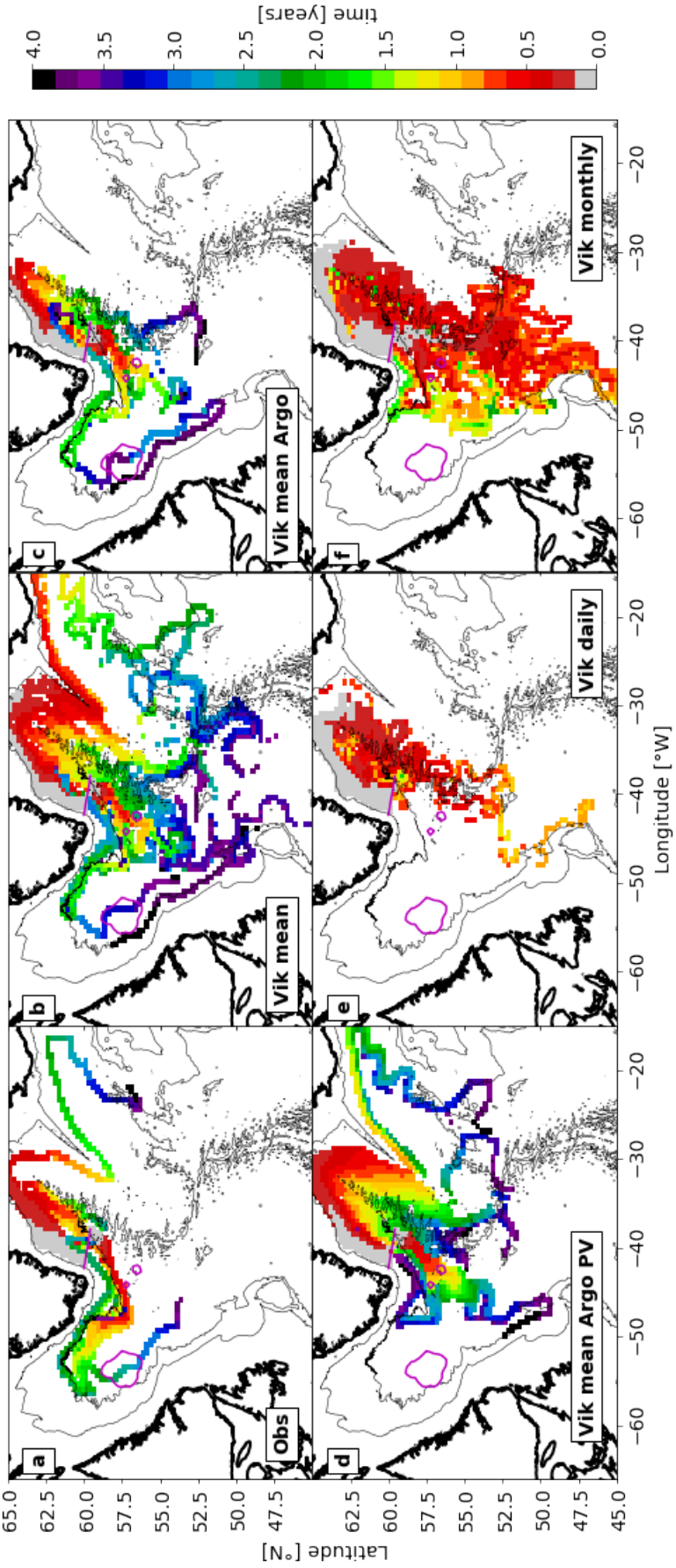

Figure 3.9: *Average age maps of advective experiments with particles seeded at OSNAP-MEG. Abbreviations used as indicated in table 3.1.*

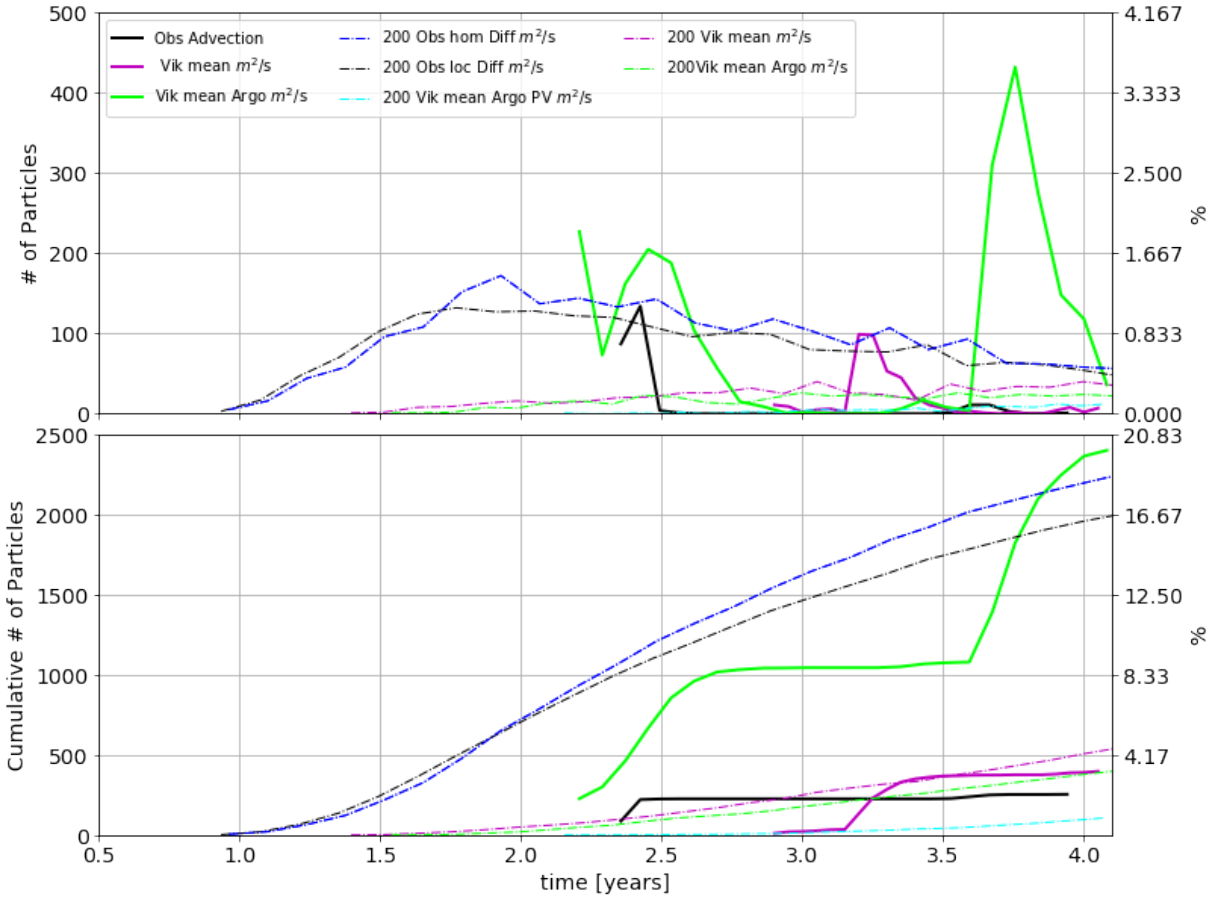

Figure 3.10: *(upper)Arrival times at cLS of particles seeded at OSNAP-MEG.(lower) Transit time density (TTD).*

recirculating back to the DWBC off the East Greenland Coast and hence not reaching the **cLS**. **Vik daily** and **monthly** are showing a direct connection between **OSNAP-MEG** with the Northwest Corner region within the 4 year trajectory calculations.

Particles seeded close to the shelf follow the DWBC backwards to the north in all experiments. The experiments show a very fast connection (within less than one year) along the DWBC pathway between the **OSNAP-MEG** and the region close to the Denmark Strait (Figure 3.9). For all experiments particles spread in the Irminger Sea and some follow the isobaths around the Irminger Sea and the western flank of the Reykjanes Ridge, where **Obs** , **Vik mean** and **Vik mean Argo PV** even show an "advective connection" to the Iceland basin (3.9 a,b,d) following the eastern flank of the Reykjanes Ridge with median travel times between the **OSNAP-MEG** and the Iceland basin within 1-2 years (Figure 3.9a,b,d).

The advective experiments with the **Vik mean** , **daily** and **monthly** fields exhibit a backward connection with the south via $45°$N. In the **Vik mean** experiments $\sim 1\%$ of the particles seeded at **OSNAP-MEG** reach $45°$N within 3.5 years (Figure 3.9b). The **Vik daily** experiments simulate a similar percentage of

Experiment	Diffusivity	Pathway		total amount [%]		time of arrival of percentiles: 25, 50, 75 % [years]	
	$[m^2s^{-1}]$	OSNAP-MEG - cLS	cLS - OSNAP-MEG	OSNAP-MEG - cLS	cLS - OSNAP-MEG	OSNAP-MEG - cLS	cLS - OSNAP-MEG
Obs	0	1	1	2.1	36.5	2.4, 2.4, 2.4	2.4, 2.7, 3.7
Vik daily	0	-	1,5	-	21.1	-, -, -	1.3, 1.6, 1.9
Vik monthly	0	-	1,5	-	17.3	-, -, -	1.2, 1.4, 1.6
Vik mean	0	1,5	-	3.3	-	3.2, 3.3, 3.3	-, -, -
Vik mean Argo	0	1	1,5	20.0	3.1	2.5, 3.6, 3.8	3.2, 3.2, 3.2
Vik mean Argo PV	0	-	-	-	-	-, -, -	-, -, -
Obs - hom	200	1, 4	1	18.8	22.7	1.8, 2.3, 3.0	2.0, 2.5, 3.2
Obs - loc	200	1, 4	1	16.7	18.4	1.8, 2.3, 3.0	2.0, 2.4, 3.0
Vik mean	200	1	1,5	4.5	2.7	2.6, 3.1, 3.6	2.8, 3.3, 3.8
Vik mean Argo	200	1, 5	1,5	3.3	2.5	2.6, 3.1, 3.7	2.8, 3.4, 3.7
Vik mean Argo PV	200	-	-	0.9	0.7	3.2, 3.7, 3.9	3.1, 3.6, 3.9

Table 3.2: *Percent of particles seeded at cLS / OSNAP-MEG arriving at the respective target patch OSNAP-MEG /cLS and their travel times. The different panels show the respective experiments advective and advective-diffusive similar to table 3.1. Pathways are given with numbers which are defined in figure 3.1 and the synthesis figure 3.20.*

particles reaching $45°$N within the first year of simulation and hence connecting the two regions three times faster (Figure 3.9e). This is far exceeded by the **Vik monthly** experiments, where $\sim 60\%$ of the particles trespass $45°$N during the first year of trajectory calculation.

Apart of **Vik daily** all advective experiments show two pulses of particle arrival and a total of $20 - 80\%$ of the total seeded particles passing through the south Greenland Convection patch (**SG**) within the first three years of trajectory integration (Figure 3.11 ,Table 3.3), where the majority of particles have passed **SG** within 1 year. The two pulses of particle arrival can be related to the different seeding positions at **OSNAP-MEG**, where the second peak is related to particles seeded close to the Greenland shelf-break. The **Vik daily** experiment shows a much lower total number ($\sim 2\%$) of particles passing through the **SG** within 4 years, here the particles rather follow the western flank of the Reykjanes Ridge towards the south.

3.4.1.2 advective-diffusive Experiments

All backward advective-diffusive experiments (Table 3.1), apart from **Vik mean Argo PV**, show the pathway defined by the anticyclonic recirculation in the Labrador Sea connecting **OSNAP-MEG** and **cLS** (**pathway 1**, Figure 3.12). The **Obs** experiment additionally features a second pathway touching the southeastern part of the convection patch coming directly from the southern Tip of Greenland (Figure 3.12 upper panel) (**pathway 4** in the following), where the same amount of particles take **pathway 1** and **4** . $\sim 20\%$ of the over all seeded particles now reach the **cLS** which is ten times more than in the advective **Obs** experiments. The particle arrivals peaks at ~ 1.8 years and 50% of the total particles that arrive take ~ 2.3 years travel time. The respective TTD does not fully reach the plateau after 4 years of particle trajectory integration (Figure 3.12 lower panel). **Pathway 4** is not apparent in the model experiments.

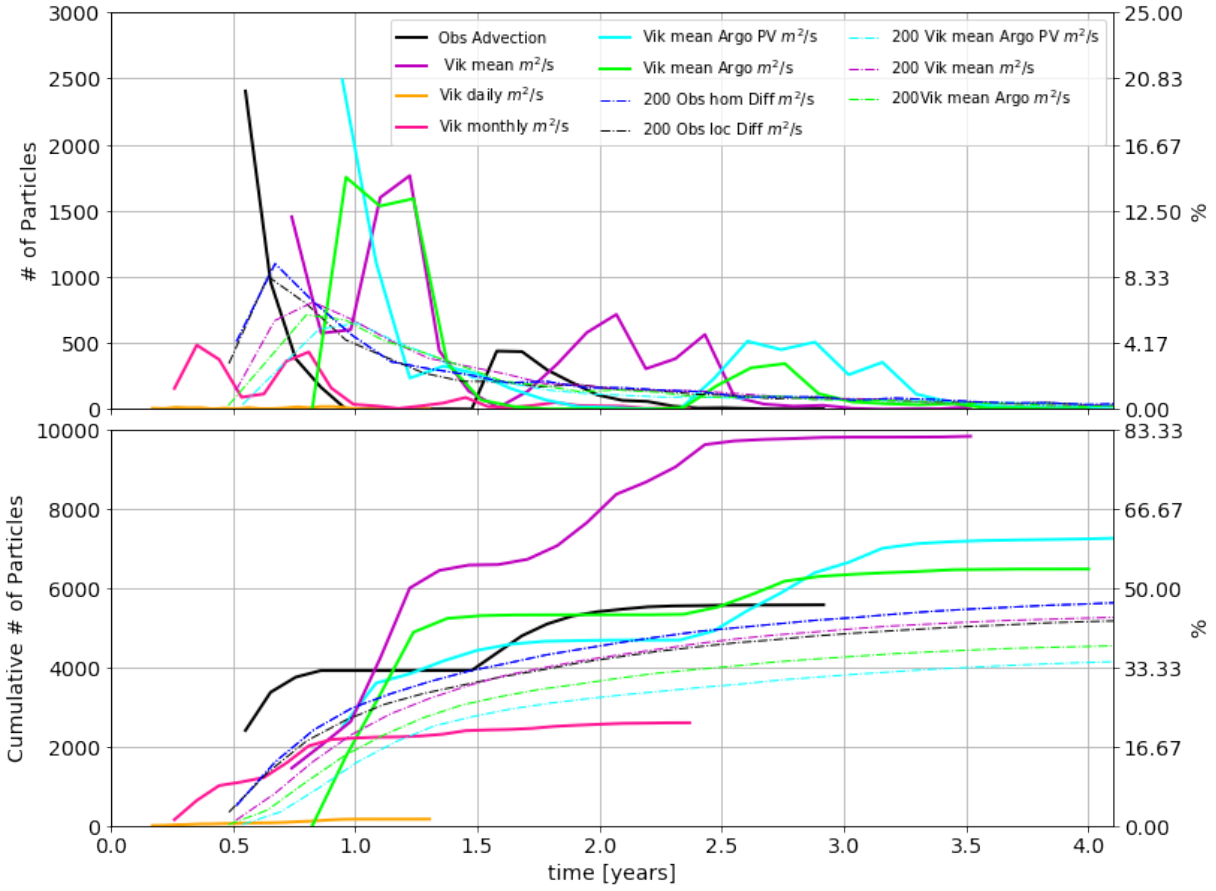

Figure 3.11: *(upper)Arrival times at the south Greenland convection patch (SG) of particles seeded at OSNAP-MEG.(lower) Transit time density (TTD).*

For **Vik mean** and **Vik mean Argo** lower numbers of particles reach **cLS** within 4 years: $\sim 5\%$ (similar to advective) for the former and $\sim 3\%$ (20% in advective) for the latter. The particles get mainly through **pathway 1** to the **cLS** but another pathway connecting **OSNAP-MEG** and the **cLS** through the Orphan Knoll region and the DWBC along the Newfoundland shelf break gains importance (**pathway 5** in the following) (Figure 3.1)(Figure 3.12). Parts of **pathway 5** are also present in the advective experiments **Vik mean** and **Vik mean Argo PV**, though they do not reach the **cLS**. For **Vik mean** and **Vik mean Argo** the number of particles arriving per time is still increasing and the TTD plateau is not reached, thus the time scales respective to the two different pathways can not be derived explicitly.

In both experimental setups, advective and advective-diffusive, of **Vik mean Argo PV** less than 1% of the particles reach the **cLS** within the 4 years (Figure 3.13,Table 3.1).

Less particles reach the **SG** $(30 - 40\%)$ compared to the advective experiments, but in a similar time ~ 1 year (Table 3.3) .

Experiment	Diffusivity $[m^2 s^{-1}]$	total amount [%]		time of arrival of percentiles: 25, 50, 75 % [years]	
		OSNAP-MEG - SG	cLS - SG	OSNAP-MEG - SG	cLS - SG
Obs	0	46.4	36.5	0.6, 0.6, 1.6	1.7, 1.9, 2.2
Vik daily	0	1.4	22.7	0.4, 0.7, 0.9	1.2, 1.4 1.7
Vik monthly	0	21.7	17.3	0.4, 0.6, 0.8	1.0, 1.3, 1.5
Vik mean	0	81.8	-	1.0, 1.1, 2.0	-, -, -
Vik mean Argo	0	53.9	3.14	1.0, 1.1, 1.2	1.6, 1.6, 2.3
Vik mean Argo PV	0	60.4	-	1.0, 1.1, 2.6	-, -, -
Obs - hom	200	47.0	40.8	0.7, 1.0, 1.8	1.6, 2.0, 2.7
Obs - loc	200	43.1	36.0	0.6, 1.0, 1.8	1.6, 1.9, 2.5
Vik mean	200	43.8	9.9	0.8, 1.1, 1.8	2.0, 2.7, 3.4
Vik mean Argo	200	37.9	10.3	0.8, 1.1, 1.8	1.9, 2.7, 3.3
Vik mean Argo PV	200	34.5	4.0	0.9, 1.2, 1.8	2.6, 3.3, 3.8

Table 3.3: *Percent of particles seeded at cLS or OSNAP-MEG arriving at the south Greenland convection patch (SG) (Figure 3.1) and their respective travel times. The different panels show the respective experiments advective and advective-diffusive similar to table 3.1. Pathways are given with numbers which are defined in figure 3.1 and the synthesis figure 3.20.*

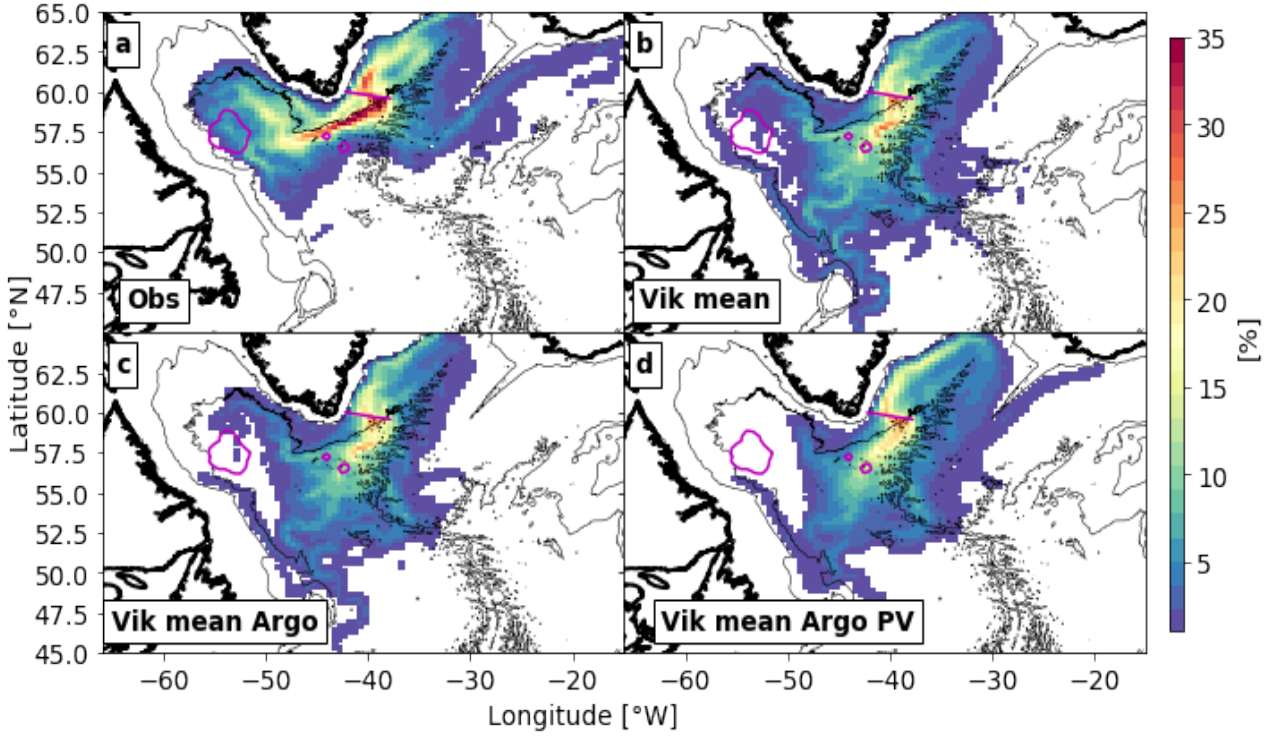

Figure 3.12: *Probability maps of advective-diffusive Lagrangian experiments with particles seeded at OSNAP-MEG. With a constant diffusivity of $200 m^2/s$. The trajectories were calculated backward. Abbreviations used as indicated in table 3.1.*

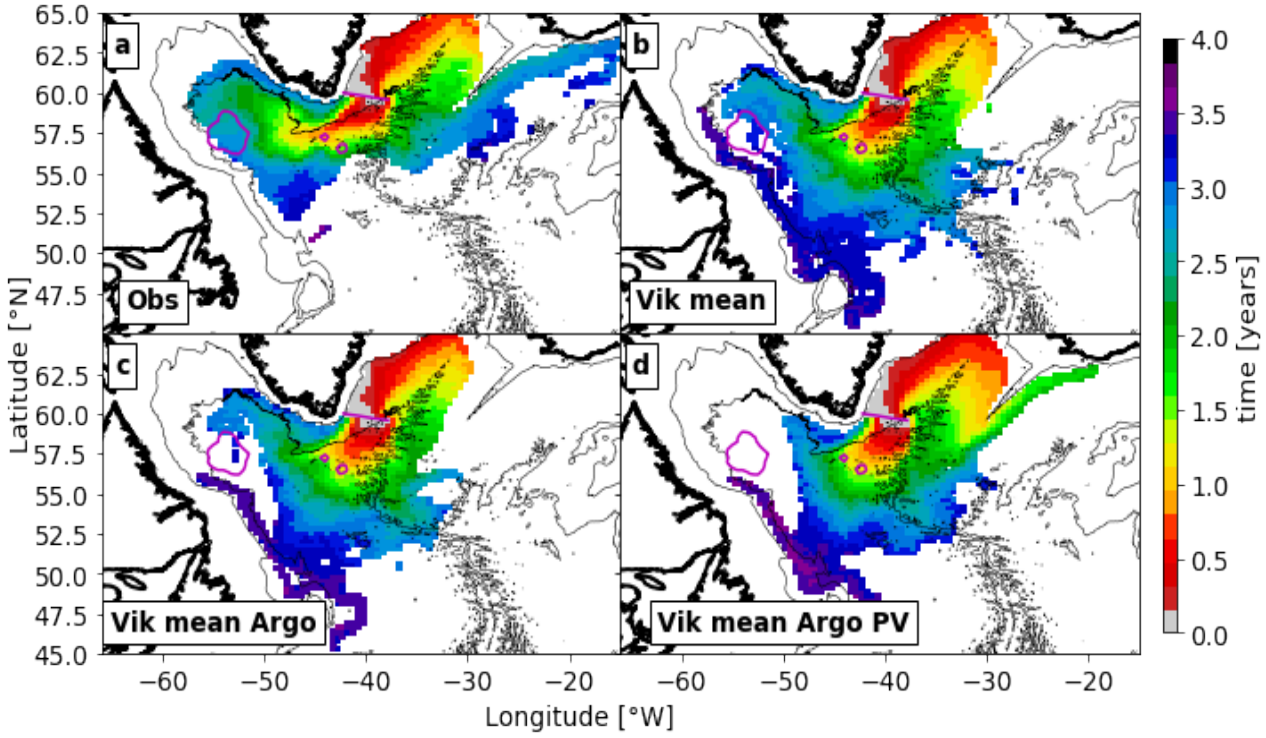

Figure 3.13: *Average age maps of experiments with particles seeded at OSNAP-MEG. Trajectories were calculated backward. The respective times per bin are presenting the median of the first arrival time of all particles passing through the bin. Abbreviations used as indicated in table 3.1.*

3.4.2 Seeding at cLS

To evaluate the spreading of particles from **cLS** two experiments - advection only and advective-diffusive - were carried out and are presented in the following.

3.4.2.1 advective Experiments

The forward advective **Obs** experiment features **pathway 1** just as in the "backward" experiments (Figure 3.14 a, 3.15). Particles arrive in two peaks which are not fully resolved with the 4 years of particle integration (Figure 3.16) and can be related to recirculation in the central Labrador Sea. The first plateau at $\sim 26\%$ of the particle arrival TTD is reached after ~ 2.6 years when after 3.5 years more particles start to arrive and $\sim 37\%$ of the total seeded particles have reached **OSNAP-MEG** after 4 years.

In the model experiments the recirculation in the Labrador Sea is part of a closed recirculation defined to the west of $45°$W. Even though **Vik mean** exhibits a connection between **OSNAP-MEG** and **cLS** in the backward advective experiments this pathway is vanished here (Figure 3.14 b). The recirculation is shifted towards the west Greenland shelf break in **Vik mean**, **Vik mean Argo** and **Vik mean Argo PV** in comparison to the **Obs** experiments where in **Vik daily** and **Vik monthly** the position is more comparable (comp. Figure 3.8 and 3.14).

In **Vik mean** and **Vik mean Argo PV** none of the particles leave the Labrador Sea within 4 years suggesting long (+4 years) retention time once particles were supplied to the Labrador Sea. Some particles partly follow the DWBC southeastward and then get deflected back into the Labrador Sea or towards the north $48 - 50°$N at the Orphan Knoll region. This pathway is prolonged to the **OSNAP-MEG** section (**pathway 5**) in the **Vik daily**, **monthly** and **Vik mean Argo** experiments. In the **Vik mean Argo** and **Vik monthly** experiments **pathway 1** is as populated as **pathway 5**. Particles reach the Irminger Sea within an average time of 1.5 - 3 years (**Vik daily** (20%), **monthly**(20%) and **Vik mean Argo** (3%)) (Table 3.2,Figure 3.14 and 3.15). For **Vik daily**, **monthly** the particles arrive within one bulk of particles peaking at ~ 1.5 years (Figure 3.16).

Particles reach the **SG** within 1-2 years, for the **Vik daily**, **monthly** an **Vik mean** on **pathway 1** and **5** and via **pathway 1** exclusively for **Obs** (Figure 3.15, Figure 3.17).

For the **Obs** experiment up to $\sim 18\%$ of the particles leave the domain via the DWBC $45°$N within the first 1.5 years (Figure 3.1,**pathway 2**). In all other advective experiments less than 1% of the particles leave the domain towards the south via $45°$N.

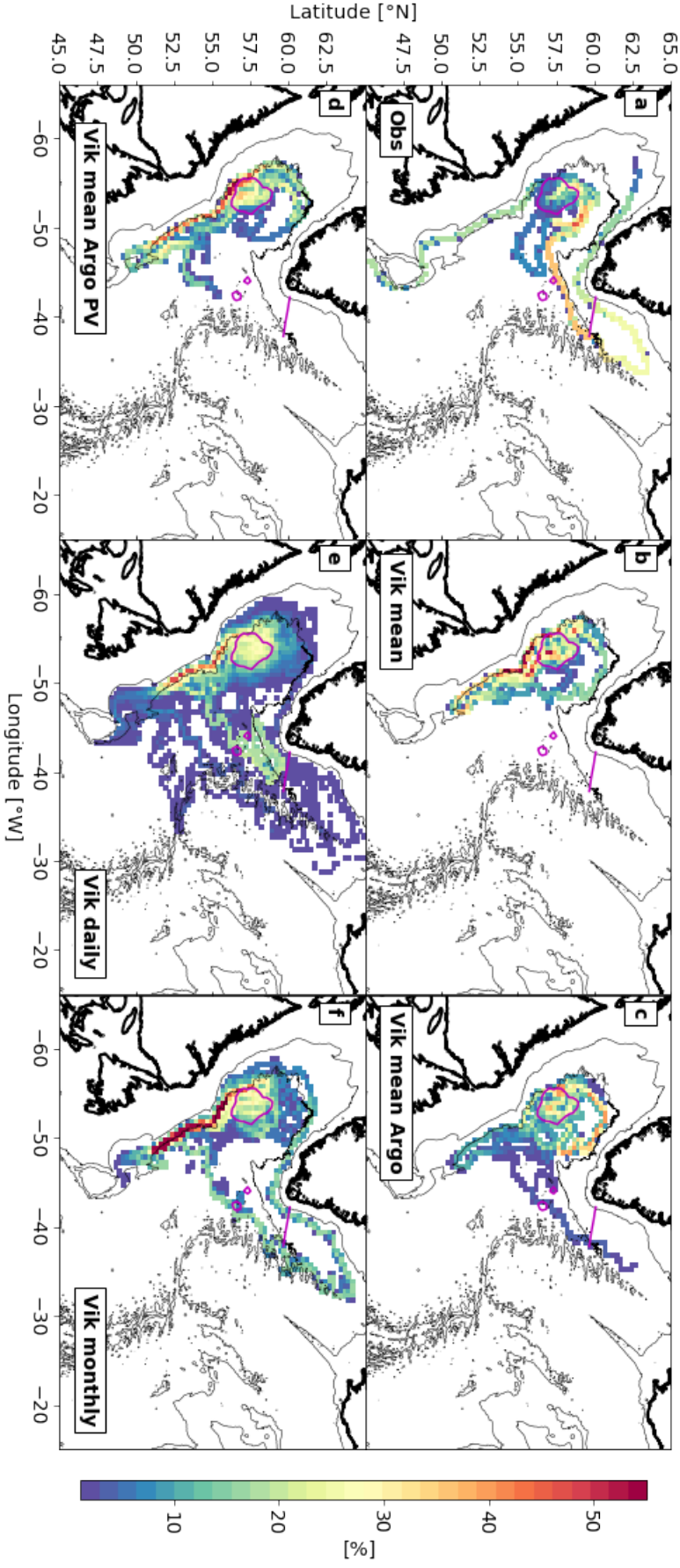

Figure 3.14: *Probability maps particles seeded at central Labrador Sea. Trajectories were calculated forward. The different panels show the respective fields similar to figure 3.8.*

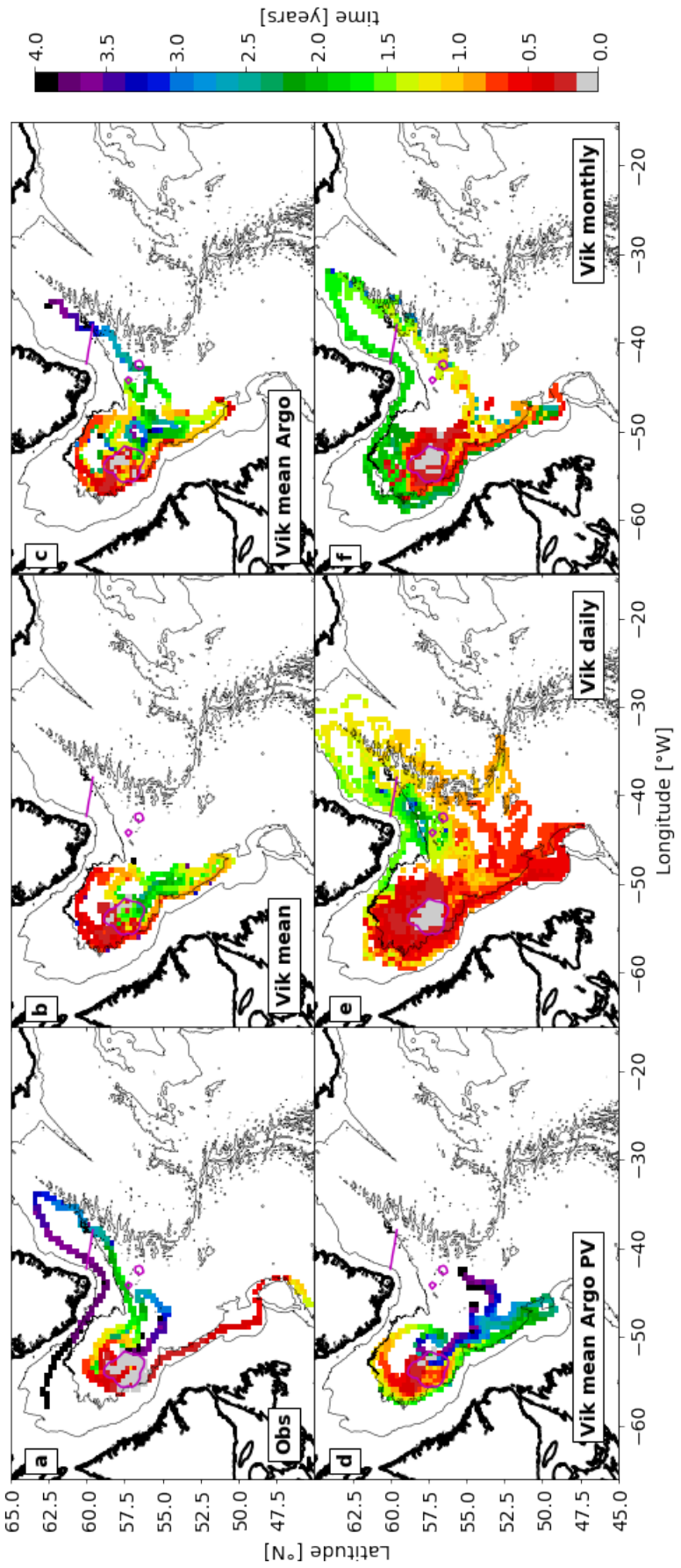

Figure 3.15: *Average age maps of particles seeded at central Labrador Sea. Trajectories were calculated forward. The respective times per bin are presenting the median of the first arrival time of all particles passing through the bin. The different panels show the respective fields similar to figure 3.8.*

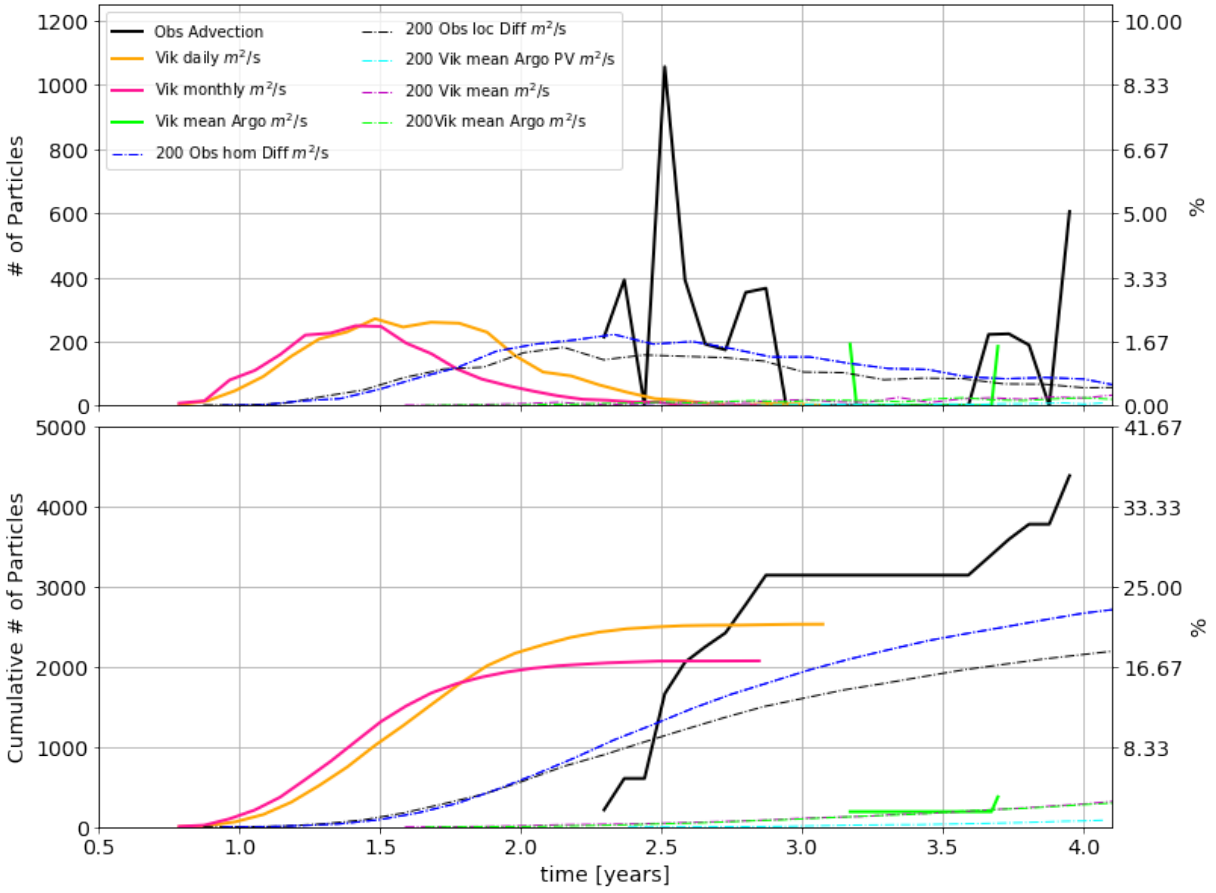

Figure 3.16: *(upper)Arrival times at OSNAP-MEG of particles seeded at cLS.(lower) Transit time density (TTD).*

3.4.2.2 advective-diffusive Experiments

The advective-diffusive experiments all show a more populated **pathway 1** (Figure 3.18) connecting **cLS** and **OSNAP-MEG** in comparison to the advective experiments. Within 2.5 years particles reach **OSNAP-MEG** in the **Obs** experiments (Figure 3.19) and overall $\sim 23\%$ reach the section in 4 years (Figure 3.16). Apart from **Vik mean Argo PV**, where the recirculation is defined to the Labrador Sea west of $45°$W and no particles leave the Labrador Sea towards the Irminger Sea, 3 years of travel time are found for the model experiments (**Vik mean**,**Vik mean Argo**, Figure 3.19), which is confirmed by the TTDs (Table 3.2,Figure 3.16).

All four experiments feature particles following the DWBC towards the south along the Newfoundland shelf break(Figure 3.18). The spreading along this DWBC pathway is very fast and the particles reach the Orphan Knoll region within 0.5 - 1.5 year (Figure 3.19). This pathway is more populated in the experiments using model output in any form than in th **Obs**. At $50°$N or $48°$N in the Orphan Knoll region near the Northwest Corner, particles following the DWBC get either deviated back to the Labrador Sea (all four), deviated towards the east subpolar North Atlantic via **pathway 3** (all four, Figure 3.1) or deviated towards

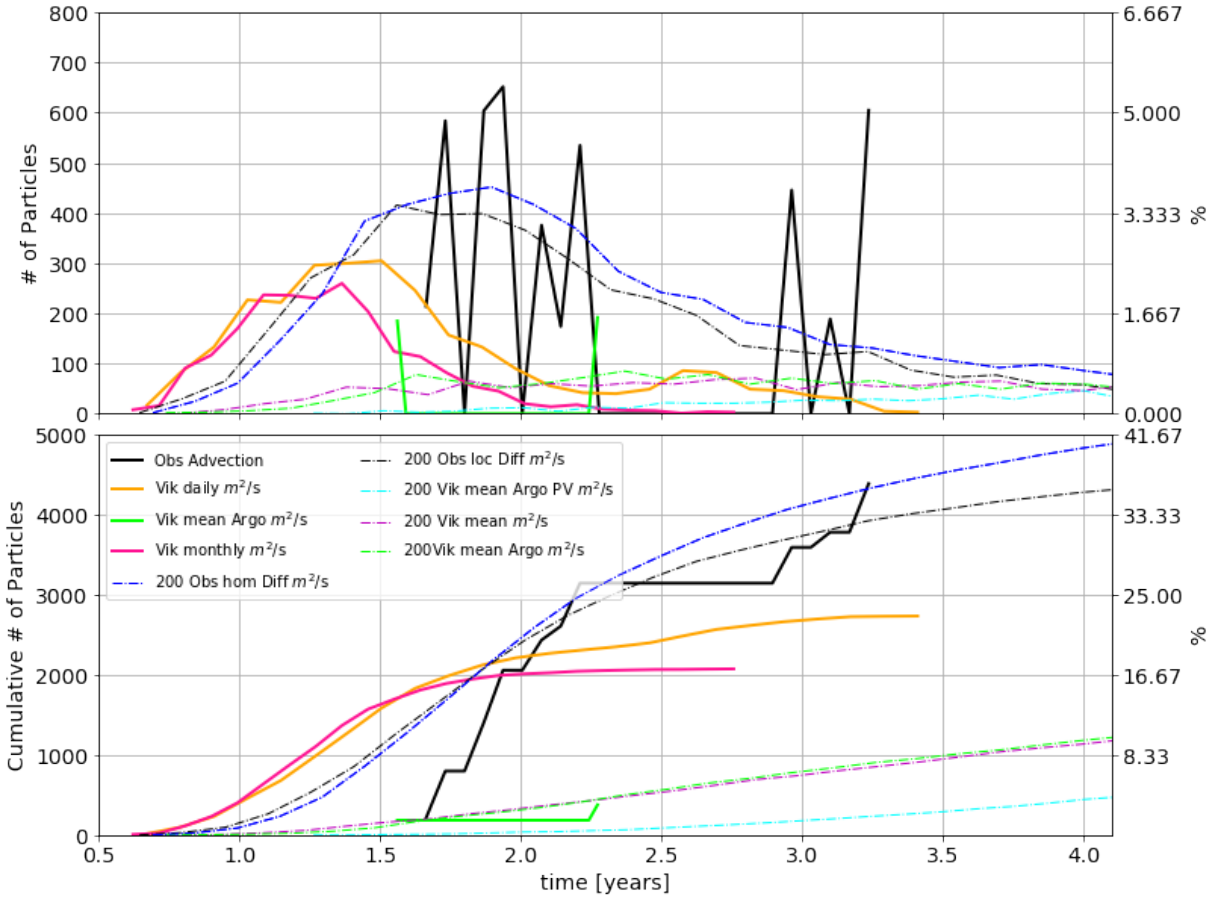

Figure 3.17: *(upper)Arrival times at SG of particles seeded at cLS.(lower) Transit time density (TTD).*

the north and the Irminger Sea via **pathway 5** (**Vik mean**,**Vik mean Argo**). In the **Vik mean** and **Vik mean Argo** experiments less than 3% of the particles reach the **OSNAP-MEG** section within 4 years (Figure 3.16 Figure 3.19,Table 3.2). No particles reach the Iceland basin within the 4 years of particle simulation.

All advective-diffusive experiments reach the **SG**. In the model based experiments 10% pass through **SG** over 4 years, whereas in the **Obs** experiments it is four times more particles. In all four advective-diffusive experiments less than 1% of the particles leave the domain via $45°$N.

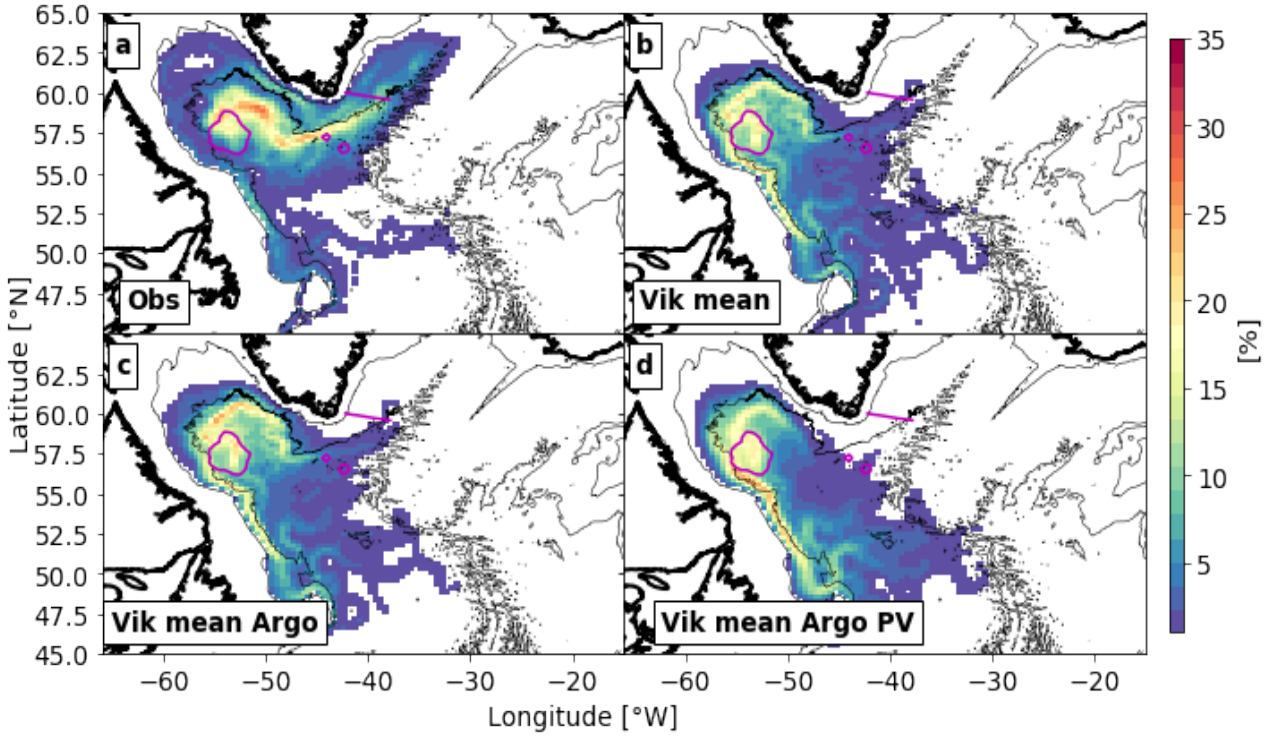

Figure 3.18: *Probability maps particles seeded at central Labrador Sea. Trajectories were calculated forward. The different panels show the respective fields similar to figure 3.12.*

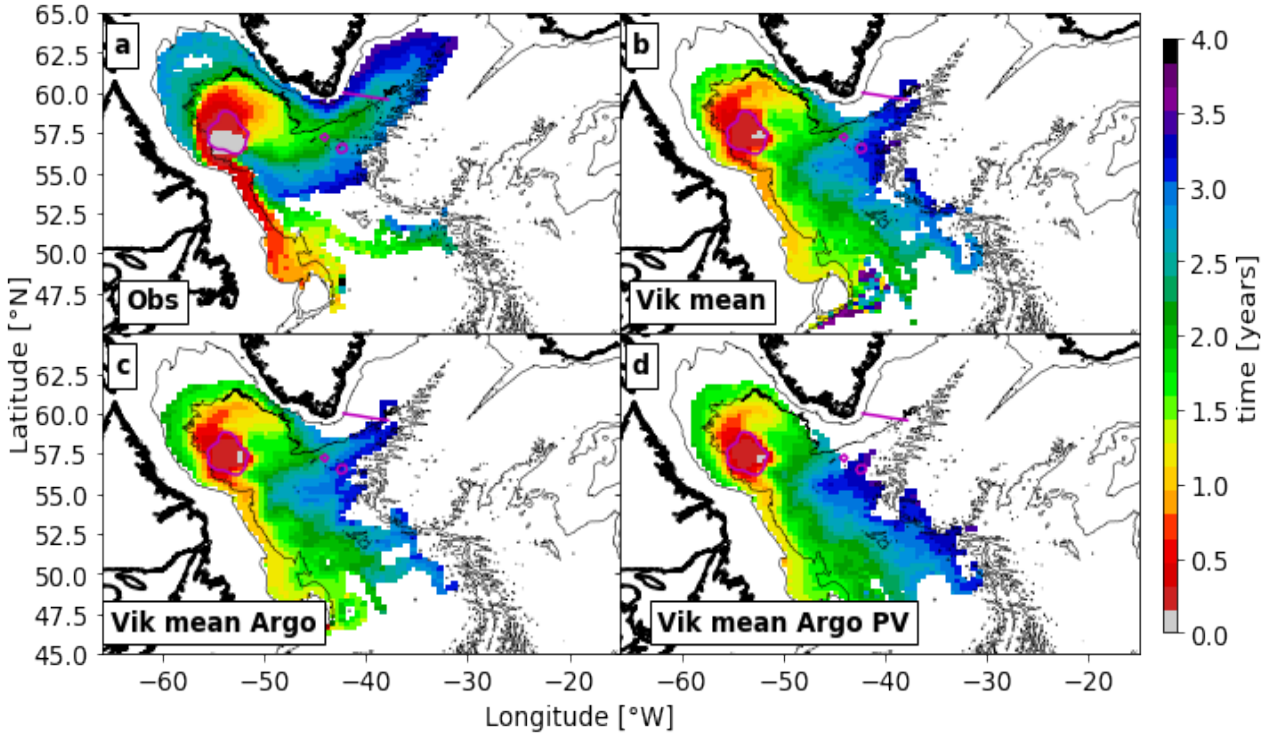

Figure 3.19: *Average age maps of particles seeded at central Labrador Sea. Trajectories were calculated forward. The respective times per bin are presenting the median of the first arrival time of all particles passing through the bin. The different panels show the respective fields similar to figure 3.12.*

3.4.3 Main Particle Pathways

All of the particles that reach the convection patch starting from the **OSNAP-MEG** in the **Obs** and $\sim 90\%$ in the **Vik mean** and **Vik mean Argo** advective experiments take **pathway 1** (Appendix, Figure 3.22). The other 10% get advected on **pathway 5**. The inverse direction from **cLS** to **OSNAP-MEG** presents a slightly altered picture with both pathways being similarly populated in **Vik mean Argo** and $\sim 90\%$ taking **pathway 5** in **Vik daily** and **monthly** (Appendix Figure 3.23).

In the "advective diffusive" experiments the picture is shifting towards **pathway 1** in all experiments, with half of the particles connecting **cLS** and **OSNAP-MEG** taking this route (Appendix Figure 3.24 and 3.25). In the **Obs** experiments the other half take **pathway 4** or interior pathways, where as in the model based experiments one third take **pathway 5** and the rest connect the two regions via the interior.

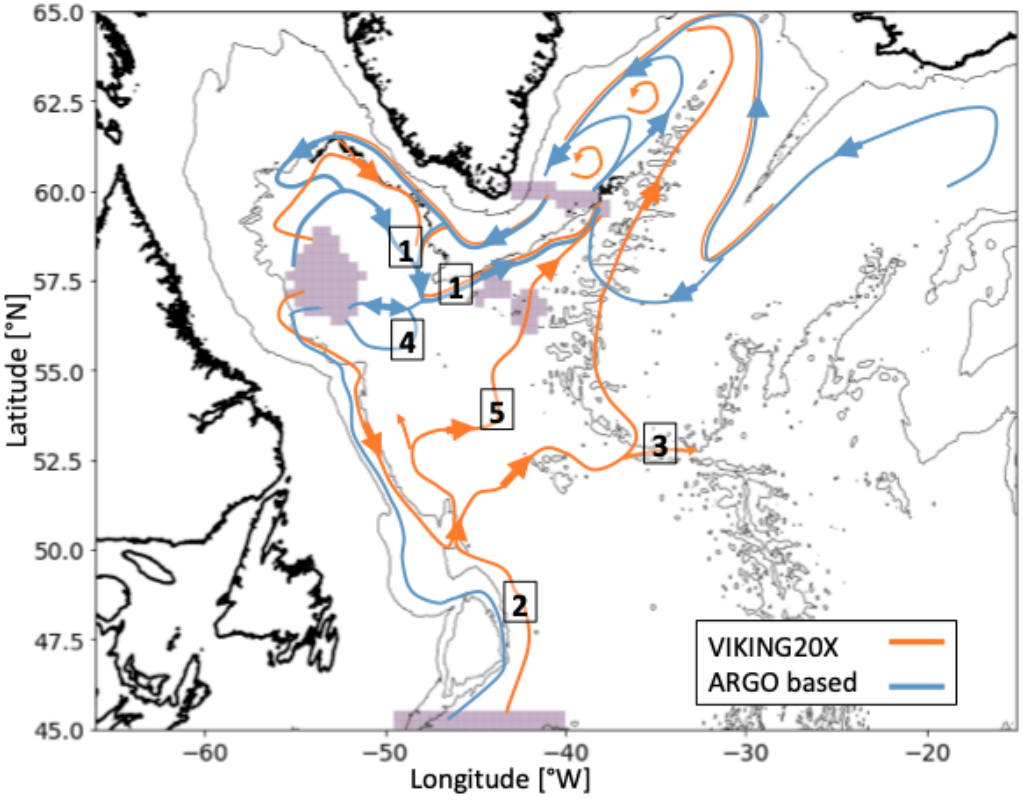

Figure 3.20: *Schematic map of main particle pathways derived from Lagrangian particle experiments. This map extends the previously in figure 3.1 presented export pathways of LSW from the cLS region to the subpolar North Atlantic with the pathways connecting cLS and OSNAP-MEG forward and backward in the experiments. The regions of seeding and of arrival at the south Greenland convection site or the $45°N$ section are marked in gray. Pathways taken predominantly in the experiments using any of the model fields are marked in orange and pathways taken in the experiments using fields coming from experiments with the Argo based Eulerian velocity fields are marked in blue.*

Overall the **Obs** experiments suggest the that the largest number of Lagrangian particles connect the northwest of the convection patch and the eastern most part of the **OSNAP-MEG** with the fastest travel times. Additionally, a connection between the southeast region of the convection patch through **pathway 4** is possible. In the model based experiments the northern part of the convection patch and the southwestern part of the convection area are likely connected to **OSNAP-MEG** (dependent on the resolution of the model output). Though the timescales of the travel times depend on the pathway taken.

The backward and forward experiments with the mean model output in any form predict far less connectivity between the **cLS** and the **OSNAP-MEG** within 4 years. Though high connectivities ($10 - 80\%$) between either seeding location with **SG** are found. Travel times from **OSNAP-MEG** to **SG** are very coherent around 1 year, where as from **cLS** to **SG** the "advection" experiments imply faster travel times than in the advective-diffusive case ($\sim$1 year difference) (Table 3.3).

The **Vik daily** and **Vik monthly** experiments seem to be dominated by mesoscale eddy activity (Figure 3.8,Figure 3.14). These dynamic structures connecting the Northwest Corner and the Irminger Sea, only get reproduced in the advective backwards **Vik mean** and **Vik mean Argo PV** experiments from **OSNAP-MEG**. The forward connectivity of the **cLS** and the **OSNAP-MEG** is also governed by these mesoscale eddies which get lost during temporal and spatial averaging and interpolation (Figure 3.14). Introduced diffusivity on the **Vik mean** and **Vik mean Argo** fields can result in comparable spatial spreading structure, but in still lower (10% of the **Vik daily**) connectivity between the two regions. Overall the major pathways concur between mean and temporarily varying model field experiments, even though travel times are twice as long as in the experiments using the mean model field (Table 3.2). The mesoscale eddies simulated in the temporarily varying model field increase the connectivity from the **cLS** to the **OSNAP-MEG**. The connectivity in the forward experiments with $\sim 20\%$ of the seeded particles connecting the two regions in **Vik daily/monthly** is not as strong in the advective-diffusive experiments $\sim 3\%$. Even though, the **Vik mean Argo PV** experiments did not express any connectivity of the two regions at all, the spreading patterns were comparable to the **Vik daily** and **Vik mean**.

3.5 Discussion and Conclusion

There are two major pathways connecting the convection patch and the **OSNAP-MEG** and vice versa, **pathway 1** and **pathway 5** (Figure 3.20,Table 3.2). Both pathways function in either direction of particle simulation (forward/backward). The population of the pathway taken is dependent on the seeding location and the respective forward or backward integration, the spatial and temporal resolution of the velocity field and the applied diffusivity (Figure 3.21). The experiments with **Obs** prefer the former and the experiments with the model feature both pathways. **pathway 1** follows the recirculation in the Labrador Sea along the Greenland shelf break towards the Irminger Sea. It connects the northern part of the convection patch with

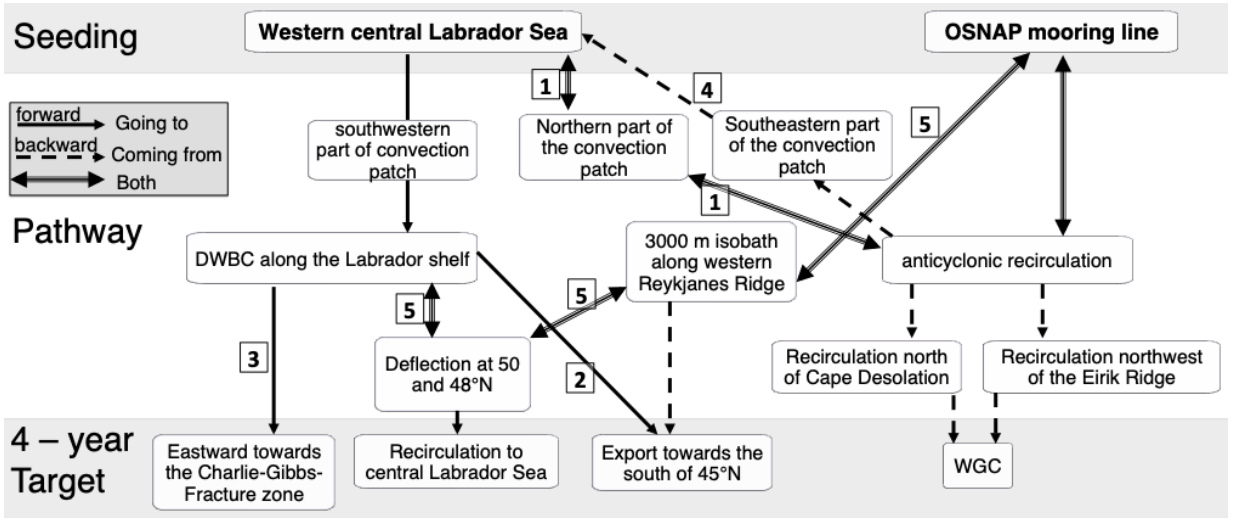

Figure 3.21: *Schematic of particle pathways derived from Lagrangian particle experiments with seeding in the convection patch in the central Labrador Sea and at the OSNAP-MEG. The numbers represent the same pathways as in figure 3.20.*

the Irminger Sea interior. This pathway is proposed as well in previous spreading schematics *Daniault et al.* [2016]; *Lavender et al.* [2000]; *Rhein et al.* [2002]; *Straneo et al.* [2003]; *Sy et al.* [1997]; *Yashayaev* [2007]; *Yashayaev and Clarke* [2008].

Pathway 5 connects the two regions via the DWBC at the Newfoundland shelf break then turning to the north/ northwest at $50/48°$N at the Orphan-Knoll region. The particles then follow the 3000m isobath of the western flank of the Reykjanes Ridge towards the central Irminger Sea. **Pathway 5** thereby connects the southwestern part of the **cLS** with the interior Irminger Sea. This pathway was only found in the experiments conducted using the model output, similarly to a previous Lagrangian study with the high resolution ocean model FLAME done by *Bower et al.* [2009] simulating travel times of 2-10 years. Consequently, the connectivity between central Labrador and Irminger Sea is expected to be sensible to the strength of the DWBC and its deflection at the Orphan Knoll region in the model. In observations individual Argo floats were found to follow this pathway [*Fischer and Schott*, 2002; *Lavender et al.*, 2005], but our experiments based on the Argo based Eulerian velocity fields did not specifically feature it as a major pathway. This is not surprising, being probably caused by mesoscale eddy transport [*Bower and Hunt*, 2000; *Dengler et al.*, 2004], this effect is lost during the preparation of the Eulerian velocity field from Argo data [*Fischer et al.*, 2018]. The representation of **pathway 5** in the model experiments could be related to a stronger DWBC and a stronger Northwest Corner, the related shedding of mesoscale eddies can probably result in an enhanced connection between the Northwest Corner region and the Irminger Sea (Figure 3.2, [*Marshall and Tansley*, 2001]). The strength of this interaction could be dependent on the dynamic state of the subpolar North Atlantic, e.g. the Gyre strength.

A third possible spreading pathway (**pathway 4**) was only featured in the advective-diffusive Argo based backwards experiments, connecting the southeast of the convection region via the region south of Greenland with the Irminger Sea. This pathway was found to be as important as **pathway 1**. Dependent on the diffusivity **pathway 4** could represent a "short cut" connecting the central Labrador and the central Irminger Sea. Though, due its dependence of diffusivity is not expected to shorten the travel time between **cLS** and **OSNAP-MEG**. Additionally, the **Obs** forward experiments with seeding at **cLS** with and without diffusivity parameterization imply, that the southward export of LSW along the DWBC is very dependent on the diffusivity at the Orphan Knoll and the greater Northwest Corner region. In the purely advective experiments $\sim 18\%$ of the seeded particles leave the domain via $45°$N which coincides with estimates of 21% from *Rhein et al.* [2002] and 15% from *Smethie et al.* [2000]. Already very weak diffusion reduced the southward transport by the DWBC sufficiently to stop southward export along the DWBC and leave particles to rather recirculate in the Orphan-Knoll region and the Labrador Sea or being deflected toward the north or the northeast towards the Charlie-Gibbs fracture zone. The effect of diffusivity is not insignificant in the region concerning the connectivity of the two basins and an enhanced understanding of it could help to further quantify the export pathways and possible regions important for the export of LSW from the Labrador Sea.

The estimated time scales for the connection between the Labrador and Irminger Sea, starting at the defined seeding regions, coincide with the range of literature values : ~ 1.5 years (forward) for the **Vik daily** and **monthly** ($\sim 20\%$), 2-3 years (forward,backward) for the Argo based experiments (advective-diffusive, $\sim 20\%$) and 3-4 years for all experiments conducted with the model mean (advective **Vik mean Argo** $\sim 20\%$, all other $\sim 3\%$). A similar connectivity was derived between the two regions by *Rhein et al.* [2002] $\sim 20\%$. The performed experiments clearly imply less connection of the inner Labrador Sea with the Irminger Sea in the mean model experiments than in the **Obs**. This could be related to a stronger dynamic separation between the recirculation and the DWBC in the model in the mean fields.

Furthermore, LSW entering the convective regions in both basins can precondition for subsequent convection in the following winter [*Pickart et al.*, 2003b; *Rhein et al.*, 2002; *Zou and Lozier*, 2016]. Thus, reventilated LSW could be very similar in its temperature, salinity or potential vorticity properties and hard to distinguish from (upper) LSW formed in the central Labrador Sea [*Pickart et al.*, 2003b; *Zou and Lozier*, 2016]. *Straneo et al.* [2003] and *Fischer et al.* [2018] stated, that the spreading of particles within the Labrador Sea is strongly driven by the interplay of advective and diffusive effects, hence the relative location of the convection to the circulation pattern, the strength of the recirculation and the diffusivity play a crucial role for the spreading of Labrador Sea Water. Accordingly, rapid spreading within 6 months to one year from the Labrador Sea to the Irminger Sea described in *Koltermann et al.* [1999]; *Sy et al.* [1997] could result from:

- Strong advection along the recirculation pathways
- Convection directly in the mid basin advection around southern Greenland which connects LS with IS.
- Enhanced diffusive interaction between the convection region and the recirculation pathways
- Convection south of Greenland underneath the Greenland tip jet (travel times of ~ 1 year, Table 3.3) [*Pickart et al.*, 2003b; *Piron et al.*, 2016]

.

None of the experiments featured a forward connection of the convection patch and the Iceland basin within the 4 years of trajectory integration. This is congruent to a study of *Zou and Lozier* [2016] which implies timescales of $\geq 20yr$ for the connectivity of the Labrador Sea and the Iceland basin. Overall, the results suggest a non negligible role of the recirculation regions in the Irminger and Labrador Sea as well as the role of ocean eddies at Orphan Knoll, the Eirik Ridge and north of Cape Desolation on the overall spreading of LSW within the subpolar North Atlantic. The latter three are regions of high variability which can influence the interaction between the DWBC and the inner basins [*Cuny et al.*, 2002].

Several questions beyond the scope of this study arise, concerning the comparability of deep convection strength and region in observations and ocean models, where ocean models tend to represent deep convection stretched along the recirculation pathway around the Labrador Sea [*Handmann et al.*, 2018]. Additionally, the interaction between the basin interior and the DWBC is a subject which is closely related to the differences in dynamics in observations and models (stronger DWBC), which is related to the overall spreading of LSW.

This study contains the following limitations:

- Isobaric 2-D velocity fields :

The Lagrangian experiments were conducted on isobaths neglecting vertical velocities, but true Lagrangian floats follow all three components of the oceanic velocity fields [*D'Asaro*, 2003]. To evaluate the actual influence of vertical velocities on the Lagrangian trajectories, 3-D Lagrangian particle experiments could be conducted with the model output. Furthermore, the functioning of Argo floats raised the question of comparability of the Lagrangian experiments to trajectories of Argo floats. Argo floats surface every ten days and hence, after surfacing and sinking to their parking depth, the previous drifting cycle and the new drifting cycle are decorrelated [*Bower et al.*, 2009; *D'Asaro*, 2003]. In contrast, for a limited number of floats, *Fischer and Schott* [2002] found that floats left the DWBC also at parking depth, presumably due to eddy motion interacting with the deep flow. Hence above, the Argo trajectories were compared to the resulting pathways of the experiments.

- Constant diffusivity :

The preliminary experiments revealed that a locally varying diffusivity did not have a great influence on the spreading patterns (Figure 3.6). The subpolar North Atlantic in the region of interest was expected to have a weak to no diffusivity suppression as for example in the region of the ACC [*Klocker et al.*, 2012] hence a constant diffusivity value within literature estimates was applied. The experiments with the different temporal and spatial model resolutions imply, that major pathways can be reproduced by this method, even if $\Delta \mathbf{X}_b(t)$ which accounts for all subgrid-scale processes was chosen to be very simple, though discrete connectivity values may vary. The regions of recirculation like the Eirik Ridge, Cape Desolation and the Orphan Knoll region can play a major role in the spreading of LSW.

- Connectivity asymmetries - Different amounts of particles connecting the Irminger and Labrador Sea in the backward and forward experiments (tables 3.2 and 3.3) :

These could be caused by the seeding strategy of this study, which was not proportional to the local strength of the currents nor the backward results from previous experiments (random normal seeding see section 3.3.3.3). As *Durgadoo et al.* [2019] explains forward and backward experiments only tend to lead to similar results when the seeding in both is adjusted to the results of the other.

Aditionally, the recirculation pattern in the Labrador Sea is only known from snapshot like ship surveys and from Argo floats. Extending the OSNAP WEST array with one or two moorings in the recirculation regime could help to improve the estimation of the role of the recirculation. This of course is a question of funding and ship time, but would help to shed light on the formation and spreading of LSW, which is consequently liked to the overall connection between deep convection activity and the AMOC strength.

- Spatial and temporal restrictions of Eulerian velocity fields :

A Lagrangian analysis and its results, such as connectivity measures, are only as good as the underlying Eulerian velocity fields, regarding their temporal and spatial resolution [*Griffies et al.*, 2009; *van Sebille et al.*, 2017]. One has to take into account that complete observed velocity fields at 1000-1500m are not existing with greater temporal or spatial resolution than the mean for the entire Argo period and the resolution from *Fischer et al.* [2018]. Estimated Argo drifting velocities on the parking depth can rather be interpreted as Eulerian velocities for individual 10 day drift segments. The accuracy to represent the real mean ocean velocity fields through the Argo based velocity field of the SPNA published by *Fischer et al.* [2018] could be assessed by subsampling high-resolution OGCM output with ARGO like moving Lagrangian floats and then applying the respective methods described in *Fischer et al.* [2018]. The representation of the mean model output compared to the fields derived through ARGO subsampling can then be estimated an be used as an uncertainty estimate on the Argo derived fields. Additionally, extending the OSNAP WEST

array with one or two moorings featuring current meters, hydrography sensors and ADCP further off shore in the recirculation regime could have a great value to investigate the formation and spreading of LSW and to improve the understanding of the connection between deep convection activity in the Labrador Sea and the related spreading.

For the applied simplifications, the derived travel times and connectivities concur reasonably well with literature values.

Appendix

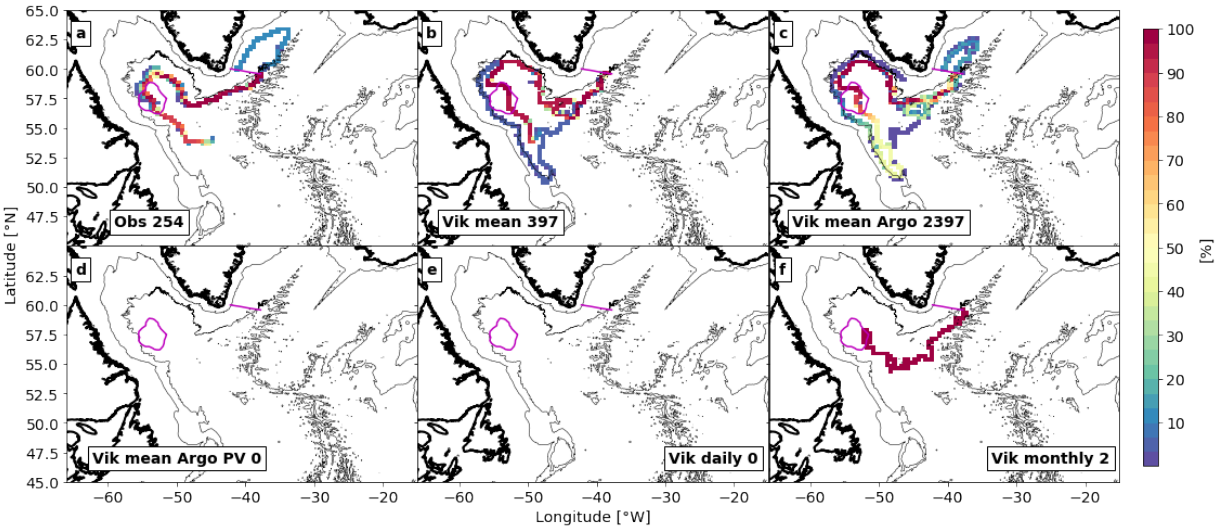

Figure 3.22: *Probability maps of particles reaching cLS starting backwards from OSNAP-MEG in advective experiments. The total the number of different particles per bin are divided by the number of total particles connecting the two regions. Abbreviations used as indicated in table 3.1. Numbers after Experiment abbreviation give the total number of particles connecting the two regions.*

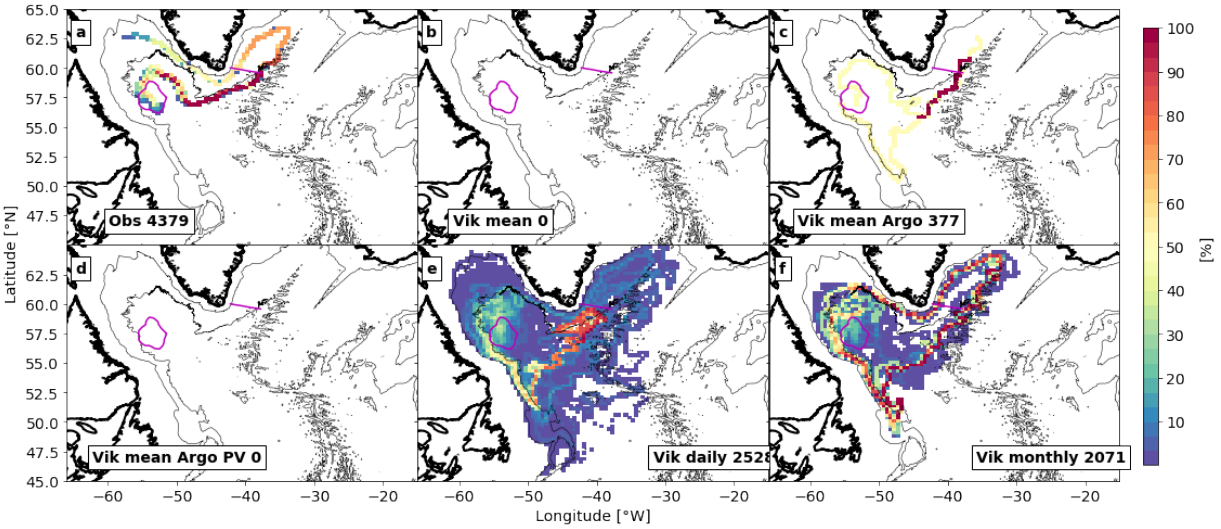

Figure 3.23: *Probability maps of particles reaching OSNAP-MEG starting forward from cLS in advective experiments. Maps are computed as described in figure 3.22. Abbreviations used as indicated in table 3.1. Numbers after Experiment abbreviation give the total number of particles connecting the two regions.*

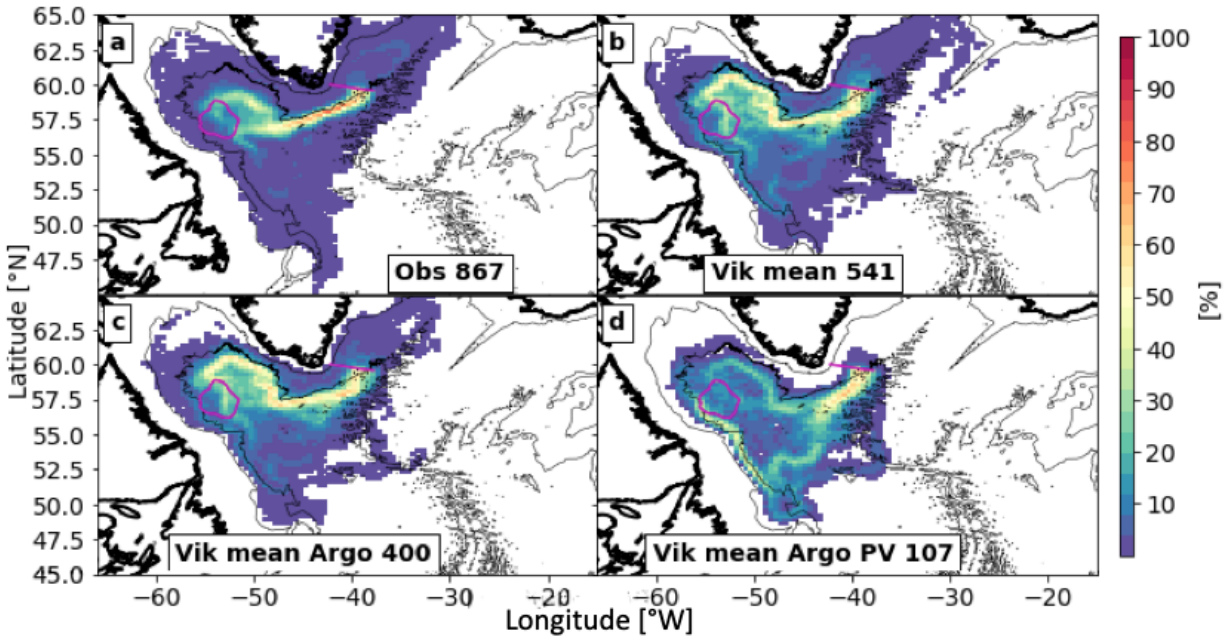

Figure 3.24: *Probability maps of particles reaching cLS starting backwards from OSNAP-MEG in advective-diffusive experiments. Maps are computed as described in figure 3.22. Abbreviations used as indicated in table 3.1. Numbers after Experiment abbreviation give the total number of particles connecting the two regions.*

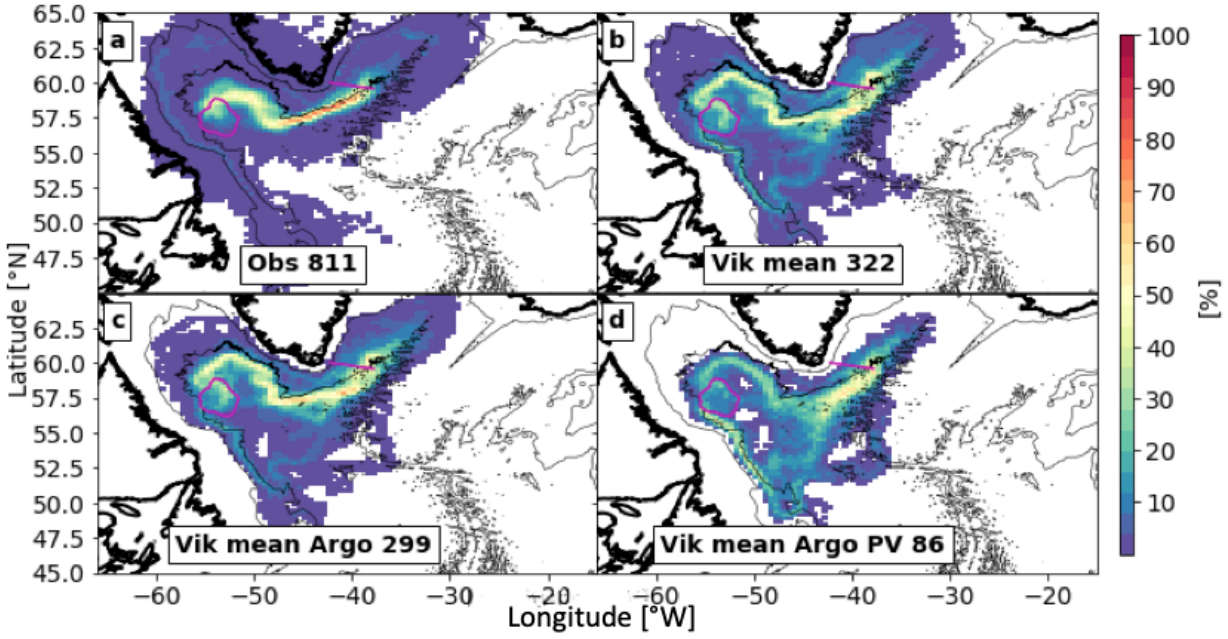

Figure 3.25: *Probability maps of particles reaching OSNAP-MEG starting forward from cLS in advective-diffusive experiments. Maps are computed as described in figure 3.22. Abbreviations used as indicated in table 3.1. Numbers after Experiment abbreviation give the total number of particles connecting the two regions.*

4. OSNAP Model study

This chapter aims to bring the horizontal volume, heat and freshwater transports of the currents in the subpolar North Atlantic into context with the AMOC-strength in the subpolar North Atlantic. Transports and the AMOC strength,in the high-resolution ocean model VIKING20, are computed at two sections, namely the OSNAP section [*Lozier et al.*, 2017] and a section along the Greenland-Scotland ridge composed of the Denmark Strait section [*Jochumsen et al.*, 2012] and a section along the Iceland-Scotland Ridge [*Chafik and Rossby*, 2019]. Related variabilities are brought into context with the water mass transformations in the three basins of the SPNA: the Labrador and Irminger Sea and the Iceland basin. Variability and coherence of the current transports and water mass transformation rates in the basins are evaluated on three different density levels and brought into relation to the model AMOC strength at the sections and at the $26.5°$N RAPID array. Furthermore, the model values are evaluated with literature.

4.1 Abstract

The relation of the meridional overturning circulation in the Atlantic (AMOC) and the horizontal circulation of the subpolar gyre are assessed between the Overturning in the Subpolar North Atlantic (OSNAP) section and a section spanning the Greenland-Scotland Ridge (GSR) within the high-resolution ocean model VIKING20. Transports were calculated in three density classes to account for the "upper" AMOC ($\sigma_2 \leq$ 36.79 kg/m^3/ $\sim \sigma_0 \leq$ 27.72 kg/m^3)), the LSW (36.79 kg/$m^3 < \sigma_2 <$ 37.03 kg/m^3/ 27.72 kg/$m^3 < \sigma_0 <$ 27.88 kg/m^3) and the LNADW ($\sigma_2 \geq$ 37.03kg/m^3/ $\sigma_0 \geq$ 27.88kg/m^3) component. The model shows a volume balance in the northward transport of the North Atlantic Current (**NAC**) and the net southward transport of deep waters for the GSR and the eastern leg of the OSNAP section (OSNAP EAST), with AMOC strengths of 6.6 ± 0.9 Sv for the former and 17.2 ± 3.0 Sv for the latter. The upper limp, crossing the OSNAP EAST section can be decomposed in the **NAC** (17.9 ± 4.9Sv) and the Irminger Current (**IC**,22.7 ± 2.8Sv) transports, where the IC transports exceed literature values by ~ 10Sv. This excess import is compensated through a similarly higher southward transport east of Greenland (37.2 ± 3.5Sv). For the western part of the OSNAP array the volume balance is influenced by the import of water through the Davis strait (2.3 ± 0.7Sv). The analysis of basin related water mass transformation rates leaves the Labrador Sea as similarly important site of Labrador Sea water (LSW) formation as the Irminger and Iceland basin combined (~ 8 Sv), where the Iceland basin (5.1 ± 1.2 Sv) forms three times as much LSW as the Irminger Sea (1.6 ± 2.8 Sv). In all three basins water mass formation is governed by the transformation of upper AMOC limb water to LSW. Additionally, mixing of NEADW with lighter waters is playing a similarly

important role in the Iceland basin. Statistical analysis explaining the major modes of variance, represents the subpolar gyre activity and the strength of NAC input to the subpolar North Atlantic (SPNA). The results imply enhanced boundary currents during years of deep convection in the 1990's concurring with stronger NAC transport to the Iceland basin.

4.2 Introduction

The subpolar North Atlantic (SPNA) is a crucial region for the transformation of warm and salty surface waters to cold and fresh deep waters [*Lozier*, 2012]. The "upper limb" of the Atlantic meridional overturning circulation (AMOC) is defined from the ocean surface to the density surface where the overturning stream function reaches its maximum and represents the northward transport of warm and saline waters [*Sarafanov et al.*, 2012]. The "lower limb" defines everything below this maximum (North Atlantic Deep water, NADW) and represents the fresh and cold southward return flow. Due to the strong vertical variation of isopycnal depths from east to west in the SPNA, AMOC analysis in depth coordinates underestimates the actual water mass transformation north of $45°$N. In depth space the northward and southward transports partly compensate each other within the same depth layer which disguises the maximum AMOC near the NADW formation regions, shifting the observed maximum to lower latitudes ($\sim 25°N$) [*Holliday N. et al.*, 2018; *Xu et al.*, 2014; *Zhang*, 2010]. In the subtropical North Atlantic the AMOC estimation in depth and density space does not reveal great differences due to relatively stable isopycnal depths [*Xu et al.*, 2014], though it implies a crucial difference in the SPNA. Hence, the SPNA AMOC strength is preferably computed in density space (Equation 1.1). Its strength is widely perceived as the amount of warm and saline surface water being overturned as a function of time. The overall magnitude of the AMOC strength (16-18 Sv) is rather independent of latitude [*Bacon*, 1997; *Bringedal et al.*, 2018; *Chafik and Rossby*, 2019; *Daniault et al.*, 2016; *Lherminier et al.*, 2010; *Lozier et al.*, 2019; *McCarthy et al.*, 2015; *McCartney and Talley*, 1984; *Mercier et al.*, 2015; *Sarafanov et al.*, 2012; *Talley*, 2013; *Willis et al.*, 2004; *Østerhus et al.*, 2019] but multiple modeling studies showed that its variability is not coherent on interannual to decadal time scales between the subtropical and subpolar latitudes [*Bingham et al.*, 2007; *Lozier*, 2010; *Williams et al.*, 2014]. To evaluate this relationship in observations the need to continually measure the AMOC strength at various latitudes emerged and led to the two basin wide mooring arrays RAPID-MOCHA-WBTS on the subtropical latitude 26.5°N (since 2004) [*Smeed et al.*, 2016] and OSNAP (since 2016) in the subpolar gyre [*Lozier et al.*, 2017] (Figure 4.1). The OSNAP array is a two legged observational transbasin effort. Its western component OSNAP WEST spans the Labrador Sea from southern Labrador to southwestern Greenland. Its eastern component OSNAP EAST spans the North Atlantic basin from southeastern Greenland to the northwest coast of Scotland [*Holliday N. et al.*, 2018; *Lozier et al.*, 2017, 2019].

The subpolar North Atlantic is alimented with warm and saline water from the subtropics through the **NAC** and with cold and fresh deep waters through the overflows from the Nordic Seas. The SPNA interacts with the Nordic Seas and the Arctic Mediterranean through the Greenland-Scotland Ridge (GSR, Figure 4.1) [*Hansen and Østerhus*, 2000]. The GSR is the gateway of northward transport of warm and saline surface waters to the Arctic and southward transport of the densest components of the North Atlantic Deep water (NADW), which is formed north of the Ridge. The shallowest component of the NADW, the Labrador Sea Water (LSW), is formed south of the ridge in the Labrador Sea. The basins of the subpolar North Atlantic, the Labrador and Irminger Sea and the Iceland basin, play a big role in deep water formation which is thought to be closely linked to the AMOC variability [*Böning et al.*, 2006; *Brandt et al.*, 2007; *Lozier et al.*, 2019]. Although model studies implied a relation between the formation of deep water in the Labrador Sea [*Böning et al.*, 2006; *Brandt et al.*, 2007] with the strength of the DWBC and a link between the overflow strength [*Danabasoglu et al.*, 2010; *Yeager and Danabasoglu*, 2012] and the overall AMOC. Observational studies could not find evidence for this close connection. They show that the export of the overflows at the GSR are stable in contrast to changes of the AMOC south of the GSR [*Olsen et al.*, 2008] and that transports in the DWBC in years of enhanced deep water formation show no clear intensification at the exit of the Labrador Sea [*Zantopp et al.*, 2017]. Hence, the Irminger and Iceland basin are expected to play a major role concerning the variability of the AMOC strength [*Lozier et al.*, 2019].

The GSR transports and the respective AMOC strength are observed through composites of direct ship based current measurements by a weekly ferry and from moored current meters in the Denmark strait and the Faroe-Shetland Channel [*Rossby et al.*, 2018]. In conjunction with data from the subpolar North Atlantic (e.g. OSNAP, Ovide) this data open the possibility to compute basin balances for water mass transformation and heat loss in the two subpolar North Atlantic basins [*Lherminier et al.*, 2010; *Sarafanov et al.*, 2012].

The interaction between surface currents, deep currents, water mass transformation and the AMOC strength is hence not as simple as previously expected and this chapter brings these different components of the circulation in the SPNA into relation. This study utilizes a high resolution model ($1/20°$) which was shown to represent the subpolar North Atlantic and its major currents convincingly enough [*Behrens et al.*, 2017; *Breckenfelder et al.*, 2017; *Handmann et al.*, 2018]. Transports in three density classes are computed for the OSNAP section and the GSR section (Figure 4.1) which enclose the three subpolar North Atlantic basins: the Iceland and Irminger basin and the Labrador Sea. By using a simple box model approach [*Lherminier et al.*, 2010; *Sarafanov et al.*, 2012] the water mass transformation rates between the three density classes and the respective heat loss to the atmosphere are computed. The Irminger and Iceland basin are separated by the shallow Reykjanes Ridge and are thought to solely exchange deep waters along the Reykjanes Ridge and through deep passages and troughs in the Ridge. To close the budgets for the

single boxes an additional section connecting the OSNAP and GSR section via the Reykjanes Ridge and a section to close the northern passage to the Canadian Archipelago to the Labrador Sea, the Davis Strait, are included in the computations. 50-years (1958 - 2009) of model output are analyzed concerning the volume, heat and freshwater transports in relation to the AMOC strength and the water mass transformation rates in the 3 ocean basins. The key questions of this chapter are:

- How much water of the lower AMOC limb is formed per basin in the SPNA in the model?
- Are there common modes of variability of the currents in the subpolar North Atlantic and are they related to the AMOC strength and/or the water mass transformations?

The model findings are finally compared to established observed values in the subpolar North Atlantic.

The model setup and applied methods are presented in section 4.3. Section 4.4 evaluates the hydrographic and dynamic properties of the OSNAP and GSR section. It further evaluates the AMOC strength and the rates of water mass transformation of the three subpolar basins. A discussion and the conclusions drawn from this study are presented in section 4.5.

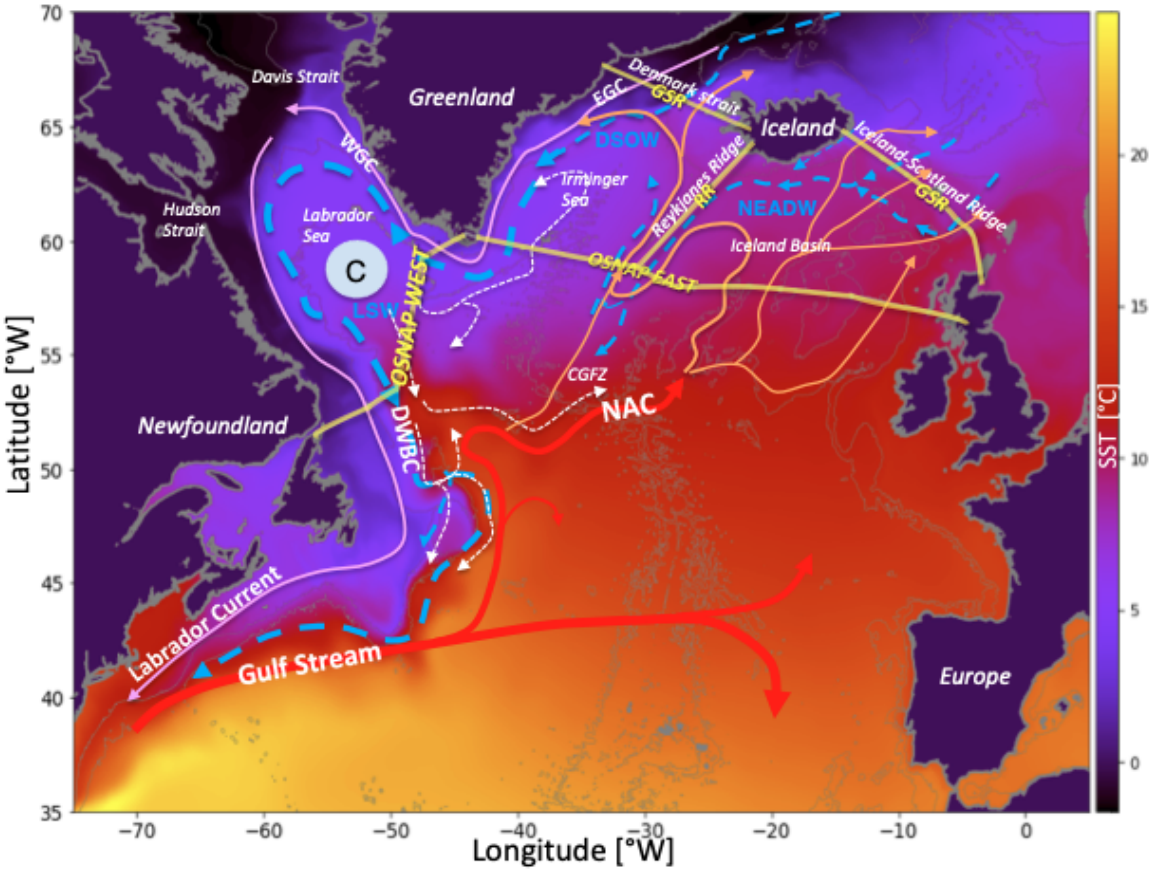

Figure 4.1: *Schematic view of the subpolar North Atlantic ocean.The key sections (OSNAP, GSR-Greenland-Scotland Ridge, yellow), as well as the currents (red,orange,light blue, NAC- North Atlantic Current, WGC - West Greenland Current, EGC - East Greenland Current, DWBC- Deep Western Boundary Current) and water mass names (light blue, LSW -Labrador Sea Water, DSOW - Denmark Strait Overflow water, NEADW - Northeast Atlantic Deep water) are superimposed on the mean sea surface temperature field (1958-2009) output from VIKING20. Red and orange colors depict warm and salty surface currents and light blue dashed lines depicts the dense, deep southward return flow (adapted from [Handmann et al., 2018]).The white dashed lines show possible pathways of LSW starting at its formation region in the Labrador Sea (C).*

4.3 Data and Methods

4.3.1 Ocean Circulation Model

The ocean general circulation model VIKING20 is based on a global eddy-permitting configuration of NEMO [*Barnier et al.*, 2015], ORCA025, with $1/4^\circ$ resolution and contains a high resolution nest of $1/20^\circ$ resolution between $32^\circ N$ and $85^\circ N$ in the North Atlantic. This nest is introduced using the Adaptive Grid Refinement in Fortran method (AGRIF two-way nesting) [*Debreu and Blayo*, 2008; *Sheng et al.*, 2005] to enhance the horizontal resolution. The model contains 46 depth levels with increasing thickness (6 - 200m (below 1000 m)) and partial bottom cells to account for high resolution topography (ETOPO2, GEBCO) [*ETOPO*, 2001; *Ioc*, 2008]. After a 30 year spin-up period based on a coarser ($1/4^\circ$) model configuration, the model generated 60 years of hindcast output from 1948 - 2009. This period is forced with the Co-ordinated Ocean-ice Reference Experiments data set (CORE.v2) [*Griffies et al.*, 2009; *Large and Yeager*, 2009]. Monthly means generated from the daily output were used here.

VIKING20 has been already validated in multiple studies and the major weaknesses and strengths are well known. Although the model shows a stronger barotropic component than observations and a northward shift of the Northwest Corner [*Breckenfelder et al.*, 2017], it reproduces the major structures of the horizontal circulation. It simulates the depth and structure of the winter mixed layer depth in March in the subpolar North Atlantic comparable to observations. Its mixed layer is stretched along the Labrador shelf break towards the southeast, which has not been observed in the real ocean [*Handmann et al.*, 2018; *Holte and Straneo*, 2017]. Regardless of a very different model hydrography than the observed (too warm, too saline), the model is able to reproduce the relative observed hydrographic changes from 1960 to 2009 in the central Labrador Sea [*Handmann et al.*, 2018]. The magnitude of the overflow component at the Denmark strait, the DWBC at $53^\circ N$ as well as the magnitude and interannual to seasonal variability of the AMOC in depth coordinates at $26.5^\circ N$ are nicely reproduced contrary to the variability on longer time scales [*Behrens*, 2013; *Behrens et al.*, 2017; *Handmann et al.*, 2018]. For further model details and validations the reader is referred to e.g *Behrens* [2013]; *Böning et al.* [2016]; *Breckenfelder et al.* [2017]; *Handmann et al.* [2018]; *Mertens et al.* [2014].

4.3.2 Methods

To extract the to sections (OSNAP,GSR) from the model, the model was subsampled to sections passing through grid points close to the actual positions of moorings in the OSNAP array [*Lozier et al.*, 2019], the Denmark Strait [*Jochumsen et al.*, 2012] and in the Faroe-Shetland Channel [*Berx et al.*, 2013; *Hansen and Østerhus*, 2007]. The sections were utilized with the horizontal and vertical resolution native to the model output. Here, no vertical or horizontal interpolation of the model to mooring instrument positions from observations were conducted. The original velocities along the original tripolar model grid are used along

the sections (Figure 4.2). Rotation of the velocities to real North-South, East-West vectors can lead to interpolation related errors as well as to spurious artifacts each time the relative angle between the original model grid and the section of interest is changing. Hence, the volume transport for each single grid box is calculated (Figure 4.2):

$$V = (v \cdot x_{grid_v} \cdot z_{grid_v}) \quad or \quad V = (u \cdot y_{grid_u} \cdot z_{grid_u}) \tag{4.1}$$

where u/v represent the velocities at the respective point (x,y,z) on the original model grid $grid_u$ ($grid_v$) along the section. x_{grid_v} (y_{grid_u}) and z_{grid_v} (z_{grid_u}) are the length of the grid box in x/y direction and the length of the vertical grid box along the model grid. The transport along a section is the sum of all grid box transports along it. The sea surface height was taken into account for the transports of the uppermost grid box.

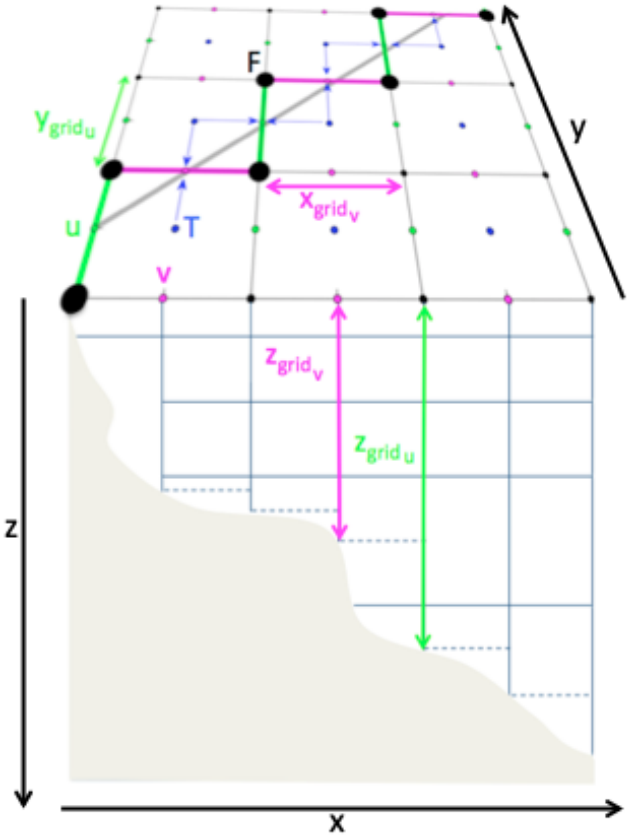

Figure 4.2: *The Arakawa-C grid of the VIKING20 model. The thick grey line marks the desired section. The green and pink lines show the actual extracted model section.*

To compute the total transport along a section the single grid box transports have to be summed up. Consequently the AMOC strength at the sections (OSNAP,GSR,OSNAP EAST,OSNAP WEST) can be computed in depth and density space using equation 1.1 in its discrete form:

$$AMOC = max\left[\sum_{\sigma_{top}}^{\sigma_{bottom}} \sum_{\theta_w}^{\theta_e} V d\theta d\sigma\right] \tag{4.2}$$

Where, first the transports along the section (θ longitude) from east (e) to west (w) are summed then the sum over the densities σ from top to bottom is computed. The AMOC strength at $26.5°$N was computed with the output of the VIKING20 global model ORCA025. The AMOC was computed in depth and density space in order to visualize the effect in the subpolar North Atlantic and to broadly compare the AMOC strength with literature.

Furthermore, depth integrated transports per position of the section can be summed up along the section in order to estimate (minima and maxima) the spatial extent of the represented in- and outflow components (currents) through the respective section [*Holliday N. et al.*, 2018]. For the OSNAP section the cumulative transport was computed starting at Newfoundland summing all depth-integrated transports up towards Scotland. For the GSR section the accumulated transports were summed up starting from Scotland towards Greenland. The resulting minima and maxima were then used as spacial intervals to compute current transports .

All transports, as well as the AMOC strength, were evaluated in density space. For this reason the original model output was transformed from z-coordinates into density space. The following density space was defined:

$$\sigma_0 - Intervall = \begin{cases} 24.0\,kg/m^3 \leq \sigma_0 < 26.5\,kg/m^3 & \sigma_0 : \sigma_0 = 24 + 0.2 \cdot n; n = n \in \{0, 1, \dots 13\} \\ 26.5\,kg/m^3 \leq \sigma_0 < 28.1\,kg/m^3 & \sigma_0 : \sigma_0 = 26.5 + 0.01 \cdot n; n = n \in \{0, 1, \dots 152\} \\ 28.1\,kg/m^3 \leq \sigma_0 < 30.0\,kg/m^3 & \sigma_0 : \sigma_0 = 24 + 0.2 \cdot n; n = n \in \{0, 1, \dots 11\} \end{cases}$$

$$\sigma_2 - Intervall = \begin{cases} 30.0\,kg/m^3 \leq \sigma_2 < 36.0\,kg/m^3 & \sigma_2 : \sigma_2 = 24 + 0.2 \cdot n; n = n \in \{0, 1, \dots 30\} \\ 36.0\,kg/m^3 \leq \sigma_2 < 37.5\,kg/m^3 & \sigma_2 : \sigma_2 = 26.5 + 0.01 \cdot n; n = n \in \{0, 1, \dots 141\} \\ 37.5\,kg/m^3 \leq \sigma_2 < 40.0\,kg/m^3 & \sigma_2 : \sigma_2 = 24 + 0.2 \cdot n; n = n \in \{0, 1, \dots 14\} \end{cases}$$

Transports and the AMOC were then calculated in 3 density classes, where the upper was defined according to the results of the AMOC analysis of this study and the lower two were defined accordingly to *Handmann et al.* [2018]:

- upper AMOC: $\sigma_2 \leq$ 36.79 kgm^{-3} / $\sigma_0 \leq$ 27.72 kgm^{-3}
- LSW: 36.79 kgm^{-3} $< \sigma_2 <$ 37.03 kgm^{-3} / 27.72 kgm^{-3} $< \sigma_0 <$ 27.88 kgm^{-3}
- LNADW: $\sigma_2 \geq$ 37.03kgm^{-3} / $\sigma_0 \geq$ 27.88kgm^{-3}

The zonally integrated meridional temperature transport, commonly named the meridional heat transport (MHT) was computed relative to a reference temperature of 0°:

$$MHT_{Net} = \int_{z_{top}}^{z_{bottom}} \int_{x_e}^{x_w} Q \cdot dzdx \quad with \quad Q = \rho \cdot c_p \cdot V \cdot \Theta_{pot} \tag{4.3}$$

where, Q is the heat at each grid cell, V is the volume transport defined in Equation 4.1, $\rho \cdot c_p = 4.1 \cdot 10^6 [J/(Kg \cdot °C)$ is used for the volumetric heat capacity (density of seawater ρ times the specific latent heat c_p), Θ_{pot} is the potential temperature, z is integrated from top to bottom and x is the distance along the section, which is integrated from east x_e to west x_w. Throughout this paper the term "temperature transport" and MHT will be used synonymously even if the volume balance is not zero (trend in sea surface height (SSH), temporal resolution of the output (monthly))(for further discussion about MHT and temperature transport see e.g [*Warren*, 1999])

The meridional freshwater transport (MFT) was computed:

$$MFT_{Net} = -\int_{z_{top}}^{z_{bottom}} \int_{x_e}^{x_w} \frac{S - \bar{S}}{\bar{S}} \cdot V dz dx \quad with \quad \bar{S} = \overline{\frac{\sum A \cdot S(t)}{\sum A}} \tag{4.4}$$

where S is the salinity, $\overline{S}$ is the weighted mean salinity over the section (($A = x \cdot z$) area) or the basin (($A = x \cdot y \cdot z$) volume) over the period from 1958 to 2009 and V is the volume transport defined in Equation 4.1. The Freshwater flux over the section was computed with equation 4.4 using the volume weighted mean salinity ($\overline{S}$) of the basin 35.069 psu (Table 4.7, SPNA). The difference between mean salinities $\overline{S}$ between the SPNA and the sections (Table 4.1) gives rise to freshwater transport differences of less than 1 $\%$, hence the $\overline{S}$ of the SPNA is used for all freshwater transport computations. The depth integral can be replaced by density both equations 4.3 and 4.4 (like in Equation 4.2).

section/basin	$\overline{S}$ [psu]
OSNAP	35.063
OSNAP EAST	35.11
OSNAP WEST	34.97
GSR	35.063
SPNA	35.069

Table 4.1: *Volume/area weighted mean salinities for the sections and the subpolar North Atlantic (definition Table 4.7).*

To compute water mass transformation rates and heat fluxes the Irminger basin and Iceland basin were further split by a section connecting the OSNAP line and Iceland along the Reykjanes Ridge (RR Figure 4.1, Basin definitions: Table 4.7). The northern boundary of the Labrador Sea was closed with a section through Hudson and Davis Strait. Volume, heat and freshwater proportions for each section were computed, subsequently the rates of the basins emerged from the transport calculations.

Chapter 2, figure 3 shows the model time-depth evolution of the annual potential temperature in the central Labrador Sea which reveals periods of enhanced and weak convection in the model. One period with weak deep convection (1968 - 1978) and one with strong convection (1988 - 1998) were defined to analyse their mean march mixed layer depth (MLD) at the GSR (Figure 4.4 a) and the OSNAP section (Figure 4.7 a) in conjunction with the strength of the currents at the respective section.

To study the connectivity of the basin balances and current transports in relation to the atmospheric forcing, in particular the NAO as major mode of atmospheric variability, spectral analysis was done for every density level for each current and basin as well as for the computed AMOC maximum time series at OSNAP, OSNAP EAST, OSNAP WEST and the GSR. Welch's method [*Welch*, 1967] with taper lengths of 25 years were used to estimate of the power spectral density. The confidence bounds are estimated through Monte Carlo approach with 1001 realizations of pure red noise (AR1 process) containing same auto-correlation, mean, variance, and data distribution as the data. The 95% confidence level and the 50% mean state where estimated for each time series to evaluate the significance of the respective spectral peaks. For comparability reasons only the significant frequencies (points) and the related peak (circle) are presented in the following (Figure 4.14).

For the spatial analysis of the principal components of all basin related transport time series and water mass transformations per basin empirical orthogonal function (EOF) [*Wilks*, 2011] analysis was performed. To prepare the time series for the EOF analysis, anomaly transport time series where computed by subtracting the respective climatology from 1958 to 2009. Since time series are dominated by inter-annual variability [*Handmann et al.*, 2018] a 12 month moving average was applied. Furthermore, the transport anomalies represent northward or southward transports, hence for easier interpretation of the EOF results the absolute time series had to be computed. The principal components and the EOFs are presented unscaled.

4.4 Results

4.4.1 Greenland-Scotland Ridge

The Greenland-Scotland Ridge (GSR) separates the Nordic Seas from the Atlantic Ocean. It is the major site of volume exchange between the Nordic basins and the Atlantic. The GSR acts as a sill for the waters formed in the Nordic Seas and mainly allows exchange of surface and intermediate waters. From east to west the model reproduces not only the upward sloping isopycnals but also captures the current structure at the GSR as it is known from observations (4.3 b,4.4 b) [*Hansen and Østerhus*, 2000; *Jochumsen et al.*, 2015; *Mastropole et al.*, 2017; *Rossby and Flagg*, 2012; *Østerhus et al.*, 2008, 2019]. According to the currents represented, the section was split into subsections (Figure 4.4 c, subsection intervals Table 4.8).

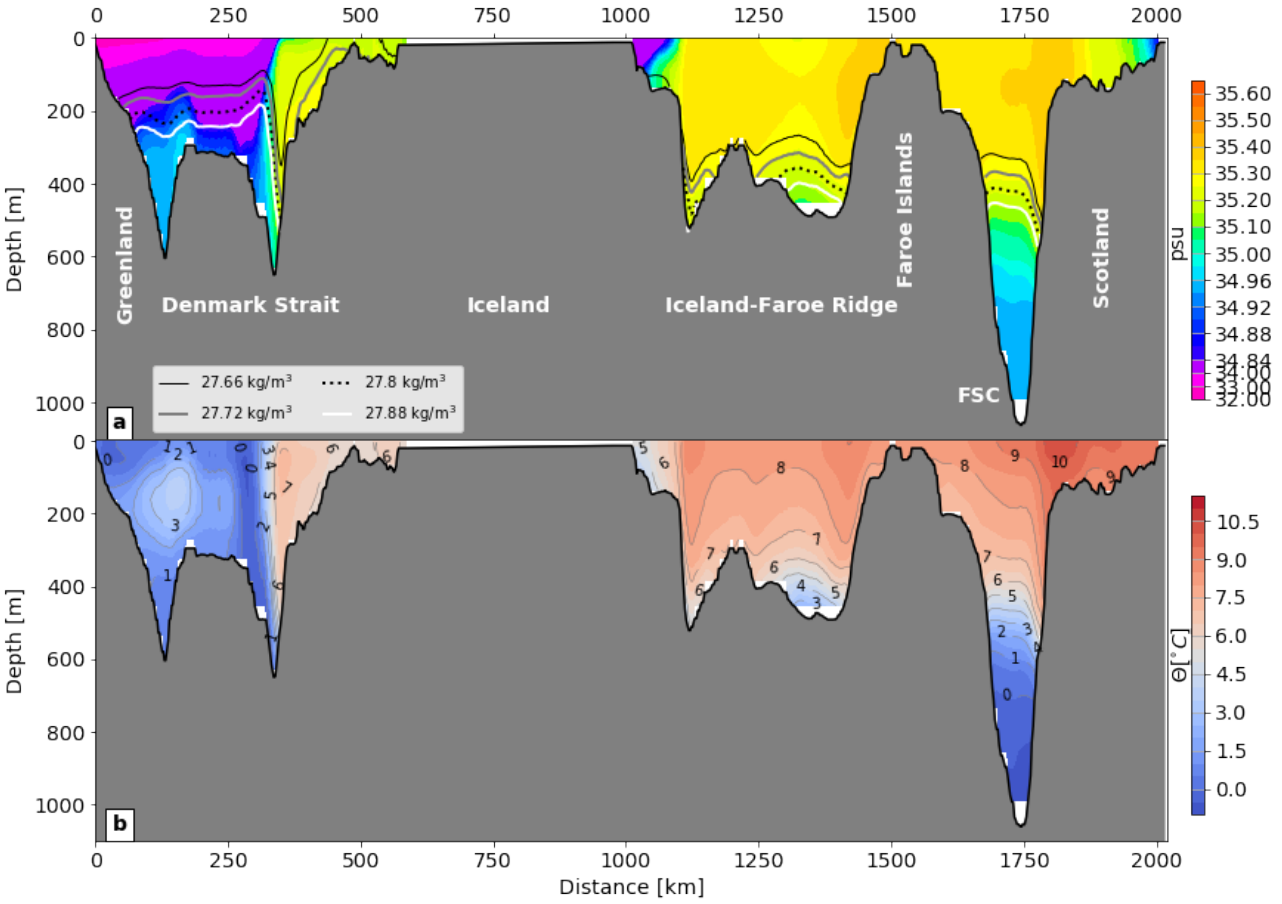

Figure 4.3: *Greenland-Scotland Ridge mean salinity (1958-209) a) and mean potential temperatures b). σ_0 isopycnals are marked in a) in contours.*

It simulates the northward slope current on the Scotland shelf break (the Shetland Branch (**SB**)) which carries warm ($\geq$ 6.5 $°C$) and saline ($\geq$ 35.25 psu) **NAC** water through the Faroe-Shetland Channel (**FSC**) and on the Scottish shelf (Figure 4.4). Further northward currents with similar temperature and salinity as the **SB**) are the two **NAC** branches of the Faroe Branch (**FB**) west of the Faroe Islands and east of Iceland and the northward Icelandic Irminger Current (**IIC**) west of Iceland. At these four locations where

the **NAC** passes the GSR northwards (Figure 4.4, **SB**, 2 branches of the **FB**, **IIC**) a very barotropic velocity structure persists with mean maximum velocities of 0.33 ± 0.07 m/s near the east Iceland shelf break (peak velocities of 0.6 m/s). The combined currents transport 10.6 ± 1.7 Sv northwards which accounts for a mean northward heat transport over the section of 0.35 ± 0.05 PW (Table 4.2).

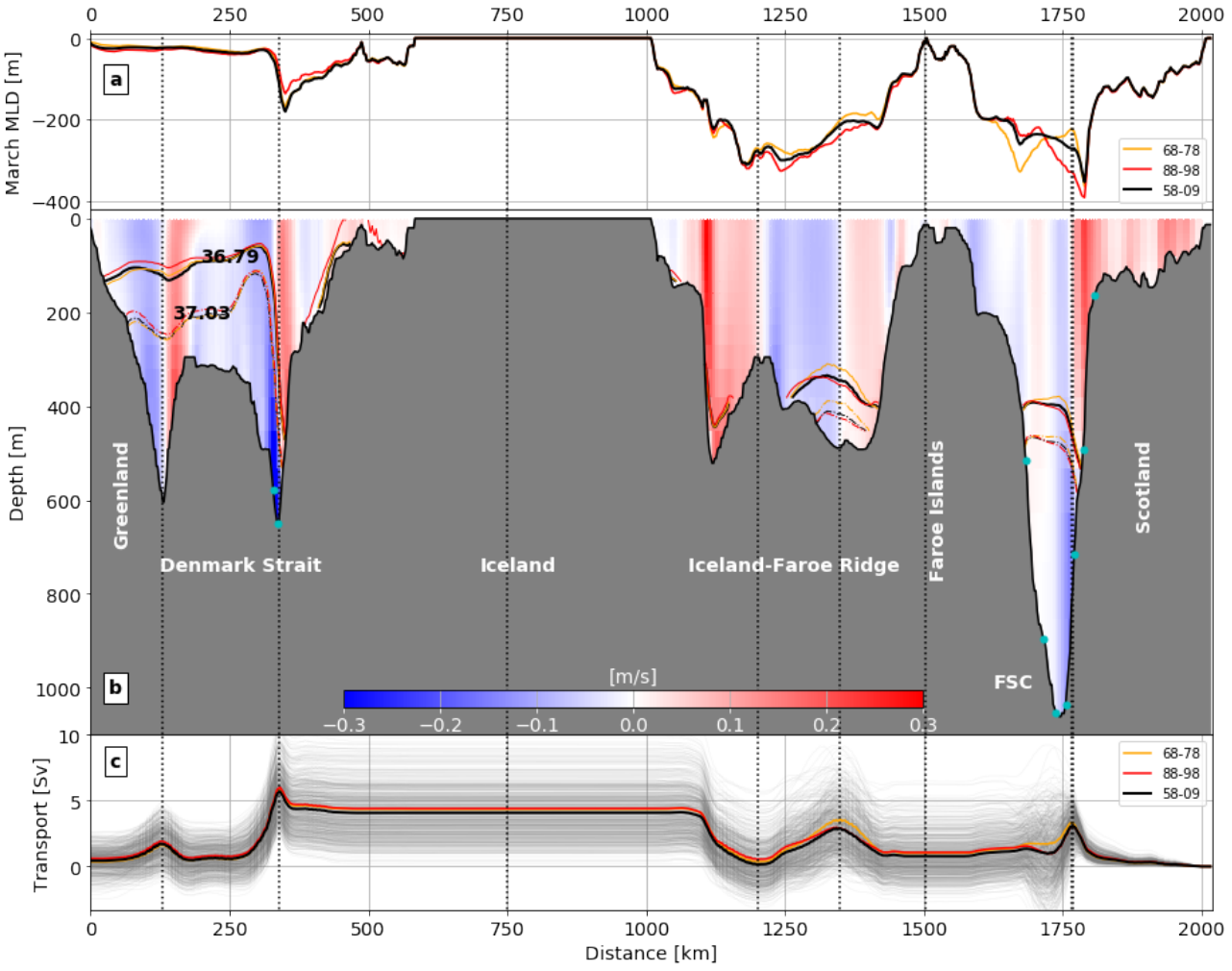

Figure 4.4: *a)The mean mixed layer depth in march for 3 temporal periods of the model run. b) mean velocity (1958 - 2009) along the GSR section with superimposed mean potential density $\sigma_2 = 36.79$ kg/m^3 (above upper AMOC) and $\sigma_2 = 37.03$ kg/m^3 ($sigma_2$-boundary between LSW and LNADW) and observational mooring positions [Berx et al., 2013; Jochumsen et al., 2012]. c) Monthly cumulative depth-integrated transports along the section from Scotland to Greenland (grey). Current separations are marked with dotted lines. Averaging periods for the respective variables are marked in black (1958 - 2009), orange (1968 - 1978) and red (1988 - 1998).*

Dense intermediate waters formed in the Nordic Seas then flow south through the Faroe-Shetland Channel (**FSC**),the Iceland-Faroe Ridge (**IFR**) (Iceland-Scotland Overflow Water or Northeast Atlantic Deep Water (NEADW)) and the Denmark Strait (**DS**) (Denmark Strait Overflow Water (DSOW)). The densest southward transports are found at depth in the Denmark Strait ($\leq$ 34.96 psu, $\leq 3\ ^{\circ}C$) and in the Faroe-

Shetland Channel (($\leq$ 35 psu, $\leq$ 4 $^{\circ}C$)). The water passing the Iceland-Faroe Ridge is more saline ($\geq$ 35 psu, $\leq$35.35 psu) and warm ($\geq$ 4 $^{\circ}C$) compared to the deep overflows of the **FSC** and the **DS**. Additionally, the cold and fresh surface current on the east Greenland shelf, the East Greenland Current (**EGC**) providing a pathway for the export of sea ice and runoff from the Arctic towards the south is featured in the model. The northward currents transport 10.6 ± 1.7 Sv and 0.35 ± 0.05 PW heat to the Nordic Seas. At the four sites of southward transport (**FSC**, **IFR**, **DS**, **EGC**) the water is generally colder and fresher than the surroundings. These currents account for a total southward transport of 10.2 ± 1.6 Sv and a southward meridional heat transport of 0.10 ± 0.05 PW, resulting in a net transport of 0.4 ± 0.9 Sv towards the north and a heat loss of 0.25 ± 0.05 PW north of the GSR section.

87% of the northward heat transport passes through the section east of Iceland (0.21 ± 0.05 PW). A mean southward freshwater transport of 0.11 ± 0.03 Sv over the GSR, with nearly equal parts passing through the Denmark Strait (0.05 ± 0.03 Sv) and the section between Scotland and Iceland (0.05 ± 0.01 Sv) was found (Table 4.2).

Section	Literature		VIKING20	
	MHT [PW]	MFT [Sv]	MHT [PW]	MFT [Sv]
GSR	0.264 ± 0.027[1]	-0.104 ± 0.01[1]	0.25 ± 0.05	-0.11 ± 0.03
	0.264 ± 0.027[5]			
	0.313[3]			
DS	0.022[3]		0.03 ± 0.01	-0.05 ± 0.01
		0.065 ± 0.011[4]		
	0.28 ± 0.08[2]			
ISR	0.29[3]		0.21 ± 0.05	-0.05 ± 0.03

Table 4.2: *Meridional heat (MHT) and freshwater transport (MFT) at GSR and the two subsections Denmark strait (DS) and Iceland-Scotland Ridge (ISR). Literature values from:* [1] *Chafik and Rossby [2019],* [2] *Jochumsen et al. [2012],*[3] *Østerhus et al. [2005],* [4] *de Steur et al. [2017],*[5] *Rossby et al. [2018]*

Within the observational uncertainties (due to instrument precision, methods and temporal variability) most of the model transports correspond very nicely to the values present in literature (Table 4.3 and 4.2). Two currents which exhibit major differences to the observed are the **FB** and the southward return flow of the **IFR**. Both of them exceed the observed values by ~ 2 Sv. This could be related to recirculation or meanders of the Faroe Branch over the Iceland-Faroe Ridge.

Section	Abbreviation	Literature [Sv]	VIKING20 [Sv]
Inflows :			
Shetland Branch	**SB**	$\sim 3.2 \pm 0.5$[1]*	3.0 ± 1.0
		3.7[8]	
		3[10]	
		2.34 ± 0.34[12]	
Faroe Branch	**FB**	3.8 ± 0.5[1]	6.0 ± 1.3
		3.3[8]	
		6[10]	
		4.46 ± 0.7[12]	
Icelandic Irminger Current	**IIC**	0.9 ± 0.1[1]	1.6 ± 0.3
		1[8]	
		1.04 ± 0.15[11]	
		0.88[12]	
Overflows :			
Faroe-Shetland Channel	**FSC**	2.2 ± 0.4[1]	2.2 ± 1.6
		2.2 ± 0.2[6]	
		2.7[9]	
		2.2 ± 0.2[12]	
Iceland Faroe Ridge	**IFR**	0.4 ± 0.3[1]	2.7 ± 1.0
		0.7[4]	
		0.8[5]	
Denmark Strait overflow	**DSO**	3.2 ± 0.5[2]	4.0 ± 1.0
		3.5 ± 0.5[3]	
		3.54 ± 0.16[11]	
Surface outflows :			
East Greenland Shelf	**EGC**	1.7 ± 0.2[1]	1.3 ± 1.0
		1.8 ± 0.5[7]	
		1.5 ± 0.16[11]	

Table 4.3: *Greenland-Scotland transports in Sv at the designated subsections (currents) (derived see section 4.3.2). Literature values from* [1] *Østerhus et al. [2019],* [2] *Jochumsen et al. [2017],* [3] *Harden et al. [2016],* [4] *Perkins et al. [1998],* [5] *Beaird et al. [2013],* [6] *Hansen et al. [2016],* [7] *de Steur et al. [2017],* [8] *Hansen and Østerhus [2000],* [9] *Berx et al. [2013],* [10] *Childers et al. [2015],* [11] *Harden et al. [2016],* [12] *Rossby et al. [2018]. *(Sum of Faroe-Shetland Atlantic and European Shelf inflow)*

During the period of enhanced deep water formation the mean march MLD is very similar to the mean and only small differences between this period and the weak deep convection period were found (Figure 4.4 a). The MLD is generally very shallow $\leq 400m$ at the GSR and the transports do not appear to be varying depending on the SPNA deep water formation activity (Figure 4.4 c and 4.5).

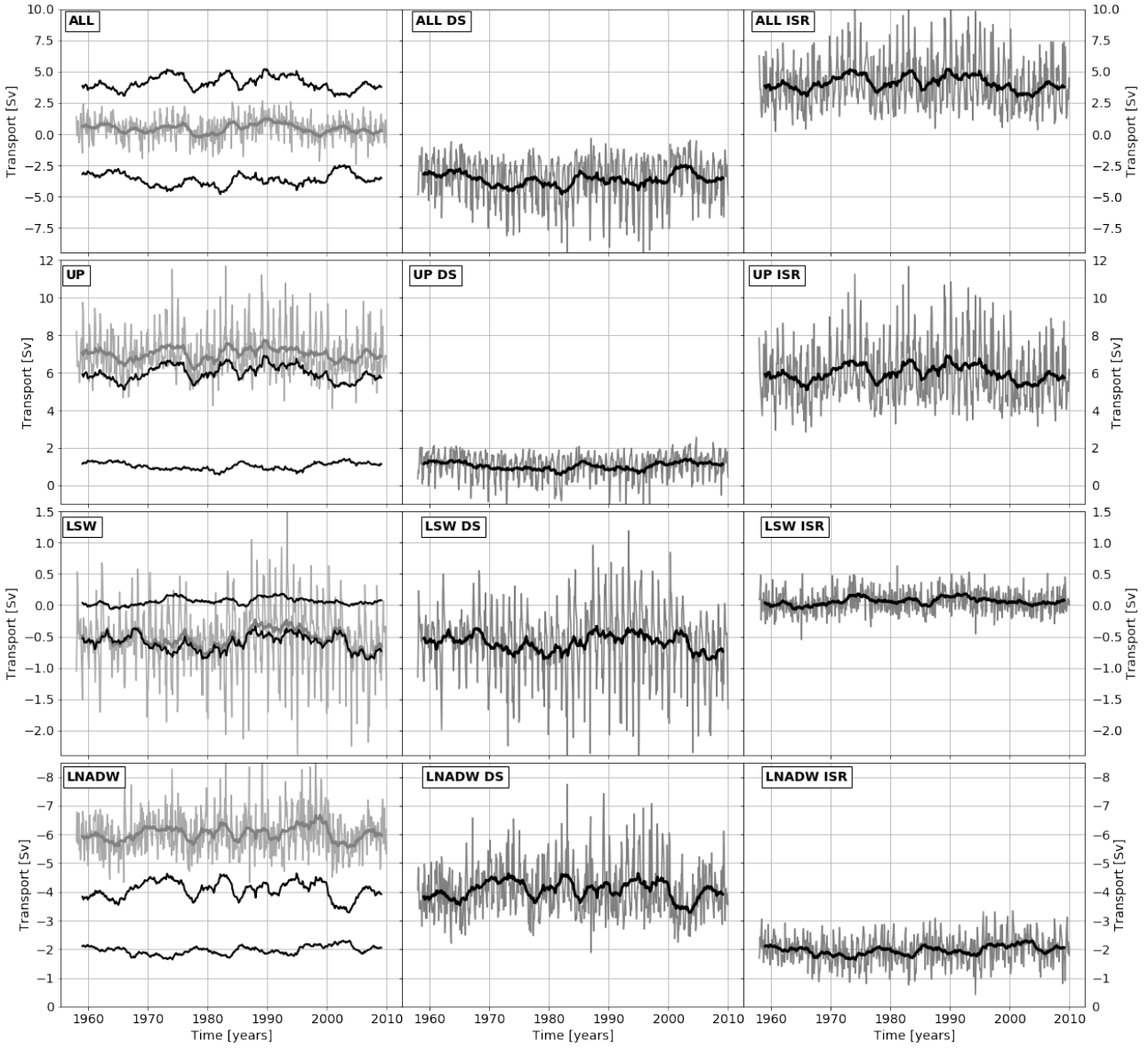

Figure 4.5: *From left to right the transport time-series at the GSR, DS and ISR section. The transports where computed for the entire water column (ALL) and the upper AMOC limb and LSW and LNADW water mass components at each respective section. The monthly mean values are depicted in grey and the 24 month running mean is marked in black/ dark gray. For comparison in the plots concerning the full GSR transport the time series of DS and ISR transport are also shown.*

The overall transport of the GSR section is 0.4 ± 0.9 Sv and the multi-annual variability is small (± 0.3 Sv). This is caused by opposing transports of the two subsections (DS and ISR) (Figure 4.5 top row). The net northward transport of upper AMOC water (7.0 ± 1.1 Sv) and its related transport variability is dominated on the monthly and multi-annual by the ISR section (6.0 ± 1.1 Sv)(Figure 4.5 second row). The net southward transport of LSW over the section is small (0.54 ± 0.53 Sv) and is dominated by the DS transports (0.6 ± 0.6 Sv). The Denmark Strait (4.0 ± 0.9 Sv) dominates the net southward LNADW transport (6.0 ± 0.7 Sv) towards the SPNA, with double the transport of the ISR (2 ± 0.7 Sv) (Figure 4.5 bottom row), which is comparable to observations (Table 4.3). Throughout the 50 years of model run the LSW and LNADW components appear fairly stable on longer time scales.

4.4.2 OSNAP

The North Atlantic current (**NAC**) brings warm and saline surface waters to the SPNA. The major part flows through the OSNAP EAST section east of the Reykjanes Ridge which is resulting in sloping isopycnals from east to west over the OSNAP EAST section [*Holliday N. et al.*, 2018; *Lherminier et al.*, 2010; *Lozier et al.*, 2019; *Mercier et al.*, 2015; *Sarafanov et al.*, 2012]. The model simulates upward sloping isopycnals from east to west with high salinities ($\geq$ 35 psu) and temperatures ($\geq$ 8.5 °C) mainly in the subsection east of the Reykjanes Ridge reaching to depths $\leq$ 1000m (Figure 4.6 b and 4.7). At OSNAP EAST all warm and saline northward currents, through the Rockall Trough (**RT**), the Hatton-Rockall-Plateau (**HRP**), the North Atlantic Current at the eastern Iceland basin (**NAC**) and the Irminger current on the western flank of the Reykjanes Ridge (**IC**) (Figure 4.7 b), transport 45.1 ± 6.1 Sv with an respective meridional heat transport of $1.14 + / - 0.15$ PW . Where 60% of the heat is imported through the east of the Reykjanes Ridge (0.71 ± 0.14 PW).

The East Reykjanes Ridge Current (**ERRC**) and the transports on the east Greenland shelf break constitute the main southward transports at OSNAP EAST. The transports on the east Greenland shelf are a combination of the shallow (≤ 500m), warm ($\geq$ 5-6 °C) and saline (~ 35.1 psu) Irminger current, the cold ($\geq$ 3 °C) and fresh ($\geq$ 34.84 psu) east Greenland shelf current and the DWBC (~ 35.0 psu, $\geq$ 3-4 °C) and will be called **EGC** in the following to facilitate the reading (Figure 4.6 b and 4.7). The southward transports through OSNAP EAST almost balance the OSNAP EAST inflow with $44.9 + / - 6.1$ Sv and a MHT of $0.79 + / - 0.14$ PW, where 80% of the heat are exported through the west of the Reykjanes Ridge (0.65 ± 0.08 PW). The net transport over the section is 0.3 ± 0.9 Sv with a related northward net heat transport of 0.35 ± 0.05 PW.

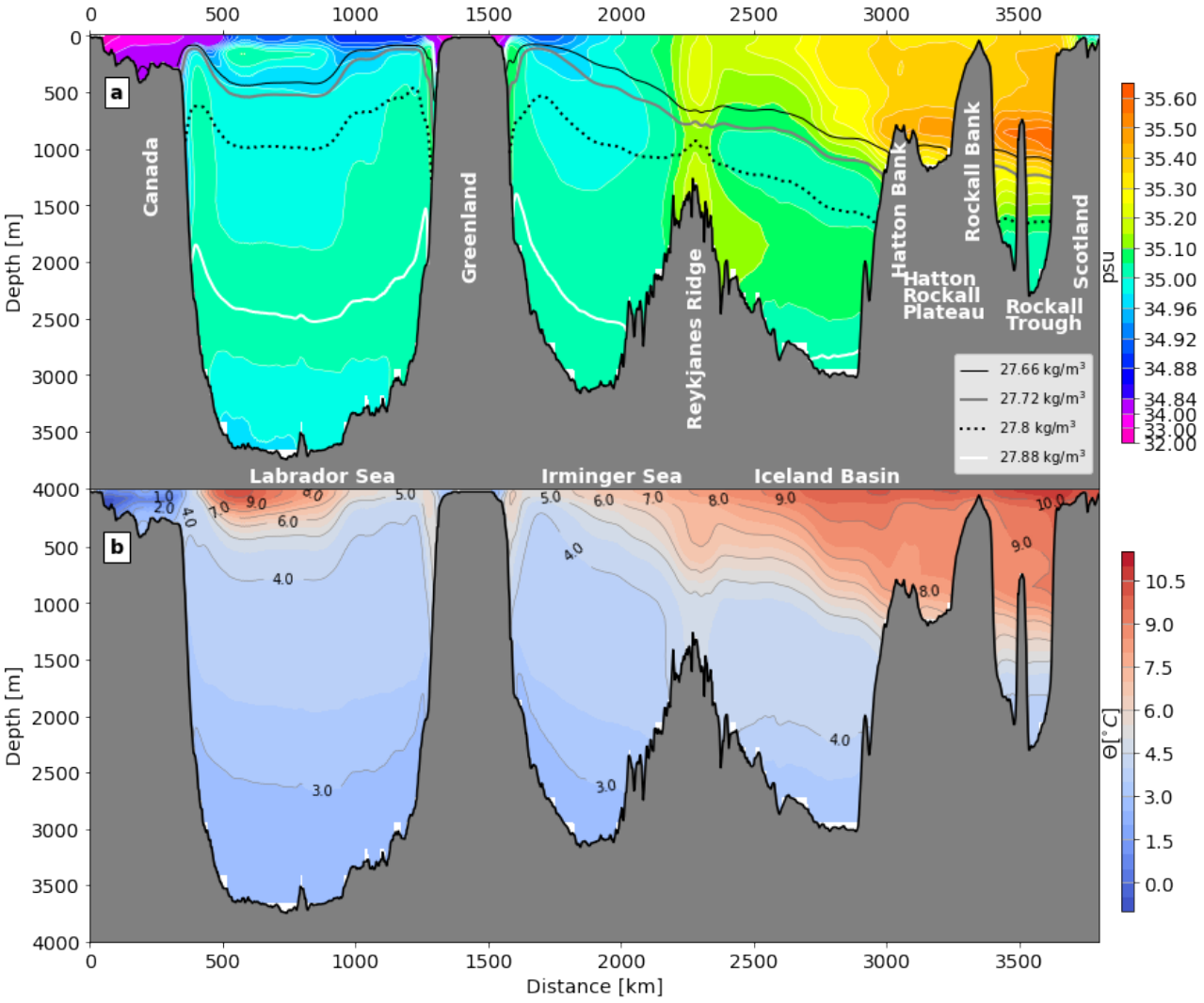

Figure 4.6: *OSNAP mean salinity (1958-209) a) and mean potential temperatures b). σ_0 isopycnals are marked in a) in contours.*

The warm and saline Irminger current hugs the west Greenland shelf in the Labrador Sea at similar depth as on the eastern Greenland side in the Irminger Sea. The cold and fresh east Greenland shelf current is as well featured on its western shelf with similar properties (Figure 4.6 b and 4.7). Additionally, the DWBC transports cold and fresh deep waters along the west Greenland shelf break into the Labrador Sea. All northwestward currents along the west Greenland shelf are called West Greenland Current (**WGC**) in the following. Additionally, there is a temporarily strongly varying import of warm ($\geq$ 9 °C) and saline ($\sim$ 35.1 psu) surface waters ($\leq$ 500m) in the south western interior part of the Labrador Sea (**LS int**) (Figure 4.6 b and 4.7 c). All currents bringing water to the Labrador Sea through OSNAP WEST, mainly the inflow of the **WGC**) and the inflow through **LS int** account for $38.0 + / - 5.1$ Sv and 0.67 ± 0.09 PW heat input to the Labrador Sea. The Export from the Labrador Sea, via the cold ($\leq$ 2 °C) and fresh ($\geq$ 34.84 psu) Labrador Current on the Labrador shelf (**LC**), the cold ($\leq$ 4 °C) and fresh ($\leq$ 35.05 psu) DWBC at the

Labrador shelf break (**LS**) and the interior (**LS int**), account for $40.0 + / - 5.1$ Sv and 0.54 ± 0.07 PW (Figure 4.6 b and 4.7). This reveals a net export of 2.0 ± 0.8 Sv and a net heat import of 0.13 ± 0.05 PW over the OSNAP WEST section.

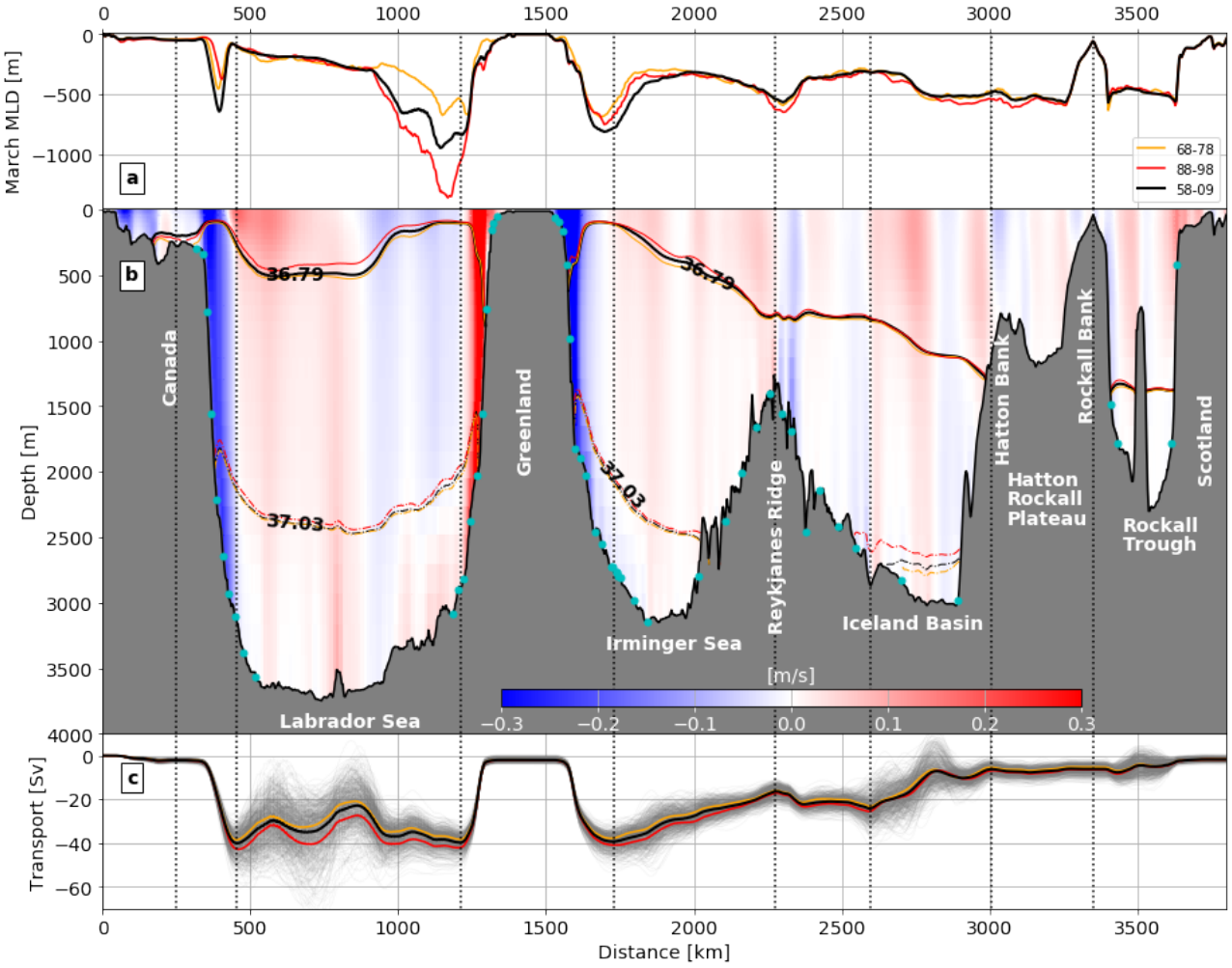

Figure 4.7: *a)The mean mixed layer depth in march for 3 temporal periods of the model run. b) mean velocity (1958 - 2009) along the OSNAP section with superimposed mean potential density $\sigma_2 = 36.79$ kg/m^3 (above upper AMOC) and $\sigma_2 = 37.03$ kg/m^3 ($sigma_2$-boundary between LSW and LNADW) and observational mooring positions [Berx et al., 2013; Jochumsen et al., 2012]. c) Monthly cumulative depth-integrated transports along the section from Scotland to Greenland (grey). Current separations are marked with dotted lines. Averaging periods for the respective variables are marked in black (1958 - 2009), orange (1968 - 1978) and red (1988 - 1998).*

The water mass occupying the major parts of the OSNAP section below 1000m is colder than 4 °C and has a salinity lower than 35.05 psu. In accordance with findings for the boundary currents by *Handmann et al.* [2018] the current structure is very barotropic over the whole section. There is a mean southward freshwater transport of 0.28 ± 0.05 Sv over the entire OSNAP section, with nearly equal parts passing

through the OSNAP WEST and EAST section (Table 4.4). The model meridional heat and freshwater transports for OSNAP,OSNAP EAST and OSNAP WEST correspond within their statistical uncertainties with literature estimates (Table 4.4).

Section	Literature		VIKING20	
	MHT [PW]	MFT [Sv]	MHT [PW]	MFT [Sv]
OSNAP	0.45 ± 0.02^{1}	-0.33 ± 0.01^{1}	0.47 ± 0.06	-0.28 ± 0.05
	0.33^{1}	-0.21^{1}		
	0.59^{1}	-0.45^{1}		
	0.39 ± 0.08^{3}	-0.21 ± 0.03^{3}		
	0.32 ± 0.13^{3}	-0.25 ± 0.08^{3}		
OSNAP EAST	0.38 ± 0.02^{1}	-0.14 ± 0.01^{1}	0.35 ± 0.05	-0.14 ± 0.03
	0.28 ± 0.06^{2}	0.17 ± 0.06^{2}		
	0.51 ± 0.08^{4}			
	0.399 ± 0.074^{5}	-0.20 ± 0.04^{5}		
		-0.20^{6}		
	0.55 ± 0.08^{7}			
OSNAP WEST	0.080 ± 0.004^{1}	-0.184 ± 0.004^{1}	0.13 ± 0.05	-0.14 ± 0.04

Table 4.4: *Meridional heat (MHT) and freshwater transport (MFT) at OSNAP and the two subsections OSNAP EAST and OSNAP WEST. Literature values from:*[1] *Lozier et al. [2019],* [2] *Bacon [1997],* [3] *Holliday N. et al. [2018],* [4] *Mercier et al. [2015],* [5] *Rossby et al. [2017],* [6] *Wijffels [2001],* [7] *Lherminier et al. [2010]*

In accordance with the currents represented, the section was split into subsections by using the local extrema of the cumulative transport along the section from west to east (Figure 4.7 c). The corresponding current transports correspond within their statistical variance with literature (Table 4.5). Only the **IC** west of the Reykjanes Ridge is ~ 10 Sv stronger, which in return is compensated by a similarly stronger **EGC**.

Section	Abreviation	Literature [Sv]	VIKING20 [Sv]
Inflows :			
Rockall Trough	**RT**	8.7 ± 1.4[1]	4.4 ± 1.9
		-2.8 ± 1.2[1]	
Hatton-Rockall-Plateau	**HRP**	-	0.11 ± 1.01
	HRP+RT	9.5[4]	
North Atlantic Current	**NAC**	~ 21.4[1] *	17.9 ± 4.9
		~ 25.9[1] *	
		~ 12[3]	
		15.5 ± 0.8[4]	
Irminger current	**IC**	13.6 ± 5.5[1]	22.7 ± 2.8
		12.0 ± 4.5[1]	
		12.0 ± 3[4]	
West Greenland Current	**WGC**	38.4 ± 2.8[1]	37.7 ± 3.5
		23.5 ± 4.3[1]	
Outflows :			
East Reykjanes Ridge Current	**ERRC**	16.0 ± 4.8[1]	7.6 ± 4.9
		10.8 ± 4.3[1]	
		10.5[4]	
East Greenland Current	**EGC**	27.0 ± 2.7[1]	37.2 ± 3.5
		23.5 ± 3.2[1]	
		32.1 ± 5.9[4]	
		34.4[5]	
		30.6[6]**	
Interior Labrador Sea	**LS int**	1.9 ± 13[1]	0.3 ± 3.2
		5.7 ± 12.0[1]	
DWBC western Labrador Sea	**LS**	41.9 ± 1.8[1]	37.9 ± 4.9
		30.8 ± 2.5[1]	
Labrador Current	**LC**	1[2]	2.1 ± 0.5
		2.7[2]	

Table 4.5: *Transport results from VIKING20 in comparison to literature values.* [1] *from [Holliday N. et al., 2018],* [2] *Wang et al. [2015],* [3] *Childers et al. [2015],* [4] *[Sarafanov et al., 2012],* [5] *[Rossby et al., 2017],* [6] *Lherminier et al. [2010],* both* **NAC** *components added from Holliday N. et al. [2018], **added EGIC and DWBC components*

The march mean MLDs of the periods with weak (1968-1978) and enhanced (1988-1998) deep water formation are overall for OSNAP EAST very similar to the 50 year mean (Figure 4.7 a). In the Labrador Sea a pronounced difference of $+\sim$ 500m (enhanced) and -$\sim$ 300m (weak) in comparison to the mean is featured by the model west of South Greenland. The OSNAP WEST section features this area as the

region of deepest convection. The MLD deepens in decades with stronger deep convection (down to ~ 1500 m) and gets more shallow in decades with shallower convection (down to ~ 700 m). Simultaneously, the strength of the boundary currents (**LS**, **WGC**, **EGC**) increases ($+ \sim 5$ Sv) or decreases (- ~ 3 Sv)(Figure 4.7 c).

The overall net transport of the OSNAP section is relatively stable at -1.7 ± 0.8 Sv. The magnitude is dominated by the net transport through the OSNAP WEST section (-2 ± 0.8 Sv) and the multi-annual to decadal variability is dominated by the OSNAP EAST section (Figure 4.8 top row) . The net import of upper AMOC water (20.9 ± 2.7 Sv) is dominated by the OSNAP EAST section (14.6 ± 3.1 Sv) whereas the multi-annual variability of the OSNAP upper AMOC import is low due to inverse of OSNAP WEST and OSNAP EAST variabilities (Figure 4.8 second row). The net transport of LSW is 15.4 ± 2.7 Sv southward over the section and is combined of similar parts through OSNAP EAST (7.3 ± 2.5 Sv) and WEST (8.12 ± 2.7 Sv) (Figure 4.8 third row). OSNAP EAST dominates the OSNAP export of LNADW to the south (7.0 ± 1.4 Sv, OSNAP WEST 0.2 ± 1.4 Sv, OSNAP 7.3 ± 1.4 Sv) (Figure 4.8 bottom row). In the 1980's the LNADW shows a regime shift to $+1$ Sv more export.

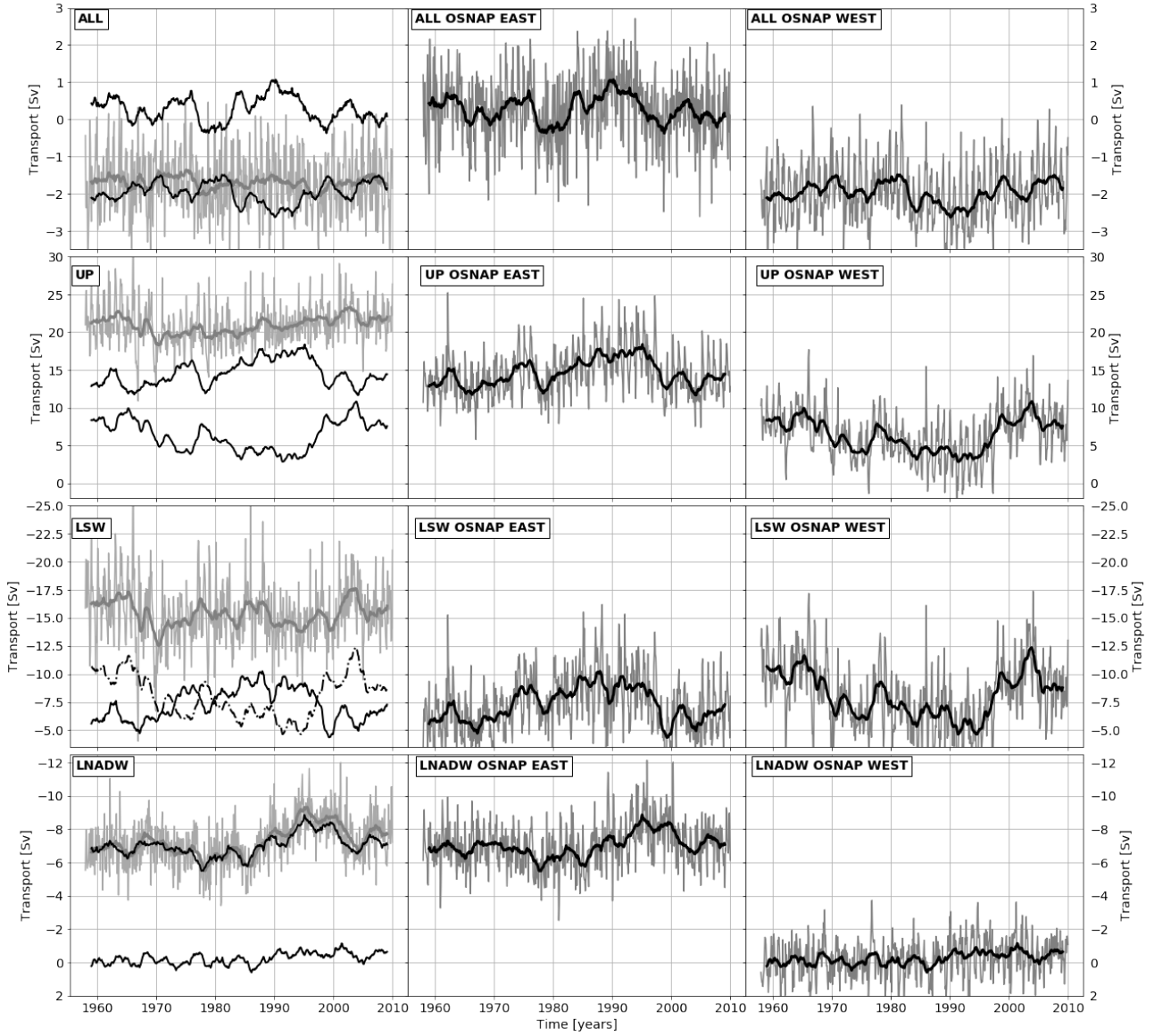

Figure 4.8: *Transport time-series at the OSNAP line, OSNAP EAST and OSNAP WEST section. The transports where computed for the entire water column (ALL), the upper AMOC limb, LSW and LNADW density classes. The monthly mean values are depicted in grey and the 24 month running mean is marked in black/ dark grey. For comparison in the plots concerning the full OSNAP transport the time series of OSNAP EAST and WEST are also shown.*

4.4.3 AMOC and water mass transformations

The AMOC strength in σ_0 density space over the OSNAP section (Figure 4.9, Table 4.6) ranges with 20.8 ± 3.0 Sv at $\sigma_0 = 27.73 \pm 0.04\ kg/m^3$ within the AMOC values found in literature:

- 14.9 ± 0.9 Sv [*Lozier et al.*, 2019] (OSNAP mooring line),
- 20.6 ± 4.7 Sv and 10.6 ± 4.3 Sv at ~ 27.7 [*Holliday N. et al.*, 2018] (ship sections along OSNAP).

For the OSNAP EAST section the AMOC strength is with 17.2 ± 3.0 Sv at $\sigma_0 = 27.65 \pm 0.06\ kg/m^3$ (Figure 4.9, Table 4.6) well comparable to literature:

- 18.1 ± 1.4 Sv (1993 -2010, shipboard sections, Ovide) [*Mercier et al.*, 2015]
- 16.5 ± 2.2 Sv at $\sigma_0 = 27.55\ kg/m^3$ (2002-2008 altimetry and hydrography at $59.5°$N)[*Sarafanov et al.*, 2012]
- 16.2 ± 0.8 Sv (2002 - 2016) (shipboard sections, Ovide) [*Perez et al.*, 2018]
- 18.4 ± 3.4 Sv at $\sigma_0 = 27.55\ kg/m^3$ (hydrography and shipboard ADCP, north of $58°$N) [*Chafik and Rossby*, 2019; *Rossby et al.*, 2017]
- 15.6 ± 0.8 Sv (2016-2018, OSNAP east moorings, Argo, Satellite data, Glider and World Ocean Atlas climatology) [*Lozier et al.*, 2019].

The overturning strength at the OSNAP WEST section in the model exceeds with 7.5 ± 3.2 Sv at $\sigma_0 = 27.74 \pm 0.21\ kg/m^3$ by a factor of 2-4 the majority of values found in literature:

- 3.9 Sv (Argo floats, hydrographic data AR7W line) [*Holte and Straneo*, 2017]
- 2 Sv (PALACE floats) [*Pickart and Spall*, 2007]
- 2.1 ± 0.3 Sv (OSNAP West moorings, Argo, Satellite data and World Ocean Atlas climatology) [*Lozier et al.*, 2019]

but fits the value of 7 Sv in a study by *Talley* [2003]. The maximum at the GSR line is found at 6.6 ± 0.9 Sv at $\sigma_0 = 27.73 \pm 0.06\ kg/m^3$, which fits nicely to the value of 7.7 ± 0.8 Sv derived by *Rossby et al.* [2018] .

Section	Depth		σ_0		σ_2 $[kg/m^3]$	
	[Sv]	[m]	[Sv]	$[kg/m^3]$	[Sv]	$[kg/m^3]$
OSNAP EAST	7.7 ± 1.4	836 ± 46	17.2 ± 3.0	27.65 ± 0.06	17.7 ± 3.0	36.66 ± 0.08
GSR	4.0 ± 0.8	329 ± 27	6.6 ± 0.9	27.73 ± 0.06	7.3 ± 1.1	36.8 ± 0.1
OSNAP WEST	1.1 ± 0.9	865 ± 473	7.5 ± 3.2	27.74 ± 0.21	9.7 ± 3.2	36.85 ± 0.06
OSNAP	8.6 ± 1.5	854 ± 35	20.8 ± 3.0	27.73 ± 0.04	22.1 ± 2.8	36.81 ± 0.06
RAPID	21.0 ± 2.8	1036 ± 74	21.2 ± 2.5	27.39 ± 0.63	21.3 ± 2.5	36.40 ± 0.85

Table 4.6: *AMOC maximum at the different sections*

The AMOC strength in density space at RAPID at $26.5°$N and at OSNAP have a similar magnitude throughout the model run (Figure 4.10 b). In depth space they appear very different in magnitude due to the stronlgy sloping isopycnals in the SPNA as explained above. Furthermore, the interannual to multi-annual variability is strongly affected by the calculation in depth or density space(Figure 4.10). A seasonal cycle of $\pm \sim 4$ Sv is featured in all σ_0 AMOC time series ,apart of the GSR, whereas in depth space, apart from the RAPID AMOC, they appear with a rather small ($\pm \sim 1$ Sv) or no seasonal cycle (Figure 4.10 c and d). Surprisingly, the AMOC time series exhibit a sudden shift of ~ 2 Sv towards greater transports in the beginning of the 1980's. This shift is not featured at the GSR section AMOC which is rather stable over the entire model run (Figure 4.10 b).

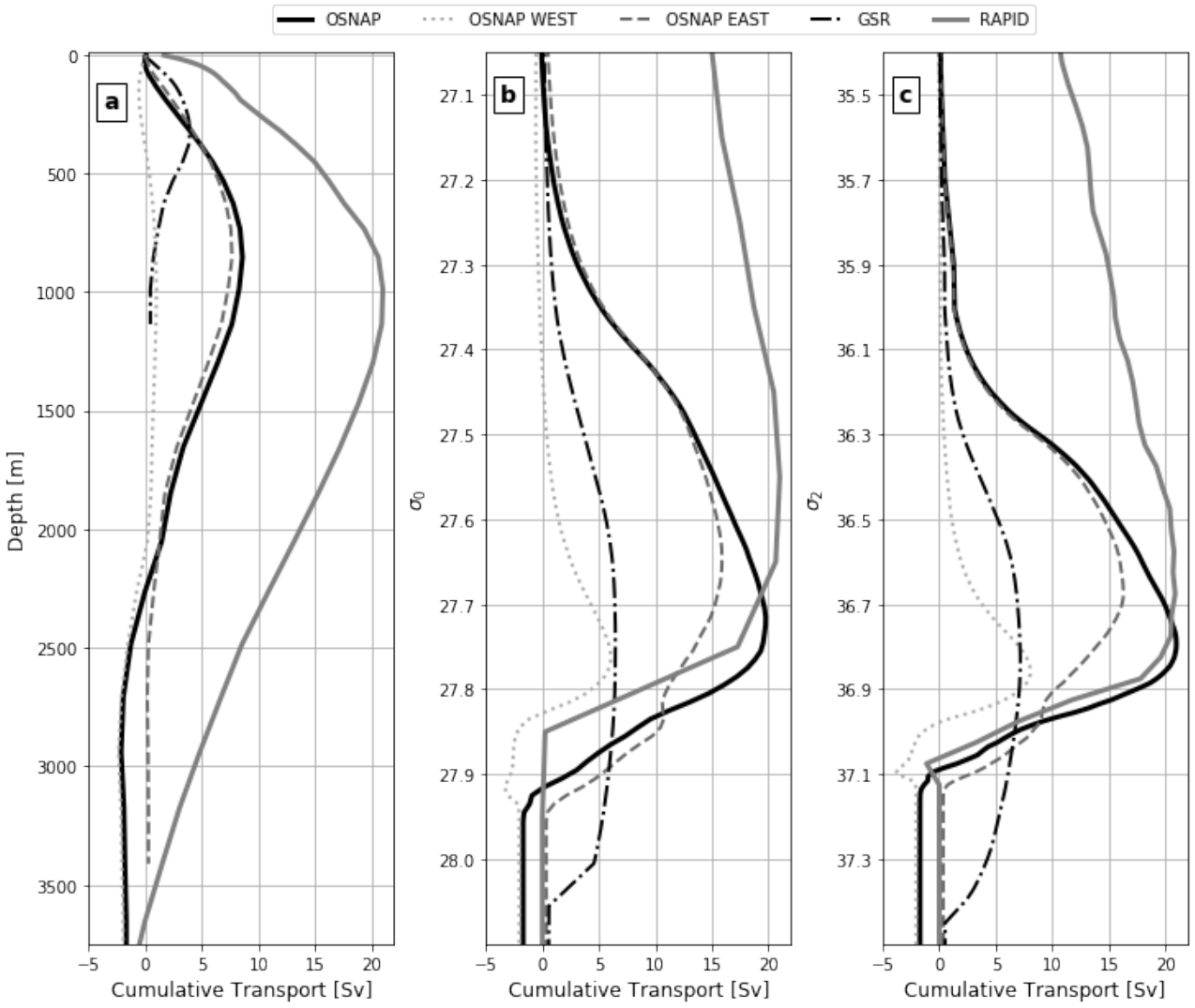

Figure 4.9: *Mean AMOC computed from the output of the VIKING20 model (1958 - 2009): cumulative sum from the surface towards the bottom. a)Depth space, b) σ_0-density space, c) σ_2-density space.*

In the following the subpolar North Atlantic is decomposed into the three basins: the Labrador Sea, the Irminger Sea and the Iceland basin to compute the heat loss from the basin and the volume and heat fluxes between the three density levels: upper AMOC limb, the LSW and the LNADW component. The basins are presented in order from east to west. As explained above, the transports were calculated for the single currents crossing the OSNAP and the GSR line. To close the basin budgets, additionally heat and volume transports were calculated through a section along the Reykjanes Ridge (10.1 ± 2 Sv, 9.1 Sv [*Sarafanov et al.*, 2012], 9.6 ± 2.1 and 13.8 ± 2.1 [*Lherminier et al.*, 2010]) and through the Davis Strait (2.3 ± 0.7 Sv, 2.6 ± 1.0 Sv [*Cuny et al.*, 2005], 1.6 ± 0.5 [*Curry et al.*, 2014]), where the model values align with literature.

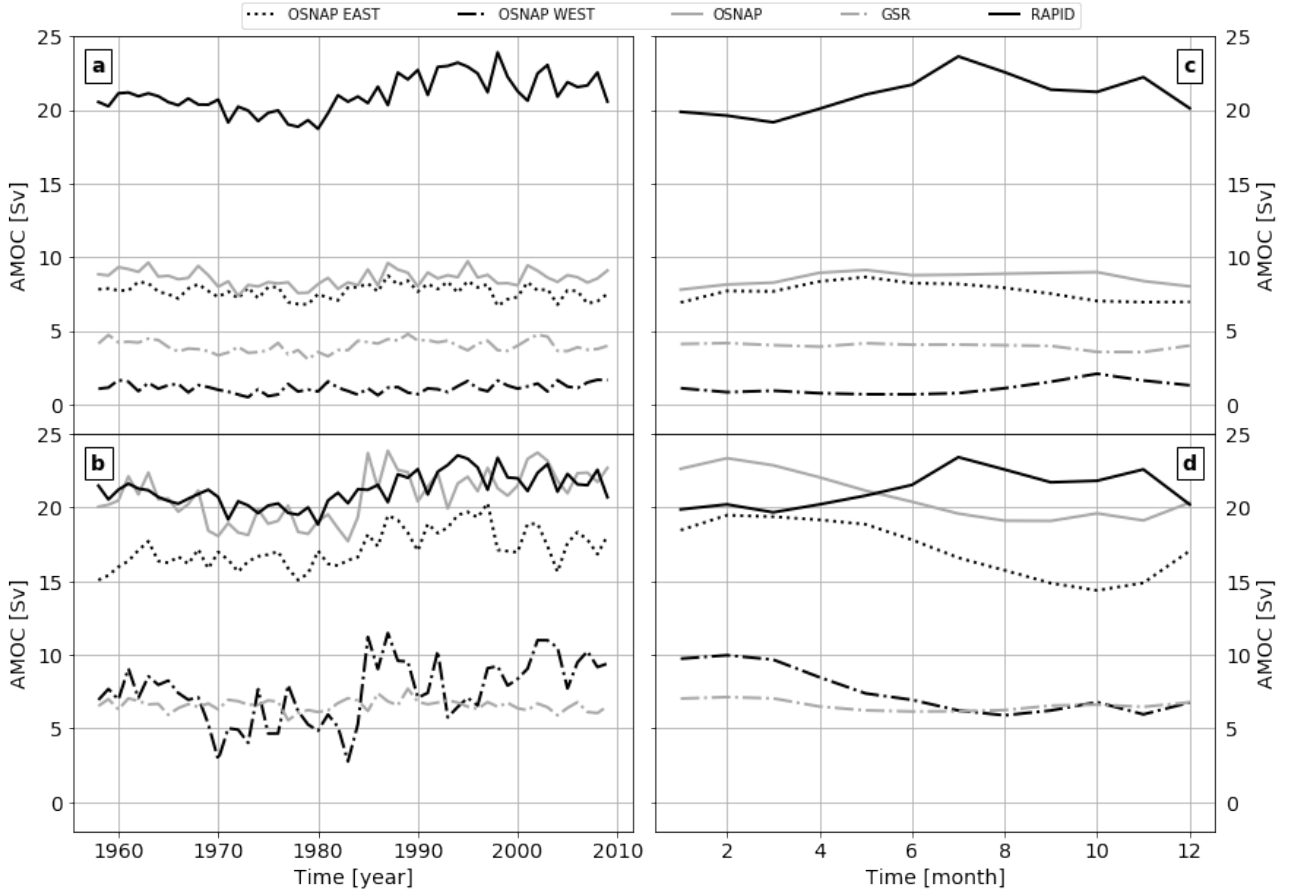

Figure 4.10: *Annual means (1958 -2009) of the AMOC at 26.5 °N at Rapid, at OSNAP EAST and WEST and the entire OSNAP and GSR section in depth space a) and in σ_0 density space b). c) and d) show the annual climatology of the AMOC at the different locations in depth and density space.*

The Iceland basin shows a net import of upper AMOC water of 3.7 ± 1.0 Sv (**NAC**,**RT**,**HRP**) (Figure 4.11 b) and a net import of LNADW (**FSC**,**IFR**) of 2.1 ± 0.5 Sv (Figure 4.11 b, d), which nearly compensated by the export of LSW (5.1 ± 1.2 Sv) (Figure 4.11 c). The water of the LSW density class is formed in the Iceland basin through heat loss of the upper AMOC limb and hence LSW formation and through mixing and stirring of LNADW with lighter water. The basin loses 0.07 ± 0.04 PW of heat (Figure 4.12 a).

The Irminger basin exhibits a similar net import of upper AMOC limb water as the Iceland basin (3.9 ± 3.1 Sv) (Figure 4.11 b). This import is nearly balanced by the combination of the net exports of LSW (1.6 ± 2.8) and LNADW (3.1 ± 1.5 Sv) (Figure 4.11 c, d). This basin loses about 0.03 ± 0.05 PW of heat to the atmosphere (4.12 a). The transport and heat balance suggests that upper AMOC water is transformed to LSW and LSW is transformed via mixing and stirring to additional LNADW.

The Labrador Sea exports on average 2.0 ± 0.8 Sv through the OSNAP WEST section (Figure 4.11 a). The two additional Sverdrups are related to the flow on the Labrador shelf which is alimented through the northern boundary of the Labrador Basin, the Davis Strait and Hudson Bay (2.3 ± 0.7 Sv) (Figure 4.11 a). This water from the Canadian Archipelago only imports 0.02 ± 0.01 PW (0.018 ± 0.017 PW [*Cuny et al.*, 2005]) of additional heat to the Labrador Sea (Figure 4.12 a). Adding this additional volume and heat transport to the transports through the OSNAP WEST section, the net heat loss of the Labrador Sea becomes 0.10 ± 0.04 PW (Figure 4.12 a). Hence, the Labrador Sea looses as much heat as the Irminger and Iceland basin combined. This correlates to the basin exports of LSW, where equally much LSW is formed in the Labrador Sea (7.7 ± 3.0 Sv) as in the two other basins (6.7 ± 2.9 Sv) (Figure 4.11 c). In the Labrador Sea LSW is formed through the transformation of upper AMOC water solely (7.4 ± 3.0 Sv; Figure 4.11 b, c).

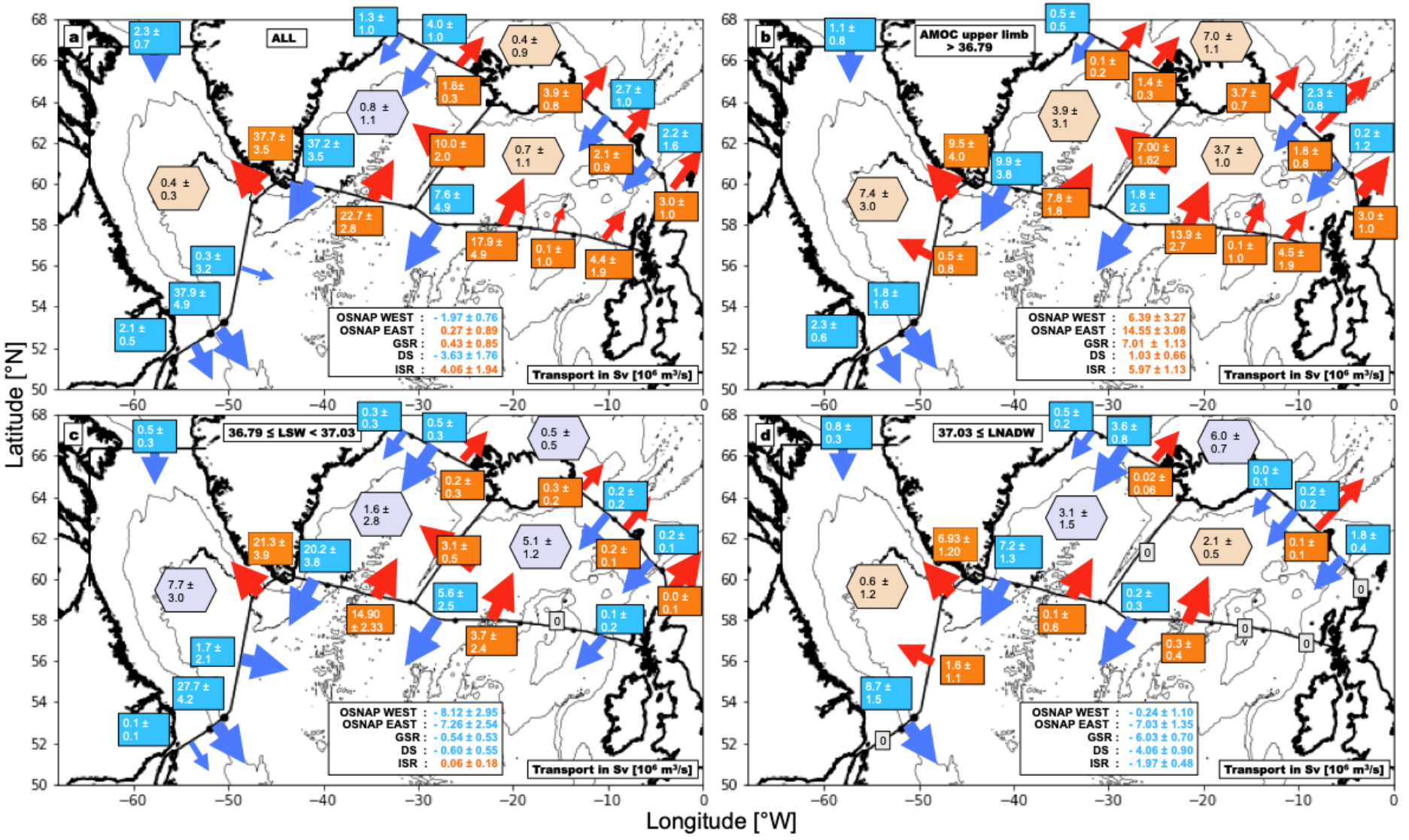

Figure 4.11: *Mean volume transports in Sv (1958-2009) for each section and subsection. The spacial extend of the subsections are marked with bullets. Northward transport and net inflow are marked in orange/red and southward and net outflow are marked in blue. The box shows the net flow over the respective section. a)Entire water column transports, b) Upper AMOC limb transports, c)LSW density class transports, d) LNADW density class transports. The arrow at the Davis strait sums all transports over the northern boundary of the Labrador Sea and implies input to the Labrador Sea.*

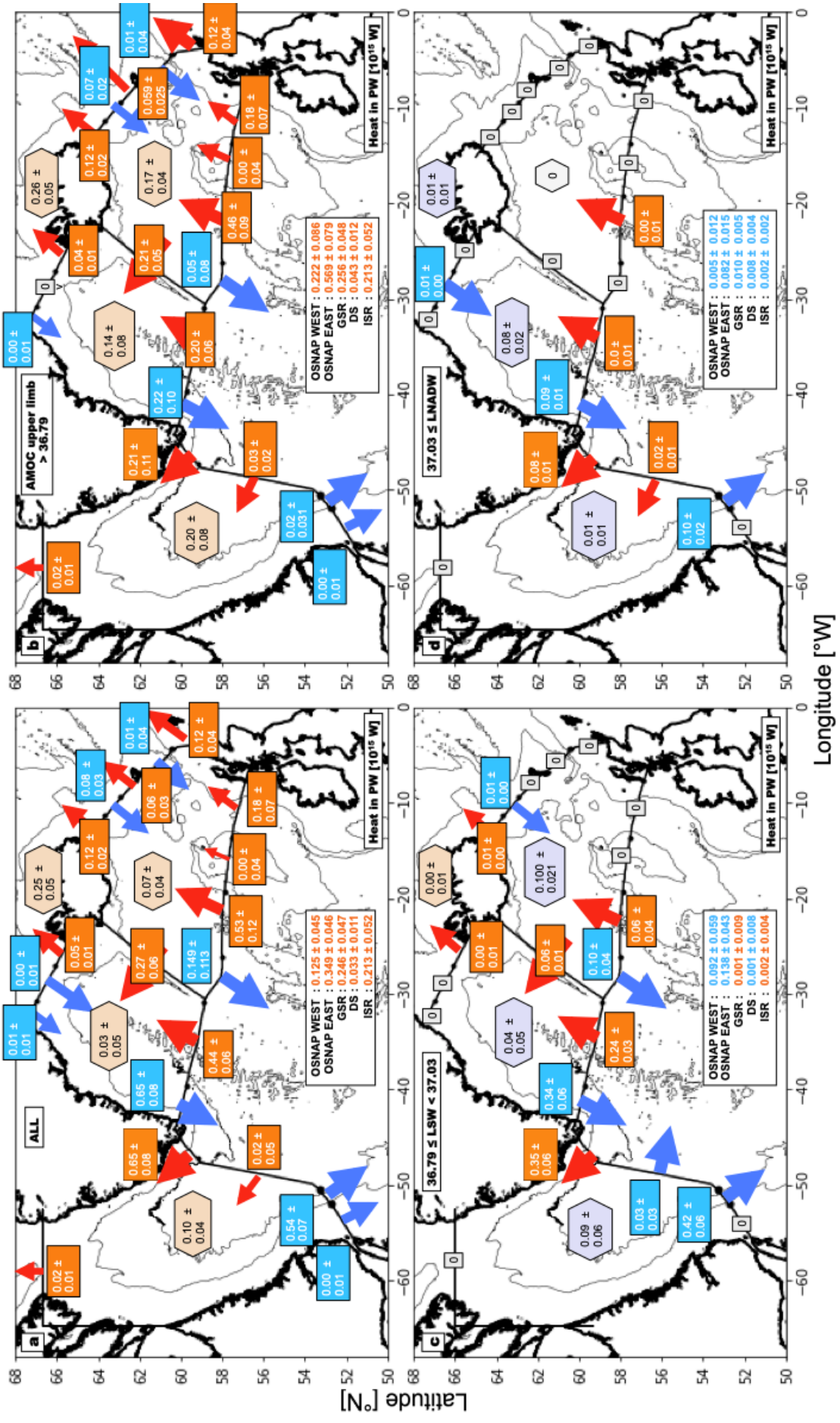

Figure 4.12: *Mean meridional heat transports (MHT) in PW (1958-2009) for each section and subsection. The map is organized as figure 4.11. a)Entire water column, b) Upper AMOC limb, c)LSW density class, d) LNADW density class.*

For periods of strong deep convection, the MLD in the Labrador Sea was found to be deepened southwest of Greenland along the OSNAP WEST section along with enhanced transport in the boundary currents (**LS**,**WGC**,**EGC**). The relation between deep convection years to the overall heat transports over the OSNAP EAST, WEST and GSR section were evaluated for the three defined density levels in the following (Figure 4.13). The heat transport anomalies a rather small (± 0.02 PW) at the GSR section and the supply of heat to the Nordic Seas is rather stable and dominated by the upper AMOC component (Figure 4.13 a). The heat transport anomalies at OSNAP EAST are twice as strong as at the GSR section (± 0.05 PW). The upper AMOC component shows a positive anomaly during the decade of deep convection. This anomaly is dominated by the heat flux through the Iceland basin (Figure 4.13 b). At the OSNAP WEST section the upper AMOC limb and the LSW have a comparable influence on the overall heat anomaly transport through the section (Figure 4.13 c). Contrary to the evolution at the OSNAP EAST section the upper AMOC limb transports less heat to the Labrador Sea during the enhanced convection period and as expected the LSW transports more.

To study the connectivity of the single calculated basin balances and current transports in relation to the atmospheric forcing, here the NAO, spectral analysis was done for the AMOC strength and the currents and basin balances in the three density classes (Figure 4.14). Welch's method was used to estimate the power spectral density. Because the interest was to enhance the understanding of the basin scale connectivity, only periods longer than 5 years were analyzed. Because the spectra were dominated by annual peaks, the time series were smoothed by a 12 month low pass filter prior spectral analysis. Since the comparison of this many spectra is challenging, I chose to only present inherent significant frequencies of each spectra (black dots figure 4.14). The respective spectral peak for each time series is marked with a circle in figure 4.14.

A significant frequency interval of variability, at longer than 5 years, is found between 12 to 20 years. These decadal periods are found in all density levels for almost all transport and AMOC time series. The NAO computed from the model forcing shows a significant peak at ~ 8 years which is not found in any of the analyzed model transports, basin balance or AMOC time series. The wind stress as well as the wind stress curl were calculated from the model output but their power spectra did not contain any significant peaks at longer time scales than 5 years.

To enhance the understanding on how the different currents interact and cohere, EOF analysis was performed for all 4 sets of transport time series (whole water column, upper AMOC limb, LSW and LNADW). The resulting principal components (PC) where then again subject to spectral analysis to estimate the main frequencies inherent to the principal components. The third EOF modes explain at their best $5 - 15\%$. Due to the complexity of the interaction of many processes like mixing and stirring through eddy activity, atmospheric forcing through winds and radiation and the varying input of the **NAC** to the subpolar North

Atlantic the third modes were not invariably interpreted but are shown for completeness. In the resulting EOF maps the colored points represent the strength of the EOF of the related current. The current positions are represented as in figure 4.11 and 4.12 and were defined as explained above.

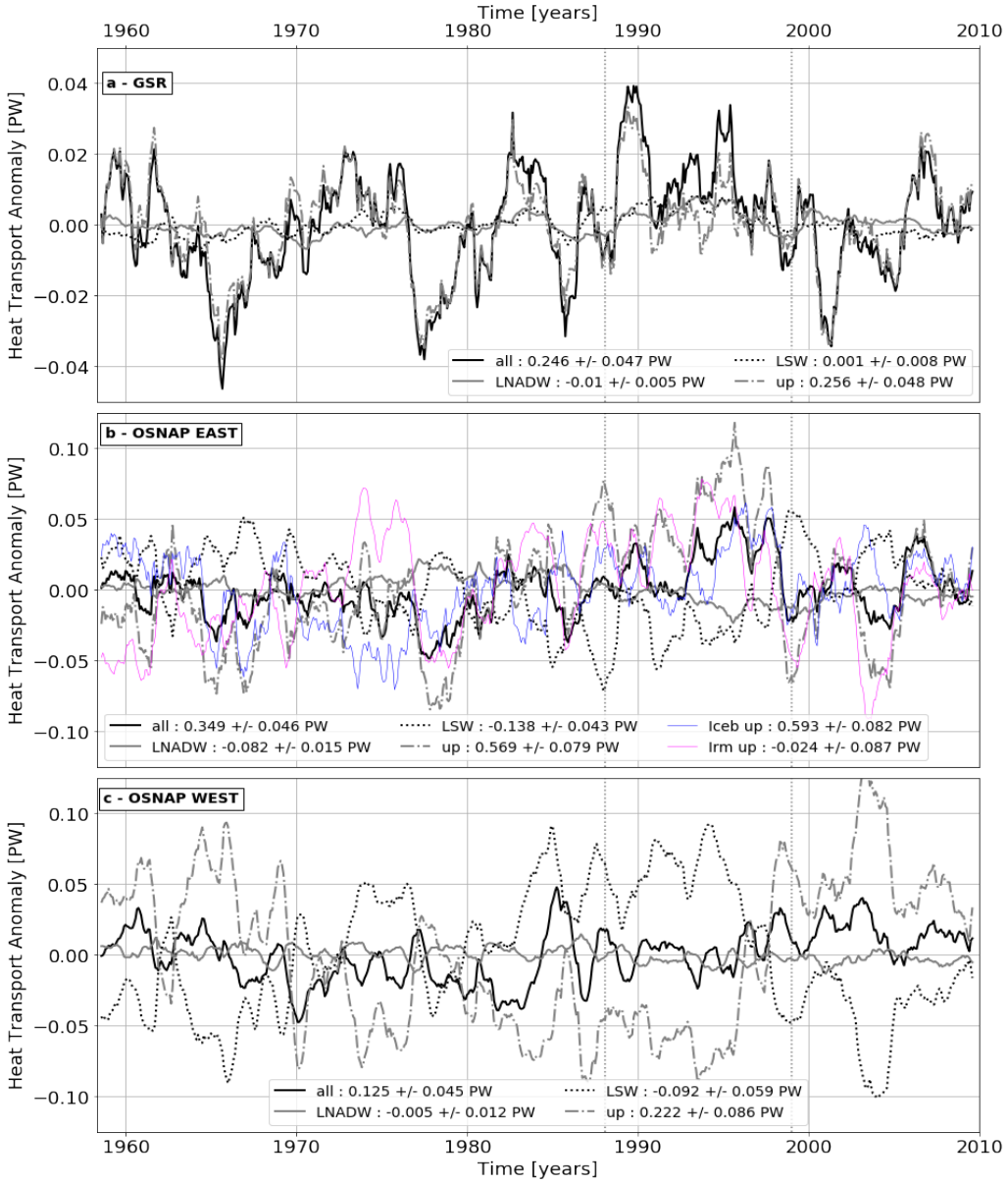

Figure 4.13: *Time series of heat transport anomalies filtered with an annual moving average at the GSR a), OSNAP EAST b) and OSNAP WEST c) section. Positive anomalies denote times of more heat input and vice versa. The legend boxes show the mean values for the respective density class. For the OSNAP EAST section the upper AMOC transport was further decomposed to the Irminger Sea (Irm) and Iceland basin (Iceb). The respective deep convection decade 1988-1998 is marked with two grey dotted lines within all panels.*

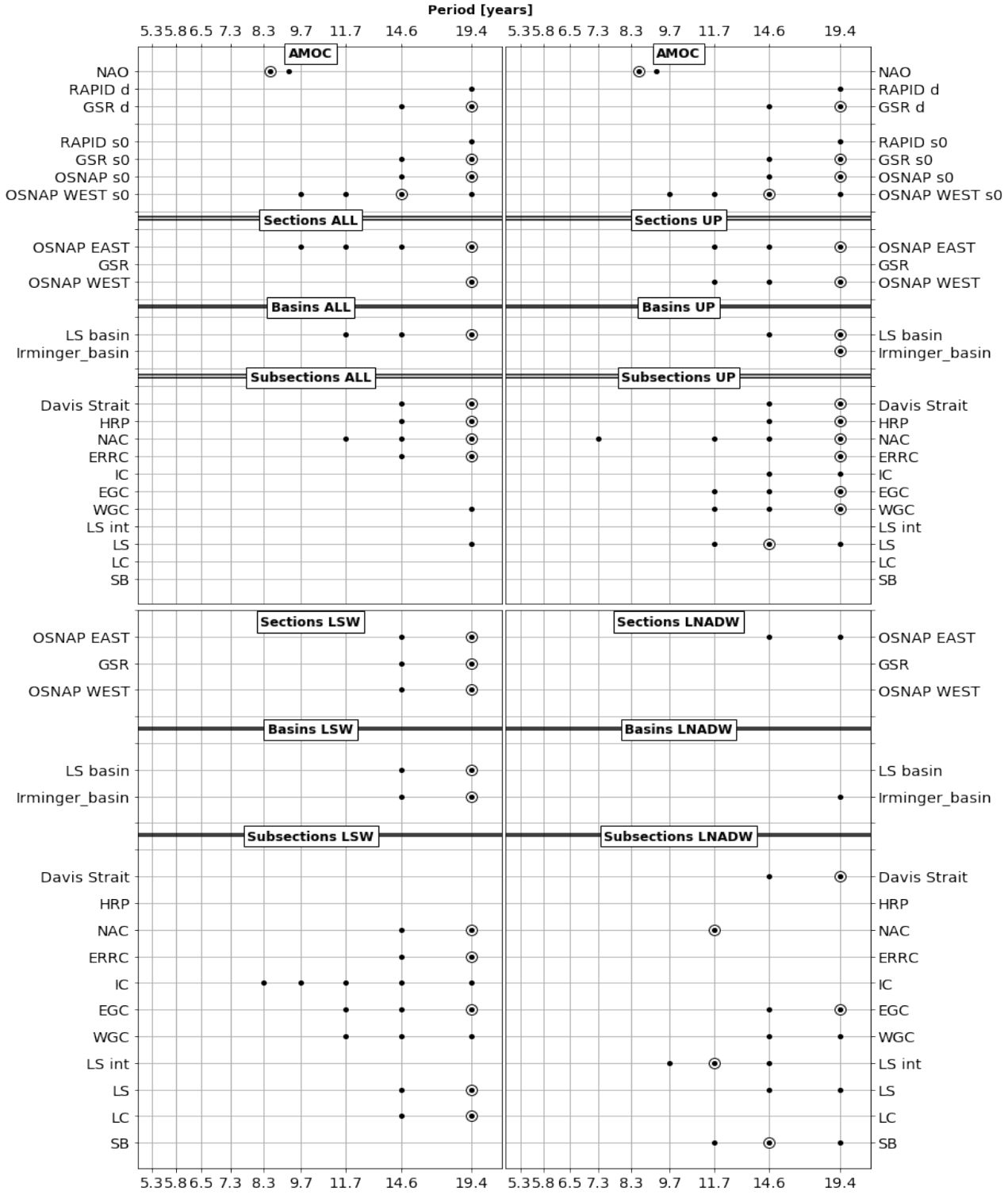

Figure 4.14: *Normalized Spectra of all transport and AMOC time series, the basin balances and the NAO. Significant periods greater than 5 years are depicted with black dots. The respective peak in the spectrum is marked with a black circle. Please find a detailed explanation of this graph in the text above. Abbreviations as in table 4.5 and 4.3. The AMOC time series are named as the respective section and the ending d stands for desity space and s0 for σ_0-space AMOC calculation.*

The upper limb EOFs show a first major mode in the **NAC** region that explains 45% of the total variance(4.15). It suggests a dominance of the **NAC** related import to the region for all upper AMOC transports in the basin and the DWBCs. The estimated PC1 spectrum shows peaks at ~ 5 and ~ 15 years (Figure 4.19 a). The second mode, explaining 23% of the total variance, is confined to the boundary currents and shelfs. It could be related to the pulsating polar outflow of melt water through the Hudson Bay and Davis and Denmark Strait. The related PC shows a seasonal cycle and contains significant frequency peaks at ~ 4 and ~ 10 years (Figure 4.19 b).

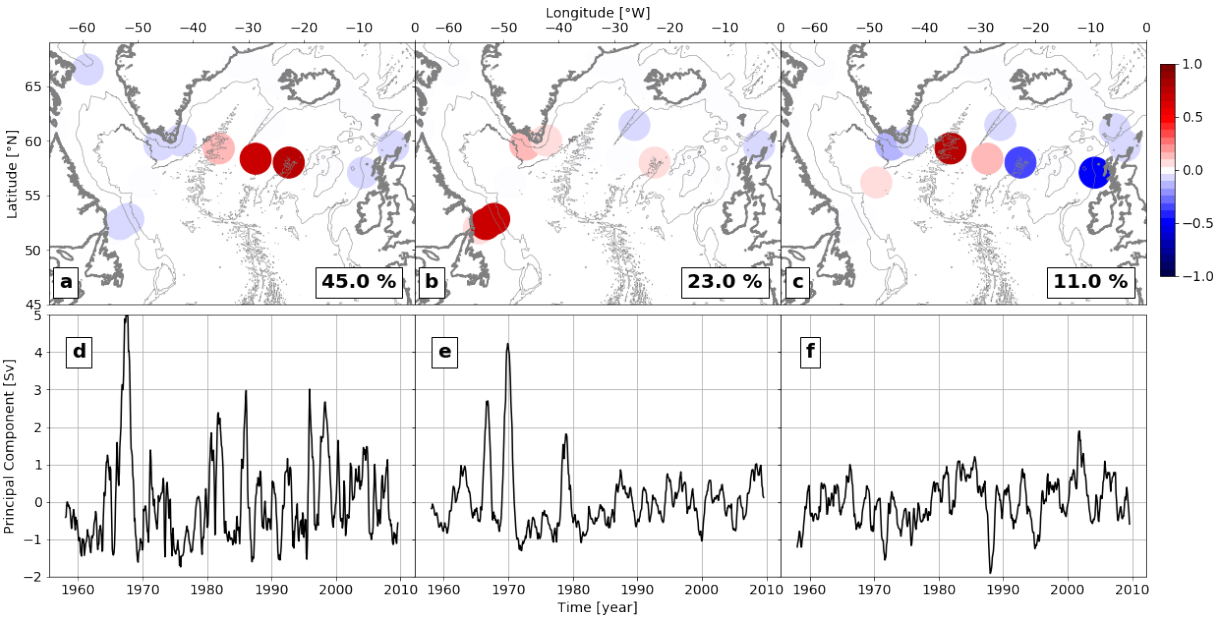

Figure 4.15: *Upper AMOC limb transport EOFs (upper panels) and their respective principal component (lower panel)(a and d, b and e and c and f). All time series at the locations depicted in figure 4.11 where used for the analysis. The EOFs and PCs are computed as described in section 4.3.2. Find related principal component spectra in the Appendix figure 4.19.*

The first LSW EOF mode represents a dipole in the Labrador Sea, explaining 51% of the variance (Figure 4.16 a). Due to the seasonality of its PC (Figure 4.16 d) it could be interpreted as the convection signal. Water mass transformation in the Labrador Sea can possibly lead to this pattern of less import through the **WGC** to the Labrador Sea and more export of LSW through the **LS**. The second EOF mode, which explains 26% of the overall variance could be interpreted as a Irminger Sea - Iceland basin dipolar mode (Figure 4.16 b). The PC of this mode peaks at ∼15 years (Figure 4.20 a).

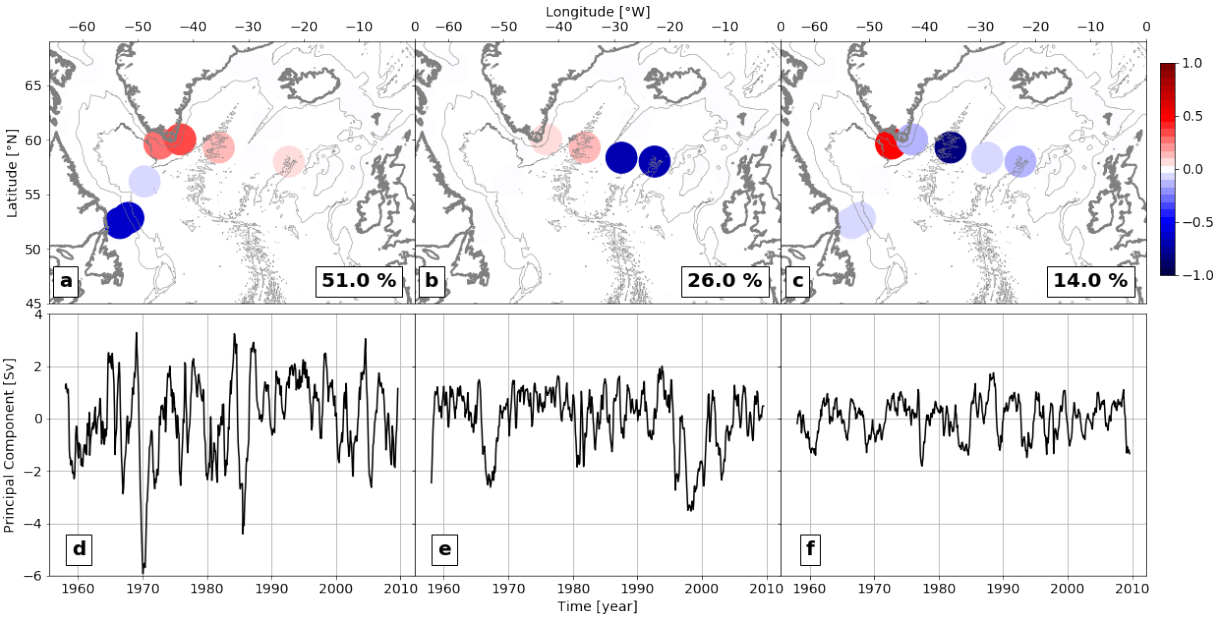

Figure 4.16: *LSW transport EOFs (upper panels) and their respective principal component (lower panel)(a and d, b and e and c and f). All time series at the locations depicted in figure 4.11 where used for the analysis. The EOFs and PCs are computed as described in section 4.3.2. Find related principal component spectra in the Appendix figure 4.20.*

The first LNADW EOF mode is explaining 67% of the total variance (Figure 4.17 a) and resembles the first mode found for the LSW EOFs (Figure 4.16 a). The Denmark Strait and the related **EGC** transports are in phase whereas the Labrador Sea export represents the counter part. This mode could be related to reservoir changes of LNADW in the Labrador Sea. The related PC spectrum shows peaks at 2 and 4 years (Figure 4.21 a). Contrary the second mode (17% of total variance) is an in phase mode of the overflows (**DSO**,**FSC**) and the Labrador sea interior (Figure 4.17 b). Here the overflows, the **EGC** and the central Labrador Sea are coherent and the related PC spectrum peaks at 12 years (Figure 4.21 b).

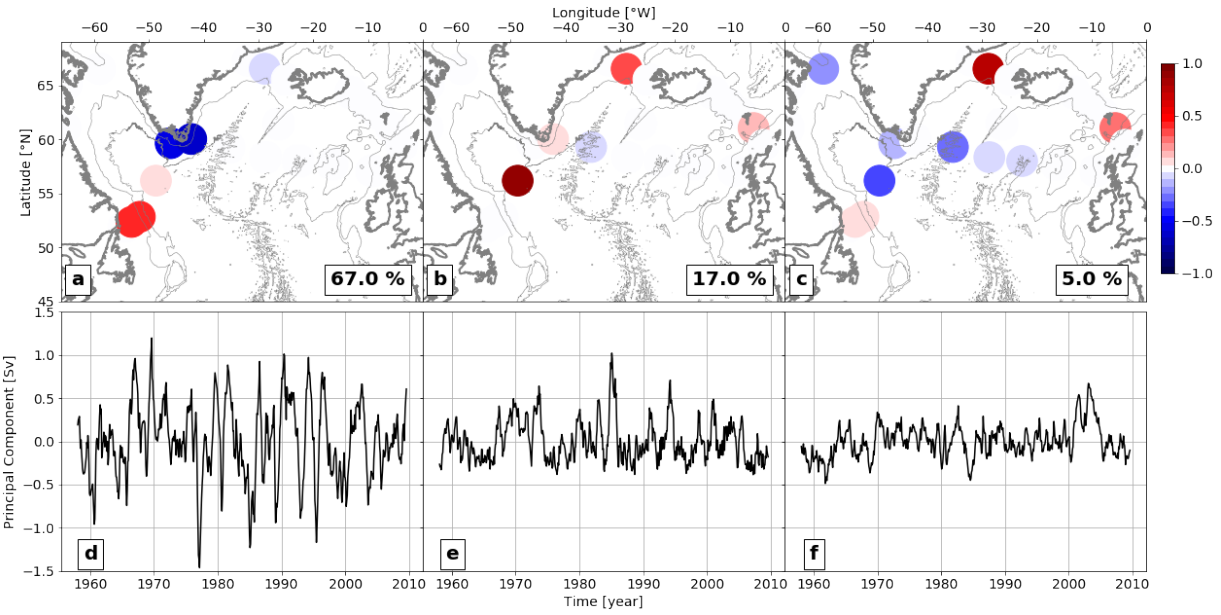

Figure 4.17: *LNADW transport EOFs (upper panels) and their respective principal component (lower panel)(a and d, b and e and c and f). All time series at the locations depicted in figure 4.11 where used for the analysis. The EOFs and PCs are computed as described in section 4.3.2. Find related principal component spectra in the Appendix figure 4.21.*

The first EOF mode for the top to bottom transports represents the subpolar North Atlantic gyre mode, where the Irminger and Labrador Sea are coherent (Figure 4.18 a). This mode is found to be constrained mainly to the west of the Reykjanes Ridge and it explains 43% of the total variance. Its PC spectrum peaks at 5 and 15 years (Figure 4.22 a). The second EOF mode could be named **NAC** mode, since all currents strongly connected to the **NAC** dynamics are coherent (Figure 4.18 b). Additionally, the Irminger and Labrador Sea form a dipole like spacial pattern. The PC spectrum of this mode, which explains 33% of the total variance peaks at 20 years (Figure 4.22 a).

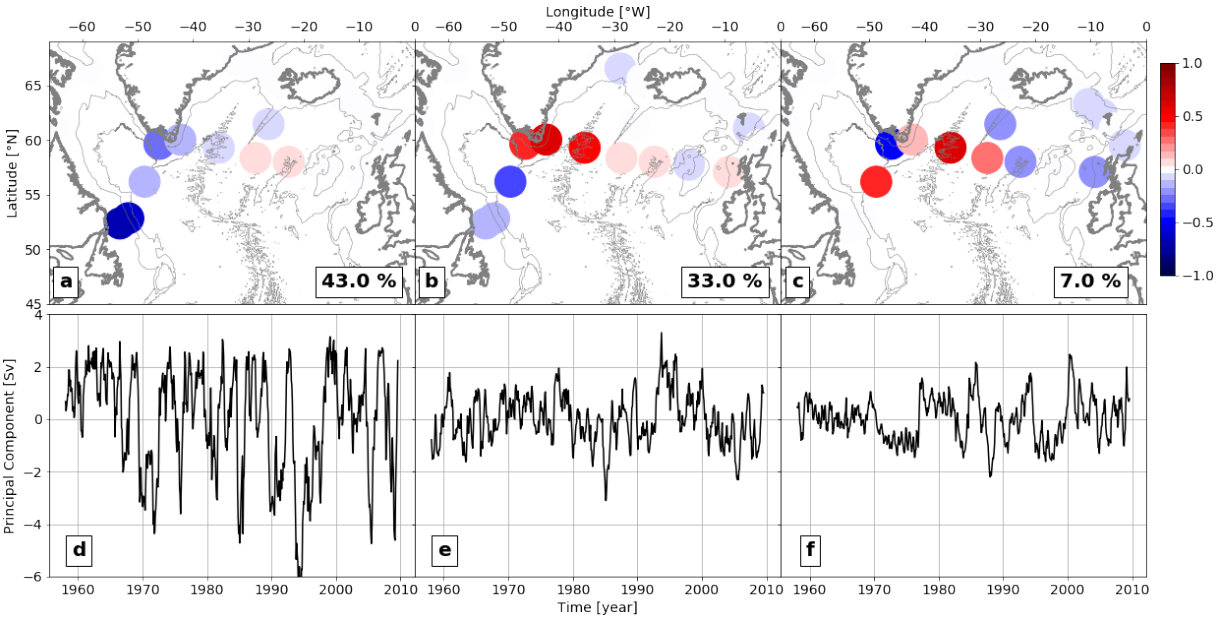

Figure 4.18: *Top to bottom transport EOFs (upper panels) and their respective principal component (lower panel)(a and d, b and e and c and f). All time series at the locations depicted in figure 4.11 where used for the analysis. The EOFs and PCs are computed as described in section 4.3.2. Find related principal component spectra in the Appendix figure 4.22.*

4.5 Discussion and Conclusions

This chapter evaluates the model representation of the AMOC at two sections in the subpolar North Atlantic. All net heat, freshwater and volume transports across the sections and the respective currents as well as the ratios of the three SPNA basins were computed and presented. Circulation elements all over the SPNA and possible links between them were compared for three density levels and the AMOC maximum was analyzed through spectral Analysis. Additionally, an EOF analysis was performed with all currents and the basin balances.

The magnitude and relative location of the currents in the VIKING20 model were assessed. The model reproduces the magnitude of the AMOC in both, the subpolar North Atlantic and at $26.5°$N (the RAPID array), compared to values published during the past 10 years (Table 4.6) [*Buckley and Marshall*, 2015].

The comparison of modeled AMOC at $26.5°$N with the subpolar AMOC across the OSNAP array indicates meridional coherence of the subpolar versus the subtropical AMOC (Figure 4.10), but only on decadal to multidecadal timescales. On short time scales the AMOC at RAPID and at OSNAP do not resemble each other strongly, thus RAPID can not be assumed to represent the AMOC at the subpolar latitudes [*Baehr et al.*, 2009]. The overall standard deviations of ± 3 Sv over the 50 years plus the variability on longer time scales of model AMOC imply that observational time series, in order to distinguish the strong seasonality and decadal variability from actual trends need to be continued for the next decades. Taking the AMOC as an oceanic key component in climate, the shorter time scales may not be as important as the decadal to multidecadal variability, but variability on time scales less than a decade may mask the longer term AMOC evolution [*Biastoch et al.*, 2008]. Furthermore, the missing consensus of the actual strength and variability of the MOC in reanalysis/assimilation products and OGCMs [*Cunningham and Marsh*, 2010] supports the need for longer AMOC time series at different latitudes.

A substantial shift of the AMOC at RAPID and at the OSNAP line of 2 Sv was found in the model AMOC time series. This shift could be related to the addition of satellite based data to the forcing or it could be a part of longer time scale ($+$ 30 year) variability. The first satellite mission with radar was the SeaSat mission 1978 [*Gould et al.*, 2013]. Before the 1980's climatologies are used as forcing fields over the ocean basins in COREv.2. The influence of changing forcing variability on the large scale ocean circulation is known and possibly using OGCM data only from 1980 onward could enhance the trust in the model results [*Sweeney et al.*, 2005] but of course it would again shorten the time series of the output.

The AMOC time series contains, just as in the few available continuous observations, strong interannual variability [*Lozier et al.*, 2019; *McCarthy et al.*, 2015]. This annual peak is represented as well in nearly all model current transports at all three density levels. Spectral analysis revealed a common longer significant timescale of 15-20 years in almost all VIKING20 currents, the AMOC strength and the basin balances (Figure 4.14). The North Atlantic Oscillation as major mode of atmospheric variability in the region contains multi-annual to decadal ($\sim$ 8 -10 years) and multi-decadal ($\sim$ 30 years) variability [*Woollings et al.*, 2015; *Zantopp et al.*, 2017] (Figure 4.14) and was found to influence sea level and temperature records of the subpolar Northeast Atlantic [*Jevrejeva et al.*, 2006]. Since the time series of ocean model output is rather short (50 years) in comparison to the 20 year peak that this study found, an influence of the NAO on the transports in the SPNA through the model forcing is possible but hard to prove on these longer timescales.

The results showed a 10 Sv stronger **IC** at the western flank of the Reykjanes Ridge. Simultaneously, the export through the **EGC** was found to be 10 Sv stronger. The model **EGC** is higher than the lowest literature value but lies in the range of strong literature values observed (Table 4.6). Comparing the mean velocity fields to *Holliday N. et al.* [2018] the weaker recirculation in the central Irminger Sea becomes

apparent in the model, which could be related to the exceeding value of **IC** magnitude. The Faroe Branch and the transport at the Iceland Faroe Ridge are also both exceeding literature values by ~ 2 Sv (Table 4.3) but could be explained by the recirculation over the Ridge [*Fogelqvist et al.*, 2003]. In VIKING20 the LSW transports over the OSNAP EAST and WEST sections play similar roles for the overall variability of LSW transport over the entire OSNAP line, whereas OSNAP EAST is clearly imprinting the variability on the LNADW density class transports (Figure 4.8). The meridional temperature and freshwater transport across the OSNAP section and its respective two subsections are well represented in the model in relation to observational estimates (Table 4.4 and 4.2 ,Figure 4.12).

EOF analysis implied the same longer time scales of 20 years for the major spatial modes (Figure 4.15 a,c, 4.16 b,4.17 b and 4.18 a,b). These modes are spatial patterns related to the activity of the subpolar gyre west of the Reykjanes Ridge and the input of the **NAC** to the SPNA. Furthermore, the convection or overflow mode, relating more export on the LSW level in the **LS** to less LSW import through the **WGC**, features similar time scales in the spectral analysis of their PCs (Figure 4.16 a and Figure 4.17 a). These results suggest a dominance of annual and lower-frequency variability in the subpolar gyre *Bingham et al.* [2007]. The major spatial patterns coincide with the pattern of the subpolar gyre derived from SSH in observations by *Häkkinen and Rhines* [2004] and in the FLAME model by *Böning et al.* [2006]. These studies defined the respective principal component as "gyre index". *Häkkinen and Rhines* [2004] explained the decrease in the subpolar gyre index by a decreased geostrophic velocity and hence a declined subpolar gyre circulation during the 1990s (enhanced deep convection) compared to the 1970s and 1980s. In analogy with these papers, the results suggest a weakening of this index during years of deep convection (Figure 4.18 d) and additionally enhanced heat import through the **NAC** into the SPNA (Figure 4.13 b) and weaker heat import into the Labrador Sea (Figure 4.13 c). The SPNA west (Labrador and Irminger Sea) and east (Iceland basin) of the Reykjanes Ridge seem to feature a dipole like pattern during this period, with a dynamically more coherent western part. This behaviour is supported by the higher than normal input of heat through the Greenland-Scotland Ridge to the Nordic Seas (Figure 4.13 a); this may be an explanation for less input of heat through the upper AMOC branch to the Irminger and Labrador Sea during this period (Figure 4.13 b, c).

Contrary, the VIKING20 analysis of the MLDs at the sections in cohesion with the strength of the cumulative transports along the sections implied that the boundary currents (**LS**, **WGC**, **EGC**) are stronger in years with enhanced MLD depths, which was reported prior for a model study with $1/12^{\circ}$ FLAME [*Brandt et al.*, 2007]. This strengthening of the boundary currents during deep convection is in contradiction with two studies stating no significant changes in the southeastward transport at 53°N during years of deep convection in observations [*Zantopp et al.*, 2017] and VIKING20 [*Handmann et al.*, 2018]. This contradiction reopens the question of how the large-scale cyclonic circulation in the SPNA and deep convection are linked. On

the one hand, increasing density gradients from the basin interior to the boundary due to deep convection could lead to enhanced boundary currents through geostrophic adjustment. On the other hand, increased boundary currents in conjunction with the usual recirculation in the Labrador Sea could lead to enhanced EKE in the Labrador Sea facilitating deep convection.

One major difference in the analysis of the boundary current strength in terms of transport could be the definition of the spacial extend of the boundary currents. In this study the boundary current was defined as the local maximum in the cumulative transports, whereas in *Zantopp et al.* [2017] and *Handmann et al.* [2018] it was defined through the mean circulation pattern of multiple ship based sections and the respective mooring array at $53°$N and was hence spatially more constraint. Furthermore, a clear baroclinic structure of the DWBC is found in observations [*Fischer et al.*, 2004; *Zantopp et al.*, 2017] whereas the model is more barotropic and features a strong velocity gradient between boundary current and recirculation. Furthermore, the convective regions in the model are stretched along the Newfoundland and Greenland shelf break [*Handmann et al.*, 2018; *Holte and Straneo*, 2017]. The preconditioning for deep convection is marked by the cyclonic circulation introducing "doming" isopycnals which in turn bring weakly stratified waters of the interior close to the surface and weaken the stratification [*Marshall and Schott*, 1999]. If the recirculation is a number of cyclonic cells seaward of the DWBC, established through baroclinic instabilities of the boundary currents [*Brandt et al.*, 2004; *Eden and Böning*, 2002; *Rieck*, 2019] their interior paths can form a large scale anticyclonic circulation around the Labrador sea. Thus, the interior Labrador Sea is not doming, but downward displaced. Increased strength of the boundary currents could lead to enhanced formation of cyclonic recirculation cells between the boundary current and the recirculation in the Labrador Sea in the model which can facilitate deep convection along the shelf breaks. This leads to some speculation about where the convection preconditioning is most effective. Eddies shed from the boundary currents were previously described and found to be related to the strength of the boundary current [*Brandt et al.*, 2004; *Eden and Böning*, 2002]. These eddies were further found to propagate not far [*Chanut et al.*, 2008]. A model study with VIKING20X by [*Rieck*, 2019] found these kinds of eddies at all latitudes ($55°$ - $60°$N) along the Newfoundland shelf break but could only determine an influence on the MLD in the western part of the Labrador Sea. Further analysis would be needed to address the difference of the establishment of deep convection in the model compared to observations in relation to the subpolar gyre circulation strength. This is not facilitated by the challenge of measuring the spatial and temporal extend of deep convection near the boundary currents.

The amount of water transformed to the LSW density class in the Labrador Sea is with ~ 8 Sv within the broad range of literature values, where the formation rates vary strongly from 1-12.5 Sv dependent on the study [e.g.*Clarke and Gascard* [1983]; *Rhein et al.* [2002]; *Smethie et al.* [2000]; *Smethie Jr. and Fine* [2001]; *Worthington* [1976]] Here, I only utilized density criteria to define LSW and waived the potential

vorticity criteria (low PV). A similar amount of LSW density class water is formed in the Irminger Sea (~ 2 Sv) and the Iceland basin (~ 5 Sv) combined, which coincides with observational based values of 7.57 Sv for the two basins combined *Chafik and Rossby* [2019]. These LSW formation rates coincide with the heat loss to the atmosphere of the three basins, where the Labrador Sea looses as much heat as the Irminger and Iceland basin together. The heat loss to the atmosphere in the two SPNA basins (0.10 ± 0.05 PW) enclosed by OSNAP and the GSR coincides nicely with estimates in literature (0.122 ± 0.079 PW, *Chafik and Rossby* [2019]).

The analysis of freshwater and heat transports conducted in this study are done although the net transport over the sections was not zero due to the temporal resolution of the used model output. The model further contains a trend in SSH due to freshwater input through precipitation, ice melting and river run off throughout the model run. This additional freshwater is not distributed evenly over the SPNA [*Dorman and Bourke*, 1981] which can lead to different net transport behavior in the different basins. Furthermore, the flow over the European shelf, the English Channel and the Nordic Sea were neglected (~ 0.1 Sv, [*Prandle et al.*, 1993]). The Volume balance not being zero also raised the question on which exact time scales the Volume balance has to be zero. One would not expect the Ekman transports induced by wind forcing on short time scales to be instantaneously compensated. Though transports related to geostrophic adjustment occurring on longer timescales are expected to be balanced.

All of these discussed results further stretch the importance of well sustained long term observations of the AMOC through e.g. the RAPID and OSNAP mooring array and a maintained fleet of Argo floats. These measurements at different latitudes are needed to enhance the understanding of the role of the overturning for the MOC and our climate system in general.

Appendix

Basin	Lon [°W]	Lat [°N]
Labrador Sea	$[-54.19, -48.49]$	$[56.17, 58.29]$
Irminger Sea	$[-40, -34.94]$	$[61.15, 63.36]$
Iceland basin	$[-20.87, -11.66]$	$[60.26, 62.93]$
SPNA	$[-59.21, -4.56]$	$[47.85, 65.85]$

Table 4.7: *Basin boxes*

Subsection Name	Distance [km]
EGC	$[0, 131)$
DSO	$[131, 340)$
IIC	$[340, 750)$
Iceland East **FB**	$[750, 1201)$
IFR return	$[1201, 1348)$
Faroe West **FB**	$[1348, 1502)$
FSC Overflow	$[1502, 1768)$
SB	$[1768, 2010)$

Table 4.8: *Distance values starting from Greenland in km for the definition of the currents/subsections at Greenland-Scotland Ridge.*

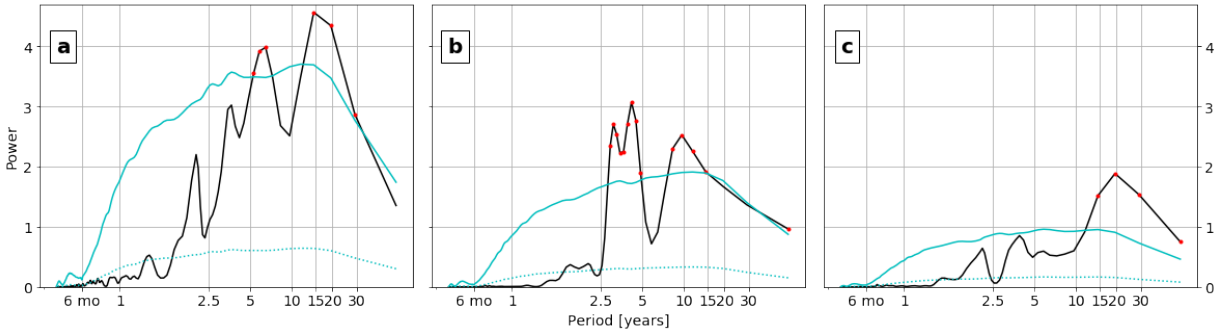

Figure 4.19: *Principal component spectrum for upper AMOC limb EOFs (Figure 4.15d, e,f). a)Pc1, b)Pc2, c) Pc3. The spectra and the related significance interval are computed as described in section 4.3.2. Red points mark significant frequencies.*

Subsection Name	Distance [km]
Labrador Shelf	$[0, 252)$
DWBC Labrador Shelf	$[252, 456)$
Central Labrador Sea	$[456, 1211)$
West Greenland	$[1211, 1500)$
East Greenland	$[1500, 1732)$
Irminger Sea	$[1732, 2278)$
Iceland basin West	$[2278, 2600)$
Iceland basin East	$[2600, 3008)$
Hatton Rockall Plateau	$[3008, 3349)$
Rockall Trough	$[3349, 4000)$

Table 4.9: *Distance values starting from Newfoundland in km for the definition of the currents/subsections at OSNAP.*

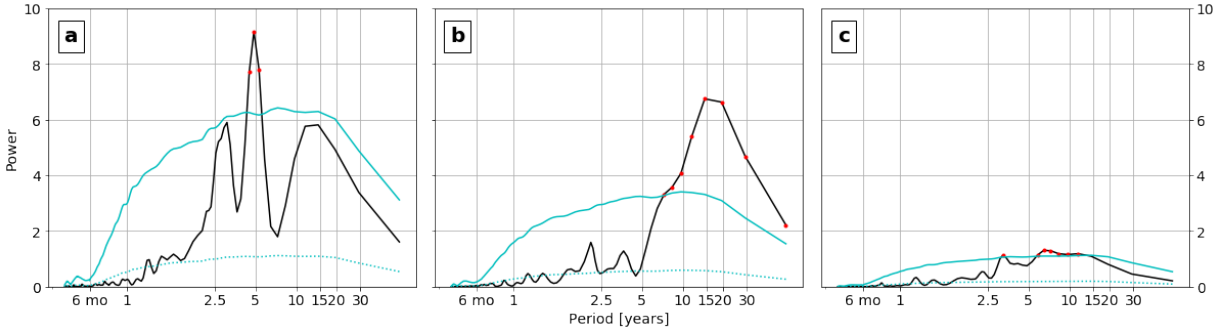

Figure 4.20: *Principal component spectrum for the LSW EOFs (Figure 4.16d, e, f). a)Pc1, b)Pc2, c) Pc3. The spectra and the related significance interval are computed as described in section 4.3.2. Red points mark significant frequencies.*

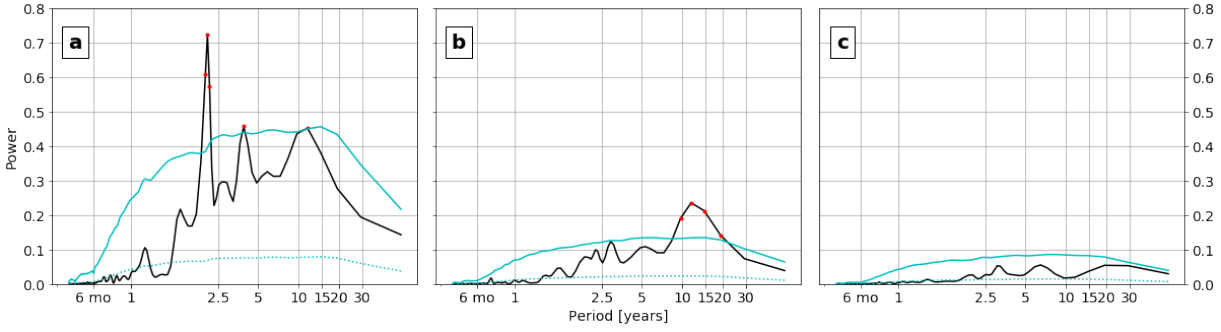

Figure 4.21: *Principal component spectrum for LNADW EOFs (Figure 4.17d, e, f). a)Pc1, b)Pc2, c) Pc3. The spectra and the related significance interval are computed as described in section 4.3.2. Red points mark significant frequencies.*

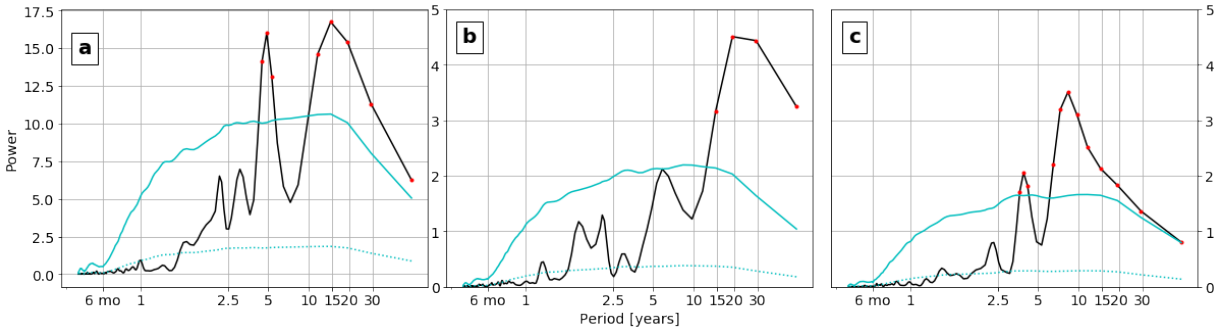

Figure 4.22: *Principal component spectrum for the whole water column EOFs (Figure 4.18 d, e,f). a)Pc1, b)Pc2, c) Pc3. The spectra and the related significance interval are computed as described in section 4.3.2. Red points mark significant frequencies.*

5. Synthesis

In this thesis, various dynamic and kinematic components of the subpolar North Atlantic were investigated on the basis of ocean models and observations. Regional to gyre scale circulation elements and the subpolar expression of the AMOC in the subpolar North Atlantic are addressed using multiple methods in two high-resolution ocean models and observations. In the course of this thesis I worked my way from a more regional to a more gyre scale perspective.

In the following a brief summary of the main findings of this thesis is given in section 5.1. Then, the three main chapters are set into relation with each other and emerging challenges are discussed in section 5.2.

5.1 Short Summary

In order to interpret the observations in the subpolar North Atlantic with the help of ocean-only models, the model fidelity in comparison to observed quantities has to be secured. A widely used quantity to evaluate ocean model performance is, apart form sea surface satellite data (e.g. temperature, salinity), the AMOC strength, which unfortunately is very challenging to measure [*Buckley and Marshall*, 2015; *Lozier et al.*, 2019; *McCarthy et al.*, 2015]. **Chapter 2** identified and derived robust and integral quantities which could be quantified adequately in both, the ocean-only VIKING20 model and observations (Argo floats, satellite, mooring and shipboard data) near the western margin of the SPNA in the Labrador Sea near 53°N . These quantities include convection depth and location in the Labrador Sea and the baroclinicity on the basin scale as well as integral circulation elements including their spatial and temporal variability on regional scales. Apart from the AMOC strength, these properties offer the possibility for further model-evaluation when more observational data become available.

Following on the model evaluation, in **chapter 3**, the high-resolution ocean model VIKING20X [*Rieck*, 2019], a new version of VIKING20, was used in conjunction with velocity fields based on Argo displacement data to asses the advective pathways, related time scales and the connection between the Labrador- and Irminger Seas at the LSW level. Lagrangian particle trajectories were computed and statistically analyzed for different temporal and spatial resolutions of the model output and brought in relation to Lagrangian experiments with the Argo based velocity fields. Purely advective trajectories and trajectories including a simple mesoscale eddy diffusivity parameterization were conducted. Beside the general cyclonic DWBC around the whole western Basin (Labrador and Irminger Seas) there were other circulation elements identified in both, the model and the observations, namely : 1) the advective anti-cyclonic recirculation pattern

in the Labrador Sea (Argo based and model based experiments) and 2) a connection of the DWBC at the Orphan Knoll and Northwest Corner region with the Irminger Sea (model based experiments only) (Figure 3.20). The relative population of each pathway was further relying on the presence or absence of the parameterized eddy diffusivity in the conducted experiments. The relatively simple approach of using an observational based velocity field (resolution of 0.5°x0.25°) and a constant eddy diffusivity parameterization reproduced the communication between the Labrador- and Irminger Seas surprisingly well [*Rhein et al.*, 2002; *Smethie et al.*, 2000]. Forward experiments with the temporarily varying output of VIKING20X reproduced a similar connection with 20% of freshly formed LSW arriving at the Irminger Sea within 1.5-3 years.

Chapter 4 is based solely on the output of VIKING20. Here, the gyre scale circulation and the multi-annual to decadal variability of the currents in the subpolar North Atlantic in relation to the AMOC at the Greenland-Scotland Ridge ($\sim 63°$N) and the OSNAP array ($\sim 58°$N [*Li et al.*, 2017]) is investigated. Additionally, the AMOC at subtropical latitudes at $26.5°$N (RAPID array) is computed and included in the evaluation. Overall, the model reproduces the observed mean magnitude of the AMOC at all three latitudes, at the GSR, OSNAP and RAPID section. Meridional coherence of the AMOC strength at OSNAP and $26.5°$N on decadal to multidecadal time scales was featured in the model. The magnitudes of current transports and the values for heat and freshwater transports over the two sections are widely consistent with observational values (Table 4.2, 4.3, 4.4 and 4.5), eventhough the model is biased toward warmer and more saline hydrography. On longer time scales (decadal) EOF analysis of the model transports featured a dipole like structure - the gyre mode [*Böning et al.*, 2006; *Häkkinen and Rhines*, 2004], where the Irminger and Labrador Sea represent one pole, and the Iceland basin the other. The Irminger and Labrador Sea are governed by coherent dynamics of the depth integrated water column, which includes the overflow sills and deep water formation in the Labrador Sea. The Iceland basin is rather influenced by the North Atlantic Current dynamics. During deep convection (1990's), the gyre index is weak (Figure 4.18 d). This phase of enhanced mixed layer depths in March at the OSNAP WEST section coincides with stronger boundary current transports and decreased heat import to the Labrador Sea through the upper AMOC component.

5.2 Emerging Challenges

With regard to the results previously summarized, a number of new questions and challenges evolved, and these will be presented in the following.

Chapter 2 found, that LSW and LNADW transport are more correlated in years of deep convection, which was further supported by a common mode of variability on interannual to decadal (5-15 years) time scales for the entire water column west of the Reykjanes Ridge (**chapter 4**), which could be accounted to the overall barotropic velocity structure of the model. At the LSW and LNADW density level this mode appeared to be related to a dipole like spatial structure between the overflow at Denmark Strait including its route along the east Greenland shelf and the formation of LSW in the Labrador Sea. Furthermore, the model results suggest a rather constant overflow at the Greenland-Scotland Ridge, hence the interannual to decadal variability imprinted by deep convection to the volume of the LSW reservoir in the Labrador or Irminger Sea can affect directly the LNADW below. In contrast to these model results *Zantopp et al.* [2017] found different major modes in the transports of LSW and LNADW in the DWBC at the exit of the Labrador Sea at $53°$N. Among the different deep water masses, the NEADW shows the highest energy on the quasi-decadal frequency band. This longer term variability could be imprinted by various processes along the pathway of the NEADW from the Iceland- to the Labrador Sea via the Irminger basin. One hypothesis is that the decadal to multidecadal variability of the NEADW is related to wind stress and wind stress curl anomalies in the SPNA associated with changes in the North Atlantic Oscillation (NAO)[*Woollings et al.*, 2015; *Zantopp et al.*, 2017]. Another hypothesis for the source of the decadal to multidecadal variability of the NEADW is a possible relation of the NADW dynamics to the gyre index [*Böning et al.*, 2006; *Häkkinen and Rhines*, 2004]. The gyre mode EOF pattern resembles a dipole like structure between the east (Iceland basin) and west (Labrador and Irminger Sea) subpolar North Atlantic. Its strength was brought into relation with decadal to multi-decadal transport changes in the subpolar North Atlantic [*Böning et al.*, 2006]. One major challenge in assessing the mechanisms and regions of variability imprint to the NADW water masses is the scarce and scattered data coverage in the SPNA. Efforts like the OSNAP array and the deep Argo project (down to 6000 m) can help to increase the spatial and temporal availability of deep circulation and hydrography data. Though the available length of the OSNAP time series is not sufficient to address longer than seasonal to interannual variability. Thus, due to the complexity of the region, models reproducing a more baroclinic ocean structure, e.g. through more vertical levels, would be an indispensable tool.

Regarding the relation between the strength of the subpolar gyre [*Böning et al.*, 2006; *Häkkinen and Rhines*, 2004] and the related DWBC during years of deep convection, no enhanced export of NADW at $53°$N was observed [*Zantopp et al.*, 2017]. Contrary, VIKING20 produces enhanced boundary currents (EGC, WGC, LS as defined in **chapter 4**) during periods of enhanced deep convection concurring with a weak subpolar gyre index (**chapter 4**). VIKING20x further featured a pathway, which first follows the DWBC to the

Orphan Knoll and Northwest Corner region and is then turned towards the north connecting the Labrador- and Irminger Sea (**chapter 3**). This pathway is expected to be related to the DWBC shedding eddies at 48°N which propagate to the north. This pathway was not featured in the Argo based experiments. Overall, this could be related to a stronger representation of the subpolar gyre west of the Reykjanes Ridge in the two OGCMs compared to observations, where the gyre is expected to be connecting all three basins of the SPNA. To estimate the role of the gyre index and expansion [*Böning et al.*, 2006; *Häkkinen and Rhines*, 2004] in observations, longer successive transport time series are crucially needed. Assessing the influence of the gyre modes and expansion during periods of weak and strong convection on weak or strong AMOC phases could help to enhance the overall understanding of the interplay between water mass formation, export and the AMOC strength. The relative role of the atmospheric conditions and the import of subtropical waters into the SPNA could further be addressed in this context. Overall, the actual role of the EOF modes described in this thesis and in [*Häkkinen and Rhines*, 2004] and [*Böning et al.*, 2006] in connection to the AMOC is not clear. Studies with multiple models (forced and coupled) focusing on this question in connection with prolonged data time series (e.g. OSNAP transport and AMOC) would help shed light on this question.

In both, **chapter 2** and **4**, no major correlations between the North Atlantic Oscillation, the related wind stress and the oceanic transports could be drawn. This could be possibly attributed to the coarse 2° x 2° resolution of the applied atmospheric forcing used in the VIKING20 and VIKING20X model, the reanalysis forcing COREv.2, which does not represent the real small-scale spatial variability. This coarse resolution affects the computation of the air-sea interaction in VIKING20 and VIKING20X. Furthermore, the ocean-atmosphere feedback is subject to information loss interpolating from the small-scale oceanic features to the atmosphere. Hence, the thermal and mechanical damping is influenced by this resolution discrepancy [*Abel*, 2018]. This missing damping in the narrow boundary current regions could also be the cause for the stronger than observed boundary currents in the models. Additionally, the combination of climatological radiation and satellite based radiation (SeaSat mission 1978 [*Gould et al.*, 2013]) in the COREv.2 forcing, introducing a jump in variability in the applied radiative forcing, is expected to influence the AMOC-strength (**chapter 4**). Variability analysis with multiple coupled ocean-atmosphere and ocean-only models would be hence of great value to asses the possible influence of the atmospheric forcing on the deep water formation and AMOC strength. The atmospheric imprints on the boundary currents and the response of the gyre scale circulation to the atmospheric forcing are crucial and should attract future research interest. Extended EOF analysis of the ocean currents and the atmosphere could be a tool bringing atmospheric and oceanic dynamics into relation.

Another issue emphasized in this thesis is the comparability of the mixed layer in the model with observations. In comparison to the mixed layer climatology by *Holte and Straneo* [2017] in the two models the mean March MLD, as an indicator for deep convection activity, is stretched along the Labrador and Greenland shelf break for the period of 1958-2009 (**chapter 2** and **chapter 3**). First of all, the spatial comparability of the convection region in the model and observation is complicated by the spacial and temporal availability of Argo data during convection in the region and the fact that there are only few Argo floats in the boundary currents. Second, the convection region and depth are defined through the MLD which is derived differently in ocean models than in observations [*Courtois et al.*, 2017]. In ocean models the MLD is usually calculated using a defined density difference (e.g. 0.01 kg/m^3, VIKING20, VIKING20X) with the surface [*Da Costa et al.*, 2005], whereas in observations the MLD is derived through a variety of different methods e.g. though a varying density threshold depending on the local reference temperature and salinity [*de Boyer Montégut et al.*, 2004], through a hybrid algorithm modeling the shape of each Argo profile by fitting lines to the seasonal thermocline and the mixed layer [*Holte and Straneo*, 2017; *Holte and Talley*, 2009] or as the depth where the oxygen concentration passes a critical value [*Castro Morales and Kaiser*, 2012]. Additionally, the observational data of depth and spatial extend of the MLD is sparse and biased toward the positions of the Argo floats and the existing moorings in the region. Due to the importance of the exact spatial extend of the deep convection for the related LSW export (**chapter 3**) the efforts to systematically estimate the MLD should be increased.This of course is a question of funding, ship time and the density of the Argo array during the respective winter months in the Labrador and Irminger Sea. The calculation of the MLD in ocean models should be adapted to the observational based methods, if not significantly inflating the computational cost of the model.

Chapter 4 computed the AMOC strength at three latitudes in the North Atlantic. The monthly model output resulted in a non-zero volume balance over the respective sections. For calculations of the AMOC at the basin-scale RAPID and OSNAP arrays, one boundary condition is that at all times, the volume balance over the respective section is zero [*Lozier et al.*, 2019; *McCarthy et al.*, 2015]. This volume conservation is a fundamental, since only one unbalanced Sv flowing into the Atlantic without returning would lead to a rise in sea surface height on the magnitude of centimeters per year [*McCarthy et al.*, 2015]. [*Bryden et al.*, 2009] showed in a study on bottom pressure sensors, that the Atlantic basin fills and drains on time scales of 5-10 days. In both arrays Ekman velocities are inferred from reanalysis winds (ERA-Interim) and are added to the surface Ekman layer [*Lozier et al.*, 2019]. Ekman transport introduce transport variability on short time scales. Surprisingly, the related AMOC time series are calculated with the boundary condition of zero net volume transport over the respective section on a daily basis [*Bryden et al.*, 2009; *Lozier et al.*, 2019; *McCarthy et al.*, 2015], which assumes a direct compensation for the Ekman component. At RAPID the upper mid ocean transport and the Ekman transport even dominate the AMOC variability [*McCarthy et al.*, 2015]. In the subpolar North Atlantic the circulation dynamics are influenced by buoyancy forcing and wind

forcing interacting in a complex manner. Hence, the influence of the Ekman component on the overall transport could be different in the SPNA than at subtropical latitudes. [*Mercier et al.*, 2015] found net transports over the Ovide section in the SPNA to be between -0.3 Sv and 2.2 Sv - Are these net transports related to longer periodic variability or even a trend ? On which time scales does the net transport over the SPNA has to fulfill the condition of zero volume transport? The time scales of net volume transport over the OSNAP array should be revisited using temporally and spatially high-resolved ocean model output in order to disentangle time scales related to the Ekman component and to the geostrophic adjustment at the respective latitude.

Appendix

Abbreviations

AABW :	Antarctic Bottom Water
ACC :	Antarctic Circumpolar Current
ADCP :	Acoustic Doppler Current Profiler
AGRIF :	Adaptive Grid Refinement in Fortran
AMOC :	Atlantic Meridional Overturning Circulation
ARGO :	global float array named after a ship in Greek mythology
AR7W :	WOCE Line AR7W, crossing the Labrador Sea passing by Ocean Weather Ship Bravo
CGFZ :	Charlie-Gibbs Fracture Zone
cLS :	Central Labrador Sea
CORE :	Coordinated Ocean-ice Reference Experiments
CGCM :	Climate General Circulation Models
CTD :	Instrument measuring the conductivity, temperature, and pressure of seawater
CFC :	Chlorofluorocarbon
DSOW :	Denmark Strait Overflow Water
DWBC :	Deep Western Boundary Current
EKE :	Eddy Kinetic Energy
EGC :	East Greenland Current
GSR :	Greenland-Scotland-Ridge

IDW : Indian Ocean Deep Water

ITCZ : Intertropical Convergence Zone

LADCP : Lowered Acoustic Doppler Current Profiler

LIM2 : Louvain la-neauve Ice Model Version 2

LNADW : Lower North Atlantic Deep Water

LSW : Labrador Sea Water

LS : Labrador Sea

MLD : Mixed Layer Depth

MOC : Meridional Overturning Circulation

MOCHA : Meridional Overturning Circulation and Heat-flux Array

NADW : North Atlantic Deep Water

NAC : North Atlantic Current

NEMO : Nucleus for European Modelling of the Ocean

NEADW : Northeast Atlantic Deep Water

NWC : Northwest Corner

OGCM : Ocean General Circulation Models

OK : Orphan-Knoll Region

OSNAP : Overturning in the subpolar North Atlantic Program

Ovide : French ship based subpolar North Atlantic observatory

OWS : Ocean Weather Ship

Parcels : Probably A Really Computationally Efficient Lagrangian Simulator

PDW : Pacific Deep Water

PDF : Probability Density function

PHC2.1 : Polar science center Hydrographic Climatology version 2.1

PV : Potential Vorticity

RAPID : Mooring array deployed in the U.K. Rapid Climate Change programme

SAMOC : South Atlantic Merdional Overturning Circulation

SAMBA : South Atlantic MOC Basin-wide Array

SG : South Greenland

SPNA : Subpolar North Atlantic

SST : Sea Surface Temperature

SSS : Sea Surface Salinity

SSSR : Sea Surface Salinity Restoring

Sv : Sverdrup= $10^6 m^3 s^{-1}$

TTD : Transit Time Distribution

WBTS : Western Boundary Time Series - Florida Current Transport Time Series

WGC : West Greenland Current

WOCE : World Ocean Circulation Experiment

Acknowledgments

"Die richtige Funktionsweise des Universums, so behaupten Sie, basiere auf dem Gleichgewicht von vier Elementarkräften: Zauber, Überzeugungskraft, Ungewißheit und verdammte Sturheit"(T. Prachett "Das Licht der Phantasie")

Vor allem danke ich Martin Visbeck dafür, dass er mir die Möglichkeit gab am GEOMAR ein für mich neues Kapitel in der Physikalischen Ozeanographie aufzuschlagen und mir die letzten 5 Jahre mit Rat und Tat zur Seite stand. Vor allem die gemeinsamen Seefahrten gaben den Raum sich über den Ozean auszutauschen und die messende Ozeanographie hautnah für mich zu entdecken. Auch wenn Martin viel unterwegs war, war während seiner begrenzten Kiel-zeit immer eine Möglichkeit da sich über Herausforderungen und den Fortschritt meiner Arbeit auszutauschen, dafür bin ich ihm sehr dankbar.

Mein besonderer Dank gilt auch Jürgen Fischer, der mich während unserer gemeinsamen Bürozeit aber auch noch bis zur letzten Sekunde mit Korrekturen und Denkanstößen unterstützte. Ohne seinen großen Erfahrungsschatz und seine Unterstützung wäre die Fertigstellung dieser Arbeit wahrscheinlich noch etwas verschleppt worden ...

Des Weiteren möchte ich Willi Rath für die Hilfe mit dem parallelisieren meines widerspenstigen Python Codes danken. Nicht nur unsere Zeit als Techniker auf der M121, sondern auch die Nachmittage die wir gemeinsam an manchen meiner Code-Probleme gebastelt haben, haben mir sehr weitergeholfen und immer Spaß gemacht.

Auch meinen Kollegen Sunke Schmidtko, Rebecca Hummels, Kristin Burmeister, Florian Schütte, Tim Fischer, Anna Canning und Henrike Schmidt gebührt an dieser Stelle mein allergrößter Dank. Ihr habt nicht nur meine in Panik geschriebenen letzten Seiten gelesen, sondern wart immer meine kleine Geomar-familie. Des Weiteren danke ich Johannes Karstensen und Siren Rühs für ihre Geduld mit mir.

Abschließend danke ich meiner Familie: Meinen Eltern und meiner Schwester, denen keins meiner Projekte zu verrückt oder abwegig erschien und die mich immer unterstützt und an mich geglaubt haben.

Particulierement j'aimerai de remercier Simon Chabot pour me motiver et croire en moi pendant ces derniers mois difficiles.

References

Abel, R. (2018), Aspects of air-sea interaction in atmosphere-ocean models, Ph.D. thesis, Christian-Albrechts Universität Kiel.

Abernathey, R., and C. Wortham (2015), Phase speed cross spectra of eddy heat fluxes in the eastern pacific, *J. Phys. Oceanogr.*, *45*(5), 1285–1301, doi:10.1175/jpo-d-14-0160.1.

Armi, L., and H. Stommel (1983), Four views of a portion of the north atlantic subtropical gyre, *J. Phys. Oceanogr.*, *13*(5), 828–857, doi:10.1175/1520-0485(1983)013<0828:fvoapo>2.0.co;2.

Ba, J., et al. (2014), A multi-model comparison of atlantic multidecadal variability, *Climate dynamics*, *43*(9-10), 2333–2348.

Bacon, S. (1997), Circulation and fluxes in the north atlantic between greenland and ireland, *Journal of Physical Oceanography*, *27*(7), 1420–1435.

Bacon, S., W. J. Gould, and Y. Jia (2003), Open-ocean convection in the irminger sea, *Geophys. Res. Lett.*, *30*(5), doi:10.1029/2002gl016271.

Baehr, J., A. Stroup, and J. Marotzke (2009), Testing concepts for continuous monitoring of the meridional overturning circulation in the south atlantic, *Ocean Modelling*, *29*(2), 147–153.

Barnier, B., et al. (2007), Eddy-permitting ocean circulation hindcasts of past decades, *Clivar Exchanges*, *42*(12 (3)), 8–10.

Barnier, B., et al. (2015), Drakkar: Developing high resolution ocean components for european earth system models, *CLIVAR Exchanges*, *65*, 18–21.

Beaird, N. L., P. B. Rhines, and C. C. Eriksen (2013), Overflow waters at the iceland–faroe ridge observed in multiyear seaglider surveys, *Journal of Physical Oceanography*, *43*(11), 2334–2351.

Behrens, E. (2013), The oceanic response to greenland melting: the effect of increasing model resolution, Ph.D. thesis, Kiel, Christian-Albrechts-Universität, Diss., 2013.

Behrens, E., A. Biastoch, and C. W. Böning (2013), Spurious amoc trends in global ocean sea-ice models related to subarctic freshwater forcing, *Ocean Modelling*, *69*, 39–49.

Behrens, E., K. Våge, B. Harden, A. Biastoch, and C. W. Böning (2017), Composition and variability of the denmark strait overflow water in a high-resolution numerical model hindcast simulation, *Journal of Geophysical Research: Oceans*.

Berloff, P. S., and J. C. McWilliams (2002), Material transport in oceanic gyres. part ii: Hierarchy of stochastic models, *J. Phys. Oceanogr.*, *32*(3), 797–830, doi:10.1175/1520-0485(2002)032<0797:mtiogp>2.0.co;2.

Berloff, P. S., and J. C. McWilliams (2003), Material transport in oceanic gyres. part iii: Randomized stochastic models, *J. Phys. Oceanogr.*, *33*(7), 1416–1445, doi:10.1175/1520-0485(2003)033<1416:mtiogp>2.0.co;2.

Berloff, P. S., J. C. McWilliams, and A. Bracco (2002), Material transport in oceanic gyres. part i: Phenomenology, *J. Phys. Oceanogr.*, *32*(3), 764–796, doi:10.1175/1520-0485(2002)032<0764:mtiogp>2.0.co;2.

Berx, B., B. Hansen, S. Østerhus, K. Larsen, T. Sherwin, and K. Jochumsen (2013), Combining in-situ measurements and altimetry to estimate volume, heat and salt transport variability through the faroe shetland channel, *Ocean Science Discussions*, *10*(1), 153–195.

Biastoch, A., C. W. Böning, J. Getzlaff, J.-M. Molines, and G. Madec (2008), Causes of interannual-decadal variability in the meridional overturning circulation of the midlatitude north atlantic ocean, *J. Climate*, *21*(24), 6599–6615, doi:10.1175/2008jcli2404.1.

Bingham, R. J., C. W. Hughes, V. Roussenov, and R. G. Williams (2007), Meridional coherence of the north atlantic meridional overturning circulation, *Geophysical Research Letters*, *34*(23).

Blanke, B., S. Bonhommeau, N. Grima, and Y. Drillet (2012), Sensitivity of advective transfer times across the north atlantic ocean to the temporal and spatial resolution of model velocity data: Implication for european eel larval transport, *Dynamics of Atmospheres and Oceans*, *55-56*, 22–44.

Böning, C. W., M. Scheinert, J. Dengg, A. Biastoch, and A. Funk (2006), Decadal variability of subpolar gyre transport and its reverberation in the north atlantic overturning, *Geophysical Research Letters*, *33*(21).

Böning, C. W., E. Behrens, A. Biastoch, K. Getzlaff, and J. L. Bamber (2016), Emerging impact of greenland meltwater on deepwater formation in the north atlantic ocean, in *Behrens* [2013].

Booth, B. B. B., N. J. Dunstone, P. R. Halloran, T. Andrews, and N. Bellouin (2012), Aerosols implicated as a prime driver of twentieth-century north atlantic climate variability, *Nature*, *484*, 228.

Bower, A., S. Lozier, and S. Gary (2011), Export of labrador sea water from the subpolar north atlantic: a lagrangian perspective, *Deep Sea Research Part II: Topical Studies in Oceanography*, *58*(17-18), 1798–1818.

Bower, A. S., and H. D. Hunt (2000), Lagrangian observations of the deep western boundary current in the north atlantic ocean. part i: Large-scale pathways and spreading rates, *Journal of Physical Oceanography*, *30*(5), 764–783.

Bower, A. S., M. S. Lozier, S. F. Gary, and C. W. Böning (2009), Interior pathways of the north atlantic meridional overturning circulation, *Nature*, *459*(7244), 243–247.

Brandt, P., F. A. Schott, A. Funk, and C. S. Martins (2004), Seasonal to interannual variability of the eddy field in the labrador sea from satellite altimetry, *Journal of Geophysical Research: Oceans (1978–2012)*, *109*(C2).

Brandt, P., A. Funk, L. Czeschel, C. Eden, and C. W. Böning (2007), Ventilation and transformation of labrador sea water and its rapid export in the deep labrador current, *Journal of physical oceanography*, *37*(4), 946–961.

Breckenfelder, T., M. Rhein, A. Roessler, C. W. Böning, A. Biastoch, E. Behrens, and C. Mertens (2017), Flow paths and variability of the north atlantic current: A comparison of observations and a high-resolution model, *Journal of Geophysical Research: Oceans*, *122*(4), 2686–2708.

Bringedal, C., T. Eldevik, Skagseth, M. A. Spall, and S. Østerhus (2018), Structure and forcing of observed exchanges across the greenland–scotland ridge, *Journal of Climate*, *31*(24), 9881–9901.

Broecker, W. S. (1991), The great ocean conveyor, *Oceanography*, *4*(2), 79–89.

Broecker, W. S. (1997), Thermohaline circulation, the achilles heel of our climate system: Will man-made co2 upset the current balance?, *Science*, *278*(5343), 1582–1588.

Bryan, F. O., M. W. Hecht, and R. D. Smith (2007), Resolution convergence and sensitivity studies with north atlantic circulation models. part i: The western boundary current system, *Ocean Modelling*, *16*(3), 141–159.

Bryan, K. (1969), A numerical method for the study of the circulation of the world ocean, *Journal of Computational Physics*, *4*(3), 347–376.

Bryan, K., and M. D. Cox (1972), The circulation of the world ocean: A numerical study. part i, a homogeneous model, *J. Phys. Oceanogr.*, *2*(4), 319–335, doi:$10.1175/1520\text{-}0485(1972)002<0319:\text{tcotwo}>2.0.\text{co};2$.

Bryden, H. L., A. Mujahid, S. A. Cunningham, and T. Kanzow (2009), Adjustment of the basin-scale circulation at 26 degrees n to variations in gulf stream, deep western boundary current and ekman transports as observed by the rapid array, *Ocean Science*, *5*(4), 421–433.

Buckley, M. W., and J. Marshall (2015), Observations, inferences and mechanisms of atlantic moc variability: a review, *Reviews of Geophysics*.

Budéus, G., W. Schneider, and G. Krause (1998), Winter convective events and bottom water warming in the greenland sea, *J. Geophys. Res.*, *103*(C9), 18,513–18,527.

Böning, C. W., and M. D. Cox (1988), Particle dispersion and mixing of conservative properties in an eddy-resolving model, *Journal of physical oceanography*, *18*(2), 320–338.

Castro Morales, K., and J. Kaiser (2012), Using dissolved oxygen concentrations to determine mixed layer depths in the bellingshausen sea, *Ocean Science*, *8*(1), 1–10.

Chafik, L., and T. Rossby (2019), Volume, heat, and freshwater divergences in the subpolar north atlantic suggest the nordic seas as key to the state of the meridional overturning circulation, *Geophys. Res. Lett.*, *46*(9), 4799–4808, doi:10.1029/2019gl082110.

Chanut, J., B. Barnier, W. Large, L. Debreu, T. Penduff, J. M. Molines, and P. Mathiot (2008), Mesoscale eddies in the labrador sea and their contribution to convection and restratification., *Journal of Physical Oceanography*, *38*(8).

Chassignet, E. P., and D. P. Marshall (2008), Gulf stream separation in numerical ocean models, *Geophysical Monograph Series*, *177*, 39–61.

Chelton, D. B., R. A. deSzoeke, M. G. Schlax, K. El Naggar, and N. Siwertz (1998), Geographical variability of the first baroclinic rossby radius of deformation, *J. Phys. Oceanogr.*, *28*(3), 433–460, doi:10.1175/1520-0485(1998)028<0433:gvotfb>2.0.co;2.

Chelton, D. B., M. G. Schlax, and R. M. Samelson (2011), Global observations of nonlinear mesoscale eddies, *Progress in Oceanography*, *91*(2), 167–216.

Childers, K. H., C. N. Flagg, T. Rossby, and C. Schrum (2015), Directly measured currents and estimated transport pathways of atlantic water between 59.5° n and the iceland–faroes–scotland ridge, *Tellus A: Dynamic Meteorology and Oceanography*, *67*(1), 28,067.

Church, J. A. (2007), A change in circulation?, *Science*, *317*(5840), 908–909.

Chylek, P., C. K. Folland, G. Lesins, M. K. Dubey, and M. Wang (2009), Arctic air temperature change amplification and the atlantic multidecadal oscillation, *Geophys. Res. Lett.*, *36*(14), doi:10.1029/2009gl038777.

Clarke, R. A., and J.-C. Gascard (1983), The formation of labrador sea water. part i: Large-scale processes, *J. Phys. Oceanogr.*, *13*(10), 1764–1778, doi:10.1175/1520-0485(1983)013<1764:tfolsw>2.0.co;2.

Cole, S. T., C. Wortham, E. Kunze, and W. B. Owens (2015), Eddy stirring and horizontal diffusivity from argo float observations: Geographic and depth variability, *Geophys. Res. Lett.*, *42*(10), 3989–3997, doi:10.1002/2015gl063827.

Courtois, P., X. Hu, C. Pennelly, P. Spence, and P. G. Myers (2017), Mixed layer depth calculation in deep convection regions in ocean numerical models, *Ocean Modelling*, *120*, 60–78.

Cunningham, S. A., and T. W. N. Haine (1995), Labrador sea water in the eastern north atlantic. part i: A synoptic circulation inferred from a minimum in potential vorticity, *J. Phys. Oceanogr.*, *25*(4), 649–665, doi:10.1175/1520-0485(1995)025<0649:lswite>2.0.co;2.

Cunningham, S. A., and R. Marsh (2010), Observing and modeling changes in the atlantic moc, *Wiley Interdisciplinary Reviews: Climate Change*, *1*(2), 180–191.

Cuny, J., P. B. Rhines, P. P. Niiler, and S. Bacon (2002), Labrador sea boundary currents and the fate of the irminger sea water, *Journal of Physical Oceanography*, *32*(2), 627–647.

Cuny, J., P. B. Rhines, and R. Kwok (2005), Davis strait volume, freshwater and heat fluxes, *Deep Sea Research Part I: Oceanographic Research Papers*, *52*(3), 519–542.

Curry, B., C. M. Lee, B. Petrie, R. E. Moritz, and R. Kwok (2014), Multiyear volume, liquid freshwater, and sea ice transports through davis strait, 2004-10, *J. Phys. Oceanogr.*, *44*(4), 1244–1266, doi:10.1175/jpo-d-13-0177.1.

Curry, R., B. Dickson, and I. Yashayaev (2003), A change in the freshwater balance of the atlantic ocean over the past four decades, *Nature*, *426*(6968), 826–829.

Da Costa, M. V., and B. Blanke (2004), Lagrangian methods for flow climatologies and trajectory error assessment, *Ocean Modelling*, *6*(3-4), 335–358.

Da Costa, M. V., H. Mercier, and A. M. Treguier (2005), Effects of the mixed layer time variability on kinematic subduction rate diagnostics, *Journal of physical oceanography*, *35*(4), 427–443.

Danabasoglu, G., W. G. Large, and B. P. Briegleb (2010), Climate impacts of parameterized nordic sea overflows, *Journal of Geophysical Research: Oceans*, *115*(C11).

Daniault, N., et al. (2016), The northern north atlantic ocean mean circulation in the early 21st century, *Progress in Oceanography*, *146*, 142–158.

D'Asaro, E. A. (2003), Performance of autonomous lagrangian floats, *J. Atmos. Oceanic Technol.*, *20*(6), 896–911, doi:10.1175/1520-0426(2003)020<0896:poalf>2.0.co;2.

Davis, R., J. Sherman, and J. Dufour (2001), Profiling alaces and other advances in autonomous subsurface floats, *Journal of atmospheric and oceanic technology*, *18*(6), 982–993.

Davis, R. E. (1991), Lagrangian ocean studies, *Annu. Rev. Fluid Mech.*, *23*(1), 43–64, doi:10.1146/annurev.fl.23.010191.000355.

Davis, R. E. (1998), Preliminary results from directly measuring middepth circulation in the tropical and south pacific, *J. Geophys. Res.*, *103*(C11), 24,619–24,639, doi:10.1029/98jc01913.

Davis, R. E. (2005), Intermediate-depth circulation of the indian and south pacific oceans measured by autonomous floats, *J. Phys. Oceanogr.*, *35*(5), 683–707, doi:10.1175/jpo2702.1.

de Boyer Montégut, C., G. Madec, A. S. Fischer, A. Lazar, and D. Iudicone (2004), Mixed layer depth over the global ocean: An examination of profile data and a profile-based climatology, *Journal of Geophysical Research: Oceans*, *109*(C12).

de Jong, M. Femke, and L. de Steur (2016), Strong winter cooling over the irminger sea in winter 2014-2015, exceptional deep convection, and the emergence of anomalously low sst, *Geophys. Res. Lett.*, *43*(13), 7106–7113, doi:10.1002/2016gl069596.

de Jong, M. F., M. Oltmanns, J. Karstensen, and L. de Steur (2018), Deep convection in the irminger sea observed with a dense mooring array, *Oceanography*, *31*(1), 50–59.

de Steur, L., R. S. Pickart, A. Macrander, K. Våge, B. Harden, S. Jónsson, S. Østerhus, and H. Valdimarsson (2017), Liquid freshwater transport estimates from the e ast g reenland c urrent based on continuous measurements north of d enmark s trait, *Journal of Geophysical Research: Oceans*, *122*(1), 93–109.

Debreu, L., and E. Blayo (2008), Two-way embedding algorithms: a review, *Ocean Dynamics*, *58*(5-6), 415–428.

Delworth, T., S. Manabe, and R. J. Stouffer (1993), Interdecadal variations of the thermohaline circulation in a coupled ocean-atmosphere model, *Journal of Climate*, *6*(11), 1993–2011.

Delworth, T. L., and M. E. Mann (2000), Observed and simulated multidecadal variability in the northern hemisphere, *Climate Dynamics*, *16*(9), 661–676.

Delworth, T. L., et al. (2012), Simulated climate and climate change in the gfdl cm2. 5 high-resolution coupled climate model, *Journal of Climate*, *25*(8), 2755–2781.

Dengler, M., F. Schott, C. Eden, P. Brandt, J. Fischer, and R. J. Zantopp (2004), Break-up of the atlantic deep western boundary current into eddies at 8 s, *Nature*, *432*(7020), 1018–1020.

Dengler, M., J. Fischer, F. A. Schott, and R. Zantopp (2006), Deep labrador current and its variability in 1996–2005, *Geophysical Research Letters*, *33*(21).

Deshayes, J., et al. (2013), Oceanic hindcast simulations at high resolution suggest that the atlantic moc is bistable, *Geophysical Research Letters*, *40*(12), 3069–3073.

Dickey, T. D. (2003), Emerging ocean observations for interdisciplinary data assimilation systems, *The Use of Data Assimilation in Coupled Hydrodynamic, Ecological and Bio-geo-chemical Models of the Ocean. Selected papers from the 33rd International Liege Colloquium on Ocean Dynamics, held in Liege, Belgium on May 7-11th, 2001.*, *40-41*, 5–48.

Dickson, R. R., and J. Brown (1994), The production of north atlantic deep water: sources, rates, and pathways, *Journal of Geophysical Research: Oceans (1978–2012)*, *99*(C6), 12,319–12,341.

Dorman, C. E., and R. H. Bourke (1981), Precipitation over the atlantic ocean, 30°s to 70°n, *Mon. Wea. Rev.*, *109*(3), 554–563, doi:10.1175/1520-0493(1981)109<0554:potaot>2.0.co;2.

Dormand, J. R., and P. J. Prince (1980), A family of embedded runge-kutta formulae, *Journal of Computational and Applied Mathematics*, *6*(1), 19–26.

Drews, A., and R. J. Greatbatch (2016), Atlantic multidecadal variability in a model with an improved north atlantic current, *Geophysical Research Letters*, *43*(15), 8199–8206.

Durbin, P. A. (2018), Some recent developments in turbulence closure modeling, *Annu. Rev. Fluid Mech.*, *50*(1), 77–103, doi:10.1146/annurev-fluid-122316-045020.

Durgadoo, J. V., A. Biastoch, A. L. New, S. Rühs, A. J. G. Nurser, Y. Drillet, and J.-R. Bidlot (2019), Strategies for simulating the drift of marine debris, *Journal of Operational Oceanography*, pp. 1–12.

Döös, K., V. Rupolo, and L. Brodeau (2011), Dispersion of surface drifters and model-simulated trajectories, *Ocean Modelling*, *39*(3), 301–310.

Eden, C., and C. Böning (2002), Sources of eddy kinetic energy in the labrador sea, *Journal of Physical Oceanography*, *32*(12), 3346–3363.

Eden, C., and J. Willebrand (2001), Mechanism of interannual to decadal variability of the north atlantic circulation, *Journal of Climate*, *14*(10), 2266–2280.

Enfield, D. B., A. M. Mestas-Nuñez, and P. J. Trimble (2001), The atlantic multidecadal oscillation and its relation to rainfall and river flows in the continental us, *Geophysical Research Letters*, *28*(10), 2077–2080.

ETOPO, U. (2001), Department of commerce, national oceanic and atmospheric administration, national geophysical data center, 2-minute gridded global relief data.

Falina, A., A. Sarafanov, and A. Sokov (2007), Variability and renewal of labrador sea water in the irminger basin in 1991–2004, *Journal of Geophysical Research: Oceans*, *112*(C1).

Fernández-Armesto, F. (2007), *Pathfinders: a global history of exploration*, WW Norton and Company.

Fichefet, T., and M. A. Maqueda (1997), Sensitivity of a global sea ice model to the treatment of ice thermodynamics and dynamics, *Journal of Geophysical Research: Oceans*, *102*(C6), 12,609–12,646.

Fischer, J., and F. A. Schott (2002), Labrador sea water tracked by profiling floats–from the boundary current into the open north atlantic, *J. Phys. Oceanogr.*, *32*(2), 573–584, doi:10.1175/1520-0485(2002)032<0573:lswtbp>2.0.co;2.

Fischer, J., F. A. Schott, and M. Dengler (2004), Boundary circulation at the exit of the labrador sea, *Journal of physical oceanography*, *34*(7), 1548–1570.

Fischer, J., J. Karstensen, M. Oltmanns, and S. Schmidtko (2018), Mean circulation and eke distribution in the labrador sea water level of the subpolar north atlantic, *Ocean Science Discussions*, pp. 1–27.

Fogelqvist, E., J. Blindheim, T. Tanhua, S. Østerhus, E. Buch, and F. Rey (2003), Greenland-scotland overflow studied by hydro-chemical multivariate analysis, *Deep Sea Research Part I: Oceanographic Research Papers*, *50*(1), 73–102.

Folland, C. K., T. N. Palmer, and D. E. Parker (1986), Sahel rainfall and worldwide sea temperatures, 1901–85, *Nature*, *320*(6063), 602.

Gastineau, G., and C. Frankignoul (2012), Cold-season atmospheric response to the natural variability of the atlantic meridional overturning circulation, *Climate dynamics*, *39*(1-2), 37–57.

Gerdes, R., C. Köberle, and J. Willebrand (1991), The influence of numerical advection schemes on the results of ocean general circulation models, *Climate Dynamics*, *5*(4), 211–226.

Goldenberg, S. B., C. W. Landsea, A. M. Mestas-Nuñez, and W. M. Gray (2001), The recent increase in atlantic hurricane activity: Causes and implications, *Science*, *293*(5529), 474–479.

Gould, J., et al. (2004), Argo profiling floats bring new era of in situ ocean observations, *Eos Trans. AGU*, *85*(19), 185–191, doi:10.1029/2004eo190002.

Gould, J., B. Sloyan, and M. Visbeck (2013), Chapter 3 - in situ ocean observations: A brief history, present status, and future directions, in *International Geophysics*, vol. 103, edited by G. Siedler, S. M. Griffies, J. Gould, and J. A. Church, pp. 59–81, Academic Press.

Griffa, A. (1996), Applications of stochastic particle models to oceanographic problems, in *Stochastic modelling in physical oceanography*, pp. 113–140, Springer.

Griffies, S. M., et al. (2009), Coordinated ocean-ice reference experiments (cores), *Ocean Modelling*, *26*(1), 1–46.

Group, L. S. (1998), The labrador sea deep convection experiment, *Bulletin of the American Meteorological Society*, *79*(10), 2033–2058.

Haine, T., C. Böning, P. Brandt, J. Fischer, A. Funk, D. Kieke, E. Kvaleberg, M. Rhein, and M. Visbeck (2008), North atlantic deep water formation in the labrador sea, recirculation through the subpolar gyre, and discharge to the subtropics, in *Arctic - Subarctic Ocean Fluxes*, pp. 653–701, Springer.

Haine, T. W. N., and T. M. Hall (2002), A generalized transport theory: Water-mass composition and age, *J. Phys. Oceanogr.*, *32*(6), 1932–1946, doi:10.1175/1520-0485(2002)032<1932:agttwm>2.0.co;2.

Häkkinen, S., and P. B. Rhines (2004), Decline of subpolar north atlantic circulation during the 1990s, *Science*, *304*(5670), 555–559.

Hall, M. M., and H. L. Bryden (1982), Direct estimates and mechanisms of ocean heat transport, *Deep Sea Research Part A. Oceanographic Research Papers*, *29*(3), 339–359.

Hallberg, R. (2013), Using a resolution function to regulate parameterizations of oceanic mesoscale eddy effects, *Ocean Modelling*, *72*, 92–103.

Handmann, P., J. Fischer, M. Visbeck, J. Karstensen, A. Biastoch, C. Böning, and L. Patara (2018), The deep western boundary current in the labrador sea from observations and a high-resolution model, *Journal of Geophysical Research: Oceans*.

Hansen, B., H. Larsen, K. Margretha, H. Hátún, and S. Østerhus (2016), A stable faroe bank channel overflow 1995–2015, *Ocean Science*, *12*(6), 1205–1220.

Hansen, B., and S. Østerhus (2000), North atlantic–nordic seas exchanges, *Progress in Oceanography*, *45*(2), 109–208.

Hansen, B., and S. Østerhus (2007), Faroe bank channel overflow 1995-2005, *Progress in Oceanography*, *75*(4), 817–856.

Harden, B. E., et al. (2016), Upstream sources of the denmark strait overflow: Observations from a high-resolution mooring array, *Deep Sea Research Part I: Oceanographic Research Papers*, *112*, 94–112.

Higginson, S., K. Thompson, J. Huang, M. Véronneau, and D. Wright (2011), The mean surface circulation of the north atlantic subpolar gyre: A comparison of estimates derived from new gravity and oceanographic measurements, *Journal of Geophysical Research: Oceans*, *116*(C8).

Holdsworth, A. M., and P. G. Myers (2015), The influence of high-frequency atmospheric forcing on the circulation and deep convection of the labrador sea, *Journal of Climate*, *28*(12), 4980–4996.

Holliday, N. P., S. Bacon, J. Allen, and E. L. McDonagh (2009), Circulation and transport in the western boundary currents at cape farewell, greenland, *Journal of Physical Oceanography*, *39*(8), 1854–1870.

Holliday N., P., S. Bacon, A. Cunningham S., F. Gary S., J. Karstensen, A. King B., F. Li, and L. Mcdonagh E. (2018), Subpolar north atlantic overturning and gyre-scale circulation in the summers of 2014 and 2016, *J. Geophys. Res. Oceans*, *0*(0), doi:10.1029/2018jc013841.

Holloway, G. (1986), Estimation of oceanic eddy transports from satellite altimetry, *Nature*, *323*, 243.

Holte, J., and F. Straneo (2017), Seasonal overturning of the labrador sea as observed by argo floats, *Journal of Physical Oceanography*, *47*(10), 2531–2543.

Holte, J., and L. Talley (2009), A new algorithm for finding mixed layer depths with applications to argo data and subantarctic mode water formation, *Journal of Atmospheric and Oceanic Technology*, *26*(9), 1920–1939.

Holte, J., L. D. Talley, J. Gilson, and D. Roemmich (2017), An argo mixed layer climatology and database, *Geophysical Research Letters*.

Hummels, R., P. Brandt, M. Dengler, J. Fischer, M. Araujo, D. Veleda, and J. V. Durgadoo (2015), Interannual to decadal changes in the western boundary circulation in the atlantic at 11° s, *Geophysical Research Letters*, *42*(18), 7615–7622.

Hunter, J. R. (1987), The application of lagrangian particle-tracking techniques to modelling of dispersion in the sea, in *North-Holland Mathematics Studies*, vol. 145, edited by J. Noye, pp. 257–269, North-Holland.

Hunter, J. R., P. D. Craig, and H. E. Phillips (1993), On the use of random walk models with spatially variable diffusivity, *Journal of Computational Physics*, *106*(2), 366–376.

Hurrell, J. W. (1995), Decadal trends in the north atlantic oscillation, *Science*, *269*, 676–679.

Hurrell, J. W., and C. Deser (2010), North atlantic climate variability: the role of the north atlantic oscillation, *Journal of Marine Systems*, *79*(3), 231–244.

Ioc, I. (2008), Bodc, 2003. centenary edition of the gebco digital atlas, published on cd-rom on behalf of the intergovernmental oceanographic commission and the international hydrographic organization as part of the general bathymetric chart of the oceans, *British oceanographic data centre, Liverpool*.

Jackson, L. C., K. A. Peterson, C. D. Roberts, and R. A. Wood (2016), Recent slowing of atlantic overturning circulation as a recovery from earlier strengthening, *Nature Geoscience*.

Jayne, S. R., and J. Marotzke (2001), The dynamics of ocean heat transport variability, *Reviews of Geophysics*, *39*(3), 385–411.

Jayne, S. R., D. Roemmich, N. Zilberman, S. C. Riser, K. S. Johnson, G. C. Johnson, and S. R. Piotrowicz (2017), The argo program: Present and future, *Oceanography*, *30*(2), 18–28.

Jevrejeva, S., A. Grinsted, J. C. Moore, and S. Holgate (2006), Nonlinear trends and multiyear cycles in sea level records, *Journal of Geophysical Research: Oceans*, *111*(C9).

Jochumsen, K., D. Quadfasel, H. Valdimarsson, and S. Jonsson (2012), Variability of the denmark strait overflow: Moored time series from 1996–2011, *Journal of Geophysical Research: Oceans (1978–2012)*, *117*(C12).

Jochumsen, K., M. Köllner, D. Quadfasel, S. Dye, B. Rudels, and H. Valdimarsson (2015), On the origin and propagation of denmark strait overflow water anomalies in the irminger basin, *Journal of Geophysical Research: Oceans*, *120*(3), 1841–1855.

Jochumsen, K., M. Moritz, N. Nunes, D. Quadfasel, K. M. H. Larsen, B. Hansen, H. Valdimarsson, and S. Jonsson (2017), Revised transport estimates of the d enmark s trait overflow, *Journal of Geophysical Research: Oceans*, *122*(4), 3434–3450.

Johnson, G. C., S. G. Purkey, and J. M. Toole (2008), Reduced antarctic meridional overturning circulation reaches the north atlantic ocean, *Geophysical Research Letters*, *35*(22).

Kang, S. M., R. Seager, D. M. W. Frierson, and X. Liu (2015), Croll revisited: Why is the northern hemisphere warmer than the southern hemisphere?, *Climate Dynamics*, *44*(5), 1457–1472.

Kayano, M. T., and V. B. Capistrano (2014), How the atlantic multidecadal oscillation (amo) modifies the enso influence on the south american rainfall, *International Journal of Climatology*, *34*(1), 162–178.

Keeling, C. D., S. C. Piper, R. B. Bacastow, M. Wahlen, T. P. Whorf, M. Heimann, and H. A. Meijer (2005), Atmospheric co 2 and 13 co 2 exchange with the terrestrial biosphere and oceans from 1978 to 2000: observations and carbon cycle implications, in *A history of atmospheric CO2 and its effects on plants, animals, and ecosystems*, pp. 83–113, Springer.

Khatiwala, S., et al. (2013), Global ocean storage of anthropogenic carbon, *Biogeosciences*, *10*(4), 2169–2191.

Klocker, A., R. Ferrari, and J. H. LaCasce (2012), Estimating suppression of eddy mixing by mean flows, *J. Phys. Oceanogr.*, *42*(9), 1566–1576, doi:10.1175/jpo-d-11-0205.1.

Knight, J. R., R. J. Allan, C. K. Folland, M. Vellinga, and M. E. Mann (2005), A signature of persistent natural thermohaline circulation cycles in observed climate, *Geophys. Res. Lett.*, *32*(20), doi:10.1029/2005gl024233.

Koltermann, K. P., A. V. Sokov, V. P. Tereschenkov, S. A. Dobroliubov, K. Lorbacher, and A. Sy (1999), Decadal changes in the thermohaline circulation of the north atlantic, *Deep Sea Research Part II: Topical Studies in Oceanography*, *46*(1), 109–138.

Koszalka, I., J. H. LaCasce, M. Andersson, K. A. Orvik, and C. Mauritzen (2011), Surface circulation in the nordic seas from clustered drifters, *Deep Sea Research Part I: Oceanographic Research Papers*, *58*(4), 468–485.

LaCasce, J. H. (2008), Lagrangian statistics from oceanic and atmospheric observations, in *Transport and Mixing in Geophysical Flows*, pp. 165–218, Springer.

Lange, M., and E. van Sebille (2017), Parcels v0. 9: prototyping a lagrangian ocean analysis framework for the petascale age, *arXiv preprint arXiv:1707.05163*.

Large, W., and S. Yeager (2009), The global climatology of an interannually varying air–sea flux data set, *Climate Dynamics*, *33*(2-3), 341–364.

Latif, M., et al. (2004), Reconstructing, monitoring, and predicting multidecadal-scale changes in the north atlantic thermohaline circulation with sea surface temperature, *Journal of Climate*, *17*(7), 1605–1614.

Laurindo, L. C., A. J. Mariano, and R. Lumpkin (2017), An improved near-surface velocity climatology for the global ocean from drifter observations, *Deep Sea Research Part I: Oceanographic Research Papers*, *124*, 73–92.

Lavender, K. L., R. E. Davis, and W. B. Owens (2000), Mid-depth recirculation observed in the interior labrador and irminger seas by direct velocity measurements, *Nature*, *407*(6800), 66–69.

Lavender, K. L., W. B. Owens, and R. E. Davis (2005), The mid-depth circulation of the subpolar north atlantic ocean as measured by subsurface floats, *Deep Sea Research Part I: Oceanographic Research Papers*, *52*(5), 767–785.

Lazier, J. (1973), The renewal of labrador sea water, in *Deep Sea Research and Oceanographic Abstracts*, vol. 20, pp. 341–353, Elsevier.

Lazier, J., R. Pickart, and P. Rhines (2001), Deep convection, *International Geophysics Series*, *77*, 387–400.

Lazier, J., R. Hendry, A. Clarke, I. Yashayaev, and P. Rhines (2002), Convection and restratification in the labrador sea, 1990–2000, *Deep Sea Research Part I: Oceanographic Research Papers*, *49*(10), 1819–1835.

Le Bras, I. A., S. R. Jayne, and J. M. Toole (2018), The interaction of recirculation gyres and a deep boundary current, *Journal of Physical Oceanography*.

Lebedev, K. V., H. Yoshinari, N. A. Maximenko, and P. W. Hacker (2007), Velocity data assessed from trajectories of argo floats at parking level and at the sea surface, *IPRC Technical Note*, *4*(2), 1–16.

Levitus, S., J. Antonov, and T. Boyer (2012), Warming of the world ocean, 1955-2010, *Geophys. Res. Lett.*, *39*(2), L02,604–, doi:10.1029/2012GL051106.

Lherminier, P., H. Mercier, T. Huck, C. Gourcuff, F. F. Perez, P. Morin, A. Sarafanov, and A. Falina (2010), The atlantic meridional overturning circulation and the subpolar gyre observed at the a25-ovide section in june 2002 and 2004, *Deep Sea Research Part I: Oceanographic Research Papers*, *57*(11), 1374–1391.

Li, F., M. S. Lozier, and W. E. Johns (2017), Calculating the meridional volume, heat, and freshwater transports from an observing system in the subpolar north atlantic: Observing system simulation experiment, *Journal of Atmospheric and Oceanic Technology*, *34*(7), 1483–1500.

Li, Q., and L. Pareschi (2014), Exponential runge–kutta for the inhomogeneous boltzmann equations with high order of accuracy, *Journal of Computational Physics*, *259*, 402–420.

Lilly, J. M., P. B. Rhines, M. Visbeck, R. Davis, J. R. N. Lazier, F. Schott, and D. Farmer (1999), Observing deep convection in the labrador sea during winter 1994/95, *J. Phys. Oceanogr.*, *29*(8), 2065–2098, doi: 10.1175/1520-0485(1999)029<2065:odcitl>2.0.co;2.

Longworth, H. R., and H. L. Bryden (2007), Discovery and quantification of the atlantic meridional overturning circulation: The importance of 25 n, *Ocean Circulation: Mechanisms and Impacts-Past and Future Changes of Meridional Overturning*, pp. 5–18.

Lozier, M. S. (2010), Deconstructing the conveyor belt, *Science*, *328*(5985), 1507–1511.

Lozier, M. S. (2012), Overturning in the north atlantic, *Annual review of marine science*, *4*, 291–315.

Lozier, M. S., et al. (2017), Overturning in the subpolar north atlantic program: a new international ocean observing system, *Bulletin of the American Meteorological Society*, *98*(4), 737–752.

Lozier, M. S., et al. (2019), A sea change in our view of overturning in the subpolar north atlantic, *Science*, *363*(6426), 516.

Lüthi, D., et al. (2008), High-resolution carbon dioxide concentration record 650,000-800,000 years before present, *Nature*, *453*, 379.

Madec, G. (2008), Nemo ocean engine, *IPSL Tech. Note*, p. 332.

Madec, G., et al. (2017), Nemo ocean engine, doi:10.5281/zenodo.1472492, revision 8625 from SVN repository.

Maltrud, M. E., and J. L. McClean (2005), An eddy resolving global 1/10 ocean simulation, *Ocean Modelling*, *8*(1-2), 31–54.

Marshall, D. P., and C. E. Tansley (2001), An implicit formula for boundary current separation, *Journal of physical oceanography*, *31*(6), 1633–1638.

Marshall, J., and F. Schott (1999), Open-ocean convection: Observations, theory and models, *Reviews of Geophysics*, *37*(1), 1–64.

Marzocchi, A., J. J.-M. Hirschi, N. P. Holliday, S. A. Cunningham, A. T. Blaker, and A. C. Coward (2015), The north atlantic subpolar circulation in an eddy-resolving global ocean model, *Journal of Marine Systems*, *142*, 126–143.

Mastropole, D., R. S. Pickart, H. Valdimarsson, K. Våge, K. Jochumsen, and J. Girton (2017), On the hydrography of denmark strait, *Journal of Geophysical Research: Oceans*, *122*(1), 306–321.

McCarthy, G. D., et al. (2015), Measuring the atlantic meridional overturning circulation at 26°n, *Progress in Oceanography*, *130*, 91–111.

McCartney, M. S., and L. D. Talley (1984), Warm-to-cold water conversion in the northern north atlantic ocean, *Journal of Physical Oceanography*, *14*(5), 922–935.

Meinen, C. S., et al. (2018), Meridional overturning circulation transport variability at 34.5° s during 2009–2017: Baroclinic and barotropic flows and the dueling influence of the boundaries, *Geophysical Research Letters*, *45*(9), 4180–4188.

Mercier, H., et al. (2015), Variability of the meridional overturning circulation at the greenland–portugal ovide section from 1993 to 2010, *Progress in Oceanography*, *132*, 250–261.

Mertens, C., M. Rhein, M. Walter, C. W. Böning, E. Behrens, D. Kieke, R. Steinfeldt, and U. Stöber (2014), Circulation and transports in the newfoundland basin, western subpolar north atlantic, *Journal of Geophysical Research: Oceans*, *119*(11), 7772–7793.

Mielke, C. L., J. Baehr, and S. Gary (2015), The north atlantic deep western boundary current: Seasonal cycle, decadal variability and relation to the atlantic meridional overturning circulation, Ph.D. thesis, Universität Hamburg Hamburg.

Nansen, F. (1912), Das bodenwasser und die abkühlnng des meeres, *Internationale Revue der gesamten Hydrobiologie und Hydrographie*, *5*(1), 1–42.

Olbers, D., J. Willebrand, and C. Eden (2012), *Ocean Dynamics*, Springer.

Ollitrault, M., and J.-P. Rannou (2013), Andro: An argo-based deep displacement dataset, *Journal of Atmospheric and Oceanic Technology*, *30*(4), 759–788.

Olsen, S. M., B. Hansen, D. Quadfasel, and S. Østerhus (2008), Observed and modelled stability of overflow across the greenland-scotland ridge, *Nature*, *455*, 519.

Palter, J. B., M. S. Lozier, and K. L. Lavender (2008), How does labrador sea water enter the deep western boundary current?, *J. Phys. Oceanogr.*, *38*(5), 968–983, doi:10.1175/2007jpo3807.1.

Patara, L., and C. Boning (2014), Abyssal ocean warming around antarctica strengthens the atlantic overturning circulation, in *AGU Fall Meeting Abstracts*.

Perez, F. F., et al. (2018), Meridional overturning circulation conveys fast acidification to the deep atlantic ocean, *Nature*, *554*(7693), 515.

Perkins, H., T. S. Hopkins, S. Malmberg, P. Poulain, and A. Warn-Varnas (1998), Oceanographic conditions east of iceland, *Journal of Geophysical Research: Oceans*, *103*(C10), 21,531–21,542.

Phelps, J. J. C., J. A. Polton, A. J. Souza, and L. A. Robinson (2013), Hydrodynamic timescales in a hyper-tidal region of freshwater influence, *Continental Shelf Research*, *63*, 13–22.

Pickart, R. S., and M. A. Spall (2007), Impact of labrador sea convection on the north atlantic meridional overturning circulation, *J. Phys. Oceanogr.*, *37*(9), 2207–2227, doi:10.1175/jpo3178.1.

Pickart, R. S., D. J. Torres, and R. A. Clarke (2002), Hydrography of the labrador sea during active convection, *Journal of Physical Oceanography*, *32*(2), 428–457.

Pickart, R. S., M. A. Spall, M. H. Ribergaard, G. W. K. Moore, and R. F. Milliff (2003a), Deep convection in the irminger sea forced by the greenland tip jet, *Nature*, *424*, 152.

Pickart, R. S., F. Straneo, and G. Moore (2003b), Is labrador sea water formed in the irminger basin?, *Deep Sea Research Part I: Oceanographic Research Papers*, *50*(1), 23–52.

Pickart, R. S., D. J. Torres, and P. S. Fratantoni (2005), The east greenland spill jet*, *J. Phys. Oceanogr.*, *35*(6), 1037–1053, doi:10.1175/JPO2734.1.

Pickart, R. S., K. Våge, G. W. K. Moore, I. A. Renfrew, M. H. Ribergaard, and H. C. Davies (2008), Convection in the western north atlantic sub-polar gyre: Do small-scale wind events matter?, in *Arctic-Subarctic Ocean Fluxes: Defining the Role of the Northern Seas in Climate*, pp. 629–652, Springer Netherlands, Dordrecht.

Piron, A., V. Thierry, H. Mercier, and G. Caniaux (2016), Argo float observations of basin-scale deep convection in the irminger sea during winter 2011-2012, *Deep Sea Research Part I: Oceanographic Research Papers*, *109*, 76–90.

Poje, A. C., A. C. Haza, T. M. Özgökmen, M. G. Magaldi, and Z. D. Garraffo (2010), Resolution dependent relative dispersion statistics in a hierarchy of ocean models, *Ocean Modelling*, *31*(1), 36–50.

Pond, S., and K. Bryan (1976), Numerical models of the ocean circulation, *Rev. Geophys.*, *14*(2), 243–263, doi:10.1029/rg014i002p00243.

Prandle, D., S. G. Loch, and R. Player (1993), Tidal flow through the straits of dover, *J. Phys. Oceanogr.*, *23*(1), 23–37, doi:10.1175/1520-0485(1993)023<0023:tfttso>2.0.co;2.

Purkey, S. G., and G. C. Johnson (2010), Warming of global abyssal and deep southern ocean waters between the 1990s and 2000s: Contributions to global heat and sea level rise budgets**., *Journal of Climate*, *23*(23).

Qin, X., E. van Sebille, and A. Sen Gupta (2014), Quantification of errors induced by temporal resolution on lagrangian particles in an eddy-resolving model, *Ocean Modelling*, *76*, 20–30.

Rahmstorf, S. (1994), Rapid climate transitions in a coupled ocean–atmosphere model, *Nature*, *372*(6501), 82.

Rahmstorf, S., L. Caesar, G. Feulner, A. Robinson, and V. Saba (2017), Observed fingerprint of a weakening atlantic ocean overturning circulation, in *AGU Fall Meeting Abstracts*.

Read, J. F., and W. J. Gould (1992), Cooling and freshening of the subpolar north atlantic ocean since the 1960s, *Nature*, *360*, 55.

Redler, R., and C. W. Böning (1997), Effect of the overflows on the circulation in the subpolar north atlantic: A regional model study, *Journal of Geophysical Research: Oceans*, *102*(C8), 18,529–18,552.

Rhein, M., J. Fischer, W. M. Smethie, D. Smythe-Wright, R. F. Weiss, C. Mertens, D.-H. Min, U. Fleischmann, and A. Putzka (2002), Labrador sea water: Pathways, cfc inventory, and formation rates, *Journal of Physical Oceanography*, *32*(2), 648–665, doi:10.1175/1520-0485(2002)032<0648:LSWPCI>2.0.CO;2.

Rhein, M., R. Steinfeldt, D. Kieke, I. Stendardo, and I. Yashayaev (2017), Ventilation variability of labrador sea water and its impact on oxygen and anthropogenic carbon: a review, *Philos Transact A Math Phys Eng Sci*, *375*(2102).

Richardson, P. L. (1983), Eddy kinetic energy in the north atlantic from surface drifters, *Journal of Geophysical Research: Oceans*, *88*(C7), 4355–4367.

Rieck, J. K. (2019), The nature and variability of eddy kinetic energy in an ocean general circulation model with a focus on the south pacific subtropical gyre and the labrador sea, Ph.D. thesis, Christian-Albrechts Universität Kiel.

Rieck, J. K., C. W. Böning, R. J. Greatbatch, and M. Scheinert (2015), Seasonal variability of eddy kinetic energy in a global high-resolution ocean model, *Geophysical Research Letters*, *42*(21), 9379–9386.

Rieck, J. K., C. Böning, and K. Getzlaff (2018), The nature of eddy kinetic energy in the labrador sea: Different types of mesoscale eddies, their temporal variability and impact on deep convection, *Journal of Physical Oceanography*.

Roach, C. J., D. Balwada, and K. Speer (2016), Horizontal mixing in the southern ocean from argo float trajectories, *J. Geophys. Res. Oceans*, *121*(8), 5570–5586, doi:10.1002/2015jc011440.

Roach, C. J., D. Balwada, and K. Speer (2018), Global observations of horizontal mixing from argo float and surface drifter trajectories, *J. Geophys. Res. Oceans*, *123*(7), 4560–4575, doi:10.1029/2018jc013750.

Roemmich, D., and C. Wunsch (1985), Two transatlantic sections: meridional circulation and heat flux in the subtropical north atlantic ocean, *Deep Sea Research Part A. Oceanographic Research Papers*, *32*(6), 619–664.

Rossby, T., and C. N. Flagg (2012), Direct measurement of volume flux in the faroe-shetland channel and over the iceland-faroe ridge, *Geophys. Res. Lett.*, *39*(7), doi:10.1029/2012gl051269.

Rossby, T., G. Reverdin, L. Chafik, and H. Søiland (2017), A direct estimate of poleward volume, heat, and freshwater fluxes at 59.5° n between greenland and scotland, *Journal of Geophysical Research: Oceans*, *122*(7), 5870–5887.

Rossby, T., C. Flagg, L. Chafik, B. Harden, and H. Søiland (2018), A direct estimate of volume, heat, and freshwater exchange across the greenland-iceland-faroe-scotland ridge, *Journal of Geophysical Research: Oceans*, *123*(10), 7139–7153.

Ruzmaikin, A., H. H. Aumann, and J. H. Jiang (2015), Interhemispheric variability of earth's radiation, *J. Atmos. Sci.*, *72*(12), 4615–4628, doi:10.1175/jas-d-15-0106.1.

Rypina, I. I., A. Kirincich, S. Lentz, and M. Sundermeyer (2016), Investigating the eddy diffusivity concept in the coastal ocean, *Journal of Physical Oceanography*, *46*(7), 2201–2218.

Rühs, S., J. V. Durgadoo, E. Behrens, and A. Biastoch (2013), Advective timescales and pathways of agulhas leakage, *Geophys. Res. Lett.*, *40*(15), 3997–4000, doi:10.1002/grl.50782.

Rühs, S., V. Zhurbas, I. M. Koszalka, J. V. Durgadoo, and A. Biastoch (2018), Eddy diffusivity estimates from lagrangian trajectories simulated with ocean models and surface drifter data–a case study for the greater agulhas system, *J. Phys. Oceanogr.*, *48*(1), 175–196, doi:10.1175/jpo-d-17-0048.1.

Rühs, S., F. Schwarzkopf, S. Speich, and A. Biastoch (2019), Cold vs. warm water route–sources for the upper limb of the atlantic meridional overturning circulation revisited in a high-resolution ocean model.

Sallée, J. B., K. Speer, R. Morrow, and R. Lumpkin (2008), An estimate of lagrangian eddy statistics and diffusion in the mixed layer of the southern ocean, *Journal of Marine Research*, *66*(4), 441–463, doi:10.1357/002224008787157458.

Sarafanov, A., A. Falina, H. Mercier, A. Sokov, P. Lherminier, C. Gourcuff, S. Gladyshev, F. Gaillard, and N. Daniault (2012), Mean full-depth summer circulation and transports at the northern periphery of the atlantic ocean in the 2000s, *Journal of Geophysical Research: Oceans*, *117*(C1).

Schmidtko, S., L. Stramma, and M. Visbeck (2017), Decline in global oceanic oxygen content during the past five decades, *Nature*, *542*, 335.

Schott, F. A., R. Zantopp, L. Stramma, M. Dengler, J. Fischer, and M. Wibaux (2004), Circulation and deep-water export at the western exit of the subpolar north atlantic, *Journal of Physical Oceanography*, *34*(4), 817–843.

Schweckendiek, U., and J. Willebrand (2005), Mechanisms affecting the overturning response in global warming simulations, *Journal of climate*, *18*(23), 4925–4936.

Sheng, J., R. J. Greatbatch, X. Zhai, and L. Tang (2005), A new two-way nesting technique for ocean modeling based on the smoothed semi-prognostic method, *Ocean Dynamics*, *55*(3-4), 162–177.

Siedler, G., J. Gould, and J. A. Church (2001), *Ocean circulation and climate: observing and modelling the global ocean*, vol. 103, Academic Press.

Smeed, D., G. McCarthy, D. Rayner, B. Moat, W. Johns, M. Baringer, and C. Meinen (2016), Atlantic meridional overturning circulation observed by the rapid-mocha-wbts (rapid-meridional overturning circulation and heatflux array-western boundary time series) array at 26n from 2004 to 2015.

Smeed, D. A., et al. (2014), Observed decline of the atlantic meridional overturning circulation 2004-2012, *Ocean Sci.*, *10*(1), 29–38.

Smethie, W. M., R. A. Fine, A. Putzka, and E. P. Jones (2000), Tracing the flow of north atlantic deep water using chlorofluorocarbons, *J. Geophys. Res.*, *105*(C6), 14,297–14,323, doi:10.1029/1999jc900274.

Smethie Jr., W. M., and R. A. Fine (2001), Rates of north atlantic deep water formation calculated from chlorofluorocarbon inventories, *Deep Sea Research Part I: Oceanographic Research Papers*, *48*(1), 189–215.

Smith, R. D., M. E. Maltrud, F. O. Bryan, and M. W. Hecht (2000), Numerical simulation of the north atlantic ocean at 1/10, *Journal of Physical oceanography*, *30*(7), 1532–1561.

Spall, M. A., and R. S. Pickart (2003), Wind-driven recirculations and exchange in the labrador and irminger seas, *Journal of Physical Oceanography*, *33*(8), 1829–1845.

Spall, M. A., P. L. Richardson, and J. Price (1993), Advection and eddy mixing in the mediterranean salt tongue, *Journal of Marine Research*, *51*(4), 797–818.

Srokosz, M., M. Baringer, H. Bryden, S. Cunningham, T. Delworth, S. Lozier, J. Marotzke, and R. Sutton (2012), Past, present, and future changes in the atlantic meridional overturning circulation, *Bull. Amer. Meteor. Soc.*, *93*(11), 1663–1676, doi:10.1175/BAMS-D-11-00151.1.

Stammer, D., and C. Wunsch (1999), Temporal changes in eddy energy of the oceans, *Deep Sea Research Part II: Topical Studies in Oceanography*, *46*(1-2), 77–108.

Stammer, D., C. Wunsch, R. Giering, C. Eckert, P. Heimbach, J. Marotzke, A. Adcroft, C. N. Hill, and J. Marshall (2003), Volume, heat, and freshwater transports of the global ocean circulation 1993–2000, estimated from a general circulation model constrained by world ocean circulation experiment (woce) data, *Journal of Geophysical Research: Oceans*, *108*(C1), 7–1–7–23.

Steele, M., R. Morley, and W. Ermold (2001), Phc: A global ocean hydrography with a high-quality arctic ocean, *Journal of Climate*, *14*(9), 2079–2087.

Stocker, T. F., and D. G. Wright (1991), Rapid transitions of the ocean's deep circulation induced by changes in surface water fluxes, *Nature*, *351*(6329), 729–732.

Stocker, T. F., Q. Dahe, and G.-K. Plattner (2013), Climate change 2013: The physical science basis, *Working Group I Contribution to the Fifth Assessment Report of the Intergovernmental Panel on Climate Change. Summary for Policymakers (IPCC, 2013)*.

Straneo, F. (2006), Heat and freshwater transport through the central labrador sea, *Journal of Physical Oceanography*, *36*(4), 606–628.

Straneo, F., R. S. Pickart, and K. Lavender (2003), Spreading of labrador sea water: an advective-diffusive study based on lagrangian data, *Deep Sea Research Part I: Oceanographic Research Papers*, *50*(6), 701–719.

Sutton, R. T., and D. L. R. Hodson (2005), Atlantic ocean forcing of north american and european summer climate, *science*, *309*(5731), 115–118.

Sverdrup, H. U., M. W. Johnson, and R. H. Fleming (1942), *The Oceans: Their physics, chemistry, and general biology*, vol. 7, Prentice-Hall New York.

Sweeney, C., A. Gnanadesikan, S. M. Griffies, M. J. Harrison, A. J. Rosati, and B. L. Samuels (2005), Impacts of shortwave penetration depth on large-scale ocean circulation and heat transport, *J. Phys. Oceanogr.*, *35*(6), 1103–1119, doi:$10.1175/\mathrm{jpo2740.1}$.

Swingedouw, D., C. B. Rodehacke, E. Behrens, M. Menary, S. M. Olsen, Y. Gao, U. Mikolajewicz, J. Mignot, and A. Biastoch (2013), Decadal fingerprints of freshwater discharge around greenland in a multi-model ensemble, *Climate dynamics*, *41*(3-4), 695–720.

Sy, A., M. Rhein, J. R. Lazier, K. P. Koltermann, J. Meincke, A. Putzka, and M. Bersch (1997), Surprisingly rapid spreading of newly formed intermediate waters across the north atlantic ocean, *Nature*, *386*(6626), 675.

Takahashi, T., et al. (2009), Climatological mean and decadal change in surface ocean pco2, and net sea-air co2 flux over the global oceans, *Surface Ocean CO2 Variability and Vulnerabilities*, *56*(8), 554–577.

Talley, L. D. (2003), Shallow, intermediate, and deep overturning components of the global heat budget, *Journal of Physical oceanography*, *33*(3), 530–560.

Talley, L. D. (2013), Closure of the global overturning circulation through the indian, pacific, and southern oceans: Schematics and transports, *Oceanography*, *26*(1), 80–97.

Talley, L. D., and M. S. McCartney (1982), Distribution and circulation of labrador sea water, *J. Phys. Oceanogr.*, *12*(11), 1189–1205, doi:10.1175/1520-0485(1982)012<1189:DACOLS>2.0.CO;2.

Talley, L. D., G. L. Pickard, W. J. Emery, and J. H. Swift (2011), *Descriptive physical oceanography: an introduction*, Academic Press.

Toole, J. M., M. Andres, I. A. Le Bras, T. M. Joyce, and M. S. McCartney (2017), Moored observations of the deep western boundary current in the nw atlantic: 2004–2014, *Journal of Geophysical Research: Oceans*, *122*(9), 7488–7505.

Top, Z., W. B. Clarke, and W. J. Jenkins (1987), Tritium and primordial 3he in the north atlantic: a study in the region of charlie-gibbs fracture zone, *Deep Sea Research Part A. Oceanographic Research Papers*, *34*(2), 287–298.

Tréguier, A.-M., S. Theetten, E. P. Chassignet, T. Penduff, R. Smith, L. Talley, J. Beismann, and C. Böning (2005), The north atlantic subpolar gyre in four high-resolution models, *Journal of Physical Oceanography*, *35*(5), 757–774.

Tréguier, A.-M., J. Deshayes, C. Lique, R. Dussin, and J.-M. Molines (2012), Eddy contributions to the meridional transport of salt in the north atlantic, *Journal of Geophysical Research: Oceans*, *117*(C5).

Trenberth, K. E., J. T. Fasullo, and M. A. Balmaseda (2014), Earth's energy imbalance, *Journal of Climate*, *27*(9), 3129–3144.

Uchida, T., R. Abernathey, and S. Smith (2017), Seasonality of eddy kinetic energy in an eddy permitting global climate model, *Ocean Modelling*, *118*, 41–58.

van Sebille, E., M. O. Baringer, W. E. Johns, C. S. Meinen, L. M. Beal, M. F. de Jong, and H. M. van Aken (2011), Propagation pathways of classical labrador sea water from its source region to 26 n, *J. Geophys. Res*, *116*, C12,027.

van Sebille, E., et al. (2017), Lagrangian ocean analysis: fundamentals and practices, *Ocean Modelling*.

Visbeck, M. (2007), Oceanography: Power of pull, *Nature*, *447*(7143), 383.

Våge, K., R. S. Pickart, G. W. K. Moore, and M. H. Ribergaard (2008), Winter mixed layer development in the central irminger sea: The effect of strong, intermittent wind events, *Journal of Physical Oceanography*, *38*(3), 541–565.

Wang, Z., I. Yashayaev, and B. Greenan (2015), Seasonality of the inshore labrador current over the newfoundland shelf, *Continental Shelf Research*, *100*, 1–10.

Warren, B. A. (1999), Approximating the energy transport across oceanic sections, *J. Geophys. Res.*, *104*(C4), 7915–7919, doi:10.1029/1998jc900089.

Weiss, R. F., J. L. Bullister, R. H. Gammon, and M. J. Warner (1985), Atmospheric chlorofluoromethanes in the deep equatorial atlantic, *Nature*, *314*, 608.

Welch, P. (1967), The use of fast fourier transform for the estimation of power spectra: a method based on time averaging over short, modified periodograms, *IEEE Transactions on audio and electroacoustics*, *15*(2), 70–73.

Wijffels, S. E. (2001), .2 ocean transport of fresh water, in *International Geophysics*, vol. 77, pp. 475–488, Elsevier.

Wilks, D. S. (2011), Principal component (eof) analysis, in *International Geophysics*, vol. 100, pp. 519–562, Elsevier.

Willebrand, J., B. Barnier, C. Böning, C. Dieterich, P. D. Killworth, C. Le Provost, Y. Jia, J.-M. Molines, and A. L. New (2001), Circulation characteristics in three eddy-permitting models of the north atlantic, *Progress in Oceanography*, *48*(2), 123–161.

Williams, R. G., V. Roussenov, D. Smith, and M. S. Lozier (2014), Decadal evolution of ocean thermal anomalies in the north atlantic: The effects of ekman, overturning, and horizontal transport, *Journal of Climate*, *27*(2), 698–719.

Willis, J. K., D. Roemmich, and B. Cornuelle (2004), Interannual variability in upper ocean heat content, temperature, and thermosteric expansion on global scales, *Journal of Geophysical Research: Oceans (1978–2012)*, *109*(C12).

Woollings, T., C. Franzke, D. L. R. Hodson, B. Dong, E. A. Barnes, C. C. Raible, and J. G. Pinto (2015), Contrasting interannual and multidecadal nao variability, *Climate Dynamics*, *45*(1), 539–556.

Worthington, L. V. (1976), *On the North Atlantic circulation*, Johns Hopkins University Press, Baltimore.

Wunsch, C. (1997), Henry melson stommel. 27 september 1920—17 january 1992: Elected for. mem. rs 1983.

Wunsch, C. (2001), Chapter 2.1 global problems and global observations, in *International Geophysics*, vol. 77, edited by G. Siedler, J. Church, and J. Gould, pp. 47–58, Academic Press.

Wunsch, C., and P. Heimbach (2013a), Two decades of the atlantic meridional overturning circulation: Anatomy, variations, extremes, prediction, and overcoming its limitations, *Journal of Climate*, *26*(18), 7167–7186.

Wunsch, C., and P. Heimbach (2013b), Dynamically and kinematically consistent global ocean circulation and ice state estimates, in *International Geophysics*, vol. 103, pp. 553–579, Elsevier.

Xu, X., E. P. Chassignet, W. E. Johns, W. J. Schmitz, and E. J. Metzger (2014), Intraseasonal to interannual variability of the atlantic meridional overturning circulation from eddy-resolving simulations and observations, *Journal of Geophysical Research: Oceans*, *119*(8), 5140–5159.

Yang, H., K. Wang, H. Dai, Y. Wang, and Q. Li (2015), Wind effect on the atlantic meridional overturning circulation via sea ice and vertical diffusion, *Climate Dynamics*, pp. 1–17.

Yashayaev, I. (2007), Hydrographic changes in the labrador sea, 1960–2005, *Progress in Oceanography*, *73*(3), 242–276.

Yashayaev, I., and A. Clarke (2008), Evolution of north atlantic water masses inferred from labrador sea salinity series, *Oceanography*, *21*(1), 30–45.

Yashayaev, I., and J. W. Loder (2016), Recurrent replenishment of labrador sea water and associated decadal scale variability, *Journal of Geophysical Research: Oceans*.

Yashayaev, I., H. M. van Aken, N. P. Holliday, and M. Bersch (2007), Transformation of the labrador sea water in the subpolar north atlantic, *Geophysical Research Letters*, *34*(22).

Yashayaev, I., N. P. Holliday, M. Bersch, and H. M. van Aken (2008), The history of the labrador sea water: Production, spreading, transformation and loss, in *Arctic-Subarctic Ocean Fluxes: Defining the Role of the Northern Seas in Climate*, pp. 569–612, Springer Netherlands, Dordrecht.

Yashayaev, I., D. Seidov, and E. Demirov (2015), A new collective view of oceanography of the arctic and north atlantic basins, *Progress in Oceanography*.

Yeager, S., and G. Danabasoglu (2012), Sensitivity of atlantic meridional overturning circulation variability to parameterized nordic sea overflows in ccsm4, *J. Climate*, *25*(6), 2077–2103, doi:10.1175/jcli-d-11-00149.1.

Zantopp, R., J. Fischer, M. Visbeck, and J. Karstensen (2017), From interannual to decadal—17 years of boundary current transports at the exit of the labrador sea, *Journal of Geophysical Research: Oceans*.

Zelenko, A., and Y. D. Resnyansky (2007), Deep convection in the ocean general circulation model: variability on the diurnal, seasonal, and interannual time scales, *Oceanology*, *47*(2), 191–204.

Zhang, R. (2010), Latitudinal dependence of atlantic meridional overturning circulation (amoc) variations, *Geophys. Res. Lett.*, *37*(16), doi:10.1029/2010gl044474.

Zhang, R., and T. L. Delworth (2005), Simulated tropical response to a substantial weakening of the atlantic thermohaline circulation, *Journal of Climate*, *18*(12), 1853–1860.

Zhang, R., and T. L. Delworth (2006), Impact of atlantic multidecadal oscillations on india/sahel rainfall and atlantic hurricanes, *Geophysical Research Letters*, *33*(17).

Zhu, J., E. Demirov, Y. Zhang, and A. Polomska-Harlick (2014), Model simulations of mesoscale eddies and deep convection in the labrador sea, *Advances in Atmospheric Sciences*, *31*(4), 743–754.

Zika, J. D., T. J. McDougall, and B. M. Sloyan (2010), Weak mixing in the eastern north atlantic: An application of the tracer-contour inverse method, *J. Phys. Oceanogr.*, *40*(8), 1881–1893, doi:10.1175/2010jpo4360.1.

Zou, S., and M. S. Lozier (2016), Breaking the linkage between labrador sea water production and its advective export to the subtropical gyre, *J. Phys. Oceanogr.*, *46*(7), 2169–2182, doi:10.1175/jpo-d-15-0210.1.

Østerhus, S., W. R. Turrell, S. Jónsson, and B. Hansen (2005), Measured volume, heat, and salt fluxes from the atlantic to the arctic mediterranean, *Geophysical Research Letters*, *32*(7).

Østerhus, S., T. Sherwin, D. Quadfasel, and B. Hansen (2008), The overflow transport east of iceland, in *Arctic-Subarctic Ocean Fluxes: Defining the Role of the Northern Seas in Climate*, pp. 427–441, Springer Netherlands, Dordrecht.

Østerhus, S., et al. (2019), Arctic mediterranean exchanges: a consistent volume budget and trends in transports from two decades of observations, *Ocean Sci.*, *15*(2), 379–399.

List of Figures

List of Tables